Bottlebrush Polymers: Synthesis, Rheology, and Self-Assembly

A DISSERTATION
SUBMITTED TO THE FACULTY OF THE GRADUATE SCHOOL
OF THE UNIVERSITY OF MINNESOTA
BY

Samuel J. Dalsin

IN PARTIAL FULFILLMENT OF THE REQUIREMENTS
FOR THE DEGREE OF
DOCTOR OF PHILOSOPHY

Frank S. Bates and Marc A. Hillmyer, Advisors

September 2015

Acknowledgements

The research in this thesis was realized with the assistance, training, and collaboration of many generous people who deserve acknowledgement. I must first thank my advisors, Frank Bates and Marc Hillmyer. You are both tremendous teachers and mentors with infectious passion for your work. With such large research groups, I have always been astounded by your ability and willingness to meet quickly for spontaneous research discussions. Thank you both for your guidance and encouragement over the past five years. I want to also thank some of the faculty members who have assisted in my thesis research. David Morse, thank you for serving on my thesis committee and providing your perspective on my experimental results. I have thoroughly enjoyed our impromptu discussions at espresso expose and on the 115 bus route. Mahesh Mahanthappa, thank you for the detailed feedback on my research and for your interest in bottlebrush polymer science. It has been a great experience discussing this research with you over the past few months. I am sure that new projects in this field will be initiated at the U of M under your guidance. Chris Macosko, thank you for making the time to meet with me throughout the past five years. All of my rheology studies were greatly assisted by your expertise and patient teaching.

I want to collectively thank both the Bates and the Hillmyer research groups. The genuine scientific curiosity of so many of the graduate students and postdocs fosters a collaborative environment with open discussions, which so frequently guide the research. I have always found that the most significant advancements in my work have derived in some way from conversations and feedback from my lab and office mates. Early in my graduate school career I received training from Louis Pitet and Thanasis Touris, who helped me learn valuable polymer synthesis techniques. Thank you both for your generous training. I have since been fortunate to work with several more influential researchers who have been instrumental in guiding my thesis work as well as my professional growth. In particular, I want to thank Justin Kennemur, Justin Bolton, and

encouragement and welcome distractions from my research. Thanks for all of your friendship, particularly during the times of working odd hours with long intervals of social vacancy. Most significantly, I want to thank my wife Molly. The passion you bring to your own work is truly inspiring, and I am incredibly lucky and motivated by you every day. Thank you for your unconditional love and encouragement.

Dedicated to my wife Molly and our family.

Abstract

Bottlebrush polymers are comb-like molecules with a high density of side chains grafted along a central backbone. Due to their unique conformational properties, bottlebrush polymers have become attractive candidates for developing new photonic bandgap materials, nanotubes and nanowires, or drug delivery vehicles, to name a few. This dissertation primarily investigates the rheological properties and self-assembly behavior of bottlebrush polymer molecules made using a variety of different polymerization routes. A considerable portion of the work is directed towards the linear rheology of model, polyolefin-based bottlebrush polymers with independently varied branch and backbone lengths. These studies demonstrate how the tight spacing between branch points effectively precludes backbone entanglement in the polymer melts, but it does not inhibit the formation of entanglements among the branched side chains. Furthermore, the relaxation profiles reveal transient scaling behavior in which the dynamics transition from Zimm-like to Rouse-like at increasing relaxation times. These results highlight the distinct conformational character of bottlebrushes at different length scales. The latter parts of this work report on the self-assembly behavior of bottlebrush diblock polymers composed of atactic polypropylene and polystyrene side chains. The diblock samples are analyzed using small-angle X-ray scattering and atomic force microscopy. Nearly all of the samples display strong segregation between the two blocks, owing to the large molar mass of typical bottlebrush polymers. Consequently, only one experimental sample displays an accessible order-disorder transition temperature. The strong segregation is also shown to affect the ability of large bottlebrush diblocks to readily achieve well-ordered nanostructures by self-assembly. Finally, results of the most symmetric (by volume fraction) diblock samples are compared with predictions of a newly developed self-consistent field theory model, yielding remarkable quantitative agreement. The theory is further utilized to conclusively establish the molecular origins of the domain scaling behavior in lamellar forming diblock bottlebrush polymers.

Table of Contents

List of Tables

List of Figures

Chapter 1

Introduction and Background

Several of the leading challenges facing modern society have been identified as areas of opportunity for advancement in polymer science, including sustainability, health care, security, and energy.[1] Polymeric materials serve as necessary components in addressing these global issues because of their broad and highly tunable properties. Polymer molecules in their simplest form are long chain-like molecules composed of repeating "monomer" units. Small adjustments to the monomer level chemistry can generate substantial modifications to the material characteristics, such as surface energy, degradability, conductivity, or responsiveness to external stimuli. Alternatively, many physical attributes of polymer materials are almost entirely governed by their macromolecular structure, *i.e.*, size, shape, and branching. These factors influence the mechanical properties (elasticity and strength), flow characteristics (viscosity and surface wetting), and miscibility with other components. The versatility of polymer molecules exposes myriad opportunities for interdisciplinary research to approach both fundamental scientific questions and pressing technological needs.

One significant area in polymer research is the study of how complex molecular architectures affect the material properties. Investigation into the influence of long-chain branching in polymers has been of interest for a many years. Scientists have considered

star polymers, comb polymers, dendrimers, pom-poms, each of which has unique consequences towards the physical behavior in the solid and fluid states. Additionally, these features strongly influence the thermodynamics of mixing with other components in blends or as additives. With advancements in controlled polymerization techniques, we now have a greater ability than ever before to synthesize polymers with precise molecular designs. The work presented in this thesis focuses on the study of "bottlebrush" polymers, with emphasis on how the highly branched structure affects both nanoscopic (self-assembly) and macroscopic (bulk rheology) properties.

1.1   Bottlebrush Polymers

Bottlebrush polymers represent a class of comb-like polymer molecules with regular branching along a central backbone (Figure 1.1). Bottlebrush polymers are an extreme case in which every single backbone repeat unit contains at least one branch, inducing substantially altered conformational behavior relative to more traditional linear polymer molecules. Due to the excluded volume effects concomitant with a high branching density, bottlebrush molecules are characterized by a wormlike, cylindrical conformation.[2-7] The unique geometry of individual bottlebrushes makes them attractive candidates for new types of self-assembled nanoparticles, with potential use as sensors or drug-delivery vehicles.[8-11] Furthermore, their large special dimensions can be exploited to design discrete nano-objects,[12] and the large number of chain-ends provides accessible sites for appending desired functionalities or chemical tags. As bulk materials, the extended molecular conformation hampers the development of intermolecular entanglements and results in materials with accelerated relaxation dynamics relative to linear polymers of the same molar mass.[13-21] Consequently, numerous applications have been proposed for bottlebrush polymers, including rheological modifiers,[22] stimuli-responsive coatings,[23] nanoporous materials,[24] supersoft elastomers,[16] and photonic bandgap materials.[25-27]
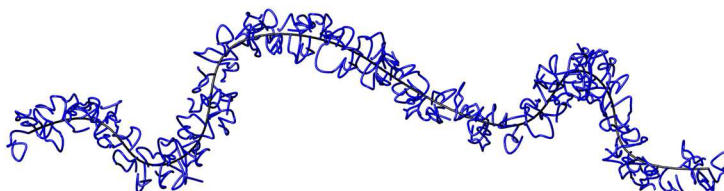
Figure 1.1. Graphic of a bottlebrush polymer chain, projected from a 3D model.

Bottlebrush polymers have recently become an active research area due to improvements in controlled polymerization methods that enable facile synthesis of polymers with well-defined molecular dimensions.[2,12,28,29] Generally, there are three methods for preparing bottlebrush polymers: grafting-to, grafting-from, and grafting-through polymerization (Figure 1.2). The grafting-to method involves the attachment of relatively short monotelechelic (functionalized on just one chain end) polymer chains to a functional polymer backbone.[30-32] One advantage of this route is that both the side chains and the backbones can be fully characterized independently. However, this method relies on a coupling reaction of two macromolecular species at tightly spaced intervals. It is therefore difficult to achieve high grafting efficiencies needed to produce well-defined bottlebrush molecules.

The grafting-from method involves the polymerization of side chains directly from a functional backbone (macroinitiator) containing a predetermined number of initiation sites.[33-38] Advantages of this method include the ability to synthesize long backbone precursors that are easily characterized and to generate a variety of bottlebrushes with altered side chain lengths from the same macroinitiator (giving a constant backbone length). This route can also enable the synthesis of highly complex, multicomponent bottlebrushes with several branch chemistries on a single backbone chain. However, this requires experimentally demanding synthetic processes, involving sequential polymerization techniques and multiple protection/deprotection steps.[39] It can also be

difficult to determine the precise initiation efficiency and the side chain length and dispersity.
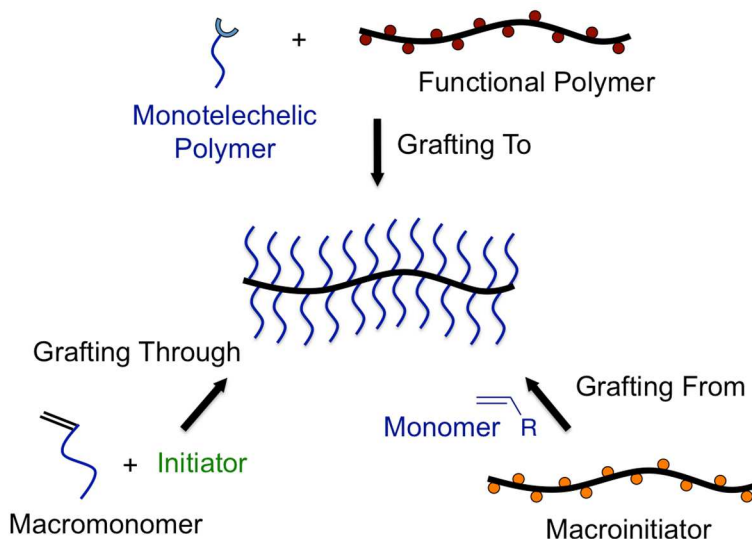
Figure 1.2. Synthetic approaches toward bottlebrush polymers. Adapted from ref 2.

Grafting-through synthesis involves the direct polymerization of monotelechelic polymer chains, referred to as macromonomers. This process is carried out in the same way as a conventional polymerization, so that macromonomer end groups are strung together to produce the backbone chains. Bottlebrush polymers made using this method are often termed poly(macromonomer)s. Like grafting-to synthesis, grafting-through has the advantage that side chains can be fully characterized prior to bottlebrush production. Additionally, this route generates molecules with uniform grafting density, containing one side chain on every backbone repeat unit. One drawback to this strategy is that it can be difficult to achieve complete macromonomer conversion, resulting in products with bimodal molecular weight distributions corresponding to the separate bottlebrush and macromonomer populations.[40]

The initial stages of this thesis research involved experimentation with different synthetic methods to generate well-defined bottlebrush polymers composed of polyolefin side chains (chapter 3). The physical properties of the new bottlebrush materials were

then investigated to gain insight on the effects of the high branch density. Specifically, the bulk polymer relaxation dynamics were examined by rheological characterization.

1.2   Rheology

The physical nature of condensed-matter materials can most generally be described as either solid or liquid. However, many materials, especially those composed of polymeric constituents, cannot be classified easily into one category or the other. Instead the materials can be described as *viscoelastic*, meaning that the response to any imposed deformation is intermediate between purely elastic (conserved energy) and purely viscous (dissipated energy). Moreover, the degree to which materials exhibit elastic and viscous properties varies with time, often behaving solid-like at short times and liquid-like at long times.[41] The classic example of a viscoelastic material is a ball of Silly Putty, which bounces when thrown against a wall due to the elasticity of the short-time response, but flows into a puddle when left unperturbed for several minutes due to the long time liquid-like behavior.[42] The field of study relating to these "complex fluids" is known as *rheology*. This is a particularly important area when evaluating the behavior of polymers, because small changes in molecular structure can lead to large changes in the macroscopic flow properties. From a practical standpoint, rheological study of high-value polymeric materials is essential for optimizing the processing conditions and tuning the mechanical performance of the final products.

The rheological behavior of traditional polymer melts (*i.e.*, the state above any characteristic melting temperature or glass transition) is primarily influenced by the presence of entanglements between overlapping polymer chains. Entanglements develop because of the expansive special extent of individual polymer coils and represent topological constraints that slow the system dynamics by limiting chain mobility. The volume pervaded by a polymer coil in the melt scales as $V_p \sim M^{3/2}$, owing to the random-walk conformation of the "Gaussian chains". Thus, the space pervaded by individual polymers increases more rapidly than the volume occupied by the chain segments ($V_{occ} \sim M$), so each chain must overlap with an increasing number of neighboring chains to

maintain constant density, causing substantial chain entanglement. One of the most significant consequences of this is the dramatic increase in melt viscosity with increased polymer size. Figure 1.3 displays on overlay of the viscosity (η) versus molar mass for several different polymer materials. This plot reveals a transition in the viscosity dependence from a linear scaling of $\eta \sim M$ to an empirically determined relationship of $\eta \sim M^{3.4}$ above some critical molar mass (M_c). This transition represents the onset of entanglement networks within the material and causes the extraordinarily strong dependence of η on molecular size.[43]
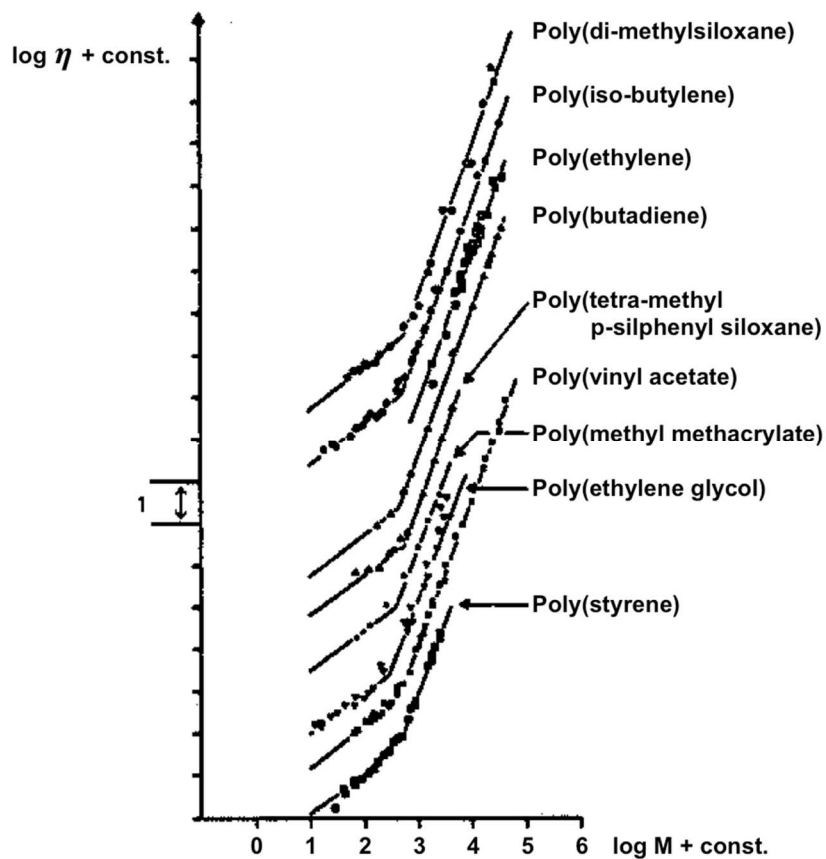
Figure 1.3. Log viscosity (η) versus log molar mass (M) for a variety of linear polymers, shifted by arbitrary shift factors for representation. Straight line fits have slopes of 1.0 and 3.4. Plot adapted from ref 43.

The formation of entanglement networks is primarily controlled by the macromolecular structure, rather than the specific monomer-scale chemistry. This is demonstrated by the universal behavior of different polymer melts shown in Figure 1.3. Consequently, structural adjustments have a large influence on the rheological behavior. Understanding of the rheological implications of branching in polymer molecules is important for both design and characterization of new polymer materials. A considerable amount of the research in this thesis focuses on the rheological behavior of polyolefin-based bottlebrush polymers (chapters 4 and 5). Details on the specific measurement techniques and data analysis are provided in chapter 2.

1.3   Polymer Phase Behavior

1.3.1   Polymer-Polymer Mixtures

Blending of two or more polymer components is a straightforward and practical method of expanding the range of physical properties available to single component systems and formulating new and useful materials. The mechanical properties of blends are highly dependent on the polymer-polymer compatibility/miscibility. Depending on the desired properties, complete miscibility may be the best scenario to attain synergistic effects. However, nearly all polymer-polymer blends are immiscible and will drive towards phase separation to produce large domains of the pure polymer components.

To understand the thermodynamics of polymer-polymer mixtures, the Flory-Huggins theory has traditionally been applied as a first approximation. Flory and Huggins developed this pioneering theory over seventy years ago as an extension of regular solution theory, designed to describe the thermodynamics of binary systems with at least one polymeric component.[49,50] The following Flory-Huggins relationship approximates the free energy of mixing for binary polymer blends:

$$\frac{\Delta F}{k_B T} = \frac{\phi_A}{N_A}\ln(\phi_A) + \frac{(1-\phi_A)}{N_B}\ln(1-\phi_A) + \phi_A(1-\phi_A)\chi \tag{1.1}$$

in which ϕ_A is the volume fraction of species A, N_A and N_B are the degrees of polymerization for species A and B, respectively, k_B is the Boltzmann constant, and χ is the segment-segment interaction parameter. The first two terms of equation 1.1 represent the purely combinatorial entropy of mixing. The final term, as originally defined by the Flory-Huggins theory, contained only the excess *enthalpy* of mixing and utilized the interaction parameter χ_0:

$$\chi_0 = \frac{z[\varepsilon_{AB} - 0.5(\varepsilon_{AA} + \varepsilon_{BB})]}{k_B T} \tag{1.2}$$

where z is the coordination number and ε_{AB} represents interactions between segments of component A and component B. Without consideration to any excess entropy effects, this definition of χ (given here as χ_0) has failed to quantitatively depict the thermodynamics of real polymer solutions and blends.[51] Consequently, the now commonly used χ parameter is actually an effective χ (χ_{eff}), which encompasses all excess free energy effects into one value. This χ_{eff} is generally fitted to the form $\chi_{eff} = \alpha/T + \beta$, where α and β are fitting parameters for enthalpic and entropic excess free energy contributions, respectively.

While adoption of this χ_{eff} parameter (which will be referred to simply as χ) is a convenient practice for reporting empirical results, it is not truly a model prediction. Furthermore, χ reflects no ϕ or N dependence in its definition. Thus, the reported values of χ can only be uniquely fit with α and β parameters for a system with fixed composition, component molecular weights, and molecular architecture, making it very difficult to draw specific conclusions about the thermodynamic origins of χ for any binary system of study.

Several corrections to the Flory-Huggins theory have been proposed and examined on polyolefin systems as a means to decouple and identify the fundamental contributions to the excess free energy of mixing in polymer blends. Four groups in particular have provided competing theories to accurately dissect and explain polymer-polymer thermodynamics. Dudowicz and Freed developed the lattice cluster theory based on statistical thermodynamics to account for local monomer interactions through segmental

shape and compressibility differences.[52,53] An alternative first-principles approach taken by Schweizer and Curro has involved modification of the reference interaction site model (RISM) for application in polymer mixtures, referred to as PRISM theory.[54,55] Graessley *et al.* have proposed a formalism based on regular solution theory that suggests phase behavior of polyolefin blends may be predicted based on the difference in solubility parameters between the mixture components.[56,57] Lastly, a field theory approach was taken by Bates and Fredrickson to extract universal thermodynamic features that contribute to nonlocal excess entropy of mixing corrections to χ.[58-60] Experimental studies involved in testing this approach led to the conclusion that the excess free energy of mixing in nearly athermal polyolefin blends is dictated by differences in the statistical segment length of each component. These entropic contributions arise from the required conformational adjustments of blended species that exhibit differences in their reference state conformational packing properties and architectural features. More concisely, the unfavorable entropic effects are attributed to "conformational asymmetry"; a measure defined by differences in the statistical segment lengths of the blended melts. The statistical segment length is defined as

$$ b = R_g \left(\frac{6}{N} \right)^{1/2} \tag{1.3} $$

where R_g is the radius of gyration of polymer coil and N is the number of statistical segments. The radius of gyration, defined as the root-mean-square, mass-weighted average distance between monomer units and the center of mass of the polymer coil,[51] is a geometric parameter that is dependent on the surrounding chemical environment. Accordingly, any disparity in the statistical segment lengths between two polymer species corresponds to differences in their reference state coil conformations, *i.e.*, conformations in the pure polymer melts. Upon mixing two species with conformational asymmetry, individual polymer coils must adjust packing conformations to fill space uniformly, thus sustaining positive excess entropy of mixing.

This effect is particularly evident in blends of highly branched and linear polymer chains. The pronounced architectural asymmetry between species produces significant entropic penalties upon mixing and drives phase separation, even in branched/linear blends composed of chains with the same monomer repeat units. This was observed in both branched/linear polystyrene (PS)[61] blends and branched/linear poly(ethyl ethylene) (PEE)[62,63] mixtures at large overall molecular weights. Theoretical predictions of Fredrickson *et al.* coincide with the results of these studies.

1.3.2   Block Polymer Self-Assembly

Block polymers represent a type of copolymer composed of two or more distinct repeat units that are chemically linked and arranged sequentially in a "block" configuration. The complexity of block polymers can be increased rapidly by adding multiple blocks to a single polymer chain, leading to possible architectures of diblocks, triblocks, multiblocks, *etc.*[64] We will focus our discussion to the simplest case of diblock copolymers. When incorporated into systems with other materials, polymeric or otherwise, block polymers can be utilized to stabilize emulsions, compatibilize two or more immiscible materials, create micellar nanoparticles, or form homogeneous mixtures with modified macroscopic material properties. Moreover, much of the intrigue in block polymers over the past few decades has been motivated by their ability to self-assemble into ordered structures with periodic features on a nanoscopic length scale.

Diblock polymers can be envisioned as two separate homopolymers joined together by their ends. As such, the theoretical development regarding polymer-polymer blend thermodynamics can be adopted for first approximation of block polymer phase behavior. The homogeneous, well-mixed state of an A-B diblock polymer melt is similar to the homopolymer blend of components A and B. Upon increasing the segment-segment interaction parameter χ (*e.g.,* lowering the temperature in most cases), the chemical incompatibility of the two blocks drives the system towards phase separation. However, the A and B components cannot phase separate on a macroscopic length scale in the case of block polymers due to the covalent connectivity of the blocks. Therefore, as the

components attempt to segregate from one another, "microphase-separated" patterns of periodic A-rich and B-rich domains are formed. Each domain is typically on the length scale of 5-50 nm, with A/B junction points of the diblock polymers localized at the domain interfaces.[65,66]

The size and morphology of the assembled nanostructures are primarily dependent on just three parameters: the total degree of polymerization, the volume fraction of each block, and the segment-segment interaction parameter (N, ϕ, and χ, respectively).[67,68] This can actually be simplified a bit further. Since the entropic and enthalpic contributions to the system free energy are inversely proportional and scale with N^{-1} and χ, respectively (see equation 1.1), the two can be combined into a composite parameter for segregation strength, χN. Thus, A-B diblock polymer phase diagrams are usually mapped as χN versus ϕ to completely define the equilibrium phases. At sufficiently high incompatibility (high χN) the system will always favor ordering, and the specific ordered morphology is dictated by ϕ. Symmetric diblocks ($\phi = 0.5$) will favor lamellar morphologies, while increasing asymmetry will lead to cylindrical or spherical ordered phases (Figure 1.4). The equilibrium structure achieved for any given diblock system is governed by a balance between the enthalpic drive to minimize interfacial area and the entropic drive to reduce chain stretching and maintain random-walk conformations. The non-lamellar morphologies provide diminished interfacial area per volume and are favored for blocks with asymmetric volume fractions, which can fill space naturally in these phases without significant chain stretching. Note: the morphologies in Figure 1.4 represent only the most commonly encountered for diblock polymers.[69] Several more complicated phases can be attained, including network (or gyroid) phases,[70] which are beyond the scope of this work.
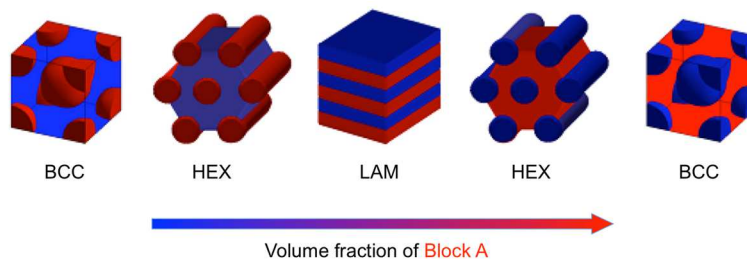
Figure 1.4. Representations of spherical (BCC), cylindrical (HEX), and lamellar (LAM) morphologies created by the self-assembly of strongly segregated diblock polymers and controlled by the relative volume fraction of each component. Figure adapted from ref 69 and ref 70.

The concept of conformational asymmetry was introduced in the previous section as an additional effect towards polymer-polymer immiscibility. In diblock polymers, conformational asymmetry influences the phase behavior beyond the magnitude of χN, as it also affects the relative stability of different ordered phases and changes the equilibrium domain spacing.[71] This originates from the disparate space-filling preferences of blocks with unmatched statistical segment lengths. Figure 1.5 displays phase diagrams produced by mean-field theory calculations of diblock polymer systems with increasing conformational asymmetry (b_A/b_B) from top to bottom. A clear shift in the phase boundaries is shown with increasing conformational asymmetry, causing the non-lamellar phases to be more stabilized when block A is the minority component. This example illustrates the complications in phase behavior that arise in simple diblock polymers with two linear components. Additional factors must be considered when branching is introduced.
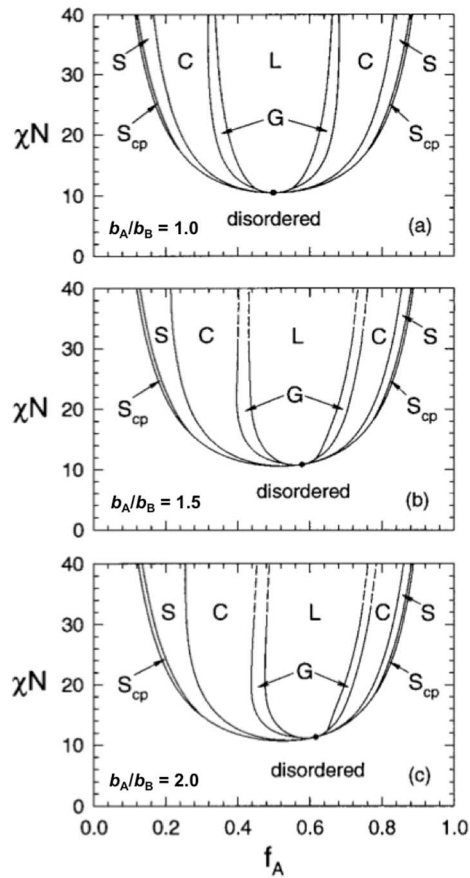
Figure 1.5. Phase diagrams of A-B diblock polymer melts with increasing conformational asymmetry, created using mean-field theory calculations. The equilibrium phases represent lamellae (L), gyroid (G), hexagonally packed cylinders (C), BCC spheres (S), and close-packed spheres (S_{cp}). Plots are shown as segregation strength (χN) versus volume fraction of block A (f_A), and the statistical segment lengths are b_A and b_B for blocks A and B, respectively. This figure was reproduced from ref 71.

1.3.3   Self-Assembly of Bottlebrush Polymers

Development of bottlebrush block polymers is of interest for creating new materials with properties that are not attainable with conventional block polymers. The dense branching structure of bottlebrush molecules gives them unique dynamic and space filling behavior, both of which affect the self-assembly of block polymer systems. Recent research has demonstrated the ability of bottlebrush diblock polymers to organize into structures with domain sizes well over 100 nm. This can be much more difficult to achieve using

traditional block polymers because of the high entanglement density that develops in high molar mass linear polymers, which causes prohibitively slow self-assembly kinetics. Bottlebrush block polymers, alternatively, can be constructed to very high molar mass while maintaining reasonably fast ordering dynamics. This behavior has been exploited to create new photonic materials with adjustable bandgaps to reflect ultraviolet, visable, and infrared light.[72] The large domains have also been used to create nanoporous materials with pore sizes exceeding 50 nm. This was achieved by the assembly of polystyrene–polylactide (PS–PLA) bottlebrush diblocks with asymmetric side chain lengths into a cylindrical morphology, such that the PLA block with shorter branches formed the cylindrical domains (Figure 1.6).[24] The PLA cylinders were then etched out to create the nanoporous monoliths. This presented an attractive route for creating porous materials with extraordinarily large pore sizes, since the backbone chain of the minority block remained intact and served as a type of pore coating after removal of the PLA side chains. This is an additional advantage of this bottlebrush architecture, which could be further tailored by adjustment of the backbone chemistry.
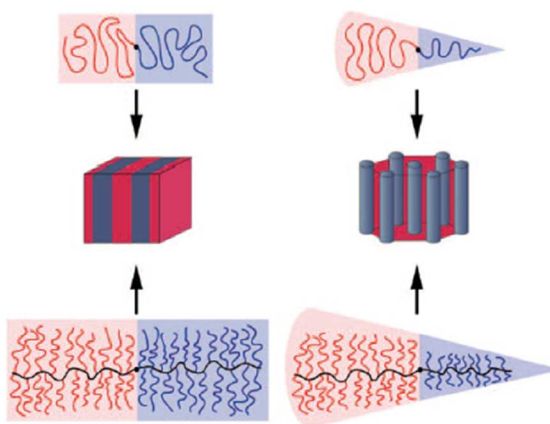
Figure 1.6. Self-assembled phases stabilized by the molecular structure of A-B diblock polymers. Morphology of linear diblocks is dictated by volume fraction (top), whereas the morphology of bottlebrush diblocks also depends on side chain symmetry (bottom). This figure is reproduced from ref 24.

Beyond the application as templates for porous materials, the previous example presents one of the only reported bottlebrush block polymer samples to self-assemble into a non-lamellar phase. The other examples were also achieved by introducing a large asymmetry in branch length, or by synthesizing brush-coil diblocks in which only one of the blocks was of bottlebrush architecture.[73-75] Runge *et al.* synthesized a large library of brush-coil diblocks (termed "comb block polymers") and evaluated their solid-state morphologies using small-angle X-ray scattering and scanning electron microscopy. The results were compiled into experimental phase diagrams, which showed that adjustments in the brush side chain length caused significant changes in the preferred morphology and dramatically skewed the phase diagram. The effect of architectural asymmetry in these studies is reminiscent of the conformational asymmetry shown in Figure 1.5. However, the shift in phase boundaries introduced by architectural asymmetry of bottlebrush block polymers can be carefully modified by independent adjustment of backbone and side chain lengths. This illustrates the versatility of the bottlebrush block polymers in tuning the resultant phase diagram.

Outside of these few examples, the majority of bottlebrush block polymers studies have maintained lamellar phases over broad range of volume fractions.[76,77] This preferred formation of flat interfaces has been attributed to the semi-rigid nature of densely branched bottlebrushes. However, the extent of this effect is undoubtly dependent on the structural parameters of the specific bottlebrush system (*e.g.*, branch length, backbone length, branch asymmetry, or absolute grafting density). This motivates further investigation into the self-assembly and phase behavior of diblock bottlebrush polymers. Accordingly, one of the aims in the work was to provide experimental contributions to the fundamental understanding of how molecular dimensions govern the phase behavior of bottlebrush block polymers.

1.4   Thesis Overview

This project was initiated with the goal of synthesizing highly branched polyolefins using a vinyl-terminated atactic polypropylene (aPP) starting material provided by the Exxon

Mobil Chemical Company. The terminal unsaturation of these molecules served as a convenient handle for chemical modification, which enabled preparation of the aPP bottlebrush polymers examined herein. The first two chapters provide relevant background relating to the current state of research in the field (chapter 1) and the specific experimental techniques used most frequently (chapter 2). The bulk of the thesis is then composed of three main parts, involving the molecular synthesis (chapter 3), rheology (chapters 4 and 5), and self-assembly (chapters 6 and 7) of model bottlebrush polymers. Finally, chapter 8 provides preliminary data and outlook to ongoing research for the project.

Chapter 2

Experimental Techniques

2.1 Polymerization Methods

The bottlebrush polymers studied in this work were synthesized by grafting through polymerization of end-functionalized macromonomers. The complete synthetic pathway therefore required a combination of polymerization methods to first create macro-monomers and then prepare the desired bottlebrush polymers. Numerous synthetic techniques were explored in this work to optimize bottlebrush preparation. This section provides background information for the most frequently used methods.

2.1.1 Free Radical Polymerization

Free radical polymerization utilizes an extremely reactive radical species to initiate and propagate the polymerization reaction.[51] Typically, a thermal initiator is employed, which decomposes upon heating and liberates the free radical species. After decomposition of the initiator, the polymerization proceeds in a three-step process of initiation, propagation, and termination (Figure 2.1). The first propagation step involves a reaction of the radical initiator with a (usually vinyl) monomer. This results in a net transformation of the monomer double bond (pi bond) to a more stable sigma bond

linking the initiator and the monomer unit, and transferring the free radical to the monomer species. This favorable propagation step is then readily repeated, consuming any surrounding monomers, and the polymer forms by a "chain-growth" mechanism. Ultimately, the active radical sites terminate by reaction with a second free radical. Termination of the chain can take place by either combination or disproportionation. Termination by combination simply involves the coupling of two free radical chain ends to form a sigma bond, resulting in a polymer with a combined molar mass of the two participating chains. Disproportionation involves the transfer of a hydrogen atom from one chain end to other, followed by an elimination reaction of the donor chain to form an unsaturated end group. Termination by disproportionation thus results in two polymer chains per termination event and a lower average molar mass than combination products. Overall, free radical polymerization generates polymers with a broad molecular weight distribution.
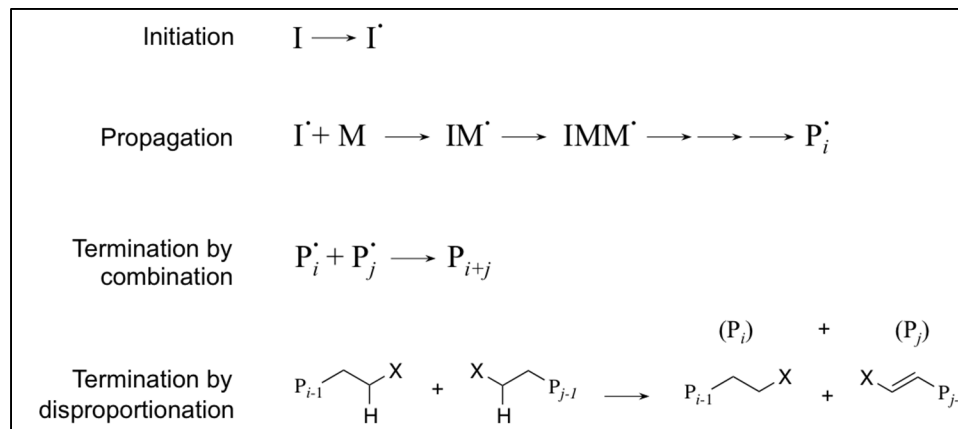
Figure 2.1. General free radical polymerization mechanism.[51]

2.1.2   Controlled and Living Polymerizations

The application of controlled and living polymerizations enables synthesis of polymer molecules with highly tuned chain length, composition, and branching architecture. Advancements in controlled polymerization techniques have vastly expanded the ability create polymer materials with low molar mass dispersity ($Đ$), which serve as model

systems. The term "living" refers to a polymerization in which no termination or irreversible chain transfer is present. Additionally, typical living polymerizations require an initiation rate (k_i) that far exceeds the propagation rate (k_p) to ensure that polymer chains begin growing at approximately the same time, propagate simultaneously, and remain active throughout the reaction.

2.1.3   RAFT Polymerization

Reversible addition-fragmentation chain-transfer (RAFT) polymerization is a controlled radical polymerization technique that employs a radical chain transfer agent (CTA) to mediate the growth rate of propagating polymer chains. RAFT polymerizations are initiated in the same way as free radical polymerizations, typically with a thermal initiator such as azobisisobutyronitrile (AIBN) or benzoyl peroxide (BPO). The activated radical adds monomer units and propagates until undergoing chain transfer to the reactive C=S double bond of the CTA, deactivating but not terminating the polymer (Figure 2.2). After some time, either the dormant polymer chain or the leaving group (R) initially bonded to the CTA is released and reactivated. The newly activated polymer propagates until encountering another CTA and repeating the process.[78-80]

The main advantage of RAFT polymerization is that all polymer chains grow simultaneously by continually switching on and off the active polymer chains through radical chain transfer to the CTA. Typical CTA's involve dithioester, trithiocarbonate, or zanthate functional groups and are chosen based on the specific monomer of interest to ensure that the rate of chain transfer is greater than the rate of propagation.[81,82] For the purposes of making well-defined block polymers *via* RAFT polymerization, reactions are usually not run to high conversion. This is because the probability of bi-radical termination events (*e.g.* disproportionation and combination) increases as the monomer concentration is depleted. Quenching the polymerizations at relatively low conversion facilitates production of a low dispersity polymer with high end-group functionality needed for further chemical modifications.
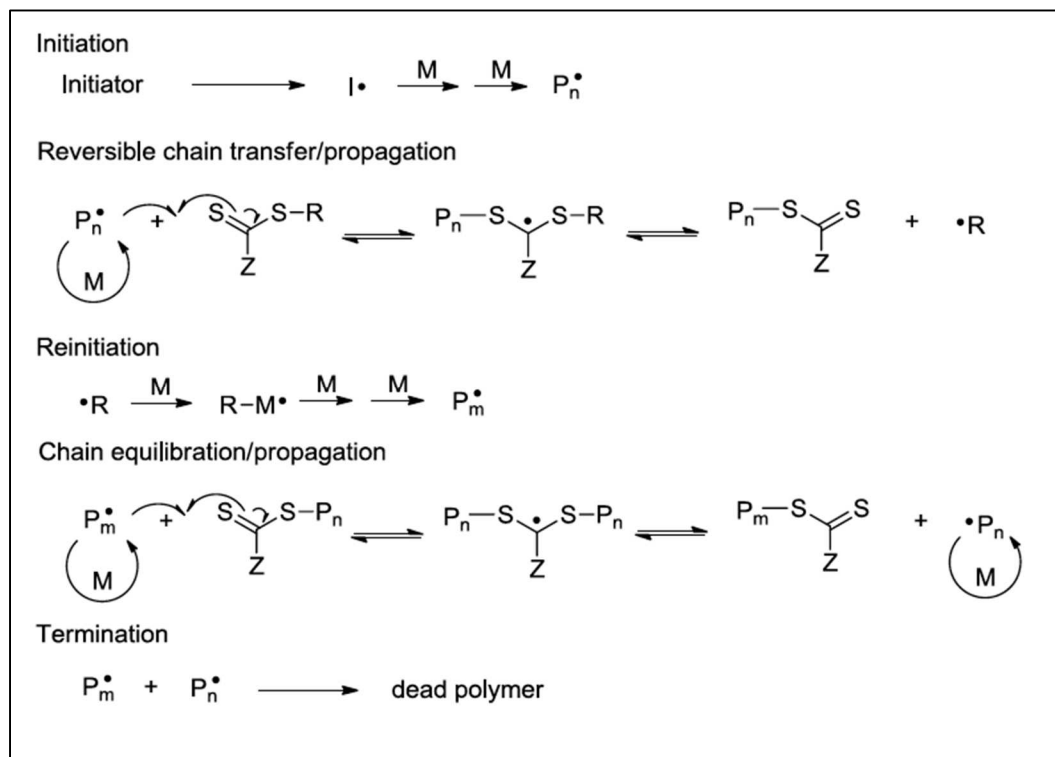
Figure 2.2. General mechanism of RAFT polymerization.[78]

2.1.4   Ring-Opening Metathesis Polymerization

Ring-opening metathesis polymerization (ROMP) is a variant of the versatile carbon-carbon bond rearrangement reaction known as olefin metathesis.[83] The overall reaction involves the breaking and reforming of C=C double bonds by a metal carbene (Figure 2.3).[84] The reaction begins with the coordination of the metal carbene to an olefin and subsequent cycloaddition to form a reversible metallocyclobutane intermediate. The intermediate undergoes electron redistribution and cleavage to produce either the starting material or the rearranged product. Since the reaction is a thermodynamically controlled process, there must be a driving force to push equilibrium towards the desired product. In the case of ROMP, this driving force is the release of ring strain.
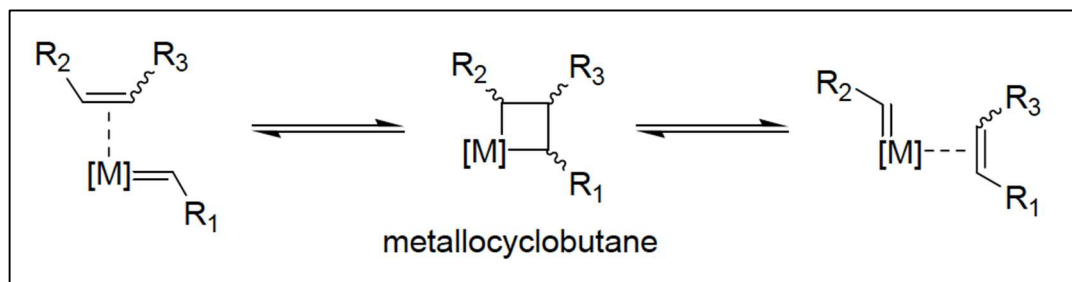
Figure 2.3. Mechanism for olefin metathesis.

The general mechanism for ROMP is shown in Figure 2.4 as a chain-growth polymerization in which cyclic olefin monomers are converted to polyalkenamers. The mechanism involves the [2+2] cycloaddition of the metal alkylidene to the unsaturated monomer and the cleavage of the metallocyclobutane intermediate to form the rearranged product. The reaction propagates as the new metalalkylidene coordinates with another unsaturated monomer and repeats the cycle until all monomer is consumed and/or a terminating agent is added. Typical cyclic olefin monomers include cyclobutene, norbornene, cyclooctene, and cyclopentene (in order of decreasing ring strain).[85]

The enthalpy released from ring strain renders the reaction essentially irreversible. However, the resulting unsaturated backbone can undergo intermolecular and intramolecular secondary metathesis reactions if the equilibrium conditions are not tuned properly (Figure 2.5). Intermolecular metathesis leads to the transfer of the metal alkylidene from one polymer end to another, maintaining the total number of polymer chains, but broadening the molecular weight distribution. Intramolecular metathesis, or "backbiting", occurs when the active metal complex at a chain end reacts with an internal double bond producing a macrocycle. To minimize secondary metathesis reactions, high monomer concentrations and low temperatures for exothermic reactions can push equilibrium toward the desired product. Further, bulky and sterically hindering monomers such as norbornenes can be used to reduce secondary metathesis reactions.
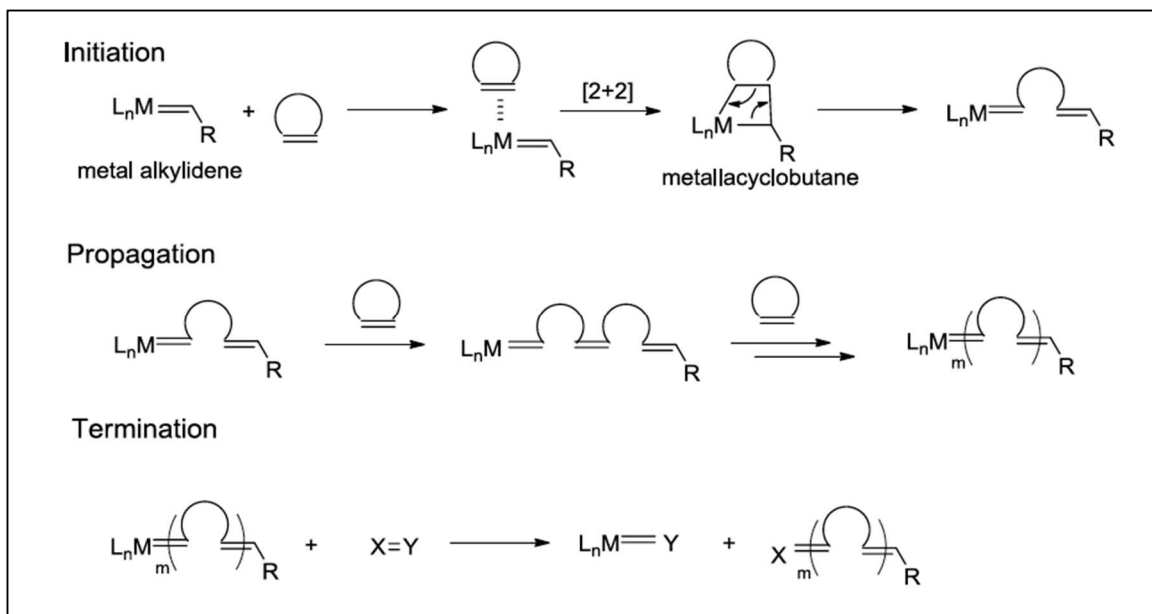
Figure 2.4. Genreal ROMP mechanism.[85]
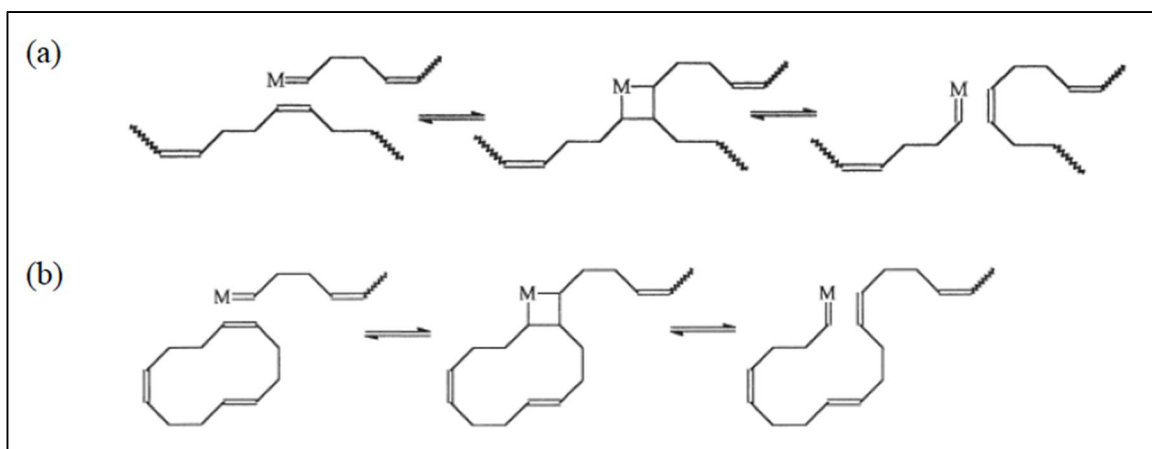
Figure 2.5. Intermolecular chain transfer (a) and intramolecular back-biting (b) metathesis reactions.[86]

Olefin metathesis and ROMP rely heavily on the metal alkylidene, transition metal catalyst for reactivity and control over product properties. Many sophisticated catalysts have been developed that exhibit high reactivity, tolerance to a broad range of functional groups, and high chemo- and stereo-selectivity. The Schrock group has developed a series of well-defined tungsten (W) and molybdenum (Mo) catalysts that show high reactivity, but also exhibit air and moisture sensitivity, low thermal stability, and poor tolerance to functional groups.[87,88] In tandem, the Grubbs group has developed ruthenium-based (Ru) catalysts with unprecedented functional group tolerance due to their low oxophilicity. Several versions of the ruthenium-based metathesis catalysts have been modified in recent years to exhibit extraordinarily high initiation and propagation rates for strained cyclic olefin monomers.[89] Many of these were utilized for bottlebrush synthesis in this research and are compared for our systems in chapter 3.

2.1.5   Anionic Polymerization

Anionic polymerizations are considered living and allow for the resulting polymer to be controlled precisely for molar mass, dispersity, and chain end functional groups.[90,91] These polymerizations exhibit living characteristics due to the stability of the ionic species, in the absence of impurities, which eliminates bimolecular coupling. The anionic species will undergo a repetitive conjugative addition reaction with vinyl monomers (Figure 2.6), and the reaction will continue until impurities are introduced or all unsaturated monomers are consumed. The main drawbacks of anionic polymerization are the limited monomer compatibility, low tolerance for functional groups, and the need for stringently clean and dry reaction conditions. This method is introduced briefly here, but is not used extensively in this research. Detailed reviews of anionic polymerization procedures are provided elsewhere.[92]
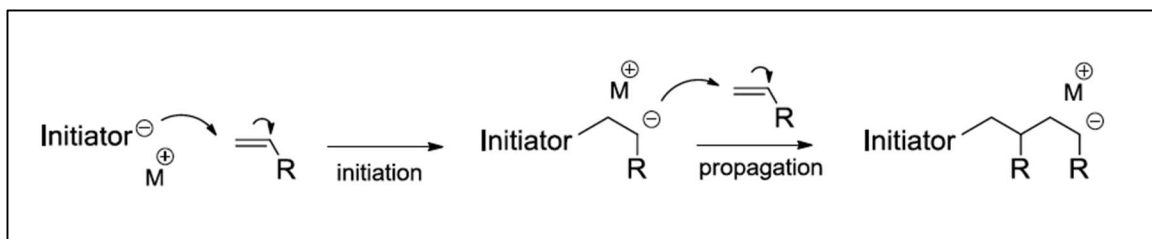
Figure 2.6. General mechanism for anionic polymerization.

2.2   Characterization Methods

Several methods were utilized to characterize the exact molecular structure, material properties, and self-assembled phases of bottlebrush polymers. Important details of the most pertinent characterization methods are discussed here. Namely, size exclusion chromatography (SEC) and nuclear magnetic resonance (NMR) spectroscopy were used extensively to characterize the molecular structure of bottlebrush polymers and the precursor macromonomer species. SEC equipped with light scattering detection was particularly important to achieve accurate analysis of the unique bottlebrush molecules. Small-amplitude oscillatory shear (SAOS) served as the primary characterization method for assessing the rheological behavior of bottlebrush homopolymers, discussed in chapters 4 and 5. Finally, the self-assembly of diblock samples was analyzed using small-angle X-ray scattering (SAXS). Beyond these techniques, differential scanning calorimetry (DSC) was used to evaluate the glass transition temperatures of bottlebrush polymers, and atomic force microscopy (AFM) and ellipsometry were employed for thin film characterization. These last three techniques are not covered in this chapter, but specific experimental details are reported as needed in chapters 3–7.

2.2.1   Size Exclusion Chromatography

SEC is the most common method of determining the average molar mass and dispersity of a polymer sample. SEC is a type of chromatography in which the polymer of interest is dissolved in a suitable solvent (referred to as the mobile phase or eluent) and pumped through a column of a tightly packed, porous stationary phase with a distribution of pore

sizes. The individual polymer molecules are then separated based on their hydrodynamic volume (V_h). For a sample of linear homopolymers of a single chemical identity, V_h will be roughly proportional to the cube of the radius of gyration (R_g). The columns are packed such that smaller molecules are allowed to enter more pores, leading to a more accessible column volume and a longer elution path relative to the larger molecules.[51] Thus, the largest species elute from the column first and gradually smaller chains elute at increasing times.

As the separated molecules elute from the column, they pass through a differential refractive index (RI) detector, which measures the change in RI of the column effluent passing through the flow cell compared to the pure eluent. The signal obtained is directly proportional to the mass concentration of polymer in the mobile phase. In order to determine a the molar mass distribution, the data is analyzed relative polymer standards of known molar mass (M) and narrow dispersity. A calibration curve must prepared by plotting the peak elution time versus M of the standards, and fitting the data with a polynomial function to empirically relate elution time to M. The number-average and weight-average molar mass can then be determined by using,

$$M_n = \frac{\sum_i c_i}{\sum_i c_i / M_i} \tag{2.1}$$

$$M_w = \frac{\sum_i c_i M_i}{\sum_i c_i} \tag{2.2}$$

where i represents the measured values at each time interval. The main limitation of using only RI detection is that it provides molar mass values relative to some polymer standard. Since the V_h of different polymer species are dependent on chemical composition and molecular architecture, there can be substantial differences between the sample and the standards, leading to inaccurate molar mass calculations.

Multi-angle laser light scattering (MALLS) detection has the advantage of providing an absolute M_w measurement at each slice (Δt) of the chromatogram. This obviates preparation of a calibration curve with standards and enables accurate characterization of

samples with branched molecular architectures. Given the compact nature of bottlebrush polymers, the V_h is generally quite small for a given molar mass causing longer elution times through the SEC column. Clearly, using a calibration curve based on linear polymer standards to characterize the size of bottlebrush molecules would be highly inaccurate. Therefore, SEC-MALLS was used to characterize the samples in this work.

Experimentally, SEC-MALLS characterization is completed by allowing the instrument software to calculate molar mass and dispersity using a known or measured dn/dc value under the given conditions (polymer, solvent, temperature, *etc.*). A common misconception when using the latter method is that the calculated M_w value of the polymer distribution is the absolute value measured directly by the light scattering detector. It should be noted that the MALLS detection is used to provide a measurement of M_w for each *slice* in the chromatogram. The values measured are then taken to be the molar mass of that slice (assuming a perfectly monodisperse distribution over the Δt of each slice), and the sample M_n and M_w are calculated using equations 2.1 and 2.2 with c_i values from the RI detector.

2.2.2   Nuclear Magnetic Resonance Spectroscopy

Nuclear magnetic resonance (NMR) spectroscopy is a commonly used technique for the characterization of organic molecules. The technique utilizes the magnetic resonance properties of isotopic atoms to provide information about their chemical environment. Hydrogen (^{1}H – 99.98%) NMR was used predominantly to characterize the polymers in this research. The chemical shift value for a unique proton is dependent on the molecular structure, neighboring functional groups, solvent, temperature, and the magnetic field to which the sample is subjected. Deuterated solvents are typically used to minimize signal interference with the structure of interest. The integration curve for a unique proton reflects the abundance of individual protons or the molar concentration. Since each proton contributes equally to the signal, the integration yields a quantitative number of each type of proton. Thus, the number averaged molecular weight (M_n) for the polymers and quantitative reaction conversion values can be calculated by end group analysis,

which compares identifiable end-group protons with those of the polymer repeat units. This analysis is only practical for relatively short polymers (~10K or less) since the relative intensity of end group protons decreases at higher molar mass. Macromonomers are particularly suited to characterization by end group analysis since they are generally short polymer chains with functional end group chemistry.

2.3   Rheological Measurements

The rheological behavior of the bottlebrush polymers in this research was examined using dynamic shear deformation measurements known as small-amplitude oscillatory shear (SAOS). This is a common method used to probe the viscoelastic properties of materials. In this section, we first review the properties of interest and then describe the measurement and data analysis techniques.

2.3.1   Viscoelastic Response

The linear rheology of polymers is often studied using shear deformation between parallel plates. These tests are used to quantify the magnitude of the viscous and elastic stress responses of viscoelastic materials. For example, the deformation of an ideal elastic solid is illustrated in Figure 2.7a. In this process, the material of interest is placed between two plates with a gap height (h), and the top plate is moved with a force (F) while holding the bottom plate stable. At small strains (usually $< \sim 3\%$ to maintain linear elasticity), the stress response (σ) of the material will be directly proportional to the imposed strain (γ),

$$\sigma = G\gamma \tag{2.3}$$

where G is the shear modulus. This is analogous to the spring constant for an ideal Hookean spring, which quantifies the stiffness of an elastic solid. The stress and strain in this example are defined as $\sigma = F/A$ and as $\gamma = L/h$, respectively.

(a)

Experimental Setup   **Deformation Profile**
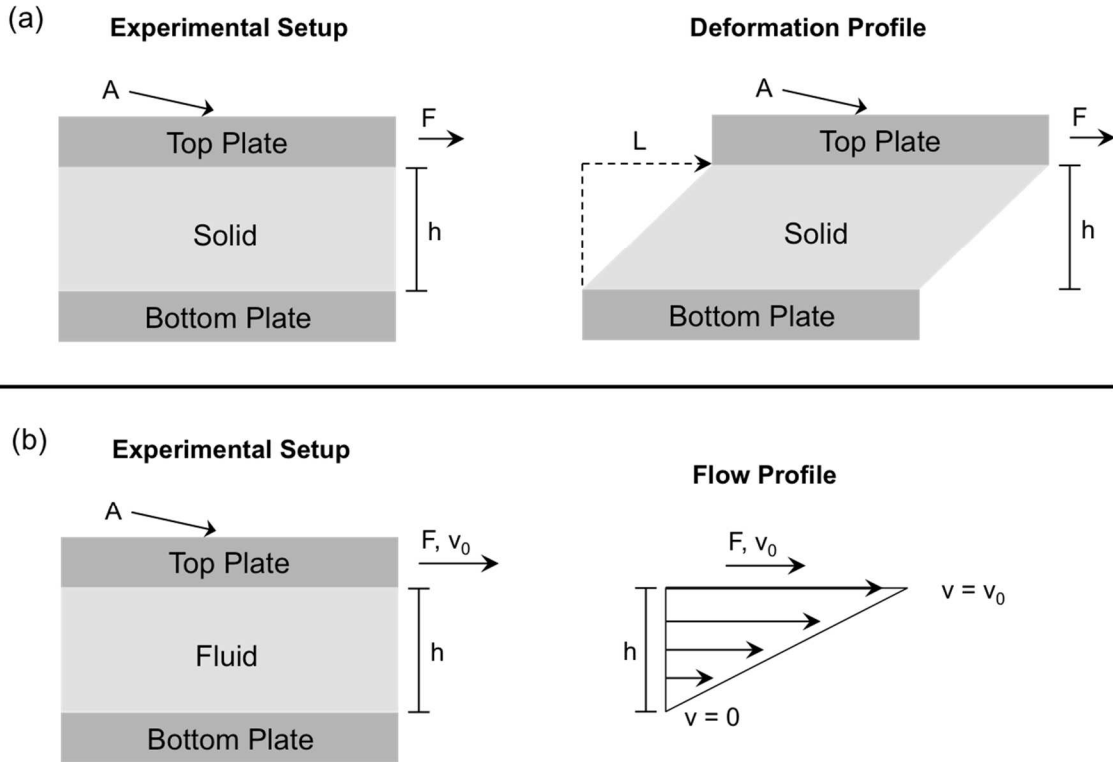
Figure 2.7. (a): Shear deformation of an ideal (Hookean) solid between parallel plates. (b): Steady-shear deformation of an ideal (Newtonian) fluid between parallel plates.

Alternatively, the stress response of an ideal Newtonian liquid is directly proportional to the imposed strain rate,

$$\sigma = \eta \dot{\gamma} \qquad (2.4)$$

where the shear strain rate in Figure 2.7b is defined as

$$\dot{\gamma} = \frac{d\gamma}{dt} = \frac{dL/dt}{h} = \frac{v_0}{h} \qquad (2.5)$$

Since polymer materials are inherently viscoelastic, the mechanical response to deformation is intermediate between these two extreme examples. SAOS analysis serves as a convenient method of resolving both the viscous and elastic material properties

concurrently.[51] A typical SAOS experiment is carried out as depicted in Figure 2.8. The polymer sample of interest is loaded between two circular plates, and the instrument imposes a sinusoidal deformation. The imposed strain takes the form:

$$\gamma(t) = \gamma_0 \sin(\omega t) \tag{2.6}$$

where γ_0 is the maximum strain amplitude and ω is the oscillation frequency. The strain rate of this deformation follows:

$$\dot{\gamma}(t) = \frac{d}{dt}\gamma(t) = (\gamma_0\omega)\cos(\omega t) = \dot{\gamma}_0\cos(\omega t) \tag{2.7}$$

The detected stress response of the material can be deconstructed into two component waves, one that is purely elastic and in-phase with the strain, and one that is purely viscous and 90° out-of-phase with the strain (Figure 2.9). This is strictly applicable only within the linear viscoelastic region, where the response of a sinusoidal deformation is also sinusoidal. (Note: the $\cos(\omega t)$ stress response of the viscous component is the same form as the sine wave offset by 90°.) The dynamic modulus is then represented as,

$$G(t) = \frac{\sigma(t)}{\gamma_0} = G'\sin(\omega t) + G''\cos(\omega t) \tag{2.8}$$

where G' is the elastic (or storage) modulus and G'' is the viscous (or loss) modulus. The dynamic modulus can also be represented in complex notation as,

$$G^*(\omega) = \frac{\sigma^*}{\gamma^*} = G' + iG'' \tag{2.9}$$

where G^* is the complex dynamic modulus and $\sigma^* = \sigma_0\exp[i(\omega t+\delta)]$. $G'(\omega)$ and $G''(\omega)$ are perhaps the most important material properties gathered from SAOS. Combined knowledge of $G'(\omega)$ and $G''(\omega)$ gives characteristic details of material's relaxation profiles. Variation of ω is equivalent to adjusting the time scale of stress relaxation. Therefore, evaluation of how $G'(\omega)$ and $G''(\omega)$ scale with ω yields important information

about the relaxation time scales inherent to the material, which is highly dependent on molecular structure.
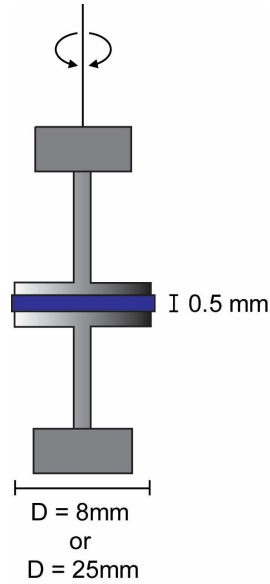
Figure 2.8. Set up of a typical SAOS experiment. The polymer sample (blue) is loaded between two plates with diameter of either 8-mm or 25-mm diameter. One plate is then oscillated at low strain amplitude to maintain a linear viscoelastic response.
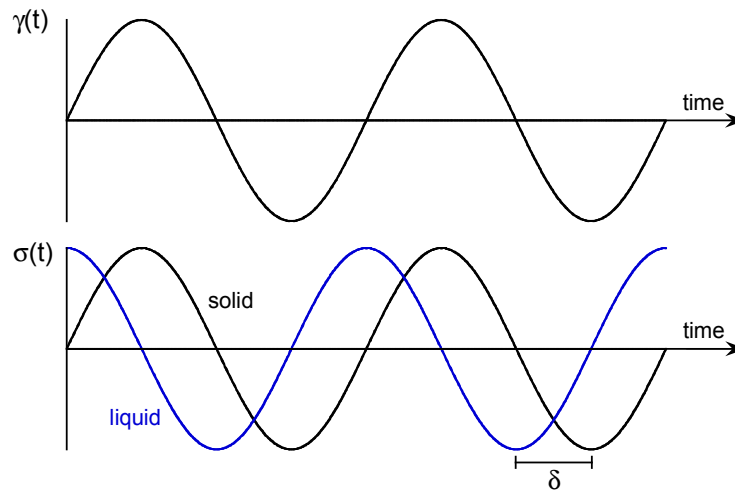
Figure 2.9. Stress responses (bottom) to an imposed oscillatory strain (top) for an ideal elastic solid and Newtonian liquid. The stress response of the Newtonian liquid is shifted 90° relative to the strain, whereas the elastic response of the solid is in phase with strain.

Precise definitions of G' and G" are given as

$$G' = \frac{\sigma_0}{\gamma_0} \cos(\delta) \tag{2.10}$$

$$G" = \frac{\sigma_0}{\gamma_0} \sin(\delta) \tag{2.11}$$

where δ is the phase angle. This is defined in Figure 2.9 as the phase shift of the stress response relative to the strain. The ratio of these two moduli defines another important parameter known as the loss tangent:

$$\tan(\delta) = \frac{G"}{G'} \tag{2.12}$$

Rather than phase angle alone, the loss tangent is often utilized to describe a given material because it represents a direct ratio of the viscous and elastic moduli.

2.3.2   Strain Sweep Tests

Strain sweeps were the first test conducted on each sample in this work to determine the linear viscoelastic (LVE) region. Oscillatory strain sweeps are dynamic measurements in which a sinusoidal deformation is applied at a constant frequency and the amplitude is stepped up to acquire response data at over a wide range of strains. Within the LVE region (small strains), the dynamic modulus remains independent of strain. At higher strain amplitude, outside of the LVE region, the dynamic moduli typically decrease with increased strain. This test is critical for ensuring all subsequent measurements are taken at strain amplitudes that remain within the LVE region, *i.e.*, to ensure the dynamic response data remain independent of the imposed deformation. If measurements are taken outside of the LVE region then the acquired material functions including G' and G" will no longer provide complete descriptions of the material response. This is demonstrated in Figure 2.10 by the non-constant moduli at high strain amplitudes, and the oscillatory

stress response that becomes distorted.[93] Since the mathematical framework for analyzing dynamic viscoelasticity in the LVE region stems on the assumption of perfectly sinusoidal response curves, these non-linear effects necessitate far more complicated analytical methods to evaluate properly.
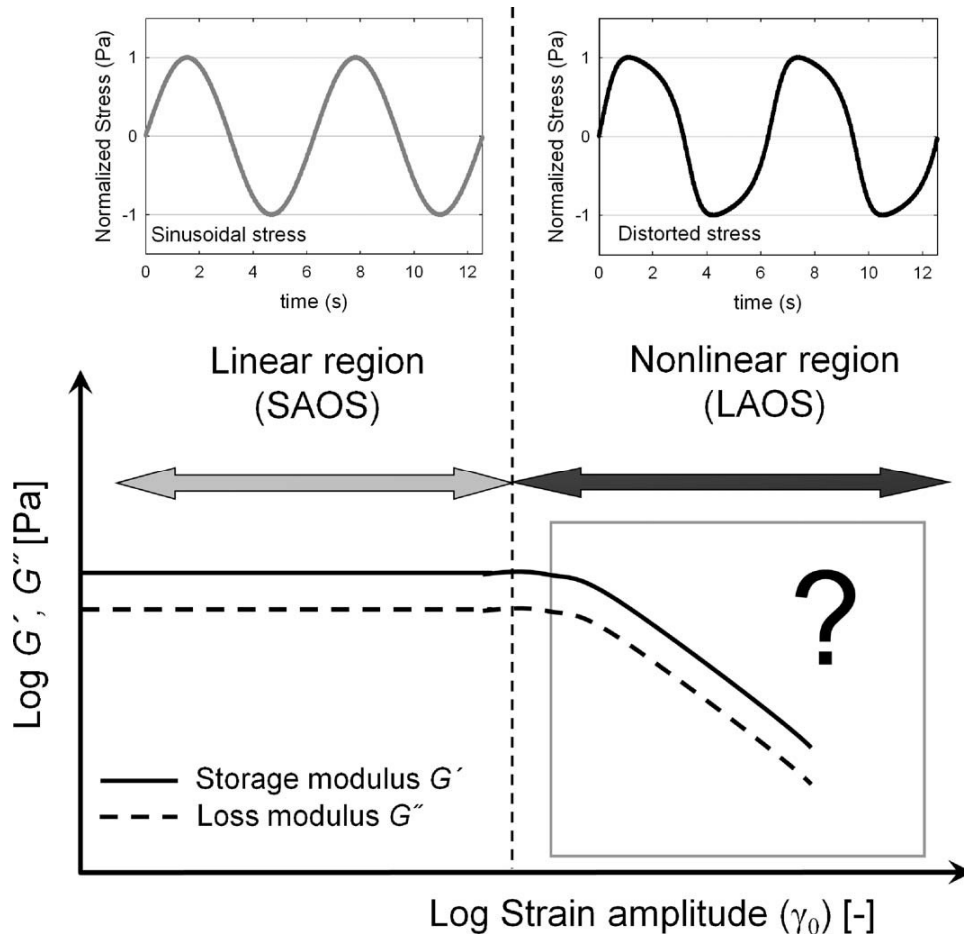
Figure 2.10. Illustration of a dynamic strain sweep experiment conducted at constant oscillation frequency. The moduli are independent of strain at small amplitudes (γ_0), defining the linear viscoelastic region. At large γ_0 the moduli begin to decrease with increasing strain, indicating non-linear effects. Examples of the oscillatory stress response in each region are presented and show the distortion of the stress wave in the non-linear regime. Figure reproduced from ref 93.

2.3.3   Time-Temperature Superposition

Polymer melts typically exhibit relaxation spectra encompassing an extremely wide range of time scales, often exceeding ten orders of magnitude in time (or frequency). It is not feasible to directly measure the entire relaxation spectrum with one experiment, because it would require an unrealistic amount of time to acquire data at all of the relevant oscillatory frequencies. By taking measurements over an experimentally convenient frequency range (0.1 – 100 rad/s) at several different temperatures, the composite relaxation spectrum can be constructed *via* time-temperature superposition (TTS) of the data sets. The principle of TTS relies upon the assumption that increasing a material's temperature accelerates the dynamics of all the intrinsic relaxation modes to an equal extent. Therefore, an increase in temperature is equivalent to scaling the relaxation time by a constant value, known as a shift factor a_T, such that:

$$G*(T_{\exp}, \omega) = G*(T_{ref}, a_T \omega) \tag{2.13}$$

Practically, TTS allows dynamic moduli data to be shifted along the logarithmic frequency (or time) axis to superimpose with data acquired at a different temperature, effectively yielding a relaxation spectrum that exceeds the experimentally probed frequency range. Application of TTS requires equivalent temperature dependence of all relaxation processes within the material. Such materials are referred to as thermorheologically simple. Thus, TTS is can become invalid for materials that do not exhibit this property, especially in multicomponent materials such as blends or block polymer melts.

2.4   Scattering Techniques

The majority of block polymer self-assembly data collected in this work utilized small-angle X-ray scattering (SAXS) as the primary characterization tool. This section reviews

fundamentals of scattering techniques and introduces the utility of SAXS characterization for diblock polymer studies.

Scattering is the physical process of reradiating propagating waves due to interaction with the medium through which they pass. As a non-invasive probe of structure, interactions, and dynamics, scattering experiments have become an essential tool for polymer scientists. Different, yet complementary structural sizes, dynamics, and chemical characteristics can be probed through the use of light, neutron, and X-ray radiation.

Scattering arises from fluctuations in the sample through which the wave travels. Incoherent scattering occurs from random fluctuations in the medium, and no phase relation or constructive pattern can be attained as a result. However, if there is a spatial correlation between the inhomogeneities, coherent scattering will emerge and allow for structural analysis.[51] When the wavelength (λ) of the incident radiation is on a comparable length scale as the scattering bodies, the resultant scattering pattern will be in-phase, since particular angles will align with planes of the scattering objects that are separated by integral multiples of λ. This wave interference pattern is defined as Bragg's Law:

$$2d\sin\left(\frac{\theta}{2}\right)=n\lambda \tag{2.14}$$

where n is a positive integer, λ is the wavelength of the incident wave, d is the interplanar distance of lattice planes, and θ is the angle between the incident and scattered waves. This is illustrated in Figure 2.11 in which the incident and scattered waves each make an angle of $\theta/2$ with the plane of scatterers. The planes are separated by d, which is dependent on the material being analyzed. By measuring the intensity of the scattered waves as a function of angle, the diffraction pattern can be obtained.

$$a = d\ sin\ \theta$$
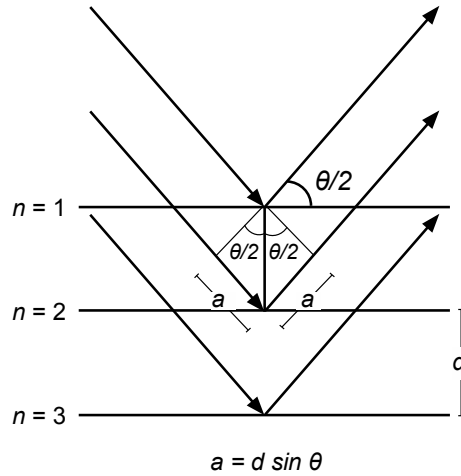
Figure 2.11. Demonstration of Bragg's law. The incident and scattered beams make angles of $\theta/2$ with each scattering plane. A distance, d, separates the planes and the added length traveled by light scattered from successive planes are denoted as a.

The scattering vector q is the difference between the incident and emitted wave vectors,

$$q = |\boldsymbol{q}| \equiv |\boldsymbol{k}_i - \boldsymbol{k}_j| = \left(\frac{4\pi}{\lambda}\right)\sin\left(\frac{\theta}{2}\right) \tag{2.15}$$

where $|\mathbf{k}| = (2\pi/\lambda)$ for both scattering vectors as required in elastic scattering events. The q vector is essential to evaluating a scattering process, and it encompasses both the scattering angle and the radiation wavelength. Combination of equations 2.13 and 2.14 gives,

$$q = \frac{2\pi n}{d} \tag{2.16}$$

This relationship describes the condition in which the q vector aligns with the reciprocal lattice vector defining the material's order ($2\pi/d$), and constructive interference arises among scattered waves from different lattice planes. Therefore, the spatial arrangement of a structured material can be determined by analyzing the dependence of the scattering

intensity on the scattering angle. Locations with peaks in intensity correspond to "Bragg peaks" that satisfy equation 2.13.

Small angle X-ray scattering (SAXS) is a type of scattering experiment that utilizes X-ray waves to probe sample ordering at a length scale of ~5-50nm.[66] This scattering technique is frequently used to study the microphase separation phenomena of diblock copolymers such as self-assembly dynamics, morphology, domain spacing, and order-disorder transitions. X-rays with a wavelength of ~1.5 Å are often used as the oscillating electromagnetic waves. Since λ is defined from the x-ray source, the detector angle, θ, must be less than 5° to access domain spacing of typical diblock copolymer microstructures.
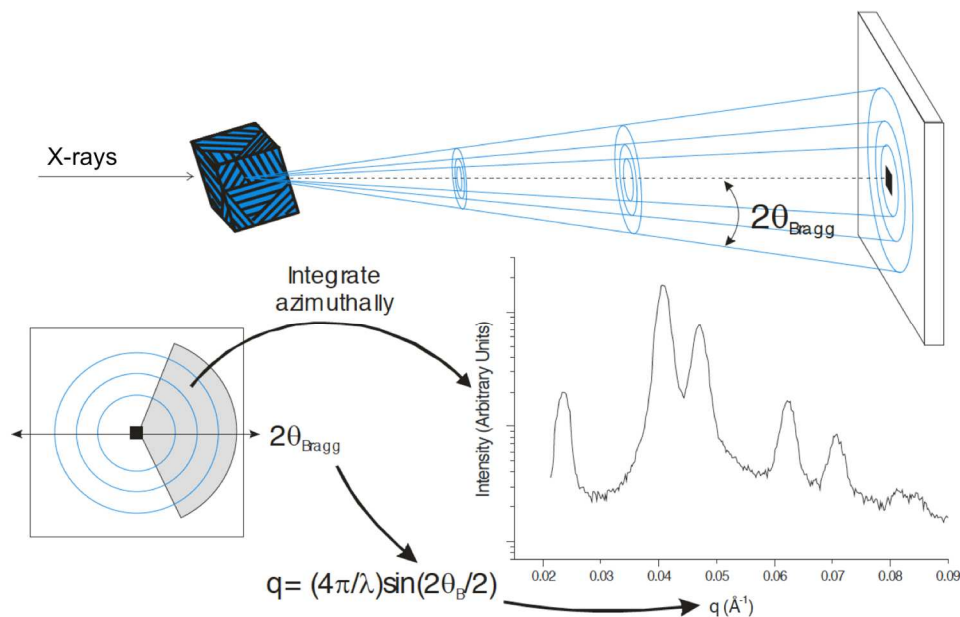
Figure 2.12. Schematic of SAXS data collection. *Top*: Experimental set up showing an incident X-ray beam and the resulting scattered X-rays with high intensity at discrete angles. These lead to distinct concentric rings on the 2D detector. *Bottom*: 2D SAXS data are typically integrated azimuthally to produce a plot with 1D intensity as a function of scattering vector q. The rings from the 2D detector appear as peaks on the resulting plot. Figure is adapted from ref 94.

The contrast in X-ray scattering arises from differences in electron densities (or the dielectric constant κ_i) between different domains. Specifically, the contrast scales as the square of the difference in electron densities as shown here:

$$Intensity \sim \left(\kappa_i - \kappa_j \right)^2 F(q)S(q) \tag{2.17}$$

In diblock systems, the A and B domains must have sufficient electron density differences to be able to distinguish scattering from the two domains. Usually this contrast is provided naturally, unless the two blocks are very chemically similar (*e.g.,* two polyolefin blocks). Equation 2.16 also displays the dependence of the actual scattering intensity on the form factor, F(q), and the structure factor, S(q). These two factors represent contributions to the overall scattering intensity related to intra-particle and inter-particle diffraction interference, respectively. The Bragg condition discussed above materializes as a structure factor phenomenon in self-assembled block polymer systems, relating to the interference caused by scattering from the different periodic domains. This can most easily be thought of using Figure 2.11. The same type of scattering effects would occur in an ordered block polymer material with aligned lamellar domains. In this case, the Bragg reflections would arise at integer multiples of the primary scattering vector (q*), as indicated by equation 2.13. Beyond the lamellar phase, more complex morphologies produce different structure factor scattering patterns. Table 2.1 provides a short list of the peak reflections for the most common block polymer morphologies.

Table 2.1. Reflections for common self-assembled block polymer morphologies.[95]

Morphologies	Allowed Scattering Reflections (q/q*)
Lamellar	1, 2, 3, 4, 5, 6…
Hexagonally Packed Cylinders	1, √3, √4, √7, √9, √12…
Gyroid	√6, √8, √14, √16, √20…
Body-Centered Cubic Spheres	√1, √2, √3, √4, √5, √6…

The brief SAXS background and pertinent structure factor scattering reflections are provided here as a basis for the experimental results and analysis provided in chapter 6. This information is used to assess the domain sizes and ordered morphologies of bottlebrush block polymers in the melt state. For a comprehensive review of this technique and further applications in block polymers, the reader is directed elsewhere.[96]

Chapter 3

Synthesis of Bottlebrush Polymers

3.1 Introduction

Bottlebrush polymers are synthesized using either grafting-from, grafting-to, or grafting-through polymerization strategies. The grafting-through method is advantageous because it guarantees complete grafting efficiency along the polymer backbone, as opposed to most grafting-to efforts reported in the literature,[28,30,97,98] and it enables thorough characterization of the polymer side chains independently from the bottlebrush molecules, unlike the grafting-from route. In this study, we selected grafting-through polymerization as the best option for synthesizing bottlebrush polymers with aPP side chains.

Despite the growing prevalence of studies in the literature focused on bottlebrush polymers, there have been relatively few examples of the polyolefin-based bottlebrushes. This is primarily because of the low reactivity of polyolefin molecules, which limits the chemical modification procedures available to functionalize and assemble such complex molecules. Nevertheless, two groups have demonstrated grafting-through polymerization of poly(ethylene-*co*-propylene) macromonomers. Rose *et al.* employed coordination-insertion polymerization using a nickel diimine complex and methylaluminoxane (MAO)

to prepare allyl-terminated poly(ethylene-*co*-propylene). This technique resulted in star-like poly(macromonomer)s with a maximum of 16 branches per molecule.[99] Kaneko *et al.* employed free-radical polymerization (FRP) of methacryloyl-terminated poly(ethylene-*co*-propylene). Limited degrees of polymerization were also observed in this study, yielding bottlebrushes with 35 branches per molecule.[100] However, FRP has proven successful in other grafting-through systems. Tsukahara *et al.* carried out seminal investigations on the FRP of macromonomers, albeit non-polyolefins, using methacrylate- and vinylbenzyl-polystyrene chains.[15,101-103] These studies found that the degree of polymerization (DP) was strongly dependent on the macromonomer size and feed concentration, and achieved bottlebrush products of $M_n \geq 10^6$ g/mol.

In this chapter, we investigate several polymerization strategies to determine the most effective synthetic route towards molecular bottlebrushes from aPP macromonomers. We begin with FRP and then progress to the more controlled RAFT and ROMP polymerization techniques. Each method was evaluated based on macromonomer conversion, reaction time, and control over bottlebrush molar mass and dispersity.

3.2   Vinyl-Terminated aPP

Two large batches of vinyl-terminated aPP (aPP-VT) were initially supplied by the ExxonMobil Chemical Company. The monotelechelic molecules were synthesized with one allyl-functionalized end group per aPP chain, according to procedures by Brant and coworkers.[104,105] The two batches of aPP-VT used in this research were characterized by ExxonMobil to have molar masses of M_n = 2108 g/mol and M_n = 859 g/mol, and are referred to as aPP-VT_2.1k and aPP-VT_860, respectively. To confirm the molecular characteristics, both batches were also analyzed as received using SEC and ^{1}H NMR spectroscopy, and the results are given in Table 3.1.

Table 3.1. Characterization of vinyl-terminated aPP samples.

Sample	Exxon Characterization		Characterization As Received	
	M_n (g/mol)	% vinyl	M_n (g/mol)[a]	$Đ$ [b]
aPP-VT_2.1k	2108	97%	2090	1.80
aPP-VT_860	859	88%	950	1.88

[a]Determined by ^{1}H NMR spectroscopy in CDCl$_3$, assuming 100% vinyl functionality. [b]Dispersity measured by SEC with chloroform mobile phase, calibrated with polystyrene standards.

Figure 3.1 displays the ^{1}H NMR spectrum for aPP-VT_2.1k. Due to the low sample molar mass, the vinyl end group peaks are easily detected in the 4.5 – 6.0 ppm region. The most deshielded proton peak is the multiplet at ~5.8 ppm, corresponding to the β-hydrogen. Both α-hydrogens of the vinyl group are located at ~5.0 ppm and appear as overlapping doublets with distinct J-couplings. The estimated coupling constants are given in Figure 3.2. Two separate regions associated with protons of the aPP repeat units arise at a much lower ppm range. The smaller region at ~1.6 ppm was used to calculate M_n of the samples since the broader region centered at ~1.0 ppm contains additional resonances from the saturated isobutyl end groups. Figure 3.3 displays the ^{1}H NMR spectrum of aPP-VT_860. In this case, the end groups are even more discernable, including the γ-carbons that arise at ~2.0 ppm. This batch has a slightly lower degree of vinyl termination and displays a small percentage of vinylidene end groups.
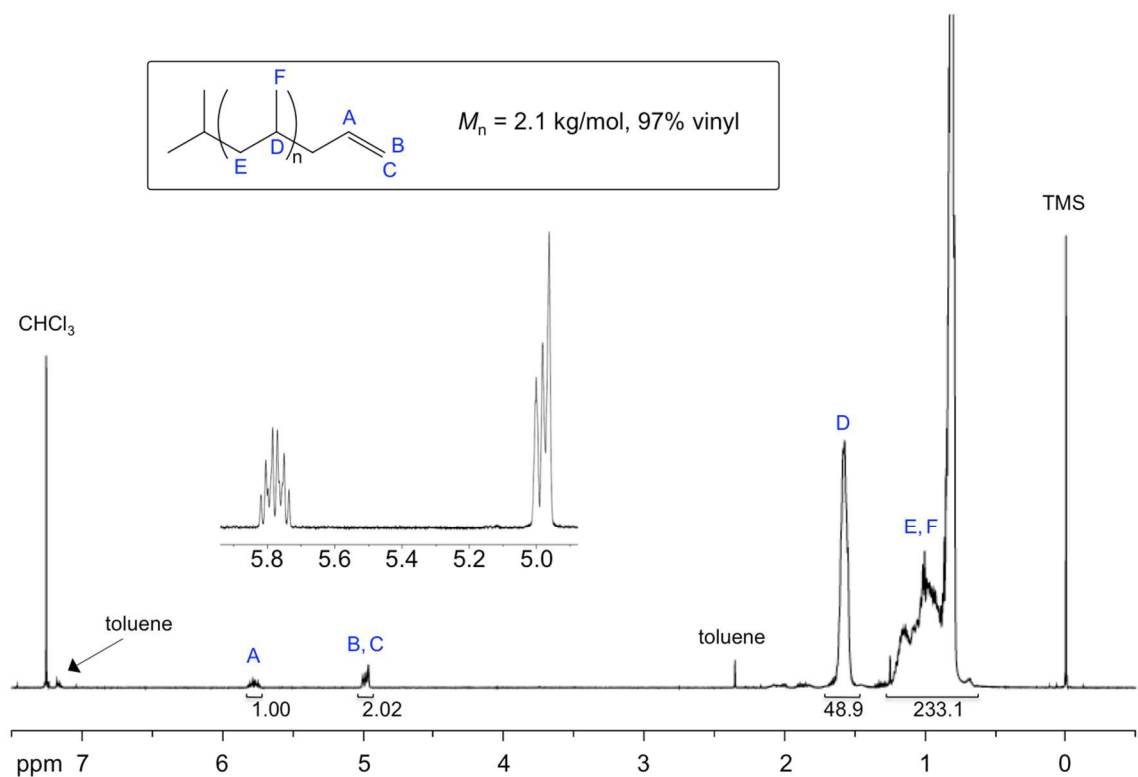
Figure 3.1. ^{1}H NMR spectrum of aPP-VT_2.1k as received (CDCl$_3$, 500 MHz).
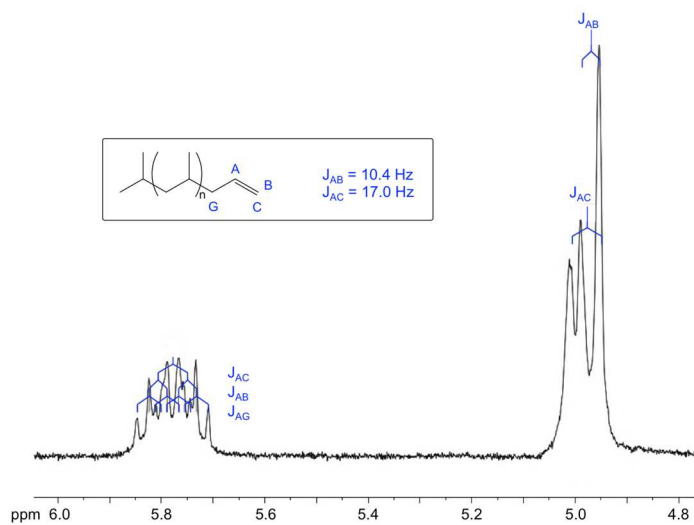
Figure 3.2. J-couplings of vinyl protons in the ^{1}H NMR spectrum of aPP-VT_2.1k.
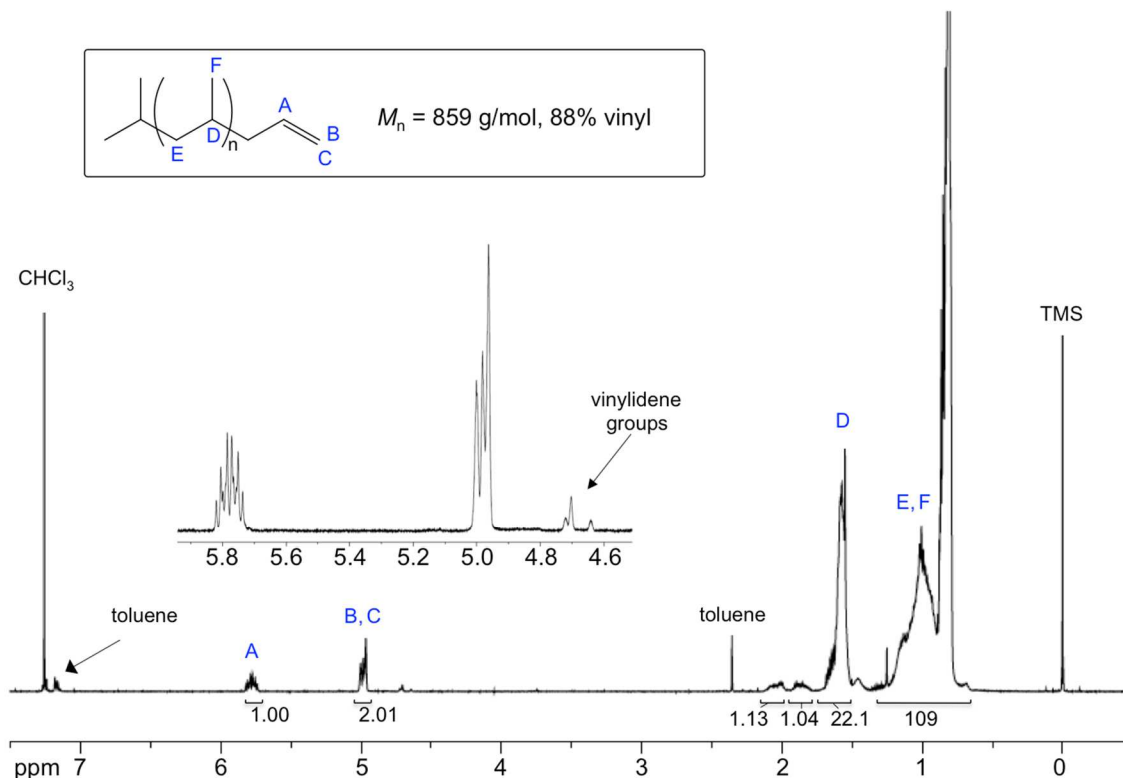
Figure 3.3. ^{1}H NMR spectrum of aPP-VT_860 as received (CDCl$_3$, 500 MHz).

3.3   Synthesis of aPP-MA Macromonomers

To synthesize bottlebrush polymers from the aPP-VT starting material using a grafting-through strategy, the aPP vinyl end group must first be functionalized with reactive groups amenable to polymerization (provided that we are not using coordination chemistry capable of directly polymerizing the vinyl functionality). To this end, a promising synthetic approach is functionalization with a methacryloyl end group, yielding ω-methacryloyl aPP (aPP-MA). This has been one of the more common functionalities reported in the literature on polyolefin macromonomers.[100,106,107]

Macromonomers were prepared through consecutive manipulations of the vinyl group. Initially, the aPP-VT_2.1k starting material was converted to ω-hydroxyl aPP (aPP-OH) using a two-step hydroboration-oxidation reaction as shown in Figure 3.4.[108-110] 9-Borabicyclo[3.3.1]nonane (9-BBN) was chosen as the hydroboration agent and is

known to undergo highly regioselective anti-Markovnikov addition to alkenes.[111] Thus, aPP-OH was exclusively produced with primary alcohol end-groups following oxidation with hydrogen peroxide. The reaction proceeded with very high conversion as evidenced by the elimination of alkene resonances in the ^{1}H NMR spectrum of aPP-OH (Figure 3.5). Integration of the triplet peak corresponding to the methylene protons neighboring the hydroxyl end-group (δ = 3.63 ppm) gave a conversion of 97%. This is much higher than previously published polyolefin hydroxylation efficiencies of 60% and 52% for vinylidene-terminated poly(ethylene-*ran*-propylene) copolymer (EPR)[100] and alkylaluminum-terminated isotactic PP (*i*PP),[112] respectively.
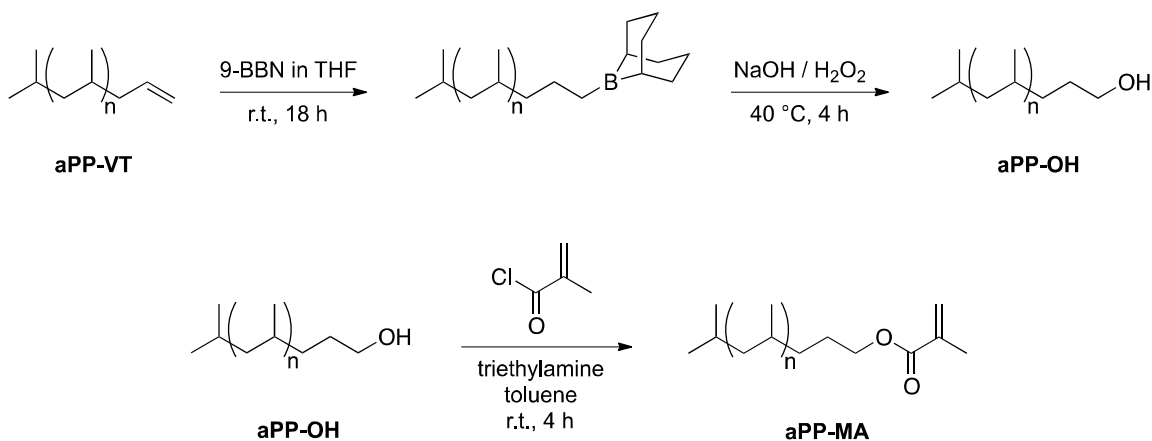
Figure 3.4. Top: Synthesis of aPP-OH using a two-step hydroboration/oxidation of the aPP-VT starting material. Bottom: Synthesis of the aPP-MA macromonomer.
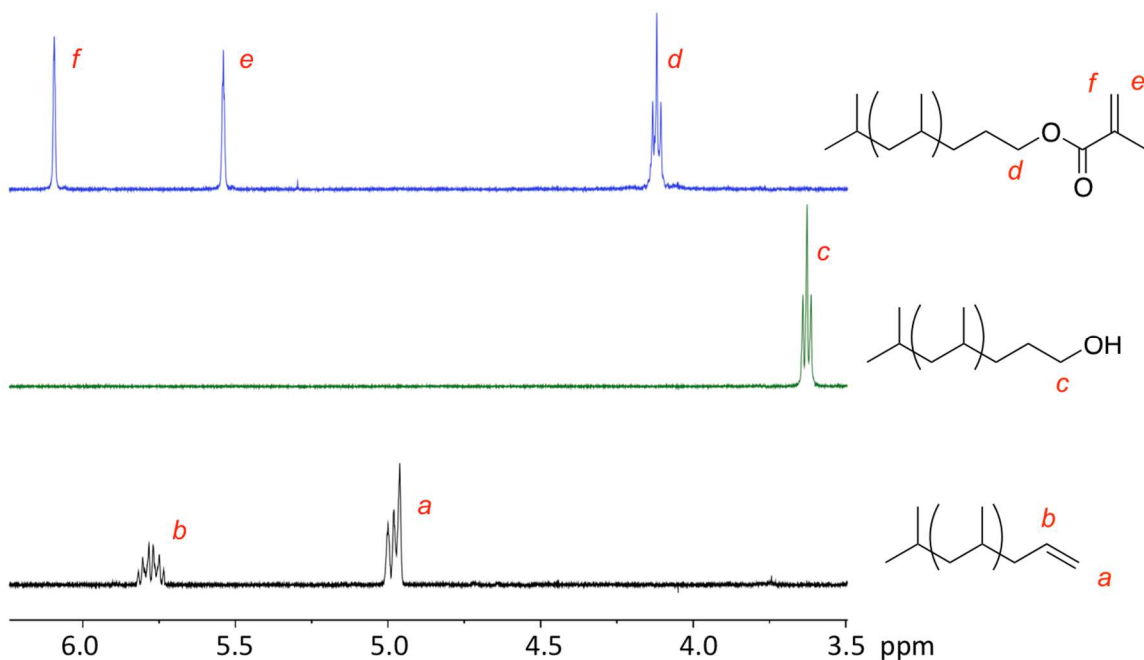
Figure 3.5. End group regions of the ^{1}H NMR spectra for aPP-VT_2.1k (bottom), aPP-OH (middle), and aPP-MA (top). Both reactions presented in Figure 3.4 proceed with near-quantitative conversion.

The hydroxyl end-group of aPP-OH was further converted by reaction with methacryloyl chloride in the presence of triethylamine as shown in Figure 3.4. Triethylamine base was incorporated to remove any hydrogen chloride produced by the reaction and assist in complete conversion of aPP-OH. The product was washed several times with cycles of dilute acid and distilled water before precipitation in methanol, yielding the aPP-MA product. This reaction also exhibited near quantitative conversion. Figure 3.5 shows the methylene protons of aPP-MA to have shifted downfield relative to their position in the ^{1}H NMR spectrum of aPP-OH. Two new singlet peaks also appear in the vinyl region of the spectrum, corresponding to the vinylidene protons of the methacrylate group. Since both the functionalization reactions proceeded with nearly quantitative conversion, it is reasonable to predict that this method could be followed to produce methacrylate-functionalized macromonomers from a variety of vinyl-terminated polymers. However, the procedure is likely less suitable for semicrystalline polymers

such as HDPE and *i*PP due to the lower solubility in organic solvents at room temperature.

After completing the functionalization steps shown in Figure 3.4, the products were characterized and found to have higher molar mass than expected relative to the aPP-VT starting material ($M_{n,aPP-OH}$ = 2.4 kg/mol and $M_{n,aPP-MA}$ = 2.5 kg/mol). This increase in molar mass was attributed to the removal of low molar mass chains during the precipitation procedure. To confirm this, more of the aPP-VT_2.1k starting material was dissolved in good solvent and immediately precipitated into methanol using the same method as was used to collect the reaction products. Indeed, ^{1}H NMR analysis of the precipitated aPP-VT revealed the same molar mass increase as observed in the aPP-OH product. SEC analysis also clearly shows a signal reduction at high elution time, which corresponds to a removal of the smallest polymer chains (Figure 3.6).
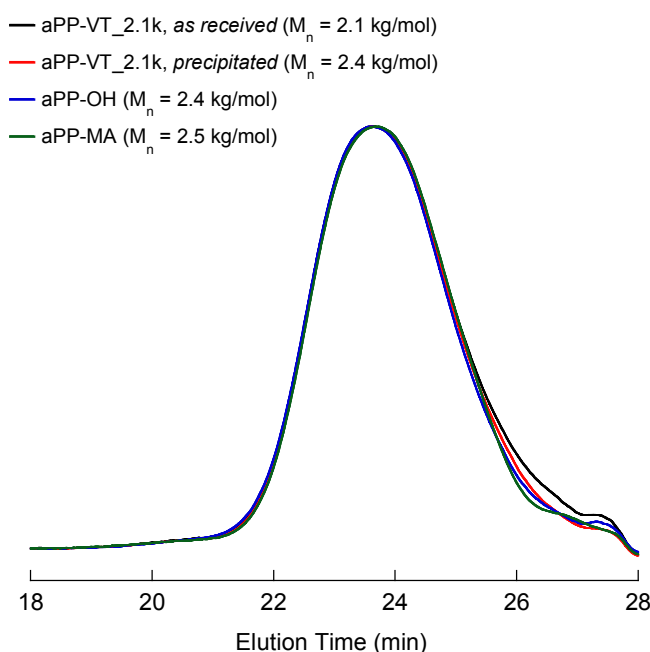
Figure 3.6. SEC traces of the indicated aPP samples after successive functionalization and precipitation procedures. The curves show a decrease in intensity at high elution times, corresponding to the removal of low molar mass fractions after precipitation into methanol. SEC measurements were taken using CHCl$_3$ mobile phase, while M_n values were calculated from ^{1}H NMR results.

3.4   Free Radical Polymerization of Macromonomers

Free radical polymerization (FRP) was the first technique attempted to synthesize bottlebrush polymers from the aPP-MA macromonomers since it is known to be a highly reactive polymerization. In comparison to systems using small monomers, the polymerization of macromonomers involves an inherently low concentration of reactive end-groups and a high starting solution viscosity. Furthermore, a high segment concentration develops around the active radical site once the first few macromonomers are added to the growing chain, which could impede further propagation. With the uncertainty of how amenable the aPP-MA macromonomers would be to polymerization, FRP served as an initial test before attempting any controlled polymerization techniques.

Two series of polymerizations were carried out in toluene at 70 °C (scheme shown in Figure 3.7) using azobisisobutyronitrile (AIBN) initiator concentrations of [I] = 5 mM and [I] = 20 mM. For each series, reactions were carried out using seven different feed concentrations of macromonomer (ranging from [M] = 20 mM – 200 mM) to assess the influence of [M] on the proceeding polymerization. Each reaction was carried out for 30 hours, and the products were analyzed by SEC-MALLS. Figure 3.8 and Figure 3.9 display the SEC traces for each series. Note that while this range of [M] seems fairly dilute, it actually corresponds to mass concentrations up to 500 mg/mL because of the large molar mass of the aPP-MA monomers. Therefore, [M] = 200 mM is near the limit of minimum solvent required to dissolve the aPP-MA.

Figure 3.8 shows the SEC traces for all of the FRP products from the [I] = 20 mM series, as well as the aPP-MA macromonomer trace. The results show a monotonic increase in product molar mass with increasing [M]. Most of the SEC traces display a wide, multi-modal distribution indicating polymerizations that are not well controlled. In fact, it is difficult to distinguish between unreacted macromonomer and the polymerization product at low [M], because the peaks are broad and close one another. It is not until [M] ≥ 80 mM that the bottlebrush polymer peak emerges as a separate distribution.
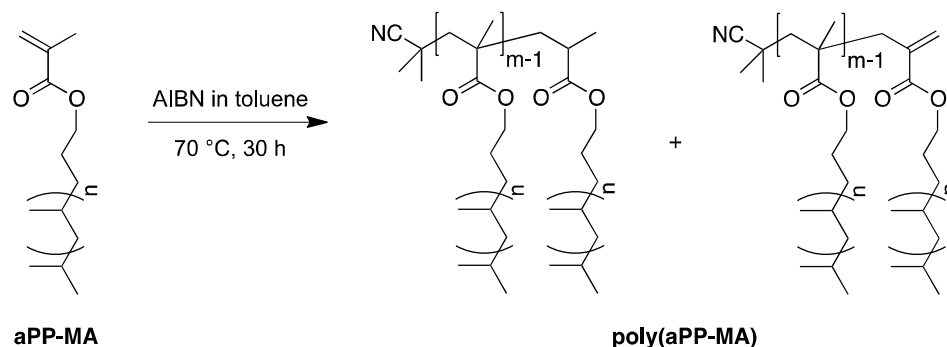
Figure 3.7. Free radical polymerization of aPP-MA. The methacrylate functional group is known to preferentially terminate by disproportionation.[51] Both disproportionation products are shown and are produced in equal amounts. The difference in end groups of the two products is expected to have very little effect on the resulting behavior since the backbone end group is surrounded by a high concentration of polypropylene segments.
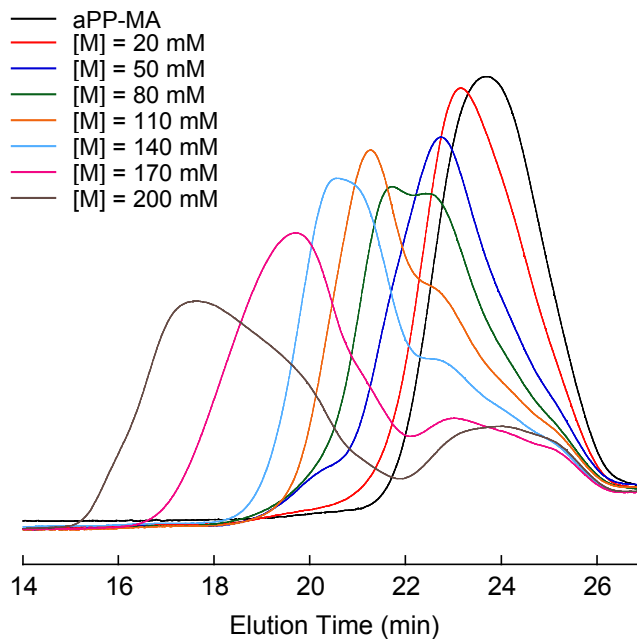
Figure 3.8. Free radical polymerizations of aPP-MA at the indicated aPP-MA concentrations, [M], using an AIBN initiator concentration of [I] = 20 mM. The eight traces are normalized to have equal integrated areas.
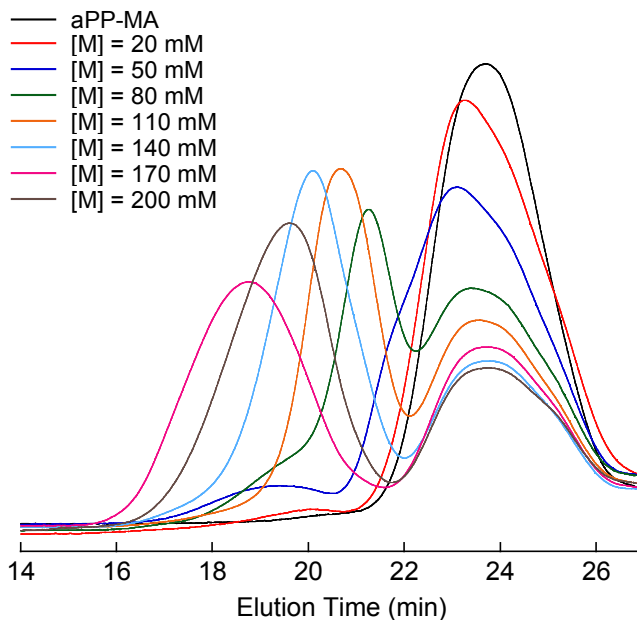
Figure 3.9. Free radical polymerizations of aPP-MA at the indicated aPP-MA concentrations, [M], using an AIBN initiator concentration of [I] = 5 mM. The traces are again normalized by integrated area.

The SEC traces for the FRP products from the [I] = 5 mM series are presented in Figure 3.9. The results at low [M] are similar to those of the [I] = 20 mM series in that no clear bottlebrush product peak emerges. However, reaction products of the higher [M] trials display much better separation from the unreacted aPP-MA. Once again the results show a consistent increase in product molar mass with [M], apart from the final reaction at [M] = 200 mM. This sample shows a reduced molar mass compared to the [M] = 170 mM sample, despite having the highest aPP-MA conversion. To analyze effects of [M] and [I], the product molar mass is plotted against [M] for both series in Figure 3.10.
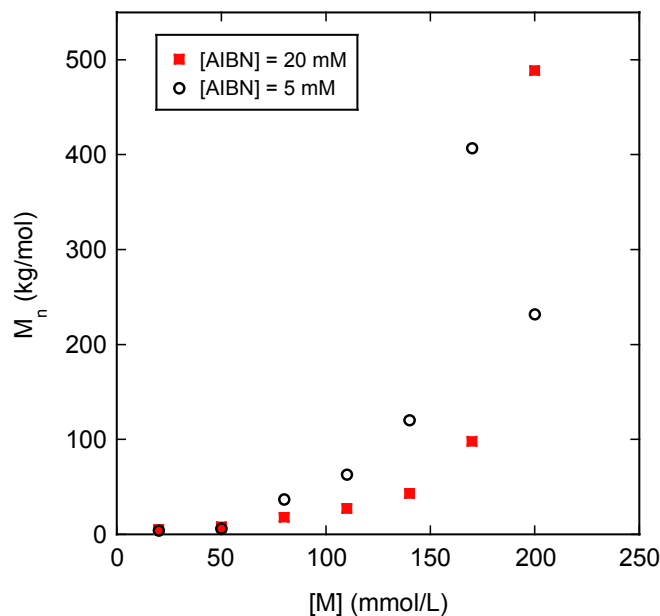
Figure 3.10. Number-average molar mass, M_n, of the free radical polymerization products versus feed aPP-MA concentration, [M]. M_n for each sample was calculated with SEC-MALLS using a THF mobile phase.

The data in Figure 3.10 reveal a dependence of the product M_n on [M] which is unique to macromonomer systems. At [M] $\leq$ 50 mM, the product M_n increases very slowly with [M] due to the slow polymerization rate associated with a low molar concentration of functional end groups. However, a sharp rise in product M_n follows in both series as [M] is increased because of the Trommsdorff effect (or autoacceleration). The Trommsdorff effect refers to the acceleration of reaction rate at high monomer conversion and is encountered in traditional FRP systems with very little solvent (*e.g.*, bulk polymerizations).[51] Acceleration occurs as the polymerization progresses due to the rapid solution viscosity increase in the absence of solvent. This in turn reduces the mobility of active radical sites lowering the rate of bimolecular termination events relative to monomer propagation steps. A similar effect arises in our macromonomer system, however, the rapid increase in product molar mass occurs with increasing [M] rather than increasing conversion. This is because the macromolecular size of aPP-MA monomers quickly increases the solution viscosity at higher [M]. Thus, the increase in

polymerization rate and product M_n is realized from the beginning of the polymerization and is not a strong function of monomer conversion.

Another result shown in Figure 3.10 is that the lower initiator concentration of [I] = 5 mM typically led to higher molar mass products. This is not surprising since a lower [I] produces a higher likelihood of propagation steps compared to bimolecular termination (k_p/k_t) for each active radical site. However, the final data point of this series shows a sharp decline in product M_n between [M] = 170 and 200 mM. This is consistent with the FRP results of Tsukahara *et al.*, which exhibit a precipitous fall in molar mass as [M] is increased towards a bulk polymerization.[102] The results in that study were attributed to the vitrification of polystyrene macromonomers at very high [M]. To further compare our results, we attempted bulk polymerizations of aPP-MA (which correspond to [M] ≈ 340 mM) using both initiator concentrations ([I] = 5 mM and 20 mM) and also found that no polymerization transpired. In our system, the bulk polymerization of aPP-MA could not be inhibited by vitrification, or by any solidification process, because aPP is an amorphous material with a low glass transition temperature (T_g ≈ −10 °C). Instead, the lack of polymerization is attributed to the fact that (1) the viscosity of bulk aPP-MA remains sufficiently high to limit aPP chain mobility, and (2) the diffusion limited radical sites are surrounded by inert aPP segments rather than reactive monomers, as is the case in bulk FRP with small monomers.

FRP of aPP-MA macromonomers enabled synthesis of bottlebrush polymers with little control over molar mass, dispersity, and macromonomer conversion. The maximum monomer conversion was 60% for the [AIBN] = 5 mM series and 71% for the [AIBN] = 20 mM data set. Still, the fact that bottlebrushes of nearly 500 kg/mol were produced indicates that the high segment density around the active radical site (associated with the multibranched structure of the propagating chain) does not preclude incorporation of macromonomers. These results motivated progression to controlled radical polymerization trials. Reversible addition-fragmentation chain transfer (RAFT) polymerization was attempted next as a means to gain further precision of the bottlebrush polymer products.

3.5   RAFT Polymerization of aPP-MA

RAFT polymerization is a form of controlled radical polymerization that utilizes a chain transfer agent (CTA) to promote rapid transfer of the active radical sites to different growing polymer species.[80] The frequent exchange of radicals allows all of the polymer chains to grow at approximately equal rates and promotes products with narrow molar mass distributions. RAFT polymerizations of aPP-MA were conducted using a similar procedure to FRP, with the addition of 2-cyano-2-propyl 4-cyanobenzodithioate as a radical CTA. This particular CTA (see Figure 3.11) was selected because it is well suited for RAFT polymerization of methacrylates.[113] AIBN was used as a thermal initiator, and a macromonomer concentration of [M] = 150 mM was chosen for all trials based on the FRP results. Multiple polymerizations were carried out at 65 °C, and variable [aPP-MA]:[CTA] ratios were used to target bottlebrush polymers of different backbone DP. Results for all of the RAFT polymerizations are given in Table 3.2.
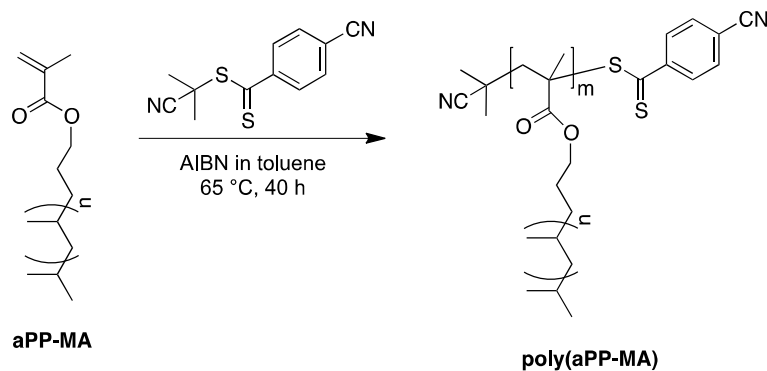
Figure 3.11. RAFT polymerization of aPP-MA macromonomers using 2-cyano-2-propyl 4-cyanobenzodithioate as a chain transfer agent (CTA).

Table 3.2. RAFT polymerization conditions and product characteristics.[a]

[aPP-MA]:[CTA]	Time (h)	M_n (kg/mol)[b]	$Đ$ [b]	Conversion (%)[c]
25	40	25	1.20	59
50	40	77	1.16	78
150	40	219	1.52	86
200	40	246	1.76	85
500	40	223	1.91	17[d]
500	115	866	1.40	43[d]

[a]For each trial, [aPP-MA] = 150 mM and [aPP-MA]:[I] = 1000. [b]Determined by SEC with MALLS detection. Dispersity ($Đ$) values reflect only the product peaks. [c]Determined by ^{1}H NMR unless specified otherwise. [d]Determined by SEC with RI detection.

Figure 3.12 presents the SEC results for the first four RAFT polymerizations listed in Table 3.2. It is clear that the product M_n increases steadily with the [M]:[CTA] ratio, demonstrating the improved molar mass control of RAFT polymerization. Additionally, the bottlebrush peaks in Figure 3.12 are much narrower than in the FRP samples, indicating products with lower dispersity. However, since the polymerizations did not achieve complete aPP-MA conversion, as demonstrated by the remnant SEC peak at high elution time, the M_n for each product is less than the targeted value.

The results for macromonomer conversion provided in Table 3.2 reveal an interesting trend. The first three samples display a rise in conversion as the [aPP-MA]:[CTA] ratio is increased. However, the conversion appears to reach a maximum at [aPP-MA]:[CTA] = 150, and the sample with the highest targeted molar mass ([aPP-MA]:[CTA] = 500) exhibits a sharp decline, attaining only 17% conversion over the 40 h reaction time. It was initially unclear whether this reduction was a consequence of some limiting poly(aPP-MA) molar mass near 250 kg/mol, or if the polymerization kinetics were significantly slowed because of the low CTA loading. To distinguish between these two possibilities, the reaction at [M]:[CTA] = 500 was repeated and allowed to run for several days. After 115 h, both the bottlebrush molar mass and macromonomer conversion were found to continue increasing linearly with time, as shown in Figure 3.13. This

demonstrates that the active radical lifetimes extend at least 5 days without termination and maintain a living polymerization character.
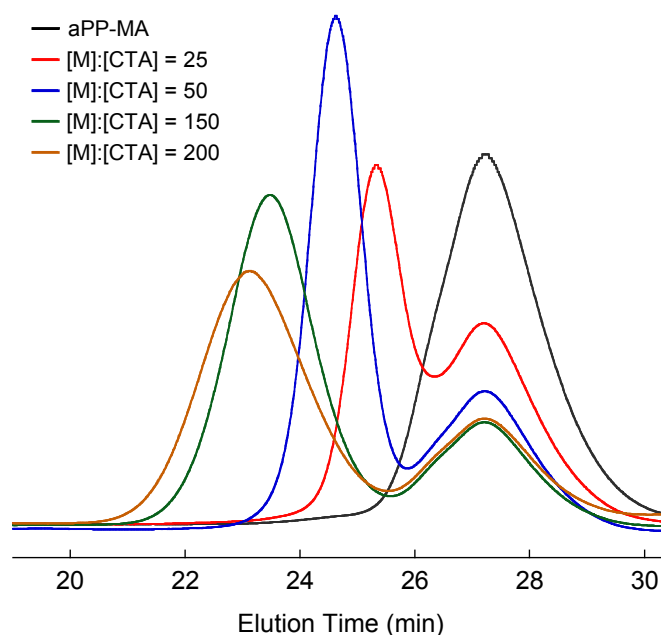
Figure 3.12. RAFT polymerizations of aPP-MA at different CTA loadings. The traces are normalized by integrated area.

The remarkable preservation of active radicals in this system is likely due to the high degree of steric shielding afforded by the local concentration of aPP branch segments. Since bimolecular termination would require the approach of two shielded radical sites, the probability becomes negligible for large bottlebrush molecules (Figure 3.14a). The shielding effect can also explain the slow rate of polymerization in the trials targeting high molar mass. In this case, the crowded active site does not completely inhibit aPP-MA propagation, as it does with termination, but it slows the rate considerably (Figure 3.14b).
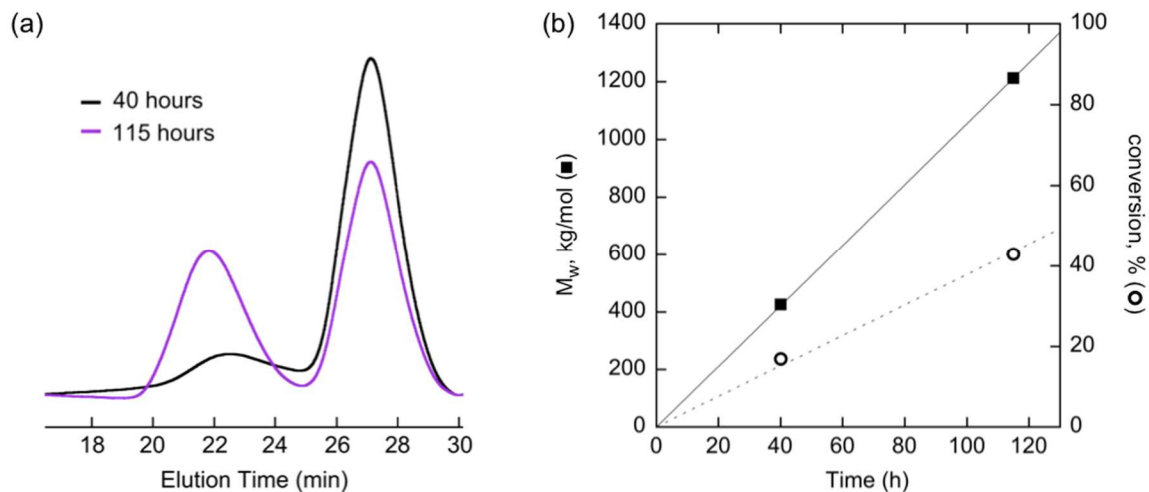
Figure 3.13. Results for RAFT polymerization of aPP-MA using [M]:[CTA] = 500. (a): SEC traces at 40 and 115 h. (b): M_w and macromonomer conversion versus time.
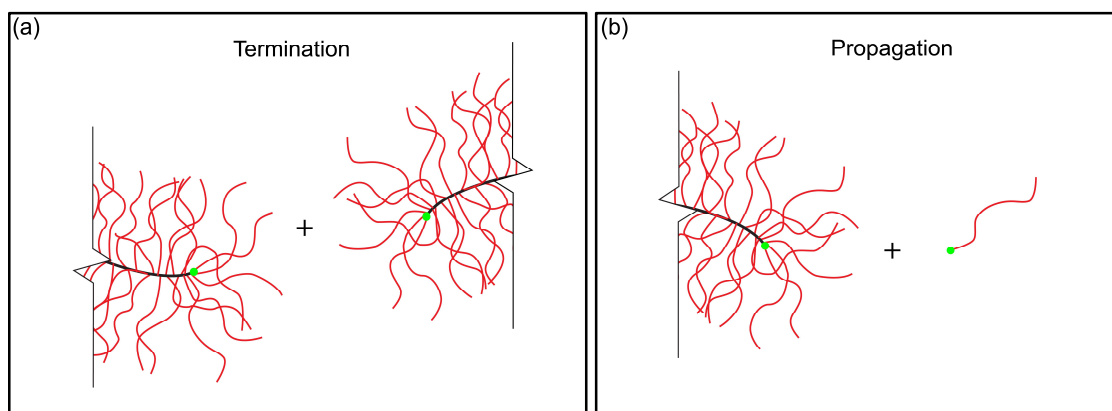
Figure 3.14. Schematic illustration of the shielding effect around the radical active sites (green). Shielding more strongly inhibits bimolecular termination (a) compared to macromonomer propagation (b).

While the polymerization rate of the [M]:[CTA] = 500 sample appears much slower than the [M]:[CTA] = 200 or [M]:[CTA] = 150 trials in terms of monomer conversion, the samples actually attain similar product molar mass (M_n = 219–243 kg/mol) over a reaction time of 40 h. Therefore, the absolute rate of propagation (*i.e.,* # of

macromonomers consumed per time) is comparable among all three samples. We believe this plateau in propagation rate derives from the saturation of steric hindrance effects as the backbone DP is increased. This viewpoint is consistent with the interpretation of Tsukahara *et al.* in rationalizing FRP results, and supports a conformational transition of bottlebrushes from star-like to cylindrical with increasing backbone length.[101]

The RAFT polymerization trials for aPP-MA macromonomers showed a marked improvement over FRP in terms of monomer conversion, dispersity, and control of product molar mass. Additionally, radical sites were found to be active and steadily polymerizing after several days. While this reflects the slow kinetics of the RAFT polymerizations, which make bottlebrush synthesis somewhat inefficient, it also highlights some unique consequences of the bottlebrush architecture that could be exploited for alternative applications. Further investigation into the effects of macromonomer concentration and reaction time of RAFT polymerizations is needed to elucidate the detailed nature of the radical stabilization effect and radical lifetime. This is an open research area that has not been explored in the literature. However, the primary synthetic goal of this project was to efficiently produce bottlebrush polymers for further examination of the rheology and self-assembly behaviors. To this end, ring-opening metathesis polymerization (ROMP) was found to be the most effective route towards well-defined aPP bottlebrush polymers and is the focus of the remainder of this chapter.

3.6   ROMP of Macromonomers

ROMP has become a commonly used polymerization technique owing to recent advancements in olefin metathesis catalysts. Many sophisticated catalysts have been developed that exhibit high reactivity, tolerance toward functional groups, and low sensitivity to air and moisture.[85,114] Ruthenium-based catalysts are particularly attractive, as they have allowed reactions to be performed at room temperature and without tedious air-free procedures.[115,116] Additionally, cyclic olefin monomers with significantly strained rings such as norbornene exhibit very high reactivity, because alleviation of ring-strain is the primary thermodynamic driving force in a ROMP reaction.[117]

One of the major drawbacks of the FRP and RAFT polymerizations described in the preceding sections was the substantial amount of unreacted macromonomer remaining in the products. ROMP serves as a good opportunity to circumvent this issue, specifically by combining the highly active ruthenium-based Grubbs metathesis catalysts with norbornenyl-functionalized macromonomers. This system offers the heightened reactivity needed to attain complete macromonomer conversion. In this section, we explore this route by first preparing norbornenyl-terminated aPP macromonomers (aPP-NB).

3.6.1   Synthesis of aPP-NB Macromonomers

Since most of the aPP-VT_2.1k was used to synthesize the aPP-MA macromonomer, aPP-VT_860 was utilized as the starting material to prepare aPP-NB. The aPP-VT_860 batch was converted to aPP-OH using the hydroboration/oxidation procedure outlined in Figure 3.4. Purified aPP-OH molecules were subsequently transformed to aPP-NB by coupling with *exo*-5-norbornene-2-carbonyl chloride (Figure 3.15). The pure *exo* isomer was used in this reaction because *exo*-substituted norbornene derivatives have been shown to participate in ROMP with Grubbs catalysts much more readily than *endo/exo* mixtures.[118] The ^{1}H NMR spectrum of the aPP-NB product is shown in Figure 3.16, along with the spectra for aPP-OH and the norbornene-carbonyl chloride reagent. End-group analysis of aPP-NB reveals one-to-one integration of the characteristic protons on either side of the ester linkage, confirming the complete conversion of hydroxyl end-groups to norbornenyl-functionalities. This functionalization procedure achieved quantitative conversion in each step, just as in the aPP-MA preparation.
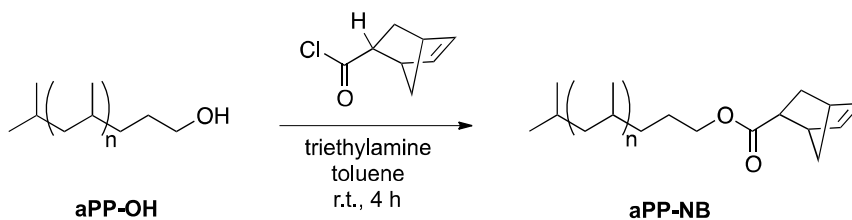
Figure 3.15. Synthesis of the aPP-NB macromonomer.
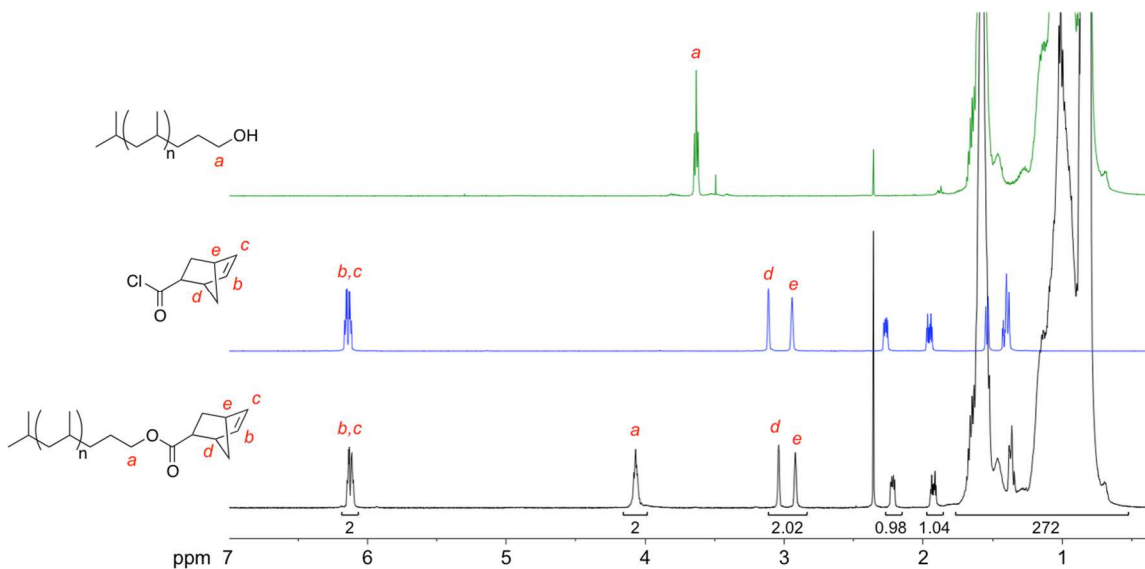
Figure 3.16. ^{1}H NMR spectra for aPP-OH (top), *exo*-5-norbornene-2-carbonyl chloride (middle), and aPP-NB (bottom). The coupling reaction presented in Figure 3.15 proceeded with quantitative conversion.

Similar to the previous functionalizations, the aPP molar mass increased with each reaction step due to the loss of short polymer chains that did not effectively precipitate into methanol during purification. Table 3.3 shows the M_n values of each functionalization product, determined by ^{1}H NMR. The molar mass increase after the first step is significant, nearly doubling the M_n of the aPP. The increase after the second step is less severe, indicating that the remaining aPP chains are large enough to have negligible solubility in methanol. Ultimately, the aPP-NB macromonomers attain nearly the same molar mass as the aPP-MA molecules ($M_{n, aPP-NB} = 2.05$ kg/mol; $M_{n, aPP-MA} = 2.5$ kg/mol).

To confirm that the molar mass increase was in fact caused by the precipitation step and not due to incomplete end-functionalization, which would result in an apparent molar mass increase by end-group analysis, we dissolved and re-precipitated the aPP-VT_860 multiple times and analyzed the polymer after each round. The results are displayed in Table 3.3 and demonstrate a clear increase in aPP molar mass.

Table 3.3. Molar mass of aPP-VT_860 after successive functionalization steps (left) or precipitations into methanol (right).

Functionalization products			aPP-VT_860 characterization	
Sample	M_n (g/mol)[a]	$Đ$ [b]	Preparation	M_n (g/mol)[a]
aPP-VT_860	950	1.88	As received	950
aPP-OH	1800	1.68	Precipitated once	1420
aPP-NB	2050	1.65	Precipitated twice	1760

[a]Determined by ^{1}H NMR. [b]Determined by SEC-MALLS.

3.6.2   First Generation Grubbs Catalyst (**G1**)

After purifying the aPP-NB macromonomers, ROMP trials were carried out following the scheme in Figure 3.17. Three Grubbs metathesis catalysts (**G1**, **G2**, and **G3**) commonly used for ROMP are displayed in Figure 3.18. Anderson-Wile and coworkers previously employed catalysts **G1**, **G2**, and **G3** for the ROMP of norbornene-terminated syndiotactic polypropylene (*s*PP) molecules and identified catalyst **G1** as the most effective.[119] Both **G2** and **G3** were found to yield poly(macromonomer)s with broad molecular weight distributions ($Đ \geq 2$) and unexpectedly low M_n values. Conversely, several recent studies have reported successful living ROMP of poly(macromonomer)s using catalyst **G3**.[120,121] Given the similarity of the aPP-NB macromonomers in this work with those in the Anderson-Wile study, and also the recent success of the **G3** catalyst, we chose to test all three catalysts and evaluate their efficacy. Polymerizations were conducted at room temperature in septum-sealed vials under an argon atmosphere at 50 mg/mL (aPP-NB in THF), and the polymerization kinetics were monitored by SEC-MALLS analysis of removed aliquots.
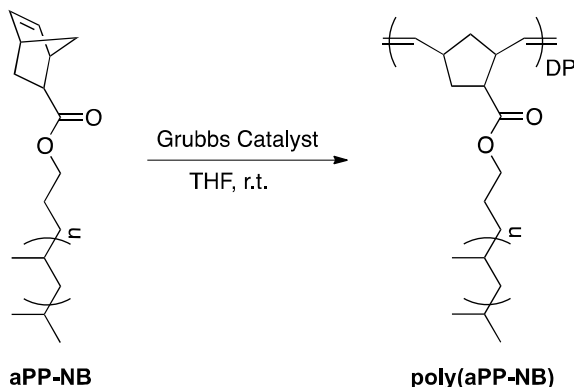
Figure 3.17. ROMP of aPP-NB macromonomers, yielding bottlebrush polymers with poly(norbornene) backbones.
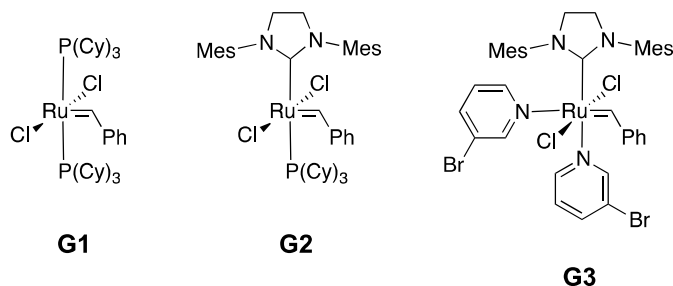
Figure 3.18. Grubbs 1st generation (G1), 2nd generation (G2), and 3rd generation (G3) catalysts.

The first test reaction employed **G1** at a catalyst loading of [aPP-NB]:[**G1**] = 50. The SEC traces of several aliquots are shown in Figure 3.19. It is apparent that ROMP of aPP-NB yields much better results than either FRP or RAFT polymerization attempts. The SEC traces in Figure 3.19 display a steady decrease in the aPP-NB macromonomer peak and an increase in product peak intensity as the reaction progressed. The product peak elution time also consistently decreases, corresponding to a molar mass increase at longer reaction times. After 18 h, the reaction achieves complete conversion of aPP-NB. The only low molar mass polymers remaining (~3 wt%) are due to the presence of non-functionalized aPP chains. Figure 3.19 also presents a plot of both molar mass and

dispersity as functions of aPP-NB conversion. The near-linear increase in molar mass with conversion and the decrease in product dispersity demonstrate the living nature of this polymerization. Consequently, the final product dispersity is much lower than the radical polymerization products, and there is no further purification required to separate bottlebrush polymers from aPP-NB impurities.
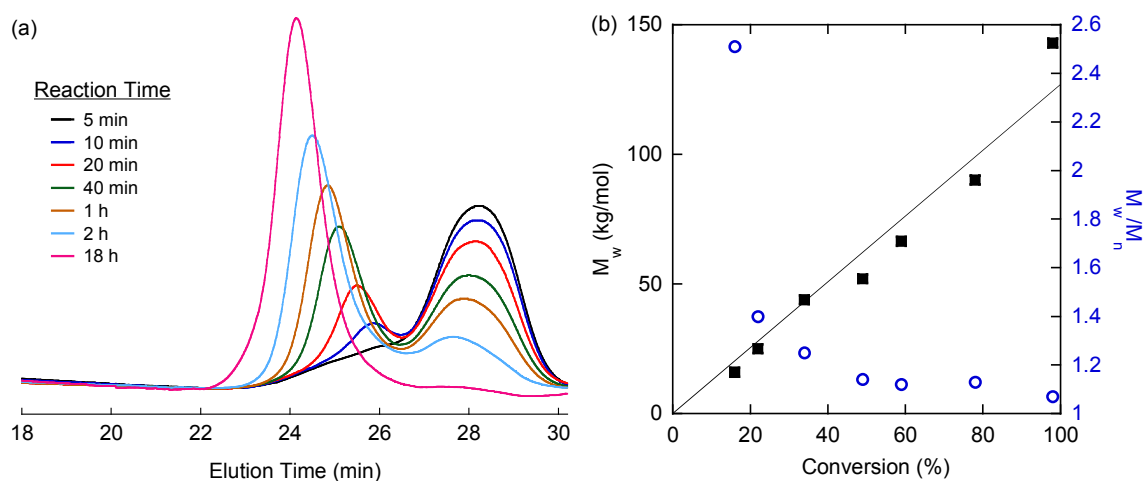
Figure 3.19. Results for ROMP of aPP-NB with G1 at a catalyst loading of [aPP-NB]:[**G1**] = 50. (a): SEC traces at several reaction times. (b): M_w and $Đ$ verses macromonomer conversion.

Following the successful first attempt, we repeated the ROMP experiment with **G1** using a five-fold lower catalyst loading of [aPP-NB]:[**G1**] = 250 in order to target ultra-large bottlebrush products. Several aliquots were taken throughout the reaction, and the SEC results are shown in Figure 3.20. The product molar mass once again appears to increase with monomer conversion, but the product peaks are not as well defined as in the previous trial. A considerable amount of intensity remains at intermediate elution time (~25 min), causing broad and bimodal overall distribution. The rate of polymerization was also reduced compared to the [aPP-NB]:[**G1**] = 50 reaction as shown in the kinetics plot in Figure 3.21. The kinetics data from both reactions are represented as $\ln([M]_0/[M])$ versus time, where [M] is aPP-NB concentration as a function of time and $[M]_0$ and is the

initial concentration. While both reactions demonstrate first-order kinetics, the decreased catalyst loading clearly leads to a diminished polymerization rate, indicated by the slopes in Figure 3.21.

The results of ROMP with **G1** yielded aPP bottlebrush polymers with low dispersity and high macromonomer conversion, especially when targeting low molar mass. The reaction time was also faster than the FRP or RAFT polymerizations. However, complete conversion still required an overnight reaction at [aPP-NB]:[**G1**] = 50, and even slower kinetics were observed at [aPP-NB]:[**G1**] = 250. Therefore, ROMP with **G1** may be prohibitively slow for synthesizing ultra-high molar mass bottlebrush polymers.
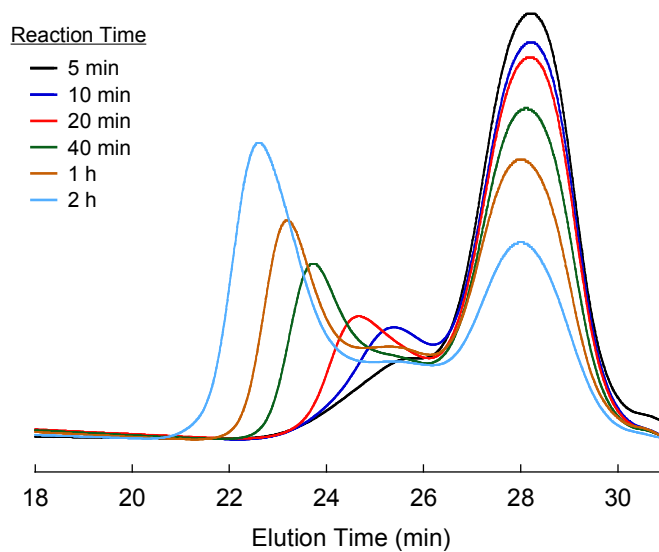
Figure 3.20. SEC traces for ROMP of aPP-NB macromonomers using a catalyst loading of [aPP-NB]:[G1] = 250 at several reaction times.
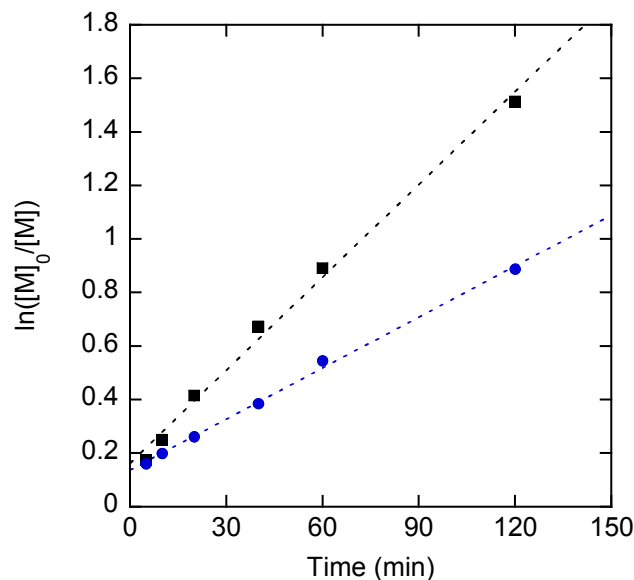
Figure 3.21. Kinetics plot for ROMP of aPP-NB macromonomers using catalyst G1 at a loading of [aPP-NB]:[G1] = 50 (squares) and a loading of [aPP-NB]:[G1] = 250 (circles). Both reactions exhibit first-order kinetics, *i.e.*, the log of monomer concentration [M] is a linear function of time. The [aPP-NB]:[G1] = 50 reaction shows a higher slope, indicating faster kinetics since the slope on this plot represents the apparent propagation rate constant (k_p^{app}).

3.6.3   Second Generation Grubbs Catalyst (**G2**)

The next catalyst screened was **G2**. The same two kinetics experiments were carried out using catalyst loadings of [aPP-NB]:[**G2**] = 50 and [aPP-NB]:[**G2**] = 250, and the results are shown in Figure 3.22. As opposed to the steady polymerization and low dispersity product achieved using **G1**, ROMP with **G2** exhibits a rapid, uncontrolled polymerization. Both experiments yield products with broad, multimodal molar mass distributions. Interestingly, the peak corresponding to the aPP-NB macromonomer disappears within 20 min for the higher **G2** loading (Figure 3.22a) and within 1 h for the lower loading (Figure 3.22b), illustrating a tremendous rate of macromonomer consumption. Nevertheless, the uncontrolled reaction products establish **G1** as a superior candidate for synthesizing aPP bottlebrushes.
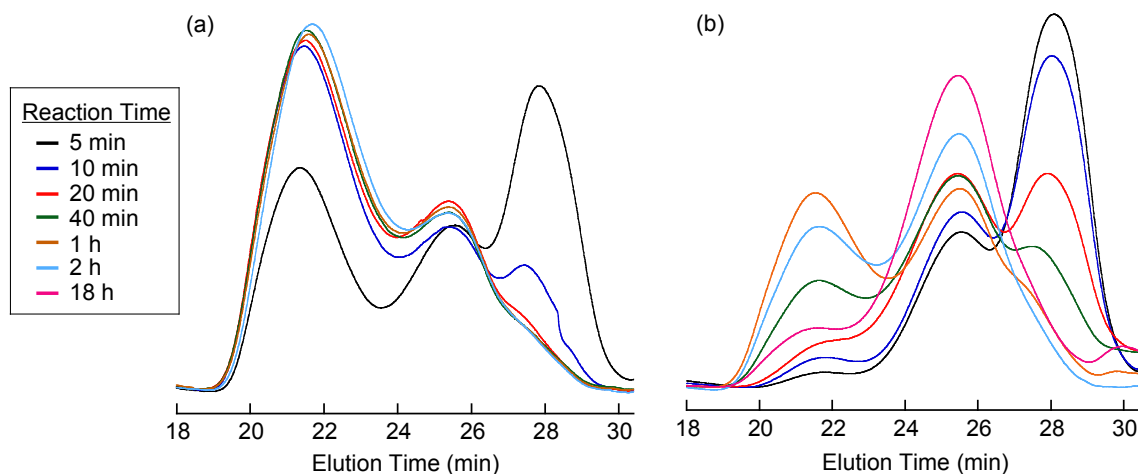
Figure 3.22. SEC traces for ROMP of aPP-NB macromonomers using catalyst G2 at several reaction times. (a): Catalyst loading of [aPP-NB]:[G2] = 50. (b): Catalyst loading of [aPP-NB]:[G2] = 250.

3.6.4 Third Generation Grubbs Catalyst (**G3**)

G3 was the final metathesis catalyst screened for ROMP of aPP-NB macromonomers. Test polymerizations were again performed using catalyst loadings of [aPP-NB]:[**G3**] = 50 and 250, and the same timing was used between aliquots as in the experiments with **G1** and **G2**. Remarkably, the SEC results reveal that the traces from all of the time points were virtually indistinguishable. This is demonstrated in Figure 3.23 where the SEC results for both trial polymerizations are shown at only the shortest and longest reaction times. In each instance the reaction was completed in 5 min, and the product peaks did not evolve with additional reaction time. Moreover, the products realized even lower dispersity than bottlebrushes obtained using **G1**. These results represent optimal polymerization performance, achieving bottlebrush polymers with low dispersity, precise molar mass control, and complete macromonomer conversion in less the 5 min.
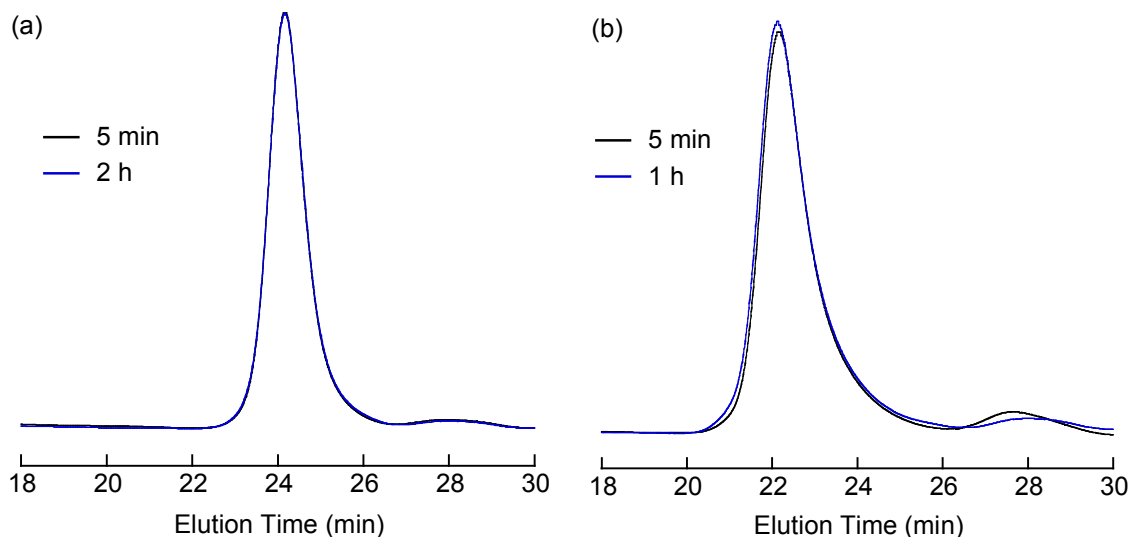
Figure 3.23. SEC traces from ROMP of aPP-NB macromonomers using catalyst G3. (a): Catalyst loading of [aPP-NB]:[G3] = 50. SEC characterization yields M_n = 137 kg/mol, $Đ$ = 1.03 (LS detection), and conversion = 97%. (b): Catalyst loading of [aPP-NB]:[G3] = 250. SEC characterization yields M_n = 500 kg/mol, $Đ$ = 1.2 (LS detection), and conversion = 96%.

Following the success of ROMP using **G3**, we scaled up to gram quantities of aPP-NB (as opposed to the 200 mg scale used in test polymerizations) and carried out three additional ROMP reactions using **G3** loadings of [aPP-NB]:[**G3**] = 65, 245, and 647. The first two reactions were essentially scaled-up versions of the two trial polymerizations, whereas the third reaction aimed to synthesize ultra-high molar mass bottlebrushes with a target backbone DP of 650. These samples were quenched at much shorter reaction times (either 10 or 20 min) because of the rapid polymerization rate observed in the initial trials.

Figure 3.24 presents the SEC traces for the scaled-up polymerizations with catalyst loadings of [aPP-NB]:[**G3**] = 65 and 245. Both reactions show identical results to the test polymerizations displayed in Figure 3.23, demonstrating the control of product molar mass enabled by this synthetic approach. Figure 3.25 displays the results of the final polymerization, which was targeting bottlebrush polymers of $M_n > 10^6$ g/mol. Clearly the kinetics became significantly slower at this catalyst loading. The reaction was still

progressing after 20 min, at which point 59 % conversion had been completed. The molar mass of the product was also greater than expected given the incomplete aPP-NB conversion. This may result from the uncertainty in measuring out a very small amount of catalyst required for the low **G3** loading. As seen with the **G1** catalyst, longer reaction times are required when targeting high molar mass bottlebrushes.
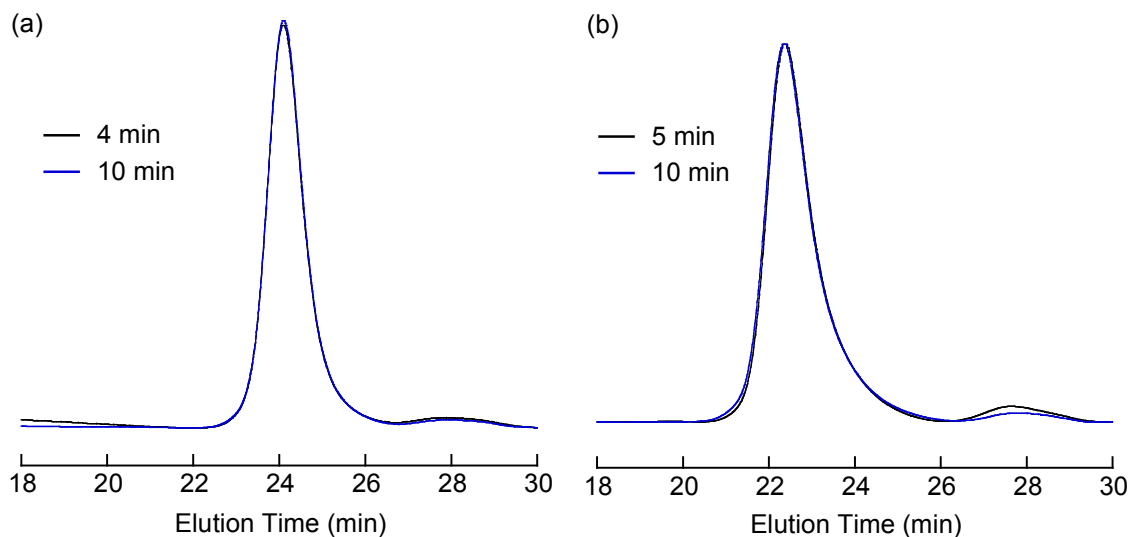
Figure 3.24. SEC traces from ROMP of aPP-NB macromonomers using catalyst G3 and scaled up to a 1 g scale. (a): Catalyst loading of [aPP-NB]:[G3] = 65. SEC characterization yields M_n = 148 kg/mol, $Đ$ = 1.03 (LS detection), $Đ$ = 1.19 (RI detection), and conversion = 97%. (b): Catalyst loading of [aPP-NB]:[G3] = 245. SEC characterization yields M_n = 478 kg/mol, $Đ$ = 1.09 (LS detection), $Đ$ = 1.43 (RI detection), and conversion = 97%.
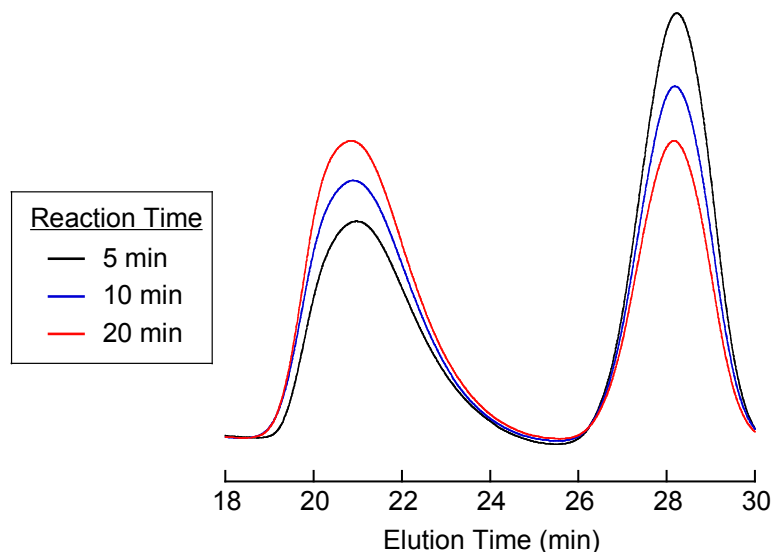
Figure 3.25. SEC traces from ROMP of aPP-NB macromonomers scaled up to a 1 g scale and using a catalyst loading of [aPP-NB]:[G3] = 647. SEC characterization at 20 min reaction time yields a product peak with M_n = 1262 kg/mol, $Đ$ = 1.37 (LS detection) and $Đ$ = 1.88 (RI detection). Conversion: 5 min (42%), 10 min (52%), 20 min (59%).

3.6.5   Comparison of Grubbs Catalysts

Table 3.4 compares the efficacy of ROMP using the three different Grubbs catalysts, maintaining consistent reaction conditions and a catalyst loading of [aPP-NB]:[catalyst] = 50. ROMP with **G1** progressed in a controlled manner, exhibiting a linear increase in product molecular weight with conversion and low dispersity. First-order kinetics were observed throughout the polymerization, and complete conversion was achieved after 18 hours (Figure 3.19 and Figure 3.21). The small peak at high elution time in the SEC trace of the final product corresponds to a ~3 wt. % of remaining macromonomer, which is attributed to the presence of non-functionalized aPP molecules in the starting material. ROMP with **G2** displayed a much faster rate of polymerization than with **G1**, but the reaction was not well controlled and resulted in a broad, bimodal molecular weight distribution. SEC-MALLS analysis of the final product revealed a wide fraction of high molecular weight bottlebrushes with a peak molecular weight centered around 1300 kg/mol, and a smaller peak centered at approximately 60 kg/mol. The dispersity reported

in Table 3.4 represents the breadth of the entire bimodal distribution. Lastly, ROMP with **G3** proved to be the most effective system. Catalyst **G3** attained a higher rate of polymerization than **G2**, achieving complete conversion in less than five minutes, and resulted in a product with even lower dispersity than ROMP with **G1**. Additionally, this reaction was allowed to continue stirring for two hours before terminating with ethyl vinyl ether. Inspection of the SEC traces after five minutes and after two hours revealed indistinguishable reaction products (Figure 3.23). Thus, no chain transfer reactions occurred after the macromonomer was fully consumed, and a narrow molecular weight distribution was maintained. The suppression of chain transfer (cross metathesis) reactions may be due to steric screening of internal double bonds by the high segment density surrounding the backbone chain.

Table 3.4. Comparison of Grubbs catalysts at a loading of [aPP-NB]:[catalyst] = 50.

entry[a]	catalyst	M_n (kg/mol)[b]	$Đ$ [b]	time to 90% conversion (min)[c]
1	**G1**	130	1.09	180
2	**G2**	177	4.81	10
3	**G3**	137	1.03	< 5

[a][aPP-NB] = 0.025 M for all entries. [b]Determined by SEC-MALLS. [c]Estimated time to achieve 90% macromonomer conversion. Time for entry 1 was based on first-order kinetics fit (Figure 3.21).

The increased reaction rates observed with **G2** and **G3** are caused by the replacement of one phosphine ligand from **G1** with a N-heterocyclic carbene ligand, which leads to a substantial increase in the propagation rate constant (k_p) of these catalysts.[122] However, this results in a low ratio of the initiation rate constant (k_i) to k_p ($k_i/k_p \ll 1$) in the case of **G2** and promotes high-dispersity polymerization products. Alternatively, the k_i of **G3** has been reported up to six orders of magnitude greater than k_i of **G2**.[123] Thus, the increased k_p of **G3** is balanced by an elevated k_i, and the k_i/k_p ratio remains sufficiently high to generate controlled polymerizations.

While the results obtained using **G1** and **G2** are similar to the findings reported by Anderson-Wile *et al.*, the results achieved using **G3** differ significantly. The most substantial difference in the reaction conditions between these studies is the polymerization temperature. ROMP reactions in the previous study were carried out at elevated temperatures (60 °C) to maintain solubility of the semicrystalline *s*PP macromonomers. These observations suggest that the reaction temperature has a considerable effect on catalyst performance and support the notion that lower reaction temperatures produce more controlled products with catalyst **G3**.[124] Based on these results, ROMP with catalyst **G3** was chosen as the best method for synthesizing bottlebrush polymers and was used to prepare all of the samples needed for rheology (chapters 4 and 5) and self-assembly studies (chapter 6 and 7).

3.7   Experimental Methods

3.7.1   Materials

All chemicals were purchased from Sigma-Aldrich and used as received unless otherwise specified. All aPP-VT samples were obtained from the ExxonMobil Chemical Company.

3.7.2   Molecular Characterization

^{1}H NMR spectra were acquired on a Bruker Avance III 500 MHz spectrometer in CDCl$_3$ solvent. Size exclusion chromatography (SEC) analysis was performed using two different instruments. Early SEC measurements, particularly for aPP-MA macromonomers and poly(aPP-MA) bottlebrushes, were run using an Agilent 1100 series liquid chromatograph (LC) with a Hewlett-Packard HP1047A refractive index (RI) detector. This instrument was calibrated with polystyrene standards and operated with a CHCl$_3$ mobile phase at 35 °C under a flow rate of 1.0 mL/min. Later measurements were taken using an Agilent 1260 Infinity LC system equipped with 3 Waters Styragel columns in series, a Wyatt DAWN Heleos II 18-angle laser light scattering detector, and a Wyatt OPTILAB T-rEX RI detector. This instrument was operated at 25 °C with a THF

mobile phase and a flow rate of 1.0 mL/min. Absolute molecular weights of aPP macromonomers and aPP bottlebrushes were determined using the in-line light scattering detector and a dn/dc value of 0.079 mL/g.[125] Further molecular characterization by matrix-assisted laser desorption/ionization mass spectrometry (MALDI-MS) was also attempted, though unsuccessfully, for the aPP-VT_2.1k sample using both dithranol and 2,5-dihydroxybenzoic acid (DHB) matrices. This result was not too surprising since non-aromatic, hydrocarbon polymers such as PP cannot readily ionize and are often difficult to examine by MALDI-MS.[126]

3.7.3   Polymer Synthesis

3.7.3.1   Synthesis of aPP-OH

The aPP-VT starting material was converted to aPP-OH *via* consecutive hydroboration/oxidation of the terminal olefin. This reaction was carried out several times for different aPP-VT starting materials and different batch sizes. Conditions for a representative reaction are outlined here. First, aPP-VT (10 g, 5.7 mmol) was dissolved in THF (50 mL) under an argon atmosphere. The solution was cooled to −20 °C before slowly adding a solution of 9-Borabicyclo[3.3.1]nonane (9-BBN) in THF (25 ml, 12.5 mmol). After stirring for 18 h at room temperature, the solution was again cooled to −20 °C and methanol (5 ml) was added slowly. Aqueous sodium hydroxide (10 ml, 6N) and hydrogen peroxide (14.2 ml, 125 mmol) were then added, and the solution was gradually heated to 40 °C and stirred for 4 hours. The resulting solution was cooled to room temperature, and the solvent was removed by rotary evaporation. The residual polymer was dissolved in chloroform (50 mL), and the solution was washed once with dilute HCl (pH of 5) and three times with deionized water in a separatory funnel. The chloroform solution was then dried over magnesium sulfate. The product was precipitated into chilled methanol (500 ml) at 0 °C and dried in vacuo. Yield: 8.71 g (87.1%); Chemical conversion of recovered product: 97%. ^{1}H NMR (500 MHz, CDCl$_3$, 25 °C): δ = 3.66ppm (t, 2H), 0.60 – 1.80ppm (m, 260H). ^{1}H NMR spectrum is presented in Figure 3.5.

3.7.3.2   Synthesis of aPP-MA Macromonomers

First, aPP-OH (5 g, 2.08 mmol), triethylamine (0.35 ml, 2.51 mmol), and toluene (20 mL) were mixed in a 100-mL round-bottom flask and degassed by bubbling with argon gas. The solution was cooled in an ice bath to 0 °C and methacryloyl chloride (0.61 ml, 6.25 mmol) was added dropwise. The solution was then allowed to warm to room temperature and stirred for 4 h. After the reaction, the mixture was opened to air and filtered, and the solvent was removed by rotary evaporation. The polymer residue was dissolved in chloroform (50 mL) and washed three times with dilute hydrochloric acid (pH of 5), three times with sodium bicarbonate solution (pH of 9), and once with deionized water. The chloroform solution was dried over magnesium sulfate, filtered, and the solvent was again removed by rotary evaporation. Finally, the product was dissolved in toluene (25 mL) and precipitated into chilled methanol (250 mL) at 0 °C. The purified product was dried in vacuo until all solvent was removed (confirmed by ^{1}H NMR). Yield: 3.81 g; Chemical conversion of recovered product: 99 %.

3.7.3.3   Free Radical Polymerization of the aPP-MA

Typically, several homopolymerizations were conducted concurrently. For each reaction, aPP-MA (50 mg) was first placed into a 2-mL glass ampule. A desired amount of AIBN solution in toluene was then added to each ampule and stirred until the aPP-MA completely dissolved. The amounts of initiator and toluene solvent were adjusted for each sample to vary the feed concentrations of [aPP-MA] and [AIBN]. The ampules were then degassed, flame-sealed under vacuum, and heated to 70 °C while stirring. After 30 h, the polymerizations were quenched in liquid nitrogen and opened to air. Product mixtures were transferred to collection vials and dried under vacuum.

3.7.3.4   RAFT Polymerization of aPP-MA

The procedure for RAFT polymerization was comparable to that of free radical polymerization, with the addition of a RAFT chain transfer agent (CTA). First, a stock solution was prepared containing AIBN (33 μg, 0.2 μmol) and a desired amount of 2-

cyano-2-propyl 4-cyanobenzodithioate CTA (dependent on the target [M]:[CTA] ratio). A 20-mL scintillation vial was then charged with aPP-MA (2.5 g, 1.0 mmol), toluene (3 mL), and 0.5 mL of the AIBN/CTA stock solution. The mixture was stirred and transferred into a 5-mL glass ampule, which was then degassed and flame-sealed under high vacuum before heating to 65 °C. After the desired reaction time, the ampule was quenched in liquid nitrogen and opened to the atmosphere. The product was transferred to a collection vial and dried under vacuum.

3.7.3.5　Synthesis of aPP-NB macromonomers

Exo-5-norbornenecarboxylic acid (10 g, 72 mmol) was dissolved in deoxygenated toluene (50 mL) in a 250-mL round-bottom flask under an argon atmosphere. Oxalyl chloride (6.2 mL, 72 mmol) was slowly added to the solution with constant stirring. Excess pressure in the reaction flask was relieved from the headspace using a bubbler. The reaction mixture was first stirred at room temperature for 30 min, then at 60 °C for 1 h and 70 °C for 1 h before cooling back down to room temperature. Any remaining oxalyl chloride was removed under gentle vacuum along with ~10% of the toluene solvent. In a separate flask triethylamine (10.3 mL, 73.8 mmol), aPP-OH (25.5 g, 13.8 mmol), and toluene (125 mL) were mixed and degassed by consecutive freeze-pump-thaw cycles. This mixture was added to the reaction flask *via* cannulation. The resulting solution was stirred for 12 h. The product was isolated by precipitating twice in copious amounts of methanol. ^{1}H NMR (500 MHz, CDCl$_3$, 25 °C): δ = 6.15ppm (m, 2H), 4.09ppm (m, 2H), 3.07ppm (s, 1H), 2.95ppm (s, 1H), 2.25ppm (dd, 1H), 1.95ppm (dt, 1H), 0.60 – 1.80ppm (m, 276H). ^{1}H NMR spectrum is presented in Figure 3.16.

3.7.3.6　ROMP of aPP-NB

In a typical reaction, aPP-NB (200 mg, 0.1 mmol) was added to a 20-mL scintillation vial and dissolved in THF (3 mL). The vial was sealed with a rubber septum and purged with argon gas. In a separate scintillation vial, a stock solution of Grubbs catalyst in THF was prepared and a portion (1 mL, 0.002 mmol) was added quickly to the aPP-NB solution. The stock solution was used within 2 minutes of its preparation to minimize the amount

of catalyst deactivation upon dissolution in solvent. The solution was allowed to stir for the desired reaction time, and the mixture was then quenched with excess ethyl vinyl ether (0.5 mL). The product was purified by precipitation in methanol (250 mL) and dried under vacuum overnight. All steps were carried out at room temperature.

Many of the ROMP experiments required removal of aliquots to study the polymerization kinetics. Aliquots were taken as follows. A 1-mL syringe equipped with a 6-inch needle was used to remove 0.2 mL of the reaction mixture (assuming a 50 mg/mL solution), and the aliquot was injected into a prepared vial containing THF (1.7 mL) and ethyl vinyl ether (0.1 mL) to immediately terminate reaction activity. The solutions were then stirred for at least 30 min before characterization by SEC. These quantities yield 5 mg/mL aliquot solutions (2.0 mL total volume), which can be directly run on the SEC without further preparation.

Chapter 4

Rheology of aPP Bottlebrushes

4.1   Introduction

The rheological properties of polymeric materials are governed by structure at the molecular level. By adjusting structural details such as stereoregularity, molar mass, or chain architecture, the bulk viscoelastic behavior can be dramatically altered. Polyolefins such as polyethylene (PE) and polypropylene (PP) are known to exhibit shear and extensional rheological responses that are particularly dependent on the degree of branching.[44] Long-chain branched polyolefins display improved elasticity and melt strength compared to their linear analogues, and the elongational properties of linear polyolefins can be tuned by blending in a desired amount of long-chain branched polymers.[45-48] Further development of highly branched polyolefins may be especially advantageous as a means to expand the breadth of properties available to commercially viable polyolefin blends and composite materials. Over the past few decades, the linear

---

Portions of the work presented in this chapter were reproduced with permission from the following: Dalsin, S. J.; Hillmyer, M. A.; Bates, F. S. *ACS Macro Lett.* **2014**, *3*, 423–427. Copyright 2014 American Chemical Society. Dalsin, S. J.; Hillmyer, M. A.; Bates, F. S. *Macromolecules* **2015**, *48*, 4680–4691. Copyright 2015 American Chemical Society.

viscoelastic properties of branched polymer melts have been studied extensively using both experiments and theoretical modeling. Several branched polymer architectures have been considered including stars,[127-133] combs,[13,133-140] H-polymers,[141] and pom-poms.[142] The dynamics of these systems are commonly described by a hierarchical relaxation process, in which the outermost branch segments relax first while the internal segments near branch points relax at later times within a solvated tube.[143-145] Thus far, less consideration has been given to the behavior of bottlebrush polymers in the melt.

In this chapter, a series of bottlebrush polymers containing aPP side chains were synthesized *via* ROMP using **G3** as the polymerization catalyst. Samples were prepared with fixed side chain length and variable backbone e DP ranging from 11–732 (M_w = 22–1500 kg/mol). The melt-state rheology of this series was investigated using small-amplitude oscillatory shear (SAOS) analysis, and the dynamic relaxation spectra and zero-shear viscosity scaling behavior were evaluated.

4.2   Characterization of aPP Bottlebrushes

In chapter 3, ROMP of the aPP-NB macromonomers was shown to be the most effective route for bottlebrush synthesis. This method was therefore employed to prepare batches of aPP bottlebrush polymers for rheological investigation. The complete reaction scheme for macromonomer and bottlebrush synthesis is given in Figure 4.1. Several samples with various backbone chain lengths were synthesized from a single batch of aPP-NB (M_n = 2.05 kg/mol) by adjusting the [aPP-NB]:[**G3**] feed ratio to target specific backbone degrees of polymerization (DPs). Reactions were carried out at room temperature in THF, and the products were quenched with ethyl vinyl ether and isolated by precipitation into methanol. The results of each polymerization are summarized in Table 4.1. The last sample listed in Table 4.1 is a traditional aPP with linear chain architecture, which serves as a control sample for evaluating the rheological behavior of the bottlebrush polymers.
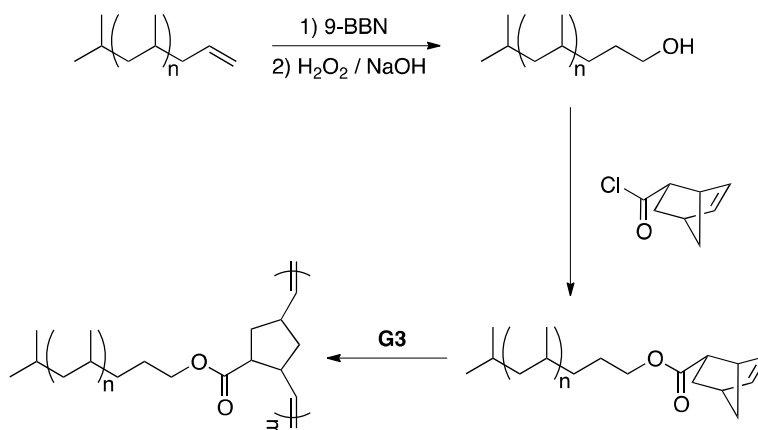
Figure 4.1. Synthesis and polymerization of aPP-NB macromonomers.

Table 4.1. Molecular and thermal characterization of aPP samples.[a]

Sample [b]	[aPP-NB]:[**G3**][c]	M_w (kg/mol)[d]	$Đ$ [d]	DP [f]	T_g (°C)[g]
aPP-NB	n/a	3.38[e]	1.65	n/a	-25.7
poly(aPP-NB)_11	10	22.5	1.07	11	-10.0
poly(aPP-NB)_26	20	53.1	1.03	26	-9.5
poly(aPP-NB)_74	65	152	1.03	74	-9.0
poly(aPP-NB)_215	150	440	1.12	215	-9.2
poly(aPP-NB)_732	485	1500	1.69	732	-9.5
aPP_Linear [h]	n/a	203	1.57	n/a	-7.0

[a]All ROMP reactions, excluding that of poly(aPP-NB)_732, were run for 10 min before termination and achieved quantitative aPP-NB conversion. Poly(aPP-NB)_732 was stirred for 4 h and attained ~94% conversion due to slower polymerization kinetics. [b]Bottlebrush samples are labeled poly(aPP-NB)_*DP*. [c]Reaction feed ratio. [d]Determined by SEC-MALLS in tetrahydrofuran. [e]M_n was determined by end-group analysis of ^{1}H NMR spectrum. M_w was determined as M_n x $Đ$ for this sample. [f]Weight-average degree of polymerization of poly(norbornene) backbone using M_{branch} = 2.05 kg/mol. [g]T_g midpoint value measured by DSC. [h]Linear aPP sample provided by the ExxonMobil Chemical Company.

The preliminary ROMP results in chapter 3 demonstrated a significant decrease in polymerization rate and an increase in product dispersity only when targeting high molar mass bottlebrushes ([aPP-NB]:[**G3**] $\geq$ 250). Correspondingly, the polymerizations in Table 4.1 with higher catalyst loadings, *i.e.*, lower [aPP-NB]:[**G3**] ratio, were completed in less than ten minutes and resulted in narrow molar mass distributions. The only sample with [aPP-NB]:[**G3**] > 250 was poly(aPP-NB)_732, which required a 4 h reaction time and exhibited the largest *Đ*. The increase in dispersity at low catalyst loading may be a result of catalyst deactivation due to possible solvent impurities or increased oxygen exposure. These types of deleterious effects would become more consequential with longer reaction times and affect the slower polymerizations to a greater extent.

Figure 4.2 displays the SEC traces of each ROMP product, as well as the trace of aPP_Linear (offset vertically). Comparison between the traces in Figure 4.2 reveals how the relationship of molecular weight versus elution time differs considerably between bottlebrush and linear polymers. Specifically, the poly(aPP-NB)_215 sample (M_n = 440 kg/mol) elutes from the columns at approximately the same time as aPP_Linear (M_n = 185 kg/mol), demonstrating that high molecular weight bottlebrushes generally elute at the same time as lower molecular weight linear polymers. This phenomenon results from the compact nature of the bottlebrush molecules. Their reduced hydrodynamic volume relative to linear polymers of the same molecular weight highlights the importance of using an SEC instrument equipped with light scattering detection to ensure absolute molecular weight determination of bottlebrush polymers.
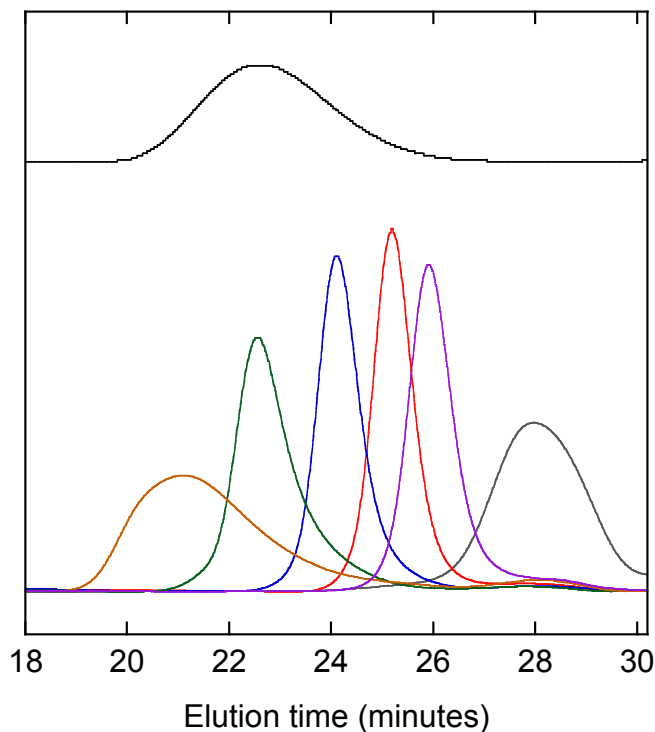
Figure 4.2. SEC traces of the aPP samples listed in Table 4.1. Curves correspond to aPP-NB (gray), poly(aPP-NB)_11 (purple), poly(aPP-NB)_26 (red), poly(aPP-NB)_74 (blue), poly(aPP-NB)_215 (green), poly(aPP-NB)_732 (orange), and aPP_Linear (black, vertically shifted), and are normalized to a constant integrated area under the curve.

Thermal analysis of the polymers was conducted using differential scanning calorimetry (DSC). Thermograms of each polymer sample are presented in Figure 4.3. The T_g value of all poly(aPP-NB)s remains approximately constant, regardless of the backbone molecular weight, and is within 3 °C of the T_g measured for aPP_Linear. This demonstrates how the T_g of bottlebrush polymers is predominantly dictated by the side chains and is minimally dependent on backbone chemistry and length.[15,103] The results are also consistent with the findings of López-Barrón *et al.*, which show that the T_g of aPP bottlebrushes trend towards that of linear aPP in the limit of high side chain length.[146] Due to its low overall molar mass, the aPP-NB macromonomer sample displayed a more depressed T_g value of −25.7 °C, which is in agreement with literature values of low molar mass linear aPP.[147]
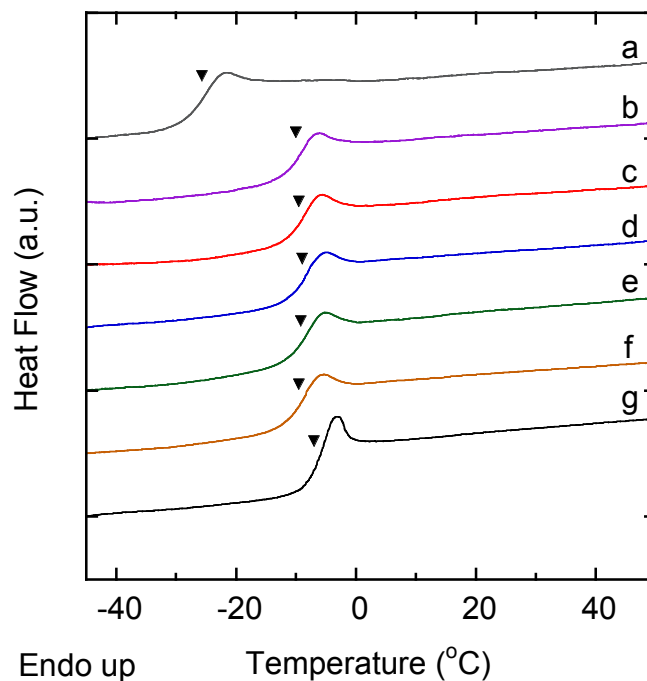
Figure 4.3. DSC heating curves of aPP-NB, poly(aPP-NB)_11, poly(aPP-NB)_26, poly(aPP-NB)_74, poly(aPP-NB)_215, poly(aPP-NB)_732, and aPP_Linear labeled (a)–(g), respectively. Markers indicate T_g midpoint values. Curves are second heating scans at 5 °C/min.

4.3   Linear Rheology of aPP Bottlebrushes

The linear rheological behavior for each of the samples listed in Table 4.1 was analyzed *via* SAOS measurements using an ARES strain-controlled rheometer. Parallel plates of 8 mm diameter and a ~1 mm gap were chosen for the majority of measurements presented in this chapter. This geometry enabled accurate data acquisition over a wide range of temperatures, whereas 25 mm plates were more susceptible to overloading the instrument torque limits at temperatures near T_g. Since the polymers studied were liquid-like at room temperature, the samples were loaded directly into the parallel plates without compression molding or any other pre-processing techniques. Further experimental details are provided in section 4.6.

4.3.1   Linear Viscoelastic Regime

All samples were first subjected to dynamic strain sweep analysis to determine the linear viscoelastic (LVE) regime. The LVE regime represents the range of strain amplitudes in which the dynamic stress response remains independent of imposed strain. At higher strain amplitudes, non-linear effects contribute to the dynamic response, and the measured material functions (*e.g.,* G' and G") no longer provide a complete description of the viscoelastic behavior. Therefore, strain sweep testing for each sample was essential to ensure that all subsequent SAOS measurements were carried out at strains within the LVE regime.

Figure 4.4 depicts the strain sweep data for poly(aPP-NB)_74. The moduli maintain constant values up to ~30 % strain, where it begins to decline with additional strain increase. Generally, the LVE regime boundary is defined as the point where G* deviates by more than 10% of the low-strain plateau value. To assure that measurements remained within the LVE regime, the maximum strain allowed for frequency sweep tests on this sample was set to 30 %. Figure 4.4 is representative of all the aPP samples tested, which displayed essentially identical strain sweep results. Furthermore, the extent of the LVE regime had little temperature dependence in the aPP samples. Additional strain sweeps were occasionally conducted when taking measurements at temperatures far higher than 25 °C, but no substantial change was observed. At temperatures much lower than 25 °C, the moduli became large enough that only very small strain amplitudes (well below the LVE regime cutoff) were required to achieve a sufficient stress signal for reliable data.
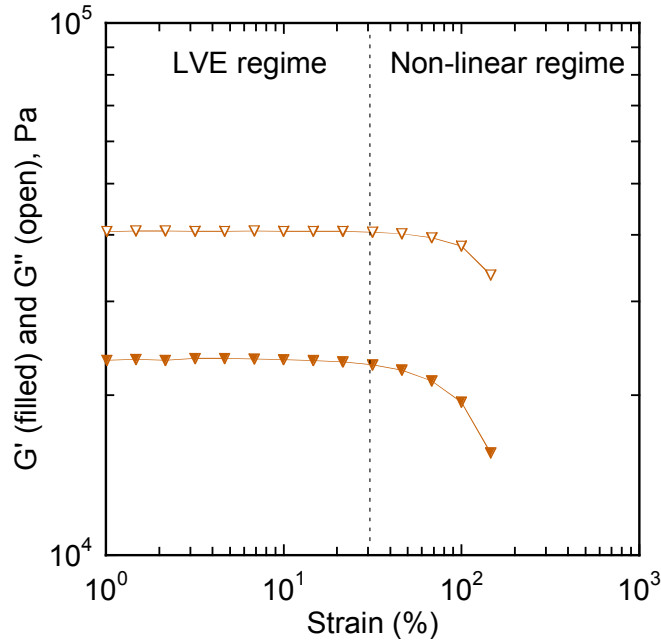
Figure 4.4. Strain sweep data for poly(aPP-NB)_74 at 25 °C and ω = 1 rad/s. Based on these data, all subsequent frequency sweep measurement were taken at strain ≤ 30 %.

4.3.2   Frequency Sweeps and Time-Temperature Superposition

After establishing the range of strain amplitudes delimiting the LVE regime, frequency sweeps were conducted to establish the dynamic relaxation profiles for each aPP sample. Measurements were repeated at several temperatures to capture information across the complete relaxation spectrum, which extends beyond the experimentally accessible frequency range. As an example, the frequency sweep measurements for poly(aPP-NB)_74 are displayed in Figure 4.5. Data collection started at 100 rad/s in each experiment, and the oscillation frequency was stepped down after each measurement to a minimum of 0.1 rad/s. The slow relaxation dynamics of glassy relaxation modes were probed by cooling the sample below room temperature. The data set at –4 °C demonstrates glassy behavior at high frequencies where G' approaches a plateau at high modulus (> 10^8 Pa). Conversely, terminal flow behavior, designated by scalings of G' ~ ω^2 and G" ~ ω, was only observed at higher experimental temperatures, *e.g.*, 25 °C and 40 °C.
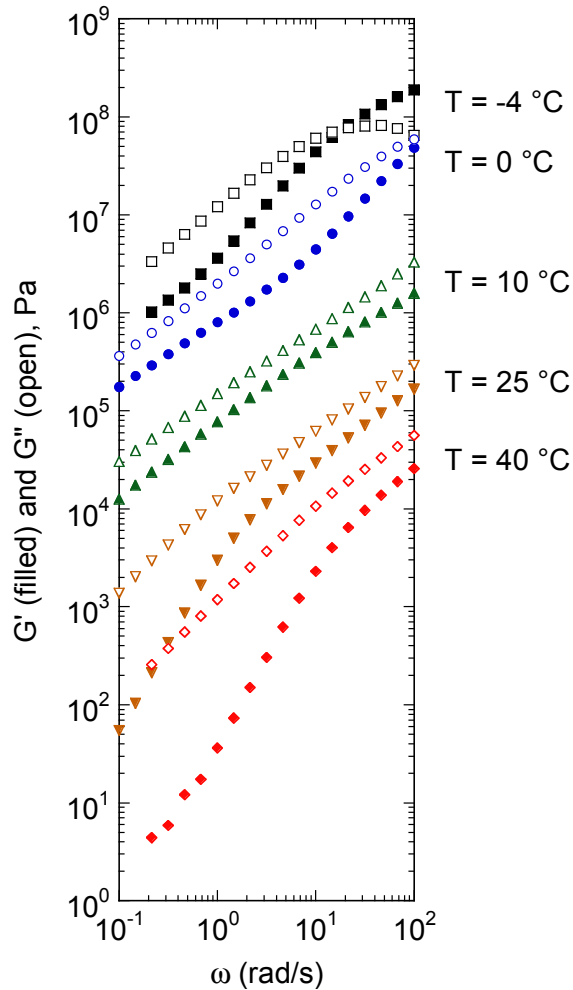
Figure 4.5. Frequency sweep data for poly(aPP-NB)_74 taken at different temperatures. No shifting was done for any data set along either axis.

Time-temperature superposition (TTS) of the data was employed to assemble a composite master curve for poly(aPP-NB)_74. The TTS principle was introduced in chapter 2 and permits data collected at different temperatures to be superimposed by shifting G'(ω) and G"(ω) along the logarithmic frequency axis. This process is strictly valid only for thermorheologically simple materials, *i.e.*, samples in which all intrinsic relaxation modes exhibit equivalent temperature dependence. Thus, application of TTS is generally suitable for homopolymer melts. The five data sets shown in Figure 4.5 were individually shifted along the abscissa by multiplying ω values by a scalar shift factor

(a_T). The reference temperature was chosen as T_{ref} = 25 °C, so the data set collected at 25 °C was not shifted (a_T = 1). The data at 40 °C were shifted left to lower frequencies (a_T < 1) and the three data sets taken at lower temperatures were shifted right to higher frequencies (a_T > 1). The resulting master curve is shown in Figure 4.6.
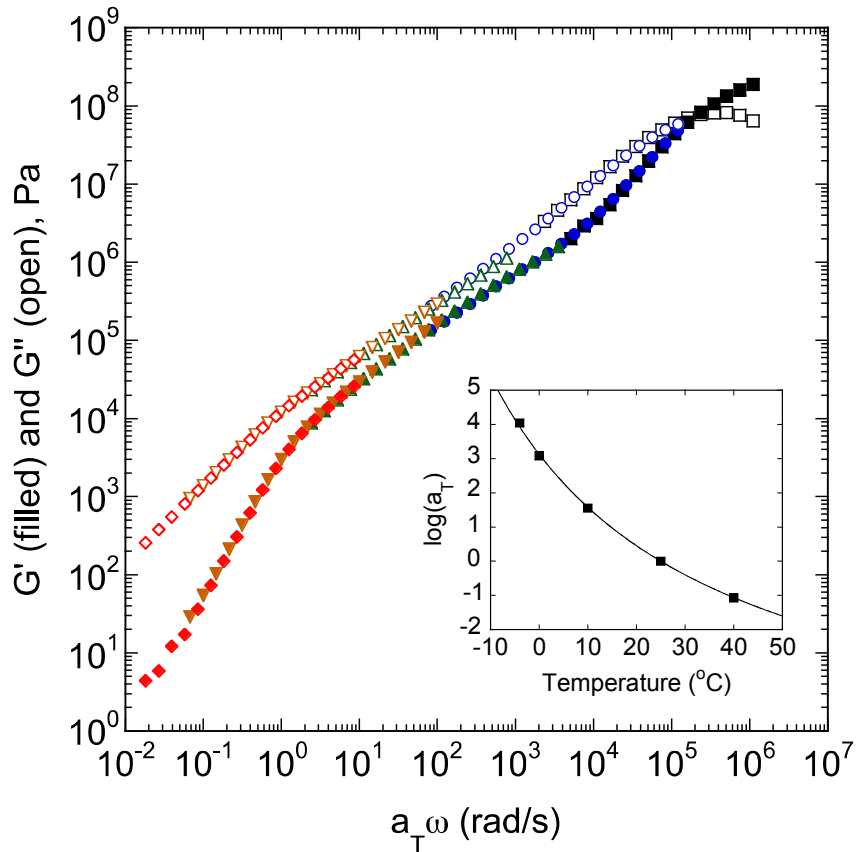
Figure 4.6. Shifted frequency sweep data for poly(aPP-NB)_74 at a reference temperature of T_{ref} = 25 °C. The distinct markers correspond to data sets taken at different temperatures, as defined in Figure 4.5. Shift factors applied to each data set are provided in the inset along with the WLF fit to the data (solid line).

The shifted data overlap very closely in Figure 4.6, yielding a continuous master curve that spans the entire relaxation profile from glassy relaxation to terminal flow. The data are plotted against reduced frequency ($a_T\omega$), and the shift factors used for each temperature are plotted in the inset of Figure 4.6. The shift factors were also fit by the Williams-Landel-Ferry (WLF) relationship,[148] shown as the solid line in the inset.

The relaxation process shown in Figure 4.6 encompasses over six decades in reduced frequency, from glassy behavior at $a_T\omega = 10^6$ rad/s to the onset of terminal flow at $a_T\omega$ = 1 rad/s. It is noteworthy that the G' data at the lowest frequencies deviate from the terminal flow scaling of G' ~ ω^2. This arises because of the low sample modulus (G*) and the predominantly viscous response (G' << G"), which generate a very weak stress response that is below the sensitivity limit of the rheometer. Therefore, the G' data in this region are not reliable and are typically disregarded. Given the successful application of TTS for poly(aPP-NB)_74, the same procedure was followed to produce complete master curves of the other aPP samples. This enabled comprehensive analysis of the bottlebrush relaxation behavior, the effects of backbone chain length, and comparison of bottlebrush rheology with the aPP_Linear melt.

4.3.3   Viscoelastic Behavior of aPP Bottlebrushes

The dynamic responses for all of the aPP samples listed in Table 4.1 were measured at various temperatures over a frequency range of 0.01–100 rad/s, just as was shown with poly(aPP-NB)_74 in the preceding section. In all cases master curves were assembled by horizontal shifting of the moduli data to a reference temperature $T_{\text{ref}} = T_{\text{g}} + 34$ °C. This T_{ref} accounts for any disparities in T_{g} among samples and represents room temperature dynamics of the poly(aPP-NB)s. Specifically, the frequency sweep data taken at 25 °C for poly(aPP-NB)_74 ($T_{\text{g}} = -9$ °C) served as the reference data for all of the TTS shifting. Master curves of aPP-NB and all five poly(aPP-NB) samples are shown in Figure 4.7, and the master curve of aPP_Linear is given in Figure 4.8. A composite plot of the applied TTS shift factors (a_T) is also presented in Figure 4.9. Shift factors from all aPP samples (including aPP_Linear) were fit with a single set of WLF parameters, $C_1 = 7.6$

and C_2 = 85 °C, indicating that the aPP materials exhibit dynamic responses with equivalent temperature dependence, irrespective of the branching structure.
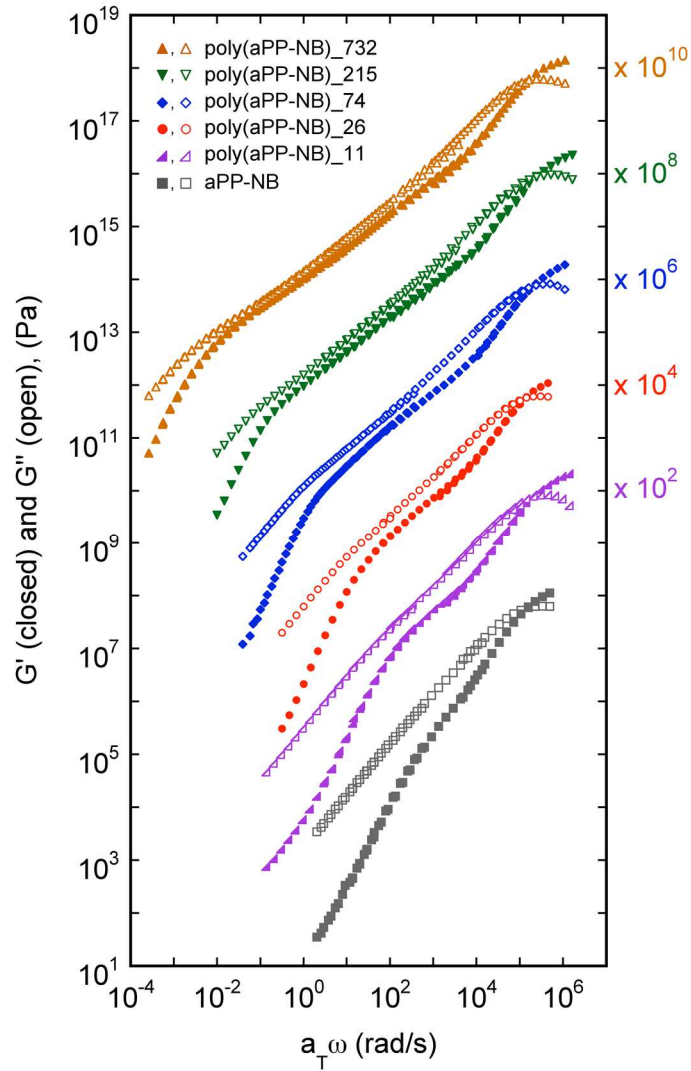
Figure 4.7. Dynamic master curves of G' (closed symbols) and G" (open symbols) for aPP-NB and poly(aPP-NB)s at a reference temperature of T_{ref} = T_g + 34 °C. Curves vertically shifted using the indicated scale factors.
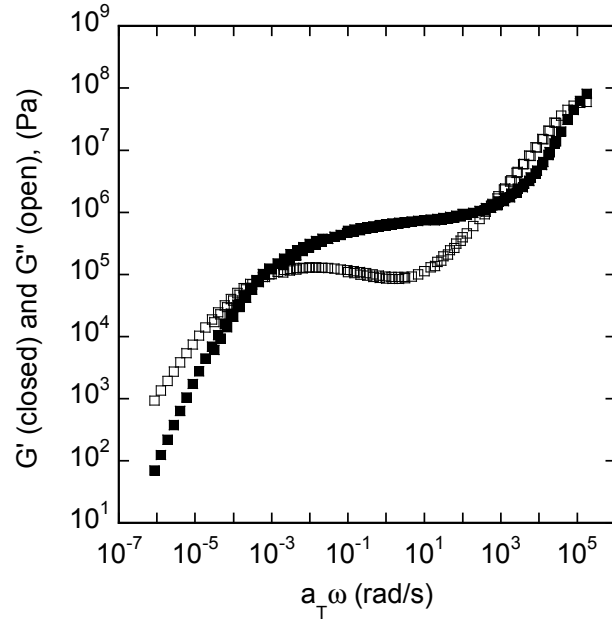
Figure 4.8. Master curve for aPP_Linear at a reference temperature of $T_{ref} = T_g + 34$ °C.
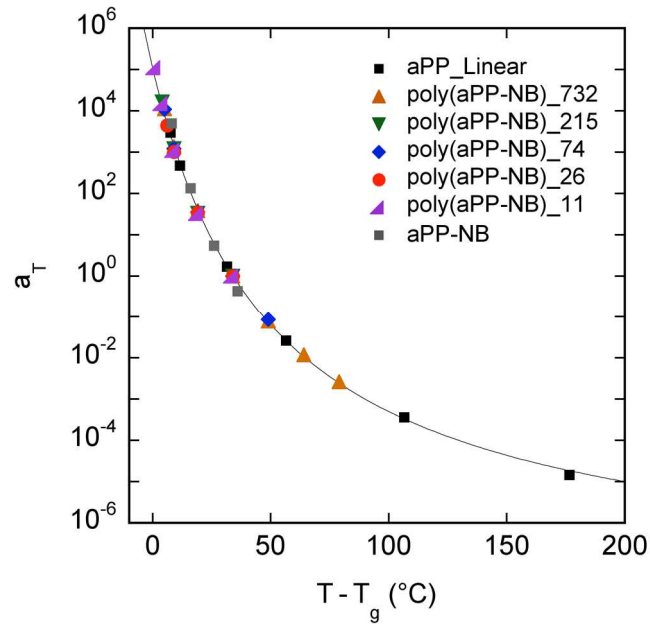
Figure 4.9. Time-temperature superposition shift factors (markers) and the WLF fit of the data (black line) at a reference of $T_{ref} = T_g + 34$ °C.

Each master curve shown in Figure 4.7 demonstrates a predominantly viscous response to the imposed deformation, as G" remains greater than G' at nearly all frequencies. The aPP-NB macromonomer sample exhibits liquid-like behavior and shows a smooth transition from glassy to terminal relaxation. This is due to its low molar mass, which is below the entanglement threshold for aPP (M_e = 3500 – 4500 g/mol).[149-151] The poly(aPP-NB) samples display a more pronounced Rouse-like relaxation at intermediate frequencies, where the breadth of this intermediate region widens as the backbone DP is increased. This expansion is consistent with the behavior of linear polymers in that increasing the polymer size causes an increase in the longest relaxation time and a delayed crossover to terminal behavior. However, unlike high molar mass linear polymers, no rubbery plateau is evident in any of the poly(aPP-NB) master curves, which suggests that the poly(aPP-NB)s remain unentangled even at molar masses greater than 10^6 g/mol. This is a fascinating consequence of the steric crowding among closely spaced side chains, which hinders the flexibility of the backbone chain and creates persistent brush molecules with large cross-sectional areas. The backbone chain length required for entanglement in the bottlebrush melts is therefore much longer than the chain length of linear polymers, and the entanglement molar mass is heightened by orders of magnitude. A very rough estimate of the expected value of M_e for this series can be calculated according to the approach by Fetters *et al.* using the average molar mass per backbone bond.[152] This calculation yields M_e = 1.5 × 10^7 g/mol, which is tenfold greater than the largest poly(aPP-NB) sample in this study.

A direct comparison between the bottlebrush polymers and aPP_Linear is more easily visualized with an overlay of the G' master curves as presented in Figure 4.10. All of the aPP samples exhibit indistinguishable behavior in the glassy-to-rubbery transition zone. This regime is associated with localized relaxations on the length scale of monomeric segments. Since aPP side chains constitute more than 95 wt. % of poly(aPP-NB)s, it is reasonable that uniform segmental relaxation emerges. A clear deviation between aPP_Linear and poly(aPP-NB)s begins to develop at a reduced frequency of 10^4 rad/s. The aPP_Linear displays a prominent rubbery plateau characteristic of a well-entangled

polymer melt, which persists for several decades in reduced frequency before ultimately entering terminal flow. Moreover, note that the molar mass of aPP_Linear is nearest to poly(aPP-NB)_74 in the bottlebrush series and is an order of magnitude less than poly(aPP-NB)_732. The fact that aPP_Linear displays the longest terminal relaxation time despite its moderate size illustrates a very weak dependence of terminal relaxation time on overall molar mass for the aPP bottlebrushes. Since neither the side chains nor the backbones of poly(aPP-NB)s form entanglement networks, the rheological dynamics of these molecules in the melt remain much faster than the linear aPP analogue.
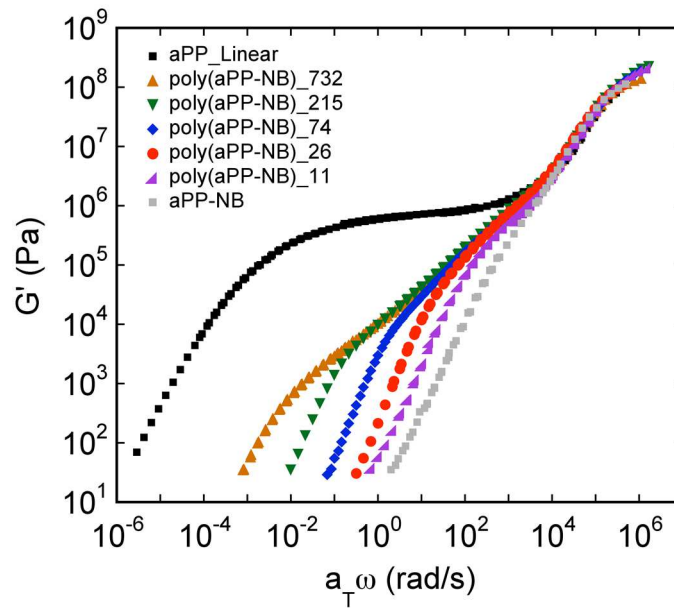
Figure 4.10. Storage modulus master curves of aPP-NB, poly(aPP-NB)s, and aPP_Linear at a reference temperature of $T_{ref} = T_g + 34\ °C$.

4.3.4   Sequential Relaxation

Figure 4.11 presents the dynamic response data for the poly(aPP-NB) samples plotted as the phase angle (δ) versus the complex modulus (G*). Van Gurp and Palmen initially proposed this type of representation as a tool to verify the applicability of TTS for specific polymer materials.[153,154] More recent studies have demonstrated the utility of the "van Gurp-Palmen" plot in elucidating structural information such as molar mass, dispersity, and branching content, as well as detecting the presence of multiple relaxation processes.[155,156] Specifically, a polymer melt with two distinct relaxation modes will generate a bimodal curve with two separate minima as occurs in many branched polymer systems, leading to a sequential relaxation mechanism.[7,17,19,135,139,142,157,158] Since the individual relaxations of the side chains and of the backbones both contribute to the dynamic response profiles of bottlebrush polymers, the van Gurp-Palmen plot serves as a useful tool for analyzing the melt rheology.
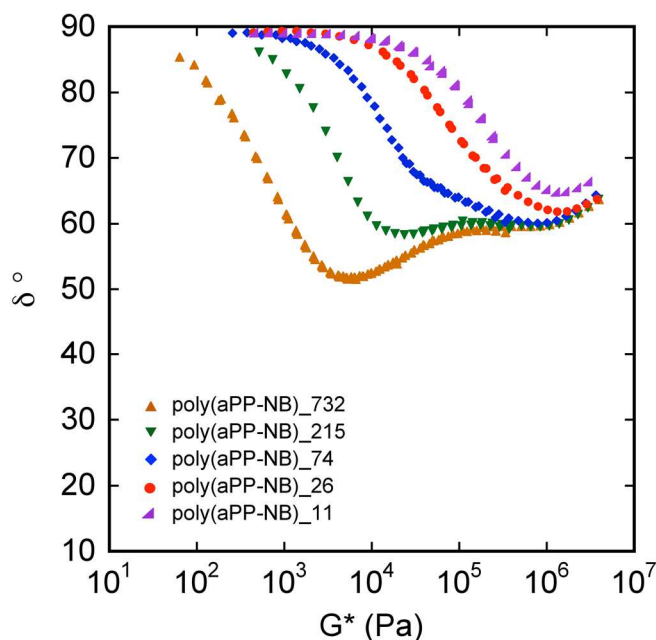
Figure 4.11. Van Gurp-Palmen plot of poly(aPP-NB)s. Data are composite from all measurements taken at temperatures above 0 °C. Low temperature data is presented in Figure 4.12.

The van Gurp-Palmen curves in Figure 4.11 exhibit a minimum in the phase angle near $G^* \sim 10^6$ Pa, which corresponds to the relaxation of aPP side chains. The location of this minimum is fixed since the side chain length is constant for all poly(aPP-NB)s. The second minimum at lower modulus pertains to the relaxation process of the entire bottlebrush molecule. This mode is distinct between the five poly(aPP-NB)s and becomes more pronounced with increasing backbone length. In fact, the second minimum is not distinguishable for poly(aPP-NB)_11 and poly(aPP-NB)_26 due to the short backbones. The longest relaxation time of the side chains dominates the dynamics of these samples, and only one distinct minimum is observed.

4.3.5   Thermorheological Complexity

As mentioned above, the van Gurp-Palmen plot was originally recommended to validate the application of TTS. Since the frequency axis is eliminated in this type of plot, no time-dependent behavior is reflected and effects of shifted relaxation times are nullified. Therefore, if the material is thermorheologically simple then data taken at all temperatures will converge onto a continuous curve without application of arbitrary shift factors. For clarity in demonstrating the double relaxation phenomenon, the data plotted in Figure 4.11 excluded any measurements taken at or below 0 °C. Figure 4.12 displays the complete van Gurp-Palmen plots for aPP-NB and the poly(aPP-NB) samples. Clearly, the inclusion of low temperature data reveals discontinuities between measurements taken at different temperatures, indicating thermorheologically complex behavior as the T_g is approached. Thus, TTS is not strictly applicable to the low temperature data despite the ostensibly seamless master curves in Figure 4.6.
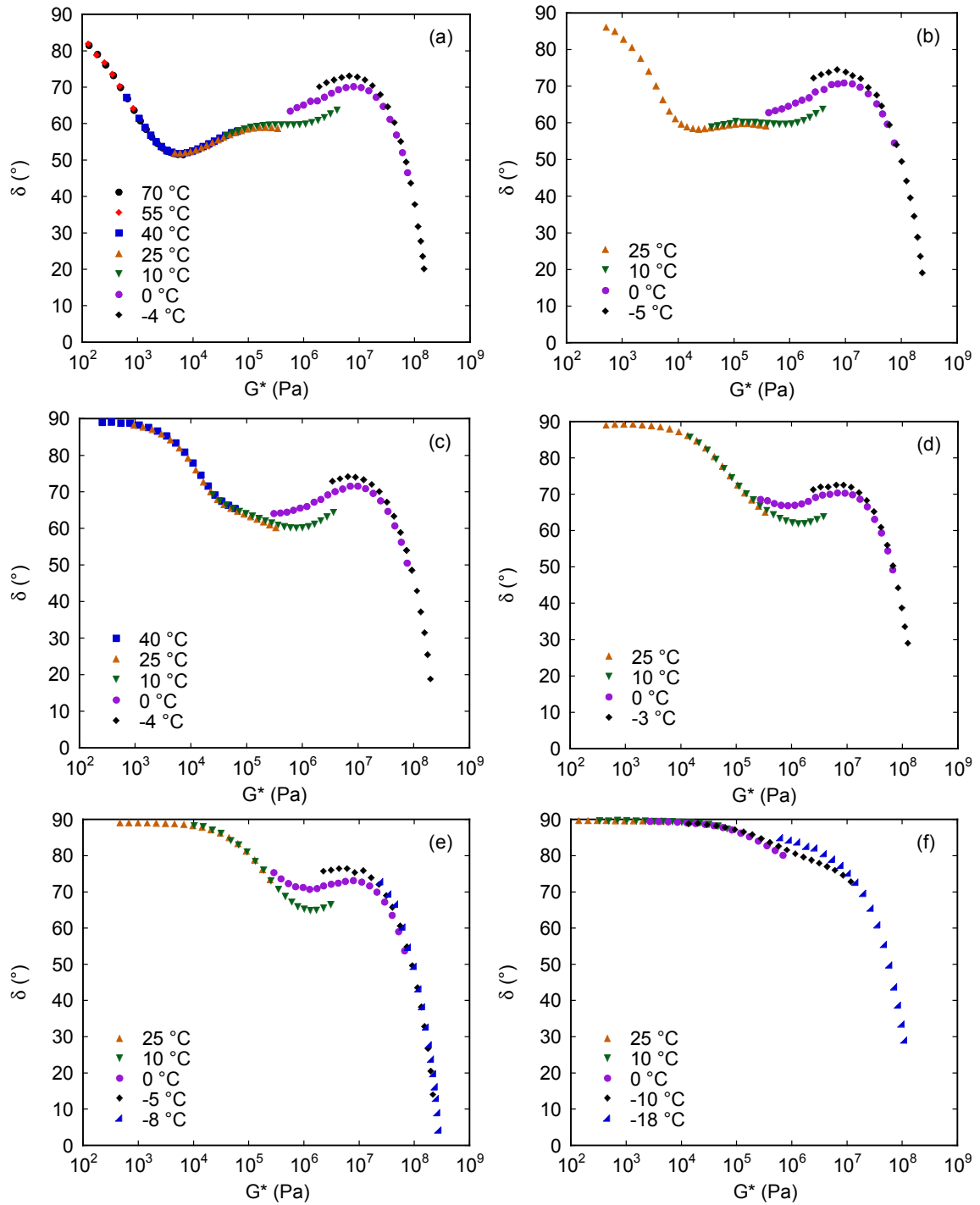
Figure 4.12. Van Gurp-Palmen plots of the dynamic response measurements for poly(aPP-NB)_732, poly(aPP-NB)_215, poly(aPP-NB)_74, poly(aPP-NB)_26, poly(aPP-NB)_11, and aPP-NB at indicated temperatures and labeled (a)–(f), respectively.

While the data in Figure 4.12 indicate thermorheological complexities, it was possible that the lower temperature data were less reliable given that measurements of high modulus materials are known to be more affected by rheometer compliance limits.[159,160] To negate any effects of instrument compliance as the T_g was approached, we repeated measurements for two of the poly(aPP-NB) samples using an adjusted sample geometry. Hutcheson and McKenna have recommended using a large sample gap to reduce torsional stiffness and a minimal plate radius to prevent compliance effects.[43,159] Therefore, we employed 3 mm parallel plates (provided by Dr. Carlos López-Barrón of the ExxonMobil Chemical Company) and loaded the samples to an increased sample gap of 1.5 – 2.0 mm. Figure 4.13 presents the dynamic response data for poly(aPP-NB)_732 and poly(aPP-NB)_26 acquired with both the 8 mm and 3 mm diameter plates.
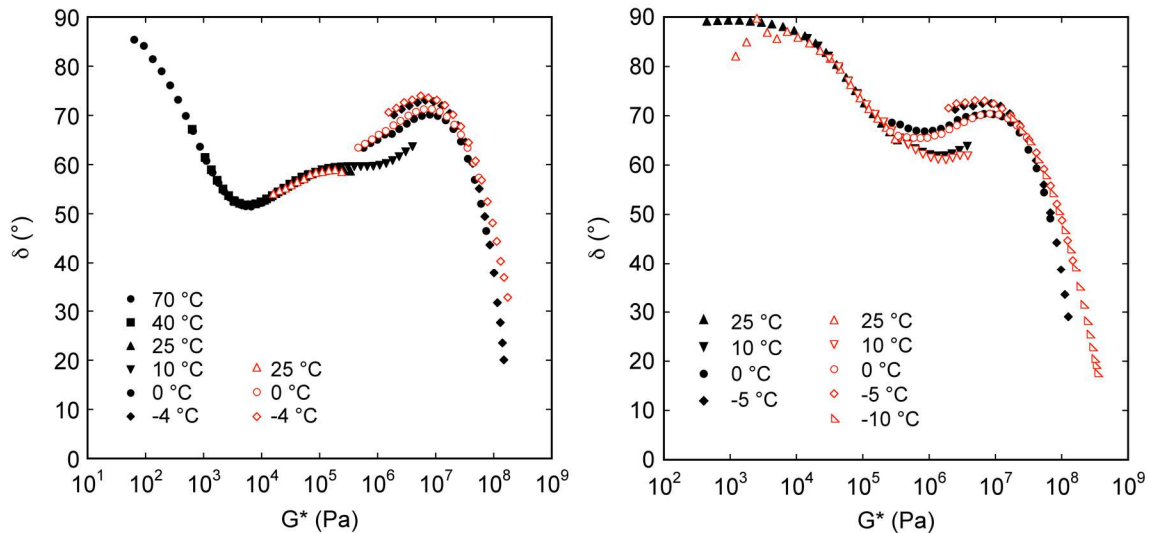
Figure 4.13. Van Gurp-Palmen plot of the dynamic response measurements for poly(aPP-NB)_732 (left) and poly(aPP-NB)_26 (right) obtained using 8 mm parallel plates (closed black symbols) and 3 mm parallel plates (open red symbols).

The data collected using both sets of parallel plates overlap closely with one another, as shown in the van Gurp-Palmen plots of Figure 4.13. Significantly, the plots reveal that discontinuities between data sets arise at the same temperatures using either the 3 mm or

8 mm plates. This reinforces our interpretation of the apparent thermorheological complexity as an inherent material property and not an artifact of the measurement. Note that the data obtained with the 3 mm plates exhibits more noise at low modulus than the 8 mm plates, which is due to the much lower stress signal obtained with the smaller diameter plates.

Thermorheological complexity near the glass transition has been reported in many linear polymer materials, including poly(styrene),[161] poly(isobutylene),[153] and aPP.[151] Plazek first investigated the linear viscoelasticity of aPP using creep deformation experiments. This material appeared to be thermorheologically simple based on the ability to construct a continuous master curve spanning thirteen decades in reduced time. However, the authors described the initial apparent thermorheological simplicity as fallacious. It was hypothesized that drawn-out creep measurements at temperatures "in the neighborhood of 0 °C" would display poor reducibility when applying TTS.[151] This conclusion is consistent with the data shown in Figure 4.12 for the poly(aPP-NB)s. Near 0 °C the value of δ begins to increase at fixed G* as the temperature is decreased closer to T_g. Though a concrete theoretical explanation of this complex behavior remains elusive (and an ongoing topic of debate),[162] it is remarkable that the same observations are found in linear and bottlebrush aPP materials. Along with the value of T_g and the high-frequency dynamic behavior, the thermorheological nature of bottlebrush polymers is governed by the chemistry of monomeric repeat units and independent of the macromolecular architecture.

4.4   Zero-Shear Viscosity Scaling

In this section we focus on the intriguing relationship between zero-shear viscosity and molar mass of the aPP bottlebrush polymers. The zero-shear viscosity (η_0) of linear polymer melts follows a power-law dependence on molar mass described by $\eta_0 \sim M_w{}^{\alpha}$. For low molar mass polymers, the viscosity obeys the Rouse model prediction, $\alpha = 1$. However, a sharp increase in the power law exponent occurs above a critical molar mass (M_c) due to the onset of entanglements. An empirical value of $\alpha = 3.4$ describes the

scaling of well-entangled melts above M_c.[43] The relationship has been studied thoroughly for several types of long-chain branched polymers as well, and a firm theoretical framework has been established. For example, star polymer melts with a given arm functionality (# of arms per molecule) exhibit even stronger dependence on molar mass than entangled linear polymers. This is because translational diffusion of the star polymer core within a reptation tube can only take place once the arms have completely retracted down to the tube radius, and the time scale of arm retraction scales exponentially with arm length.[44,163-166]

   Given the fascinating relaxation spectra of the aPP bottlebrush polymers, which were devoid of rubbery entanglement plateau regions, we hypothesized that the bottlebrush series could maintain the Rouse model prediction of $\eta_0 \sim M_w$, without scaling transitions. To test this hypothesis, zero-shear viscosities of each polymer were determined as the limiting complex viscosity (η^*) values in the terminal flow regions:

$$\eta_0 = |\eta^*(\omega)|_{\omega \to 0} \tag{4.1}$$

Figure 4.14 and Figure 4.15 depict the dynamic relaxation data as reduced complex viscosity versus reduced frequency for the poly(aPP-NB)s and for aPP_Linear, respectively. Each of the curves achieves a clear plateau value for η^* at low frequency, which was taken as η_0. The curves in Figure 4.14 also overlay closely with one another at high frequencies, which illustrates the comparable glassy relaxation dynamics among samples and validates the chosen T_{ref} as an appropriate reference. The aPP_Linear data was presented separately, because the high viscosity and long relaxation times warranted different axis ranges.
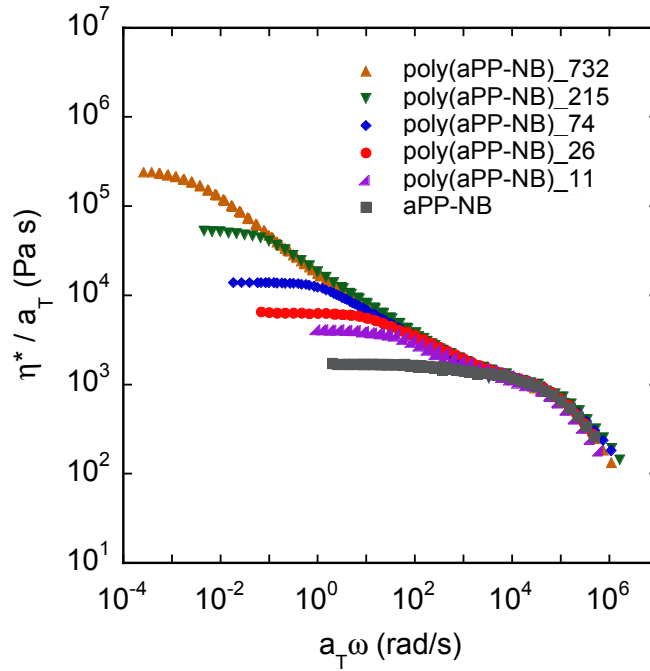
Figure 4.14. Reduced complex viscosity versus reduced frequency master curves for aPP-NB and poly(aPP-NB)s at $T_{ref} = T_g + 34\ °C$.
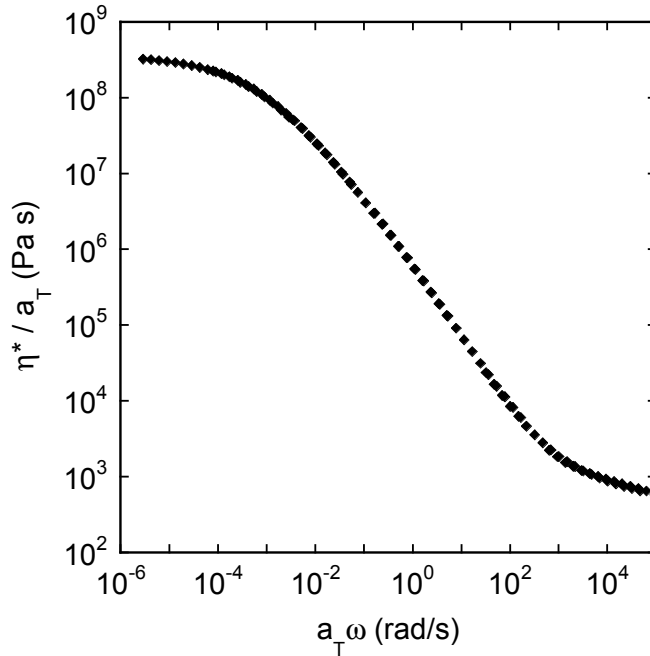
Figure 4.15. Reduced complex viscosity versus reduced frequency master curve for aPP_Linear at $T_{ref} = T_g + 34\ °C$.

Figure 4.16 presents the zero-shear viscosities of each aPP sample plotted as a function of weight average molar mass on double logarithmic axes. For comparison, the traditional scaling relationship of linear aPP was also plotted using a critical molecular weight for entanglements of M_c = 8.5 kg/mol. This critical molecular weight was estimated using the empirical relationship,[150]

$$M_c = 3.42\, M_e\, p^{-0.534} \tag{4.2}$$

where M_e is the entanglement molar mass and p is the packing length. Literature values of M_e = 4390 g/mol and p = 2.88 Å for aPP yield M_c = 8534 g/mol.[150]

The two data points in Figure 4.16 at lowest molar mass represent the aPP-NB macromonomer (gray symbol) and the hypothetical "dimer" with a backbone DP = 2 (open symbol). Since the dimer also represents a linear aPP molecule, it is expected to maintain Rouse dynamics and is plotted along the traditional aPP scaling line. The aPP_Linear sample exhibits a much higher zero-shear viscosity, which is accordant with the predicted theoretical value. In contrast, the bottlebrush samples show a significant departure from the linear aPP relationship, and two distinct scaling regimes emerge as the backbone is extended with additional side chains beyond the dimer. The low molar mass region, in the range of backbone DP = 2 – 74, represents a transition zone in which the dependence of viscosity on molar mass is extraordinarily low (α < 0.5). In the high molar mass region, DP ≥ 74, the scaling is marginally greater than the linear relationship predicted by the Rouse model (α = 1.2), reinforcing the unentangled nature of the aPP bottlebrushes.
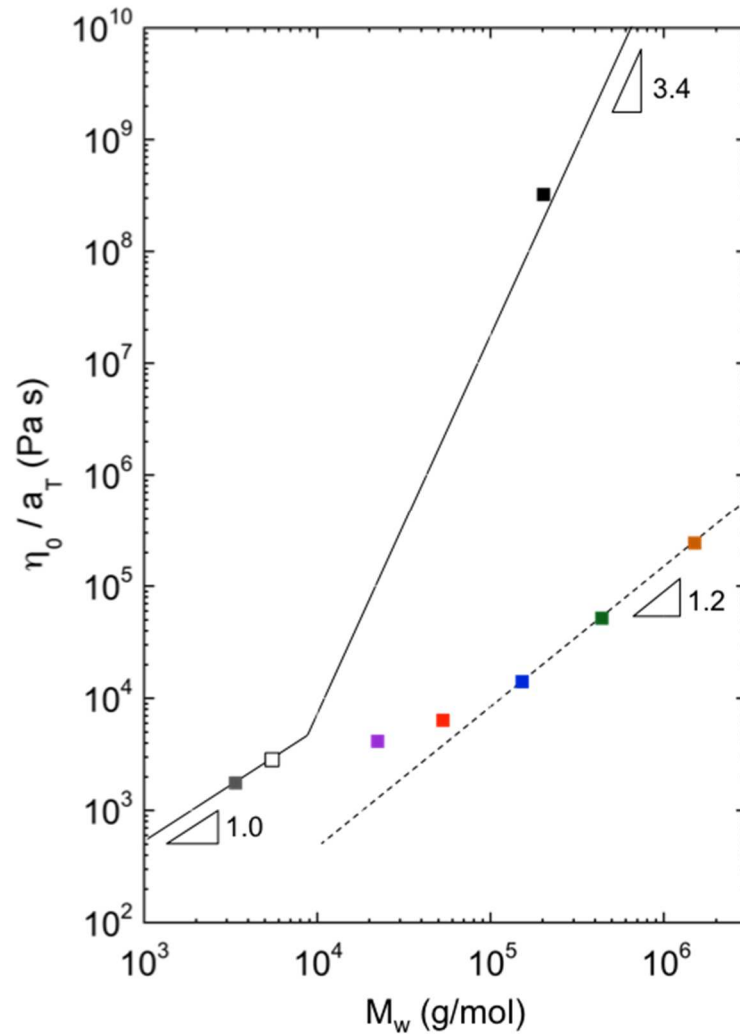
Figure 4.16. Reduced zero-shear viscosity versus weight average molecular weight at T_{ref} = T_g + 34 °C. The solid line indicates the traditional scaling of linear aPP with a critical molecular weight of M_c = 8.5 kg/mol. Data points along this line represent the aPP-NB macromonomer (gray), the aPP_Linear sample (black), and a hypothetical dimer with backbone DP = 2 (open symbol). The remaining solid markers represent poly(aPP-NB) bottlebrush samples listed in Table 4.1, and fall far below the traditional scaling line. A power-law fit to the highest molar mass data points yields a scaling exponent of α = 1.2 (dashed line).

Perhaps the most striking feature of Figure 4.16 is the weak dependence of viscosity on molar mass in the scaling transition zone, particularly considering Rouse scaling of α = 1 signifies the lower limit in traditional polymer melts. This result is fundamentally related to the conformational properties of molecules in this system. Recent investigations have found that a conformational transition occurs in bottlebrush polymers with increasing backbone DP. Bottlebrushes with sufficiently short backbones maintain a spherical or globular conformation under good solvent conditions. As the backbone length begins to exceed the length of the brush diameter (D), the molecule transitions to a cylindrical shape that extends one-dimensionally with increased backbone DP. This behavior has been shown in molecular simulations[167] and experimentally by small-angle neutron scattering measurements of bottlebrush polymers in good solvent.[168] The same type of conformational transition is assumed to occur in the melt state as the backbone length is increased. The graphics in Figure 4.17 represent the bottlebrush polymers prepared in this study. The length-to-diameter aspect ratios (L/D) of the bottlebrushes are also given for the four highest molar mass samples, assuming fully extended chain conformations. An aspect ratio of L/D = 1 is calculated to occur at a backbone DP $\approx$ 38 for this system (see section 4.6.3). Thus, the transition from a globular to cylindrical molecular conformation likely occurs between the poly(aPP-NB)_26 and poly(aPP-NB)_74 samples. This is consistent with the observed changeover between scaling regimes in Figure 4.16, *i.e.*, where the transition zone ends.

However, the shift in conformation does not directly explain the corresponding viscosity scaling in the two regimes. For instance, linear polymer chains assume a spherical, Gaussian coil conformation in the melt at all molar masses and maintain Rouse-like behavior (α = 1) prior to the onset of entanglements. So why is Rouse scaling realized for the large cylindrical bottlebrushes but not for the smaller, more spherical poly(aPP-NB) samples? We posit that this unusual behavior is a result of the space-filling nature of these molecules.
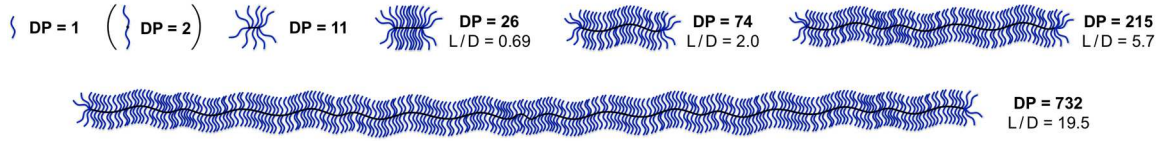
Figure 4.17. Schematic of the bottlebrush polymers, aPP-NB macromonomer, and hypothetical "dimer" with backbone DP = 2. Length to diameter aspect ratios (*L/D*) are given for the highest molar mass bottlebrushes assuming fully extended polymer chains.

As side chains are first added to the growing polymer backbone, each additional arm is forced to occupy the same local space as the previously attached arms. Thus, the continued addition of densely spaced side chains forces the resident arms to compress closer to one another. The increasingly compact molecular structure steadily restricts the number of intermolecular contacts made per repeat unit, particularly near the backbone chain, and reduces the effective friction or drag per monomer segment. Therefore, increasing the molar mass in the form of added side chains will not lend directly to the increased molecular friction, and a sub-linear ($\alpha < 1$) dependence of η_0 on M_w arises. It is not until the backbone is of approximately equal length to the brush diameter that the effective friction per monomeric segment achieves a consistent value. Further attachment of side chains simply causes one-dimensional extension of a cylindrical bottlebrush with constant radial segment density. Since the effective friction per segment is approximately constant, high molecular weight bottlebrush polymers are dynamically similar to unentangled linear polymer coils, *i.e.*, increases in the molecular weight contribute proportionally to the viscosity and result in Rouse-like scaling behavior.

4.5   Conclusions

The primary goal of this chapter was to evaluate the linear rheological behavior for a series of aPP bottlebrush polymers in the melt and to compare the results with a corresponding linear polymer material. The series included bottlebrushes with aPP side chains of $M_n = 2.05$ kg/mol, which is below the entanglement spacing of linear aPP in the

melt state. Dynamic master curves of these samples did not exhibit plateau regions at any point between glassy relaxation and terminal flow, indicating no side chain or backbone entanglement. This is a remarkable consequence of the bottlebrush architecture that may be exploited to create new types of rheological modifiers, or to modify the behavior of block polymer systems by including one or more bottlebrush blocks (as is explored in chapters 6 and 7 of this work).

Van Gurp-Palmen plots of the phase angle versus complex modulus revealed additional intrinsic characteristics of the bottlebrush polymers. First, two separate relaxation processes are distinguished, corresponding to the motion of side chains and of the entire bottlebrush molecules. Secondly, these plots highlighted the onset of thermorheological complexity as T_g was approached, which paralleled the behavior of linear aPP materials. These two observations individually represent inherent material properties that are governed by the macromolecular architecture and by the monomer scale chemistry, respectively.

Figure 4.16 displayed the zero-shear viscosity scaling behavior for the aPP bottlebrush series. Two distinct molar mass regimes emerged with disparate scaling exponents for the power-law relationship, $\eta_0 \sim M_w{}^\alpha$. Bottlebrush polymers with relatively short backbone chains exhibited unusually weak dependence of zero-shear viscosity on molar mass ($\alpha < 0.5$), which results from the decrease in net friction per segment as the side chains became more densely packed. The scaling transitioned to Rouse-like dynamics ($\alpha = 1.2$) at high molecular weight because of a sphere-to-cylinder conformational change with increasing DP of the bottlebrush backbone. These results uncover a transition that is unique to this molecular architecture, *i.e.*, bottlebrush polymers of constant side chain length.

4.6   Methods and Experimental Details

4.6.1   Rheological Characterization

All samples were examined by SAOS measurements on either 8 mm or 3 mm diameter parallel plates using a TA Instruments ARES rheometer equipped with a nitrogen convection oven. To achieve consistent temperature control at T ≤ 40 °C, nitrogen flow was supplied from a dewar of liquid N_2, rather than a room temperature compressed N_2 cylinder. All samples were first subjected to dynamic strain sweep analysis to determine the LVE regime of the materials. Frequency sweep measurements were then carried out at strains low enough to remain within the LVE region and a frequency range of 100 – 0.01 rad/s. Master curves were constructed by shifting data along the frequency axis at a reference temperature of $T_{ref} = T_g + 34$ °C. The reference temperature for aPP samples was chosen to reflect room temperature data of poly(aPP-NB)s.

The aPP samples were loaded into the parallel plates as follows. The polymer was loaded onto the bottom plate, using an excess of material needed to fill the gap between plates. Each sample was heated between 50 °C and 100 °C in the temperature-controlled nitrogen convection oven to allow the polymer to flow and cover the bottom plate. The top plate was then lowered slowly while applying a gentle oscillatory strain to (1) aid the molten polymer in completely filling the gap and (2) push out any air pockets. Once the gap was entirely filled, the sample was cooled to room temperature and excess polymer that was pushed out of the sides was carefully wiped away, leaving a clean polymer disk within the gap. A gap of 1.0 mm was used for most measurements.

4.6.2   Differential Scanning Calorimetry

Thermal analysis was performed using a TA Instruments Discovery DSC apparatus. Samples were first heated to 50 °C (10 °C/min), then slowly cooled to –50 °C at 5 °C/min, and finally heated a second time for analysis.

4.6.3   Calculation of backbone DP required for $L/D = 1$

Based on the structure of aPP-NB given in Figure 4.1, the average molecule (M_n = 2050 g/mol) would contain n = 43.5 aPP repeat units. If the radius of a bottlebrush is the distance from the end of a side chain to the norbornene ring, and the average two-carbon distance of a fully extended side chain is 0.25 nm, then the bottlebrush radius is:

$$R = 0.25nm \times (3.5 + n) = 0.25nm \times (47) = 11.75nm$$

which is again based on the aPP-NB structure in Figure 4.1. This value yields a brush diameter of D = 23.5 nm assuming branches that are fully extended normal to the backbone chain. The bottlebrush backbone is poly(norbornene), which contains five carbons per repeat unit in the main chain (or 2.5 two-carbon lengths per repeat unit). The presence of a ring in the main chain is assumed to be negligible in calculating the fully extended length. Thus, the average length per backbone repeat unit is estimated as

$$L_{r.u.} = 2.5 \times 0.25nm = 0.625nm$$

This value is corroborated by Xia *et al.*[120,142] who calculated a length of 0.62 nm per repeat unit of bottlebrush polymers with poly(norbornene) backbones based on atomic force microscopy results. To achieve a backbone length (L) equal to the brush diameter ($L/D = 1$), the backbone DP would be:

$$DP = \frac{L}{L_{r.u.}} = \frac{L}{0.625nm} = \frac{D}{0.625nm} = \frac{23.5nm}{0.625nm} = 37.6$$

Since the assumption of fully extended chains is more appropriate for the backbone than for the side chains, this value serves as the maximum DP required for L/D = 1 and is most likely an overestimate.

Chapter 5

Rheology of PEP Bottlebrushes: Branch Entanglement and Time-Dependent Relaxation Scaling

5.1 Introduction

The linear viscoelastic responses of the aPP bottlebrush polymers presented in chapter 4 were directed by contributions from two different relaxation modes, *viz.* the characteristic relaxation modes of the side chains and of the entire bottlebrush molecules. This phenomenon leads to dynamic master curves with distinctive features at well-separated time scales.[7,17-19] The first investigation to explore how systematic variation of both side chain and backbone lengths affect the rheology of bottlebrush polymers was conducted by Hu *et al.*[17] This study examined nine poly(norbornene)-*g*-poly(lactide) bottlebrush samples with backbone DP of 200, 400, and 800, and side chains of M_n / M_e = 0.2, 0.5,

---

and 1.0 (where the entanglement spacing, M_e, of linear polylactide in the melt is 8.7 kg/mol). Dynamic master curves depicted arm relaxation regimes that became more prominent with increasing side chain length. In particular, the samples with the longest side chains (M_n / M_e = 1.0) began to display plateaus in the arm regime. However, the relaxation dynamics were interpreted as predominantly Rouse-like for each of the brush samples, and an absence of entanglements was confirmed by analysis of retardation spectra. López-Barrón *et al.* more recently explored the rheology of bottlebrushes with very short side chains (composed of only 3 − 6 aPP repeat units) and studied the effects of increasing side chain length on parameters such as Kuhn length, melt viscosity, monomeric friction coefficient, and glass transition temperature (T_g).[146] Master curves of these molecules did not show independent side chain and backbone relaxation modes due to the small size of the aPP branches.

In this chapter, the effects of both side chain and backbone length on the linear rheological behavior are examined, particularly in the limit where side chains will entangle. This is a limit that has not been previously addressed in the literature. Therefore, how entanglements develop among side chains as the branch molecular weight is increased beyond M_e of the corresponding linear chains, or whether the crowded arrangement of branches along the backbone chains prevents significant entanglement remains an open question. While the series of aPP bottlebrushes in chapter 4 utilized side chains shorter than M_e of linear aPP ($M_n / M_e \approx$ 0.5), a second series of bottlebrush polymers with poly(ethylene-*alt*-propylene) (PEP) side chains above the M_e of linear PEP ($M_n / M_e \approx$ 3.5) is presented in here. The same synthesis and characterization methods utilized for the aPP series were used to prepare and analyze the PEP bottlebrush series. Specifically, polymer samples were synthesized by ROMP of norbornene-terminated macromonomers, and SAOS measurements were used to compile the full dynamic relaxation spectra for each polymer. The dynamic moduli for each of the PEP bottlebrush samples are discussed, and the salient features of the master curves are compared.

A second key objective of this chapter was to carefully analyze the dynamic moduli data and obtain quantitative scaling information to provide a more comprehensive

understanding of the Rouse-like dynamics. The complex viscosity data presented in the previous chapter for the aPP bottlebrush series highlighted the Rouse-like dependence of zero-shear viscosity on average molar mass in the high backbone DP region. However, a much weaker dependence was observed for samples with shorter backbones. Here, the scaling of complex viscosity versus oscillation frequency is scrutinized to elucidate the time-dependent relaxation behavior, and the results are compared with predictions of both the Rouse and Zimm models.

5.2   Synthesis and Characterization of PEP Bottlebrushes

A series of bottlebrush polymers with PEP side chains was developed to further explore the influence of molecular size (*i.e.*, brush length and radius) on the resulting rheological behavior. Norbornene-terminated PEP macromonomers (PEP-NB) were prepared following the reaction scheme shown in Figure 5.1, beginning with an anionically synthesized ω-hydroxyl poly(isoprene) (PI-OH) precursor polymer of M_n = 4.5 kg/mol (93% 1,4-addition).[*] Access to this well-defined batch of PI-OH precursor molecules enabled production of very low dispersity macromonomers. First, the PI-OH precursor was fully saturated by heterogeneous hydrogenation using the Pt-Re/SiO$_2$ catalyst (Dow Chemical) to generate ω-hydroxyl PEP (PEP-OH).[169] This hydrogenation step was carried out at a relatively low reaction temperature of 100 °C to ensure high retention of the hydroxyl end groups. PEP-OH was then end-functionalized with a norbornene moiety using the same procedure outlined in chapter 3. Experimental details for each of these steps, and the ^{1}H NMR spectra of PI-OH, PEP-OH, and PEP-NB, are provided in section 5.6.

Bottlebrush polymers (referred to hereafter as poly(PEP-NB)s) were synthesized *via* ROMP of PEP-NB using **G3** as shown in Figure 5.2. The only major adjustment to the procedures used for poly(aPP-NB)s was that poly(PEP-NB)s required an additional purification step to remove unreacted PEP-NB. ROMP reactions did not achieve

---

[*]This batch was prepared by Tim Gillard.

quantitative conversion, likely because of the high molar mass of PEP-NB macromonomers. The separations were carried out using fractionation procedures detailed in section 5.6. Briefly, the solvent quality of a solution of the raw poly(PEP-NB) product was slowly worsened by dropwise addition of a nonsolvent. The poly(PEP-NB) products were first to come out of solution and could be separated readily from the more soluble PEP-NB macromonomers. Molecular characterization results of PEP-NB and the purified poly(PEP-NB) samples are given in Table 5.1.
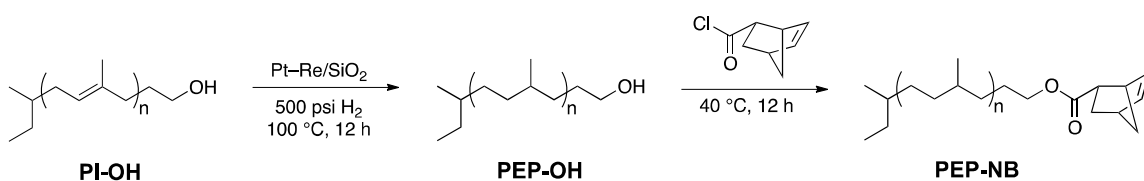
Figure 5.1. Synthesis of PEP-NB macromonomers. First, PI-OH was saturated by catalytic hydrogenation, yielding PEP-OH. The hydroxyl end group was then coupled with *exo*-5-norbornene-2-carbonyl chloride to generate PEP-NB.
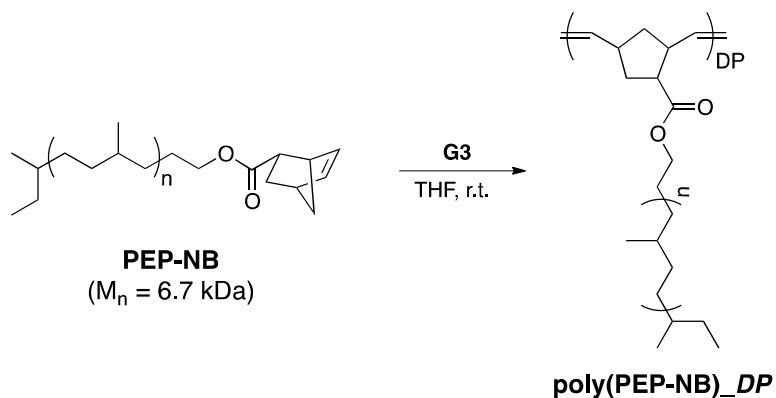
Figure 5.2. Bottlebrush polymer synthesis by ROMP of PEP-NB macromonomers using the G3 catalyst.

Table 5.1. Molecular and thermal characterization of PEP samples.

Sample [a]	M_w (kg/mol)[b]	Đ [b]	DP [d]	T_g (°C)[e]
PEP-NB	7.2[c]	1.08	-	−60
poly(PEP-NB)_13	89	1.06	13	−59
poly(PEP-NB)_125	840	1.23	125	−58
poly(PEP-NB)_627	4200	1.57	627	−58

[a]Bottlebrush samples labeled poly(PEP-NB)_DP. [b]Determined by SEC-MALLS in tetrahydrofuran. [c]M_n was determined by end-group analysis of the ^{1}H NMR spectrum. M_w determined as $M_n \times Đ$. [d]Weight-average degree of polymerization of poly(norbornene) backbone using M_{branch} = 6.7 kg/mol. [e]T_g midpoint value measured by DSC.

The SEC traces and DSC thermograms of each PEP sample are displayed in Figure 5.3 and Figure 5.4, respectively. The PEP-NB macromonomer sample shows a very narrow molar mass distribution ($Đ$ = 1.08), as does poly(PEP-NB)_13 ($Đ$ = 1.06). Similar to the aPP series, the dispersity continually increased with product molar mass, which is presumably caused by the increased effects of catalyst deactivation with lower catalyst loading. Note that poly(PEP-NB)_627 achieves a remarkably high molar mass of M_w = 4.2×10^6 g/mol, which represents the largest reported polyolefin-based bottlebrush polymer. The DSC thermograms in Figure 5.4 show nearly identical results among all four samples. This again demonstrates the independence of backbone length on the sample T_g. Unlike the aPP-NB macromonomer, however, no T_g depression is observed for higher molar mass PEP-NB (M_n = 6.7 kg/mol).
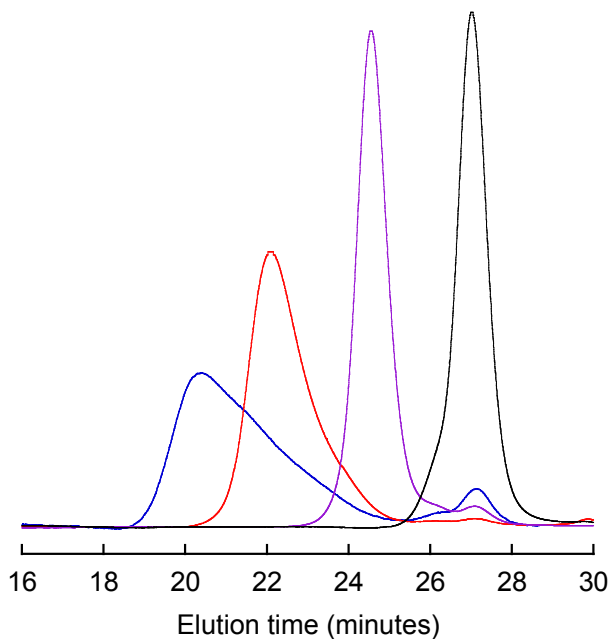
Figure 5.3. SEC traces of the PEP samples listed in Table 5.1. Curves correspond to PEP-NB (black), poly(PEP-NB)_13 (purple), poly(PEP-NB)_125 (red), and poly(PEP-NB)_627 (blue).
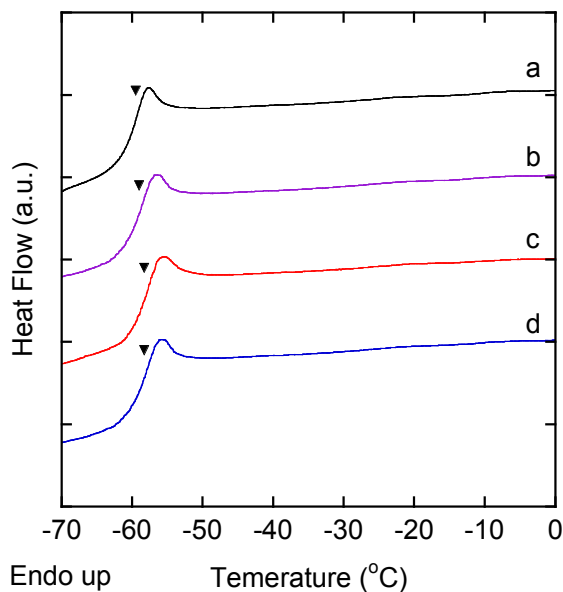
Figure 5.4. DSC heating curves of PEP-NB, poly(PEP-NB)_13, poly(PEP-NB)_125, and poly(PEP-NB)_627 labeled (a) − (d), respectively. Markers indicate T_g midpoint values. Curves are second heating scans at 10 °C/min.

5.3   Linear Rheology of PEP Bottlebrushes

The linear viscoelastic properties of the poly(PEP-NB)s were investigated using SAOS measurements to evaluate the presence/extent of side chain entanglement. PEP was chosen for this second series because it is chemically similar to aPP but has a much lower entanglement molar mass (M_e = 1,930 g/mol).[150] Thus, side chain entanglement could be promoted without requiring exceptionally long branches. The SAOS testing was carried out with 8 mm parallel plates using the same methods as were described in chapter 4. Strain sweeps were first conducted to determine the LVE regime of the PEP samples, and frequency sweep experiments were then carried out at various temperatures. The samples were once again loaded directly onto the rheometer plates with any pre-processing because of the liquid-like properties of PEP at room temperature.

5.3.1   Viscoelastic Behavior of PEP Bottlebrushes

The dynamic moduli of the poly(PEP-NB) samples were measured and master curves were constructed by TTS. Master curves for PEP-NB and each poly(PEP-NB) are plotted in Figure 5.5, and the shift factors are plotted in Figure 5.6. The TTS shift factors converge onto a single WLF fit, yielding fit parameters of C_1 = 8.4 and C_2 = 110 °C. Since there are negligible differences in T_g values between the four samples, the single WLF fit indicates equivalent temperature dependences of the dynamic moduli for each of the PEP samples. The T_{ref} for these samples was chosen to most closely match the T_{ref} of the aPP series while still using a non-shifted data set as the reference. In this case the frequency sweep data of poly(PEP-NB)_125 at −20 °C was used as the reference data set, giving a common reference temperature of $T_{ref} = T_g + 38$ °C.
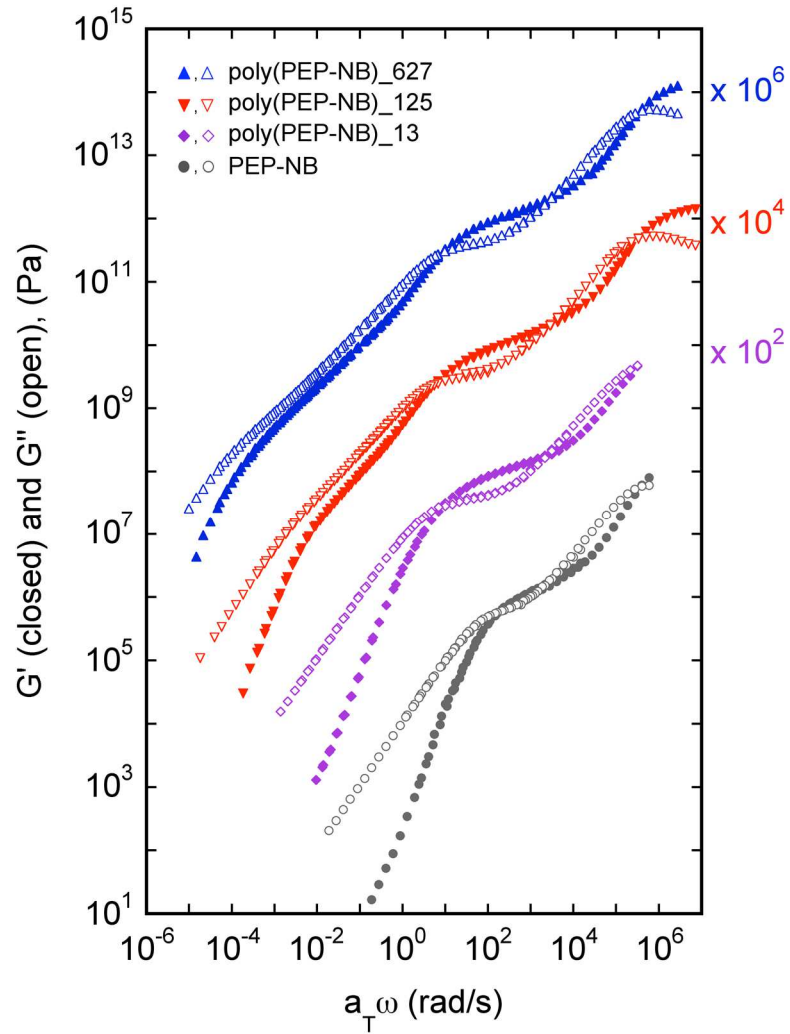
Figure 5.5. Dynamic master curves of G' (closed symbols) and G" (open symbols) for PEP samples at a reference temperature of $T_{ref} = T_g + 38\ °C$. Curves vertically shifted using the indicated scale factors.
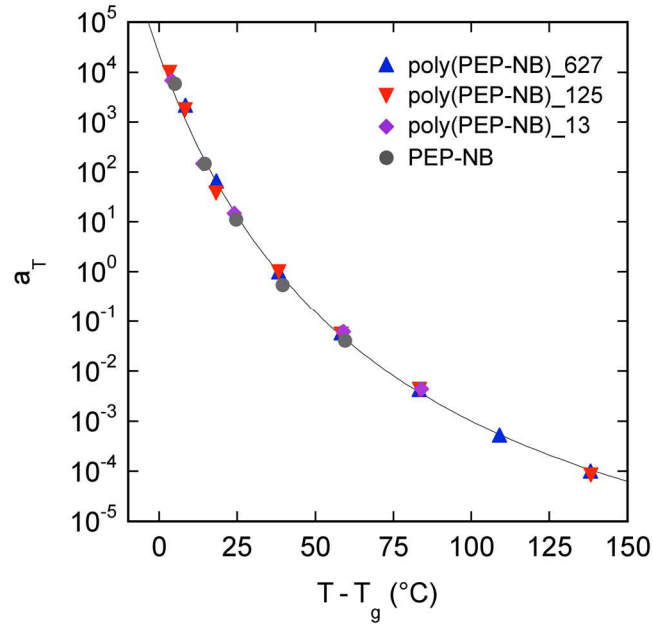
Figure 5.6. Time-temperature superposition shift factors for PEP samples (markers) and WLF fit of the data (line) at reference of $T_{ref} = T_g + 38$ °C.

The master curves in Figure 5.5 resemble those of poly(aPP-NB)s in Figure 4.7, with the addition of rubbery plateau regions from 10^1 to 10^3 rad/s, which attest to the successful formation of entanglements among the PEP branches. This results in a resolved time-scale separation between the different relaxation modes, *i.e.*, glassy, side chain, and terminal relaxation processes. Previous studies on comb polymer melts with lower grafting densities also have displayed linear rheological spectra with complete separation of branch relaxation and backbone relaxation modes;[138,140,170] however, these systems achieve significant branch and backbone entanglement due to the sparse branch spacing. Other groups have created bottlebrush polymers with greater side chain lengths; significantly, these systems did not produce branch entanglement due to the high M_e of the branches in those systems.[7,14,16,17,171] An overlay of storage modulus master curves is presented in Figure 5.7 and highlights differences in plateau regions and the locations of terminal flow regimes.
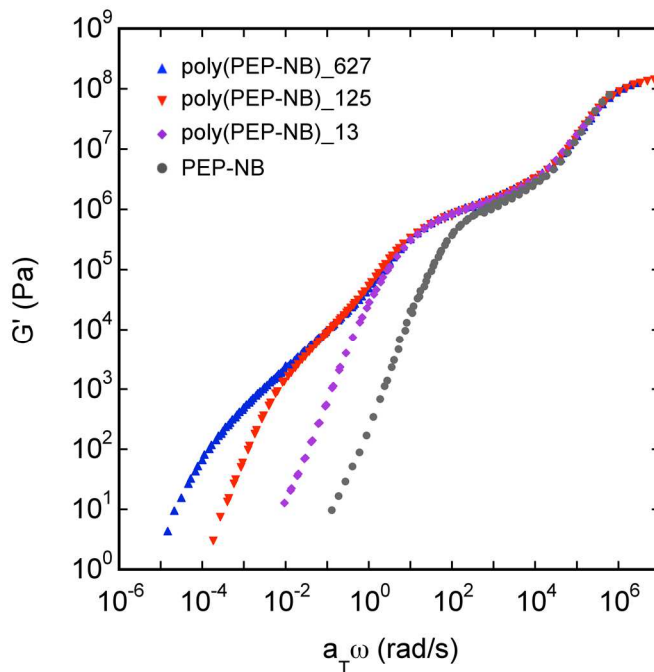
Figure 5.7. Storage modulus master curves of PEP samples at a reference temperature of $T_{\text{ref}} = T_{\text{g}} + 38\ ^{\circ}\text{C}$.

Master curves of the three poly(PEP-NB) samples show identical behavior throughout the plateau regions. This is because all three samples are entangled to the same degree due to the equivalent side chain lengths. However, the large disparity in backbone length leads to differences in the intermediate regimes of the master curves (*i.e.*, between the plateau and terminal flow zones). Poly(PEP-NB)_13 displays practically no intermediate regime and transitions to terminal flow immediately following the plateau region. This molecule is approximately star-like in configuration and does not reveal any backbone relaxation effects. The poly(aPP-NB)_125 and poly(aPP-NB)_627 samples become progressively more representative of cylindrical bottlebrushes, leading to extended intermediate regions. The ultimate changeover to terminal flow is delayed to longer relaxation times and lower modulus values with increasing backbone length, and there is no evidence of a secondary plateau that would correspond to backbone entanglement.

These characteristics are consistent with the behavior of the aPP bottlebrushes in that the relaxation profiles are qualitatively Rouse-like throughout the intermediate regime.

The master curve for PEP-NB overlaps well with the poly(PEP-NB)s at high frequencies, signifying equivalent glassy relaxation dynamics, but the plateau region is truncated relative to the poly(PEP-NB)s, suggesting a lower degree of entanglement. This occurs because PEP-NB has only half the chain length as the diameter of the poly(PEP-NB) brushes. It may be more appropriate to compare the side chain relaxation dynamics, the plateau region in this case, of the poly(PEP-NB)s with a linear PEP of twice the chain length as PEP-NB. This would represent the "dimer", or equivalently, a poly(aPP-NB) with a backbone DP of 2. According to reptation scaling,[172] a master curve of the dimer would simply display a plateau region that extends to a frequency $2^3 = 8$ times lower than that of PEP-NB. By inspection of Figure 5.7, this dimer master curve would exhibit the same plateau width as the bottlebrush samples and overlay very closely with the poly(PEP-NB)_13. This is an interesting result, because it implies that poly(PEP-NB)s with backbone DP = 2 and DP = 13 display the same linear viscoelastic profile at all relaxation times. There are two possibilities as to how this behavior might arise. One possibility is that every molecule in the series between DP = 2 to DP = 13 has nearly identical dynamics, and each master curve would overlay with poly(PEP-NB)_13 on Figure 5.7. Alternatively, it is possible that molecules successive to DP = 2 (*e.g.*, DP = 3 or 4) would show even further extended plateau regions and longer terminal relaxation times than DP = 2 due to an increased reptation time of star polymers relative to linear polymers.[127,173] In this case, however, the master curves of further successive polymers in the series (*e.g.*, DP = 9 or 10) would necessarily revert back in order to retain the master curve of the DP = 13 sample. This effect could be rationalized as a result of the increased degree of side chain crowding with higher DP brushes. The increasingly compact molecular conformation could cause a slight reduction in the number of effective entanglements and reproduce the dynamics of DP = 2 at higher DP values. Experimental exploration of the molecules in this range (*i.e.*, poly(macromonomer)s with DP = 3, 4, 5,

etc.) would help to clarify this issue but would likely require alternative synthetic strategies to ensure a precise number of branches per molecule.

Although our goal was to create bottlebrushes with side chain entanglement, it was not obvious *a priori* that effective entanglements could develop in a system with such dense packing of side chains. For instance, a bottlebrush with an extreme graft density of one branch (or more) per backbone carbon would certainly preclude the ability of branches from neighboring brush molecules to interdigitate sufficiently for entanglement, particularly for branch segments near to the backbone. (Note: the mass density of the polymer melt, governed by the packing of segments at the sub-nanometer scale, is essentially unaffected by the molecular architecture). Of course, packing constraints are relieved as side chains meander further out from the backbone since the available area per branch increases with the square of radial distance. Thus, side chains further from the backbone increasingly exhibit behavior reminiscent of linear polymers in the bulk. The question then becomes: how far from the backbone is bulk-like behavior retained? This system serves as a good test of the limits, because it utilizes amorphous side chains with low inherent M_e and promotes entanglement formation near to the backbone where branches are most crowded. The fact that the branches of poly(PEP-NB)s successfully form entanglements demonstrates that the packing constraints of this system are not sufficient to disrupt side chain overlap. To experimentally reach the limits in which entanglements would be completely inhibited by side chain crowding, bottlebrushes with lower branch M_e and M_n or with greater branch density are required.

5.3.2   Sequential Relaxation

The individual relaxations of the backbones and side chains were demonstrated for the aPP bottlebrush series in Figure 4.11 using the van Gurp-Palmen representation of phase angle (δ) versus complex modulus (G*). This type of plot proved particularly useful for identifying distinct relaxation processes, which were not discernable using only the dynamic moduli master curves. Figure 5.8 presents an overlay of the van Gurp-Palmen plots for the poly(PEP-NB) samples. Clearly, side chain relaxation is much more defined

in these samples compared to the aPP series, marked with a sharp minimum at $G^* \approx 10^6$ Pa. The well-defined minimum is indicative of a rubbery plateau region, signifying the entanglement in PEP side chains. The side chain relaxation minimum remains uniform among all three samples because of the fixed side chain length. Furthermore, the low modulus region shows a second minimum that steadily develops with increasing backbone DP, indicating the more pronounced relaxation of the entire bottlebrush.
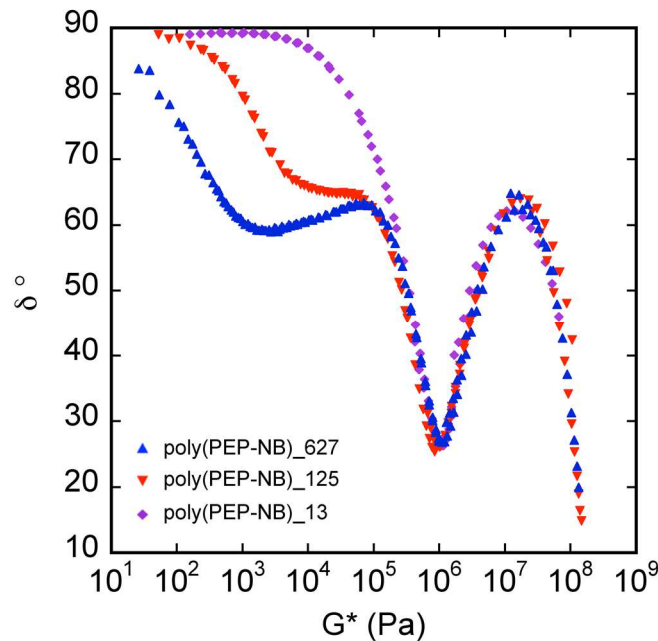
Figure 5.8. Van Gurp-Palmen plots of poly(PEP-NB)s.

The van Gurp-Palmen plots demonstrate that the prominence of the longest relaxation mode is dictated by the aspect ratio of the bottlebrush molecules, defined as the ratio of backbone length to side chain length. The magnitude of this mode can be quantified using the δ value of the second minimum. For example, poly(aPP-NB)_732 in Figure 4.11 displays a more defined (lower δ value) longest relaxation mode than poly(PEP-NB)_627, despite the latter having higher overall molar mass. This is because poly(aPP-NB)_732 has the higher length-to-diameter aspect ratio. Additionally, poly(PEP-NB)_627 exhibits a comparably defined longest relaxation mode to the much smaller

poly(aPP-NB)_215 (inverse triangles in Figure 4.11). These two samples have similar aspect ratios and achieve minimum phase angle values of 59° and 58°, respectively. It is clear, however, that the separation between the two relaxation modes is greatest for poly(PEP-NB)_627 because the modulus of the slowest relaxation mode is regulated by total molar mass.

Figure 5.9 provides a direct comparison between poly(PEP-NB)_627 and poly(aPP-NB)_732. Since the minimum phase angle of the slowest relaxation mode is dependent on bottlebrush aspect ratio, while the modulus of this mode is dictated by the total molar mass, the slowest relaxation mode of poly(aPP-NB)_732 emerges at a lower minimum phase angle but a greater modulus than that of poly(PEP-NB)_627. The dashed vertical lines in Figure 5.9 mark the modulus values of the local minima. Comparing these two values gives a good estimate of the difference between longest relaxation moduli of the two samples, but does not indicate the absolute modulus values for the slow relaxation process. A more accurate determination of the slowest relaxation modulus is achieved by locating the G* value at the inflection point of the curves, which marks the start of the terminal flow region.[155] Additionally, the slowest relaxation modulus can be estimated by

$$G = \frac{\rho RT}{M_{\text{total}}} \tag{5.1}$$

where ρ, R, T, and M_{total} are the density, gas constant, temperature, and total bottlebrush molar mass, respectively. The solid lines in Figure 5.9 identify the anticipated modulus value of the slowest mode calculated using equation 4.1 and assuming literature values for the bulk density of aPP and PEP at T = 298 K.[150] The predicted modulus for both samples is in good agreement with the data, as both solid lines are in close proximity to the inflection points of the curves. This supports the applicability of equation 4.1 and verifies that the entire bottlebrush molecule controls the slowest relaxation mode.
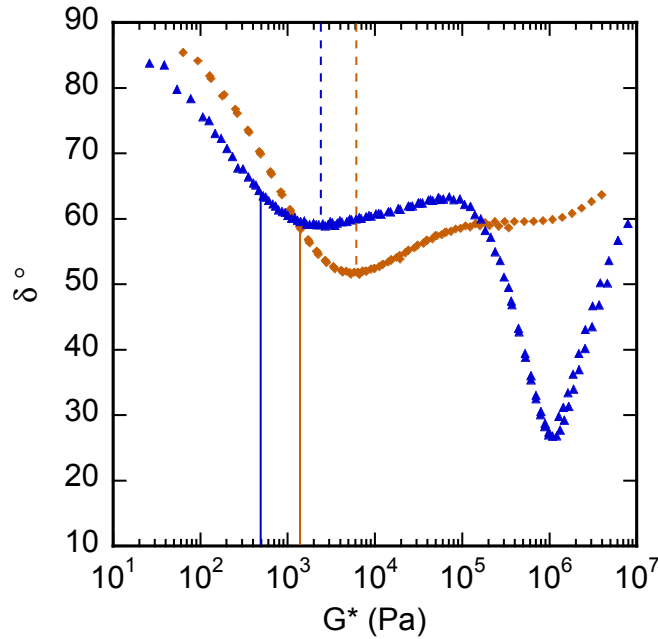
Figure 5.9. Van Gurp-Palmen plot of poly(PEP-NB)_627 (triangles) and poly(aPP-NB)_732 (diamonds). Solid lines mark the modulus estimated using equation 5.1. Dashed lines denote the modulus of the local minimum.

Unlike the aPP data shown in Figure 4.11, PEP relaxation data from all the temperatures measured were included in Figure 5.9. This is because the PEP samples exhibited thermorheologically simple behavior at all temperatures. Therefore, inclusion of all the data sets produced composite curves in the van Gurp-Palmen plots with no discontinuities. This feature emphasizes that thermorheological behavior is governed by phenomena at a sub-nanometer length scale and is more dependent on the chemical identity of polymer repeat units than the macromolecular structure.

5.4   Scaling of Bottlebrush Relaxation Dynamics

5.4.1   Rouse and Zimm Models

Until this point we have described the relaxation of bottlebrush molecules in the intermediate scaling regime as qualitatively Rouse-like. We now focus more closely on

this scaling behavior. Based on the classic theoretical Rouse and Zimm models,[174,175] the scaling of dynamic moduli at intermediate frequencies follow the relationships given by

$$\text{Rouse:} \qquad G'(\omega) \cong G''(\omega) \sim \omega^{1/2} \qquad\qquad (5.2)$$

$$\text{Zimm:} \qquad G'(\omega) \cong G''(\omega) \sim \omega^{2/3} \qquad\qquad (5.3)$$

Equivalently, the scaling of the dynamic complex viscosity for these models is given as

$$\text{Rouse:} \qquad \eta^*(\omega) \sim \omega^{-1/2} \qquad\qquad (5.4)$$

$$\text{Zimm:} \qquad \eta^*(\omega) \sim \omega^{-1/3} \qquad\qquad (5.5)$$

where complex viscosity is obtained from the dynamic frequency data as

$$\eta^*(\omega) = \frac{G^*(\omega)}{\omega} \qquad\qquad (5.6)$$

Both of these models were initially developed to describe the dynamics of polymers in dilute solutions. The Zimm model predicts faster relaxation behavior than the Rouse model and provides a better description of real polymer solutions. This is because the Zimm model corrects the scaling law of the Rouse model by incorporating effects of hydrodynamic interactions, *i.e.*, the cooperative motion of segments within a polymer coil as mediated by disturbances of the surrounding flow field. By accounting for hydrodynamic interactions, the Zimm model depicts non-draining behavior in which internal polymer segments are shielded from the exterior of the coil and do not contribute viscous drag to the system. Alternatively, the Rouse model neglects these hydrodynamic interactions and predicts a free-draining system in which all polymer segments contribute equally to the overall viscosity. The Rouse model does, consequently, describe the behavior of unentangled polymer melts quite well since hydrodynamic interactions are screened by segments of overlapping polymer chains in the melt state. The physical pictures of the two models are reintroduced here in order to assess their validity in describing the behavior of bottlebrush systems.

5.4.2   Complex Viscosity Scaling Results

We chose to examine the complex viscosity master curves of the bottlebrush samples to evaluate the scaling behavior. These plots reflect equivalent data to the complex modulus (G*) master curves and can be compared with the Rouse and Zimm models using equations 5.4 and 5.5, respectively. Figure 5.10 displays the complex viscosity master curves for each bottlebrush series along with the aPP-NB and PEP-NB macromonomer samples.
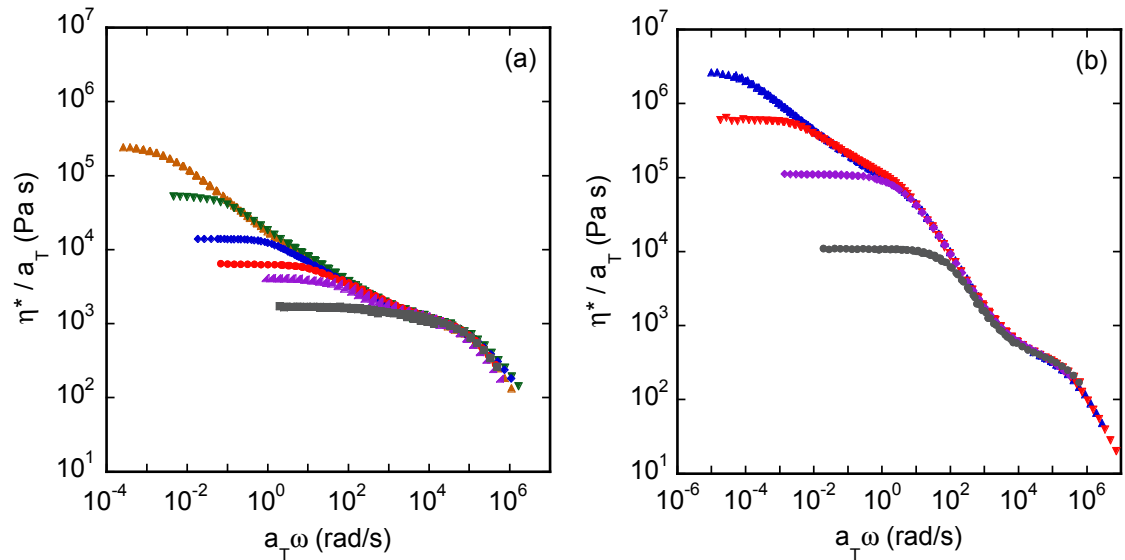
Figure 5.10. (a): Reduced complex viscosity versus reduced frequency of aPP-NB (squares), poly(aPP-NB)_11 (right triangles), poly(aPP-NB)_26 (circles), poly(aPP-NB)_74 (diamonds), poly(aPP-NB)_215 (inverse triangles), and poly(aPP-NB)_732 (triangles) at a reference temperature of $T_{ref} = T_g + 34$ °C. Reproduced from Figure 4.14 for direct comparison with poly(PEP-NB) data. (b): Reduced complex viscosity versus reduced frequency of PEP-NB (circles), poly(PEP-NB)_13 (diamonds), poly(PEP-NB)_125 (inverse triangles), and poly(PEP-NB)_627 (triangles) at a reference temperature of $T_{ref} = T_g + 38$ °C.

The complex viscosity curves in Figure 5.10 overlap at high frequencies due to the equivalent segmental relaxation behavior. The low frequency behavior is coincident with

the transitions seen in the storage modulus overlay in Figure 5.7. The macromonomer samples achieve zero-shear viscosity at higher frequencies than the bottlebrushes, which exhibit extended intermediate scaling regimes with increasing backbone DP. Given that each master curve displays uniform behavior at frequencies greater than the respective terminal flow regions, the highest molar mass samples for both the PEP and aPP series can be isolated to analyze the full relaxation spectra and quantify the scaling behavior at different relaxation times.

Figure 5.11a displays the complex viscosity master curve of poly(PEP-NB)_627. Between the glassy and terminal flow regions, this sample exhibits a steep scaling regime corresponding to the rubbery plateau, as well as an intermediate scaling regime that spans about 3.5 decades in frequency. If we assume constant power law scaling ($\eta^* \sim \omega^x$) the intermediate regime is characterized by $x = -0.33$ as indicated on the plot as a slope of −1/3, which parallels the scaling predicted by the Zimm model in equation 5.5. Additionally, we have calculated the instantaneous slope at each point along the master curve and plotted that data on a secondary ordinate axis. To reduce noise in the data due to random error at each data point, the instantaneous slopes were calculated by averaging the slope of the ten nearest data points surrounding the point of interest (see section 5.6 for details of the applied averaging method). Plotting the instantaneous slopes throughout the intermediate regime reveals that the slope of −1/3 arises as the average of a non-constant scaling. The instantaneous slope actually falls monotonically to lower values (more negative) as the frequency is decreased.

Figure 5.11b corresponds to poly(aPP-NB)_732, which has the widest intermediate scaling regime of any sample in this study, spanning more than four decades in frequency, due to its large ratio of backbone length to brush diameter. The instantaneous scaling of this sample also changes throughout the intermediate regime. The power law exponent continually becomes more negative with decreasing frequency and slowly approaches the Rouse model scaling prediction of $x = -0.5$. These results demonstrate that the previous description of bottlebrush polymer relaxation as Rouse-like is not strictly representative of the entire relaxation process.
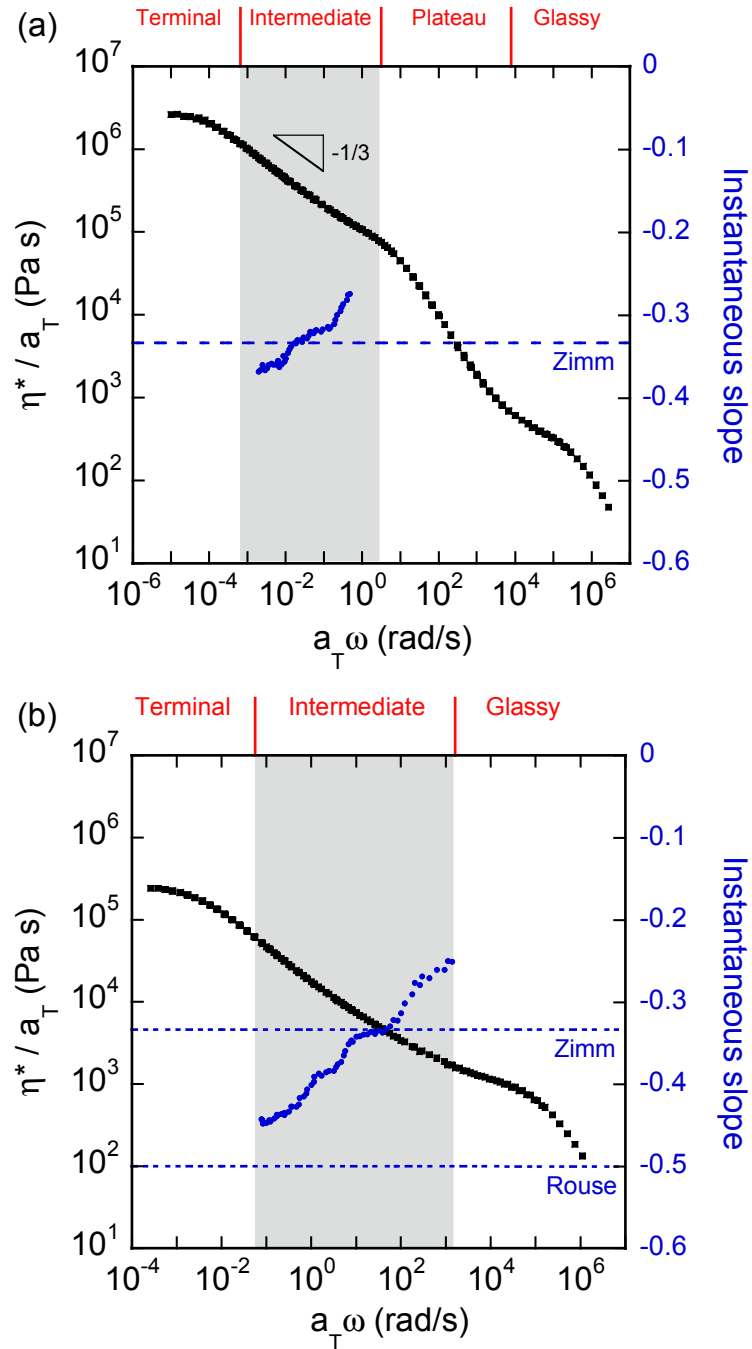
Figure 5.11. Reduced complex viscosity (squares) versus reduced frequency of (a) poly(PEP-NB)_627 at a reference temperature of $T_{ref} = T_g + 38$ °C and of (b) poly(aPP-NB)_732 at a reference temperature of $T_{ref} = T_g + 34$ °C. The instantaneous slope of the complex viscosity data is included in both plots on a secondary vertical axis (circles).

5.4.3   Discussion

The poly(PEP-NB)_627 sample displays largely Zimm model scaling in the intermediate regime of Figure 5.11a. By analogy with the Zimm model, this suggests the presence of shielded polymer segments that do not contribute to viscous drag. Unlike the Zimm model, however, the observed shielding effect does not arise due to hydrodynamic interactions. Instead, it is caused by the compact, space-filling conformation of the bottlebrush molecules at small length scales. The dense spacing of covalently bonded side chains along the backbone creates a high self-concentration and shields internal segments from contacting surrounding molecules, despite the close proximity of neighboring molecules in the undiluted state.

It is not justifiable, though, to simply apply the specific scaling of the Zimm model to this system. The true dynamics of the system are dependent on the conformations of the individual bottlebrush molecules, which are conditional depending on the DP of the backbone. For instance, poly(macromonomer)s with short backbones are more star-like and should display different dynamics than more cylindrical molecules with longer backbones. Thus, the dynamics of bottlebrush polymers should exhibit transient scaling at different relaxation times. Shorter times correspond to more compacted star-like sections and longer times correspond to the relaxation of elongated, conformationally cylindrical brush sections (illustration given in Figure 5.12). Such transient scaling behavior is best demonstrated by Figure 5.11b. At the highest frequency associated with the intermediate regime (early relaxation times), the instantaneous scaling is actually faster than the Zimm model prediction. Note: the limit of fast dynamics would yield a slope of 0, indicating a fixed viscosity value. The magnitude of the instantaneous slope continually becomes more negative at lower frequencies, passing through the Zimm model scaling value and reflecting the continually changing conformational state of bottlebrushes at longer length scales. Any relaxation time in which exact Zimm scaling is recovered is coincidental and does not imply that the Zimm model portrays the same physical situation. Ultimately, it is expected that Rouse dynamics would be retained in the limit of backbone lengths much greater than the bottlebrush diameter. In this limit, the

bottlebrush can be viewed as very thick Gaussian chain that is long enough to adopt random-walk conformations.
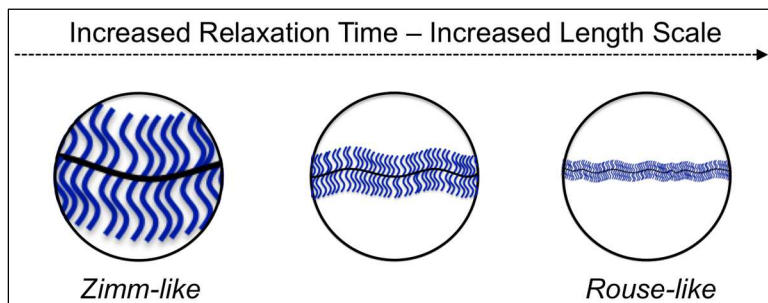
Figure 5.12. Illustration of bottlebrush polymers at different length scales, representing the pertinent molecular dimensions at increasing relaxation times.

5.5   Conclusions

The dense arrangement of side chains in bottlebrush polymer melts completely precludes entanglement of the backbone chains, as shown definitively in chapter 4. However, the effects on side chain entanglement remained unexplored. Our aPP bottlebrush series, as well as other relevant studies in the literature, focused only on bottlebrush polymers with branch lengths below the entanglement spacing, M_e. Therefore, it was unclear whether the close spacing of branches in bottlebrush polymers would inhibit the development of intermolecular branch entanglements. We addressed this issue with a second series of bottlebrush polymers containing PEP side chains of M_n = 6.7 kg/mol, which exceeds the critical molar mass for entanglement in bulk PEP ($M_n/M_e \approx 3.5$). Bottlebrushes with PEP branches served as appropriate model materials because of the relatively low M_e of linear PEP chains, which favors entanglement formation near the crowded backbone and suitably tests the influence of the dense branch spacing.

    Master curves of the PEP bottlebrushes displayed rubbery plateau regions at short relaxation times, indicating successful development of branch entanglements. Therefore, the packing constraints introduced by a spacing of one branch per poly(norbornene) backbone unit were not sufficient to suppress entanglement formation. These results

indicate that side chains do not need to extend a sizable distance from the backbone before exhibiting unrestricted, bulk-like behavior.

Beyond the presence of side chain entanglement, van Gurp-Palmen plots of the dynamic response data were also shown to develop characteristic features that signify structural details of the bottlebrush polymer molecules. Specifically, the modulus value corresponding to the longest relaxation mode was dictated by the overall bottlebrush molar mass, whereas the phase angle value of the slowest mode depended on the length-to-diameter aspect ratio of the bottlebrushes.

Finally, analysis of the complex viscosity data revealed a transient scaling behavior throughout the relaxation spectra of the largest bottlebrush polymer in each series. This behavior resulted from the conformational states of bottlebrushes at different length scales. At early relaxation times the dynamics were more Zimm-like due to the compact arrangement of polymer segments at small length scales. In this regime, many of the internal segments near the backbone are shielded from neighboring molecules. This is fundamentally different but effectively similar to the shielding of internal segments due to hydrodynamic interactions described by the Zimm model. The relaxation scaling became more Rouse-like at longer times, as the molecules more closely resembled elongated cylinders. Bottlebrushes at larger length scales can appropriately be described as dynamically analogous to unentangled Gaussian chains. These findings advance our understanding of bottlebrush polymer dynamics, and may inform the designed incorporation of bottlebrush polymers in new composite or blend materials with targeted applications.

5.6   Methods and Experimental Details

5.6.1   Synthesis Methods

The majority of synthesis methods are the same as those described in chapter 3 for aPP bottlebrush synthesis. The main difference was that preparation of PEP-NB macromonomers started with a batch of ω-hydroxyl polyisoprene (PI-OH), synthesized

by Tim Gillard *via* anionic polymerization. The synthetic procedures that were not introduced in chapter 3 are detailed in this section.

5.6.1.1   PEP-NB Macromonomers

Initially, a batch PI-OH (M_n = 4.5 kg/mol by ^{1}H NMR) was synthesized according well-known anionic polymerization protocol.[176,177] ^{1}H NMR demonstrated a preferential 1,4-addition of monomers (as represented in the structure shown in Figure 5.13 and Figure 5.14) where only 7 % of 1,2- or 3,4-addition was detected. This ensured a ω-hydroxyl PEP (PEP-OH) product following catalytic hydrogenation of PI-OH.
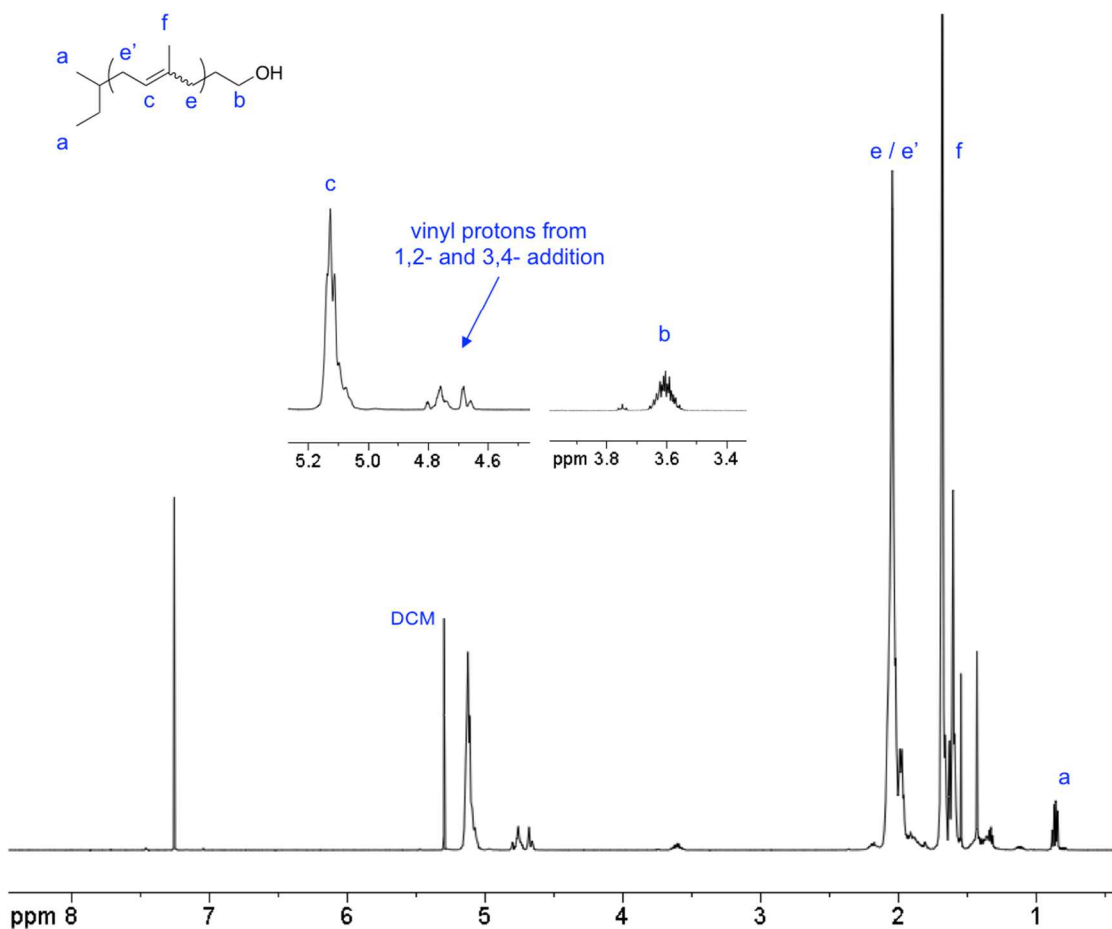
Figure 5.13. ^{1}H NMR spectrum of PI-OH (CDCl₃, 500 MHz). Integration yields 93% of repeat units connected with 1,4-addition of monomers.
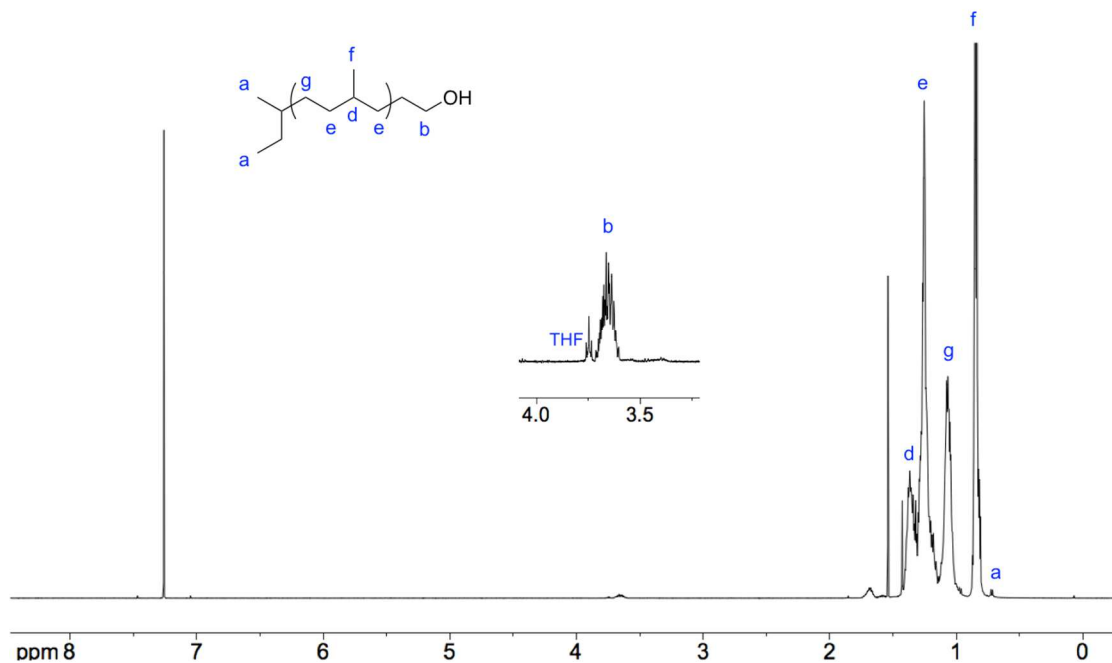
Figure 5.14. ^{1}H NMR of PEP-OH following hydrogenation of PI-OH (CDCl$_3$, 500 MHz).

Hydrogenation of PI-OH was carried out in a high-pressure vessel using a common heterogeneous platinum/rhenium catalyst on a silica support (Pt-Re/SiO$_2$) produced by Dow Chemical.[178] First, PI-OH (17 g) was dissolved in cyclohexane (500 mL) and loaded into a 1-L hydrogenation vessel along with the Pt–Re/SiO$_2$ catalyst (3.2 g). The vessel was sealed, pressurized with 500 psi H$_2$, closed off from the H$_2$ gas after 500 psi was reached, and the solution was allowed to stir at room temperature for 30 min to ensure no leaks were present in the system. After 30 min, no drop in the vessel pressure had occurred, and the mixture was heated to 100 °C and stirred for 12 h. The reaction temperature of 100 °C is relatively mild compared to the 170 °C required to saturate polystyrene chains (for PCHE synthesis) using the same catalyst. The lower reaction temperature for PI-OH is not only effective due the high amenability of polydienes to heterogeneous hydrogenation, but it is also required in this case to retain a high functionality of the unprotected hydroxyl end groups. The mixture was then cooled to room temperature, filtered to remove the catalyst, and cyclohexane was removed by

rotary evaporation. The resulting ω-hydroxyl PEP (PEP-OH) was dried on the vacuum line and characterized by ^{1}H NMR spectroscopy, as shown in Figure 5.14.

Finally, PEP-OH was further functionalized with *exo*-5-norbornenecarboxylic acid following the same protocol as the aPP-NB synthesis in chapter 3. The PEP-NB macromonomer was characterized by ^{1}H NMR and SEC-MALLS. The ^{1}H NMR spectrum is given in Figure 5.15 and gives a molar mass of $M_n = 6.7$ kg/mol.
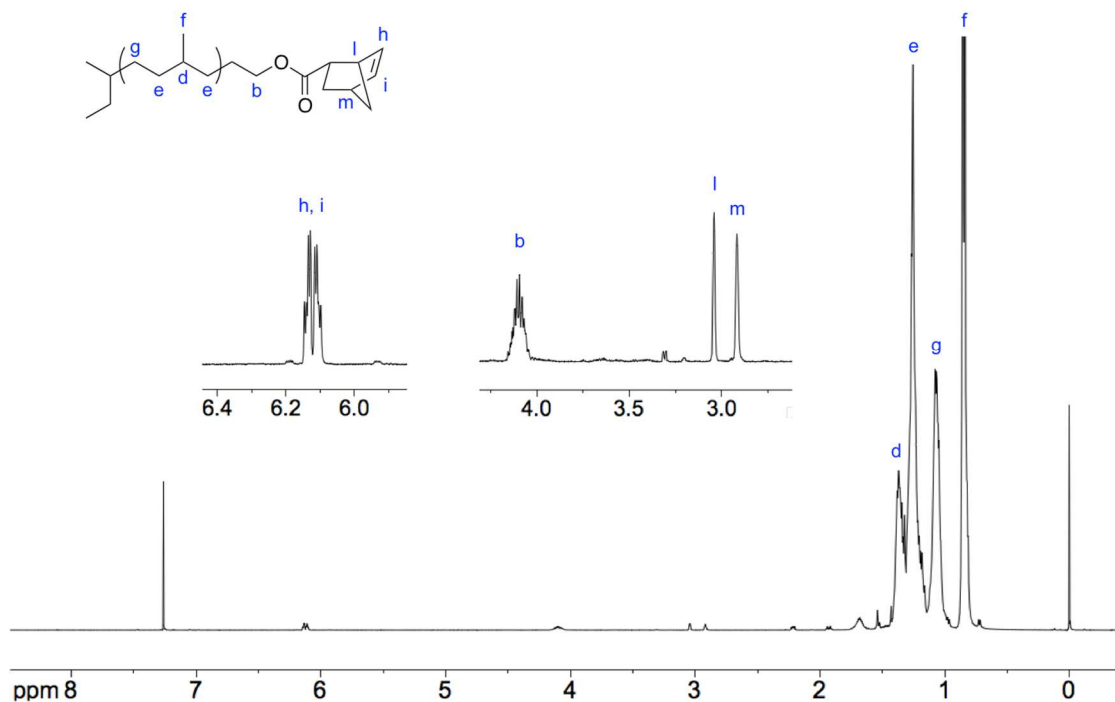
Figure 5.15. ^{1}H NMR of PEP-NB (CDCl$_3$, 500 MHz).

5.6.1.2   Poly(PEP-NB) Bottlebrush Polymers

PEP bottlebrushes were synthesized by ROMP of PEP-NB macromonomers following procedures detailed in chapter 3. The poly(PEP-NB)_13 and poly(PEP-NB)_125 samples were reacted for 2 h before terminating, while the poly(PEP-NB)_627 reaction was run for 4.5 h. Since these reactions did not achieve complete conversion, the unreacted macromonomers were removed using the following fractionation procedures. Methanol, used as a nonsolvent, was added dropwise at room temperature to a stirring solution of polymer in THF until the solution became clouded. The temperature was then increased by 2 °C and stirred until the solution clarified. The same procedure was iterated several times until the solution temperature reached 35 °C. After the final heat, stirring was stopped and the clear solution was allowed to cool slowly back to room temperature. Typically this was left overnight to settle. High molar mass bottlebrush polymers precipitated out of solution, and the supernatant solution was carefully removed using a needle/syringe assembly. Figure 5.16 displays the SEC traces of poly(PEP-NB)_125 before and after the removal of unreacted PEP-NB molecules.
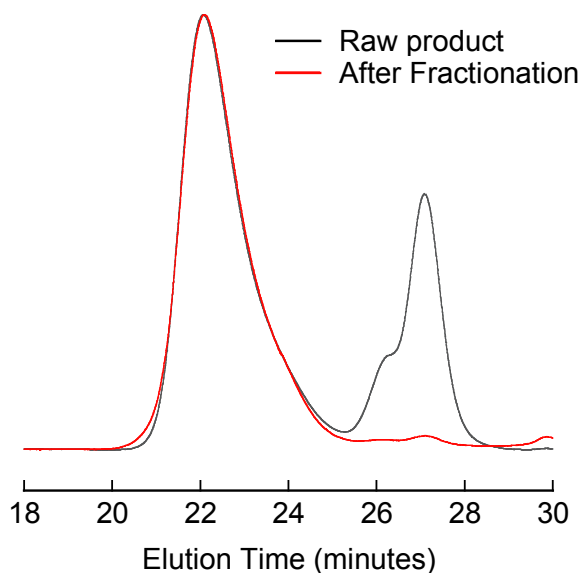
Figure 5.16. SEC traces of poly(PEP-NB)_125 before and after removal of unreacted PEP-NB macromonomers using fractionation procedures.

5.6.2   Characterization Methods

The instrumentation used for molecular characterization was the same as detailed in chapter 3, and the thermal and rheological characterizations were the same as those in chapter 4, apart from the following exceptions. SEC: Absolute molar masses of the PEP-NB macromonomer and poly(PEP-NB) samples were determined by using the in-line light MALLS detector with a dn/dc value of 0.070 mL/g, as measured by the SEC instrument assuming 100 % mass elution. DSC: Samples were first heated to 50 °C (10 °C/min), then slowly cooled to –75 °C for at 5 °C/min, and then heated a second time for analysis.

5.6.3   Averaging Method Applied in Figure 5.11.

The instantaneous slope for each data point in Figure 5.11 was determined by fitting (*via* linear regression) a data range spanning eleven data points, centered about the point of interest (*i.e.*, including the 5 nearest data points above and below the point of interest). This data range was chosen to smooth out noise caused by random error between data points while maintaining a small enough data set to give "instantaneous" slope information. An example is shown in Figure 5.17. The same data from Figure 5.11 is plotted as open symbols. The slope for the data point at a reduced frequency of $a_T\omega =$ 17.9 rad/s was calculated using the data range shown in filled red markers. A line was fit using the linear regression method, yielding a model fit of:

$$\log(\eta^*/a_T) = [(-0.339 \pm 0.002) \times \log(a_T\omega)] + (4.212 \pm 0.003)$$

This line is shown as the red dotted line. Using this fit, the slope at this data point is −0.339. This is plotted as the filled blue marker. The same procedure was done at each data point to produce the remaining slope values, shown in open blue markers.
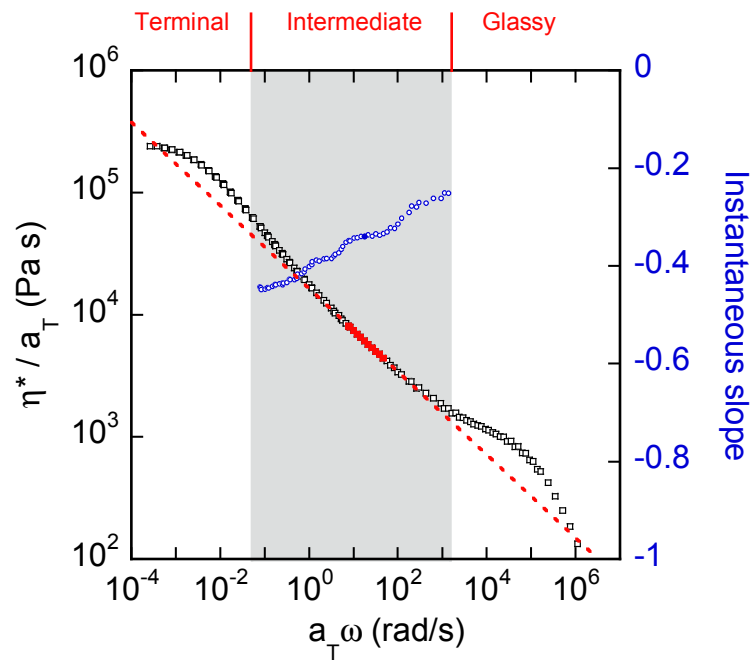
Figure 5.17. Reduced complex viscosity versus reduced frequency for poly(aPP-NB)_732 at a reference temperature of $T_{ref} = T_g + 34\ °C$. The instantaneous slopes at each point are plotted on the secondary vertical axis.

Chapter 6

Self-Assembly of Bottlebrush Block Polymers

6.1   Introduction

The self-assembly behavior of linear block polymers has been actively studied for several decades, both experimentally and theoretically, and a fundamental understanding has been developed.[67,179,180] On the other hand, the self-assembly of bottlebrush block polymers represents a new and relatively unexplored branch of macromolecular science and engineering. As we have discussed in the preceding chapters, bottlebrush polymers are typically high molar mass, but compact molecules that display extended wormlike conformations when synthesized to high backbone lengths.[2,12,28,181,182] These characteristic properties cause bottlebrush polymers to exhibit distinctive behavior compared to their linear counterparts, and make them attractive candidates for creating advanced materials with potential applications in lithography,[183] photonic crystals,[26,27,72,76] and surface coatings.[23] Prior experimental studies have demonstrated

---

Portions of chapters 6 and 7 were reproduced with permission from ACS Nano, submitted for publication. Unpublished 2015 American Chemical Society.

that diblock polymers with at least one bottlebrush block readily self-assemble into ordered morphologies with domain sizes much larger than can be attained using linear block polymers.[74-76] This is because the high entanglement density that hinders ordering in high molar mass linear polymer melts is generally absent in bottlebrush systems. Grubbs and coworkers have utilized the large domains to create photonic materials with tunable band gaps that reflect wavelengths corresponding to ultraviolet, visible, and infrared light.[27,72] Studies by Rzayev have also shown that densely branched bottlebrush diblocks have a strong tendency to form lamellar morphologies, even for systems with highly asymmetric volume fractions. This has been attributed to the semi-rigid molecular structure, which favors the flat domain interfaces afforded by the lamellar phase.[77] More recently, Gu *et al.* reported the synthesis of several symmetric bottlebrush diblocks with independently varied side chain and backbone lengths.[184] This study utilized precisely defined bottlebrush polymers to examine the self-assembly kinetics and the lamellar spacing achieved.

Despite the predominantly lamellar assembly of bottlebrush block polymer systems reported thus far, a few studies have demonstrated non-lamellar phases by introducing significant asymmetry in the side chain lengths between blocks. Bolton *et al.* reported a stabilized cylindrical phase in bottlebrush diblocks with long PS branches (DP = 45) on one half of the backbone and short branches on the other half (either PMMA of DP = 26 or PLA of DP = 15).[24,73] Runge *et al.* investigated the melt self-assembly of brush-linear or brush-coil diblocks, which represent an extreme case in terms of side chain asymmetry.[74] These polymers displayed a substantially skewed phase diagram in which cylindrical and spherical phases could be accessed with the linear component as the minority block, but not vice versa. The consideration of architectural asymmetry in bottlebrush block polymer systems is therefore essential for predicting and interpreting the resultant properties.

Due to the many independent molecular parameters, a myriad of bottlebrush copolymer architectures other than A-B diblocks can be designed. For instance, block and random copolymer brushes have been prepared by regulating the arrangement of

chemically distinct side chains along the backbone.[76,185] Alternatively, multicomponent structures such as core-shell cylinders can be synthesized by using block polymer side chains.[37,186-189] These molecules can be further tailored for specific applications by, for example, including chemically degradable blocks or by decorating side chains with a desired functionality.[37,183,186,189] To fully exploit the countless possibilities and enable controlled design of nanostructured materials from bottlebrush polymers, a more complete understanding of the self-assembly behavior is needed. With this in mind, we focus here on the simplest case, *i.e.*, self-assembly of A-B diblock bottlebrush polymers with limited side chain asymmetry. In this chapter, we aimed to collect experimental data for diblock bottlebrushes of various composition and molar mass to begin elucidating the presence and locations of transition points across the phase map. This work provides initial contributions to understanding what phases are accessible and how structural dimensions influence morphology.

6.2   Synthesis and Polymerization of PS Macromonomers

We chose to synthesize bottlebrush diblocks with aPP and PS side chains for blocks A and B, respectively. PS was selected as the second block since the self-assembly of PS-based diblock polymers has been studied extensively in the literature. Therefore, a rough estimate of the effective χ parameter could be taken from previous reports, and any new phase behavior in the bottlebrush melts could be identified as architecturally driven. To assemble diblock bottlebrush polymers, we first prepared norbornene-terminated PS (PS-NB) by end-functionalization of a ω-hydroxyl polymer precursor using the same route as described in chapter 5 for PEP-NB. Figure 6.1 displays the functionalization scheme in which *exo*-5-norbornenecarboxylic acid is coupled with an anionically polymerized ω-hydroxyl PS (PS-OH)[*] of M_n = 3.8 kg/mol, yielding a PS-NB with M_n = 4.0 kg/mol [referred to hereafter as PS-NB(4.0k)]. Unlike the preparation of aPP-NB and PEP-NB macromonomers, quantitative yield was achieved in purifying PS-NB(4.0k). The high T_g

---

[*] Synthesized by Morgan Schulze

(80 °C by DSC) assisted the product collection in this case, causing the PS to quickly vitrify upon precipitation into methanol and preventing loss of low molar mass species. ^{1}H NMR spectra of the PS-OH precursor and PS-NB(4.0k) are provided in section 6.6.
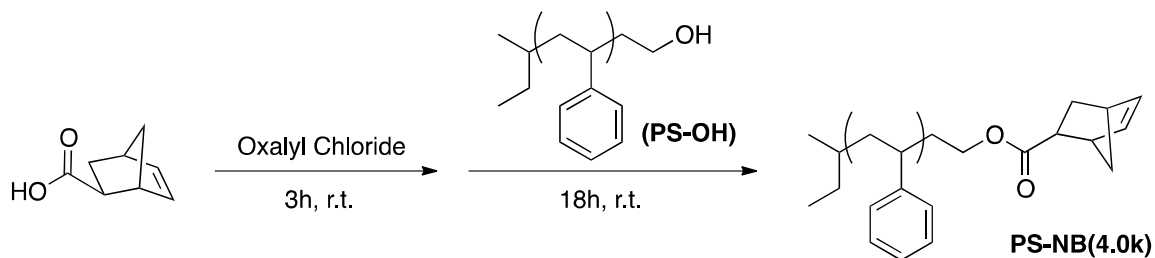
Figure 6.1. Synthesis of PS-NB(4.0k) by end-functionalization of ω-hydroxyl polystyrene (PS-OH).

The PS-NB(4.0k) macromonomer was homopolymerized by ROMP using **G3** to assess its reactivity. The reaction was carried out at room temperature in THF (50 mg/mL), and aliquots were removed rapidly from the reaction mixture. Figure 6.2 displays the SEC traces of each aliquot. This reaction progressed very quickly, achieving nearly complete conversion in ~10 min. This was not quite as rapid as ROMP of aPP-NB under the same conditions, which was completed in less than 5 min, but this is reasonable given the higher molar mass of PS-NB(4.0k). The final product also maintained a small amount (< 5 wt%) of unreacted PS molecules, which is comparable to the aPP-NB results.
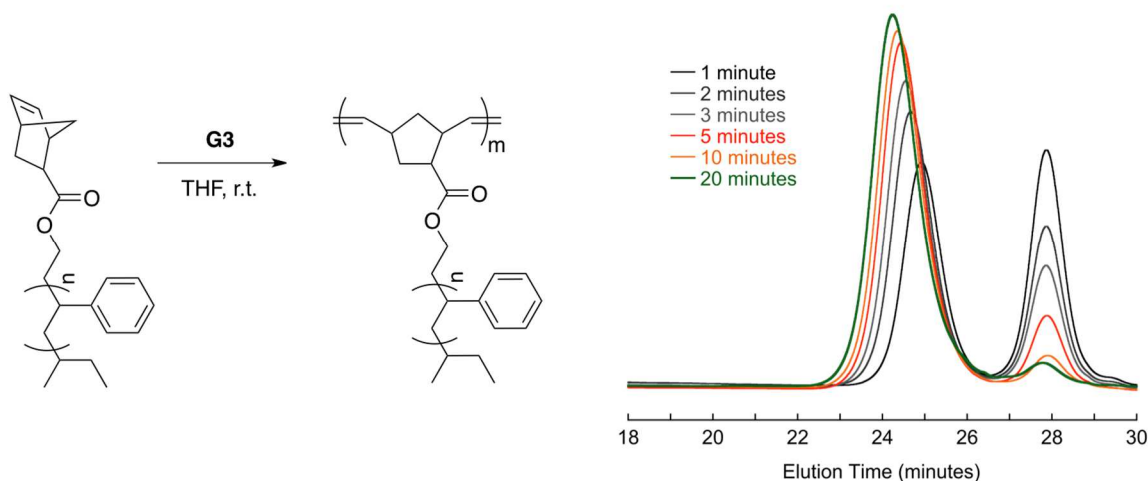
Figure 6.2. ROMP of PS-NB(4.0k) at [PS-NB(4.0k)]:[G3] = 50. SEC traces represent aliquots taken at the indicated reaction times and are normalized by integrated area.

Given the success of the initial ROMP, PS-NB(4.0k) was then used to synthesize several bottlebrush diblock samples (section 6.3.1). However, only a small amount of PS-OH was initially available for PS-NB synthesis. To produce larger quantities, subsequent macromonomer syntheses were carried out using RAFT polymerization with a norbornene-functionalized RAFT agent. This route is advantageous because it enables facile synthesis of several macromonomer samples of different chain lengths with no post-polymerization functionalization steps. Several examples in the literature have employed this method to produce norbornene-functionalized polymers with various chemistries and chain architectures (*e.g.*, diblock and triblock macromonomers).[121]

Figure 6.3 presents the pathway for further PS-NB synthesis. The prerequisite norbornenyl RAFT agent (TTC-NB) was first synthesized from *S*-Dodecyl-*S'*-(α,α'-dimethyl-α''-acetic acid)trithiocarbonate (TTC-acid) by coupling with *exo*-5-norbornene-2-methanol, as shown in Figure 6.3a. The raw product of this reaction contained byproduct impurities, which required removal by column chromatography. (The experimental procedures for this reaction and for the TTC-NB purification are given in section 6.6 along with ^{1}H NMR spectra of the raw and pure products.) The purified TTC-NB was then used for RAFT polymerization of styrene to produce several PS-NBs of

different chain lengths (Figure 6.3b). The PS-NB molar mass was controlled by the ratio of [styrene]:[TTC-NB] in the feed solution. Additionally, we targeted 40% conversion in each polymerization to avoid loss of norbornene end groups on the PS-NB products, which becomes more likely at high monomer conversion in RAFT polymerizations due to the increased probability of termination events.[190] The progress of each polymerization was monitored by ^{1}H NMR analysis of removed aliquots, and the reactions were terminated by quenching in liquid nitrogen and opening to air.

Figure 6.4 shows the SEC traces for three PS-NB macromonomers made by RAFT polymerization. Each trace displays low dispersity ($Đ \leq 1.05$) and molar masses of $M_n =$ 3.8, 8.1, and 20 kg/mol. The RAFT polymerization method enabled very precise control of the product molar mass. For example, the targeted M_n values for the two larger samples were 8 and 20 kg/mol at 40% conversion. Each of these reactions was successfully quenched at ~40% conversion, owing to the quantitative conversion calculations obtained by ^{1}H NMR analysis of aliquots, and achieved the desired M_n values. Alternatively, the target molar mass of the smaller sample was 2 kg/mol at 40% conversion. The reaction was instead run to ~75% conversion, leading to a proportionally higher M_n of 3.8 kg/mol (see section 6.6).
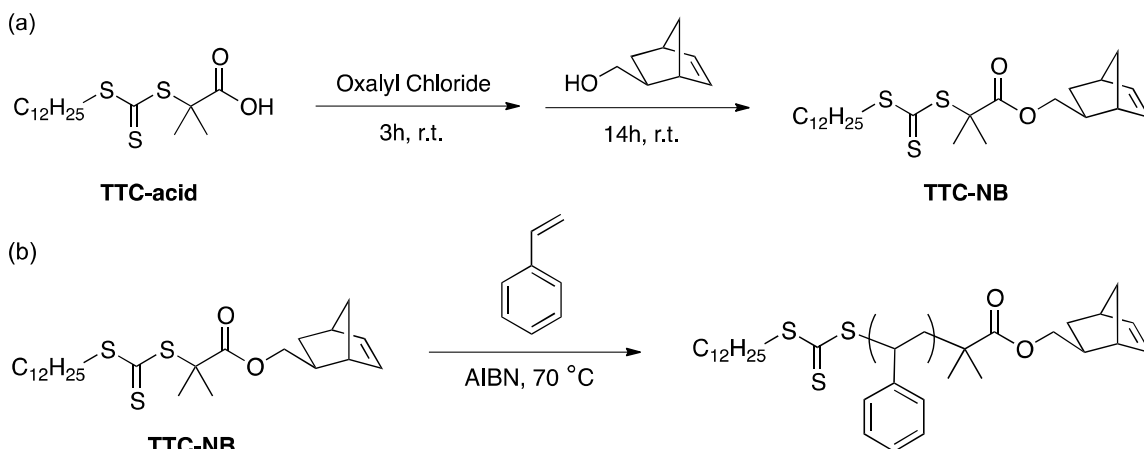
Figure 6.3. (a): Synthesis of norbornene-functionalized RAFT agent, TTC-NB. (b): Synthesis of PS-NB *via* RAFT polymerization with TTC-NB as a chain transfer agent.
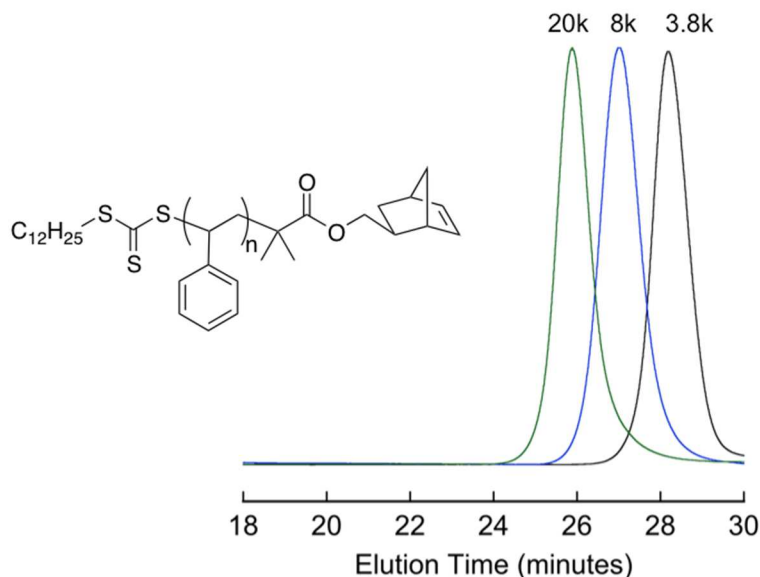
Figure 6.4. SEC traces of three PS-NB macromonomers synthesized by RAFT polymerization, resulting in the displayed molecular structure. M_n values of each sample are given above the corresponding trace.

Two of the PS-NB macromonomers (M_n = 3.8 and 20 kg/mol) were further utilized to prepare bottlebrush diblock samples. These macromonomer batches will be referred to as PS-NB(3.8k) and PS-NB(20k), respectively. Homopolymerizations for both samples were carried out using **G3** and aliquots were removed as the reaction progressed. Figure 6.5 shows the SEC traces from each reaction. The PS-NB(3.8k) macromonomer reacted very quickly, achieving ~85% conversion in the first 5 min. However, the maximum conversion attained was 87%. This points to the presence of >10% non-functionalized PS chains, which are due in part to the high conversion of the RAFT polymerization for PS-NB(3.8k). Fortunately, these low molar mass impurities could be easily removed post-ROMP by extraction with acetone, which is capable of dissolving small PS chains. The PS-NB(20k) macromonomer displayed similar results. The reaction was essentially complete in 5 min, and a small amount of unreacted PS remained, though not as much as in the PS-NB(3.8k) ROMP. The product peak also displayed a slightly higher dispersity of $Đ$ = 1.24. This is expected given the lower overall degree of polymerization.
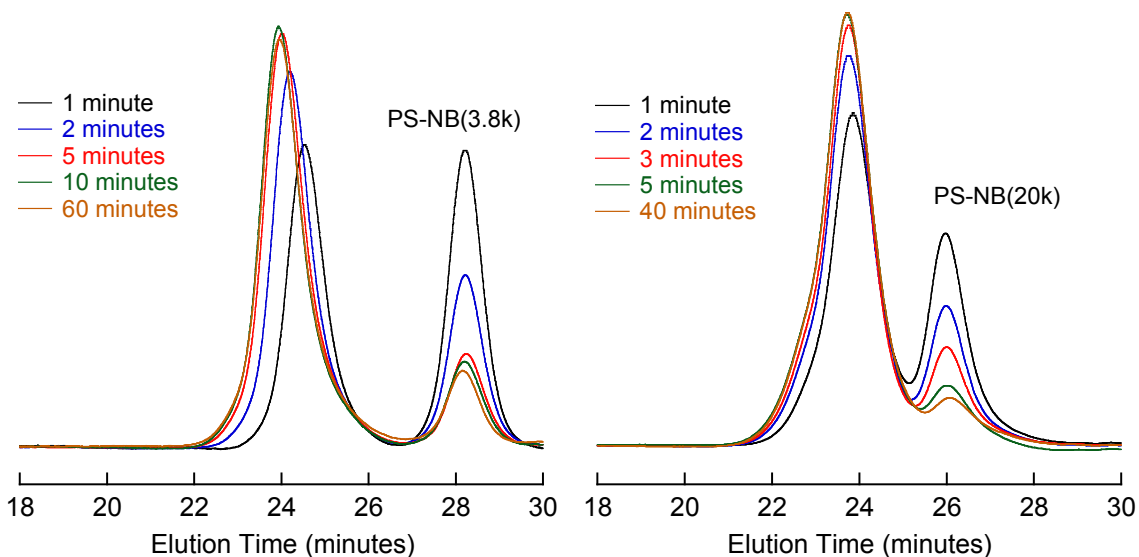
Figure 6.5. ROMP of PS-NB(3.8k) (left) and PS-NB(20k) (right). Catalyst loadings were [PS-NB(3.8k)]:[G3] = 50 and [PS-NB(20k)]:[G3] = 12.5. SEC traces represent aliquots taken at the indicated reaction times and are normalized by integrated area.

6.3   Diblock Synthesis and Self-Assembly

Diblock bottlebrush polymers composed of aPP side chains and PS side chains were prepared by sequential ROMP of aPP-NB and PS-NB macromonomers according to the synthesis scheme in Figure 6.6. Typically, aPP-NB was first added to a **G3** solution and a small aliquot was removed after 5 min for characterization of the first block. Immediately after the aliquot removal, the PS-NB macromonomer was added to polymerize the PS block from the living chain end of the poly(aPP-NB) bottlebrush backbone. Finally, reactions were terminated with ethyl vinyl ether and collected by precipitation into methanol. The self-assembly behavior in this chapter focuses on the case of our most symmetric diblocks, *i.e.*, those made using PS-NB(4.0k) or PS-NB(3.8k).
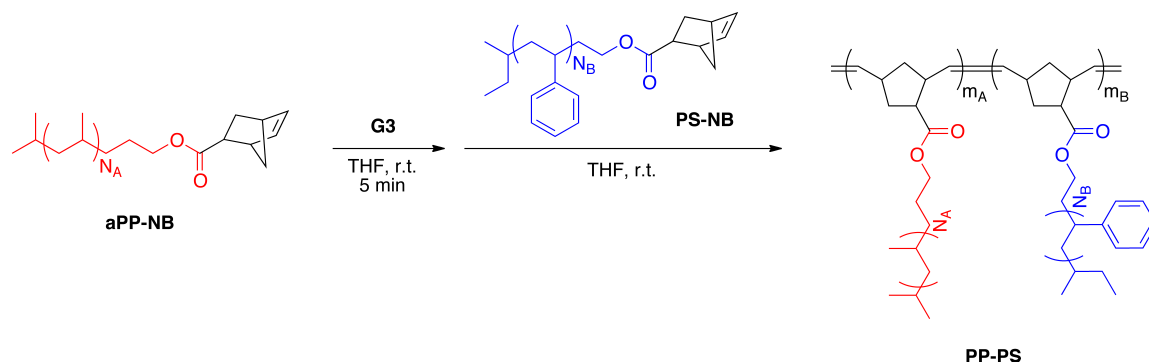
Figure 6.6. Synthesis of diblock bottlebrush polymers by sequential ROMP. The structure of PS-NB(4.0k) is shown in the scheme as an example.

Table 6.1. Molecular characterization of norbornene-functionalized macromonomers.

Macromonomer	M_n (kg/mol)[a]	$Đ$ [a]	DP [b]
aPP-NB	2.1	1.65	45
PS-NB(4.0k)	4.0	1.10	36
PS-NB(3.8k)	3.8	1.05	32
PS-NB(8k)	8.1	1.05	73
PS-NB(20k)	20.2	1.03	189

[a]Determined by SEC-MALLS in THF. [a]Chemical degree of polymerization.

6.3.1   Diblocks from aPP-NB and PS-NB(4.0k)

The first group of bottlebrush diblocks were synthesized using aPP-NB and PS-NB(4.0k). The molecular characterization of each diblock polymer is given below in Table 6.2 along with the target M_n and ϕ_{aPP} values, and the SEC traces are provided in section 6.6 (Figure 6.30 and Figure 6.31). Samples are labeled as PP-PS-#, where the given sample numbers match the sample IDs used for SAXS data collection at Argonne National Labs. For the purposes of this chapter the numbers are rather arbitrary, but used to remain consistent with our data files. Nine different diblocks were prepared for this group, ranging from M_n = 28–696 kg/mol and ϕ_{aPP} = 0.21–0.83.

Table 6.2. Molecular characterizations for the first group of PP-PS diblocks, using the PS-NB(4.0k) macromonomer for the PS block.

Sample ID	Target Values		$M_{n, \text{Diblock}}$ (kg/mol)[a]	Đ [a]	ϕ_{aPP} [b]	$DP_{aPP\text{-}NB}$ [c]	$DP_{PS\text{-}NB}$ [c]
	M_n (kg/mol)	ϕ_{aPP}					
PP-PS-1	25	0.5	28.3	1.06	0.51	6.3	3.9
PP-PS-2	50	0.5	54.2	1.05	0.51	12	7.3
PP-PS-3	150	0.5	153	1.05	0.52	35	20
PP-PS-4	150	0.2	168	1.06	0.21	14	35
PP-PS-5	150	0.8	168	1.07	0.83	65	8.6
PP-PS-6	300	0.2	407	1.24	0.21	35	84
PP-PS-7	300	0.8	311	1.23	0.82	120	16
PP-PS-8	300	0.5	368	1.20	0.61	100	41
PP-PS-9	1000	0.5	696	1.26	0.69	219	62

[a]Determined by SEC-MALLS in THF. [b]Volume fraction of aPP calculated based on the mass conversion of each macromonomer and the known densities of homopolymer melts (ρ_{aPP} = 0.85 g/mL and ρ_{PS} = 1.05 g/mL). [c]Number-average backbone degree of polymerization of each block.

Chronologically, the first samples to be synthesized were PP-PS-8 and PP-PS-7. These two samples were the only trials to polymerize PS-NB(4.0k) first, followed by aPP-NB as the second block. The SEC traces for these two samples reveal shoulders at the elution times corresponding to the poly(PS-NB) homopolymer block, indicating a small amount of PS homopolymer brushes in the final product. Alternatively, the SEC traces of the other seven diblock polymers display symmetric product peaks. These results suggest that macromonomers preferentially propagate from poly(aPP-NB) backbone chain ends rather than poly(PS-NB) backbones. When aPP-NB is added first, initiation of the PS block is faster than propagation because the initiation step involves macromonomer attachment to a poly(aPP-NB) backbone. Alternatively, when the PS block is polymerized first, the aPP-NB propagation is faster than initiation. In that case the aPP-NB chains preferentially grow onto bottlebrushes in which the aPP block has already been initiated, leaving PS homopolymer brushes in the product (see Figure 6.31).

Thus, addition of aPP-NB as the first block is favorable and was used for the remainder of the samples.

Samples were prepared for SAXS analysis by first solvent casting films (~1 mm thickness) from a THF solution. The films were then dried under vacuum and thermally annealed at 150 °C for 4 h. Solvent casting was used prior to thermal annealing to facilitate ordering since most of the samples are of high molar mass and do not have accessible order-disorder transition temperatures (T_{ODT}). The only sample to display a T_{ODT} upon heating was PP-PS-1. Figure 6.7 shows the temperature-dependent SAXS data for this sample. At 150 °C the principal peak is very sharp, indicating a consistent domain spacing in the ordered structure. The intensity of this peak slowly decreased upon heating, and between 210 °C and 220 °C the peak shape and intensity changed dramatically, indicating a transition to the disordered state. The sample was held at 220 °C for 5 min before slowly cooling. A sharp principal peak re-emerged at 215 °C and grew in intensity as it was cooled further. In contrast, none of the higher molar mass specimens displayed measurable T_{ODT}'s. For example, the next highest molar mass sample PP-PS-2, which was significantly smaller than all other diblocks except for PP-PS-1, did not exhibit an order-disorder transition at any temperature below the onset of thermal decomposition at 300 °C.

The data in Figure 6.7 also reveal a remarkable consistency of the location of q* at different temperatures. There does not appear to be any shifting in the peak position for PP-PS-1 or PP-PS-2 over a temperature range spanning 200 – 250 °C. This turns out to be a recurring feature in all of the bottlebrush diblock samples, which is likely caused by the compact molecular structure of the bottlebrush molecules. Unlike linear polymers with random-coil molecular conformations, bottlebrush molecules occupy a large fraction of their pervaded volume. This may lead to molecular dimensions and, consequently, ordered domain spacing with less variability as a function of temperature.

Figure 6.8 displays the SAXS profiles taken at 150 °C for each of the symmetric samples in Table 6.2. The black arrows included in the plot represent the expected lamellar reflections at integer multiples of q*, and the SAXS patterns are consistent with

states of lamellar order. PP-PS-2 and PP-PS-3 also clearly show extinction of the even reflections ($2q*$ and $4q*$) resulting from the near 50/50 volume fractions. The $q*$ peak steadily decreases with increased sample molar mass, demonstrating the increased domain spacing of the larger bottlebrush polymers. SAXS data for PP-PS-9 was obtained using an incident beam of lower energy (longer X-ray wavelength) than the other samples, enabling measurement of $q*$ at a lower q-range. This sample displays $q* = 0.042$ nm^{-1}, indicating a microphase separated morphology with large domain spacing (~150 nm). Qualitatively, this sample also exhibited a blue hue after solvent casting caused by the large domain sizes capable of reflecting light in the visible range.
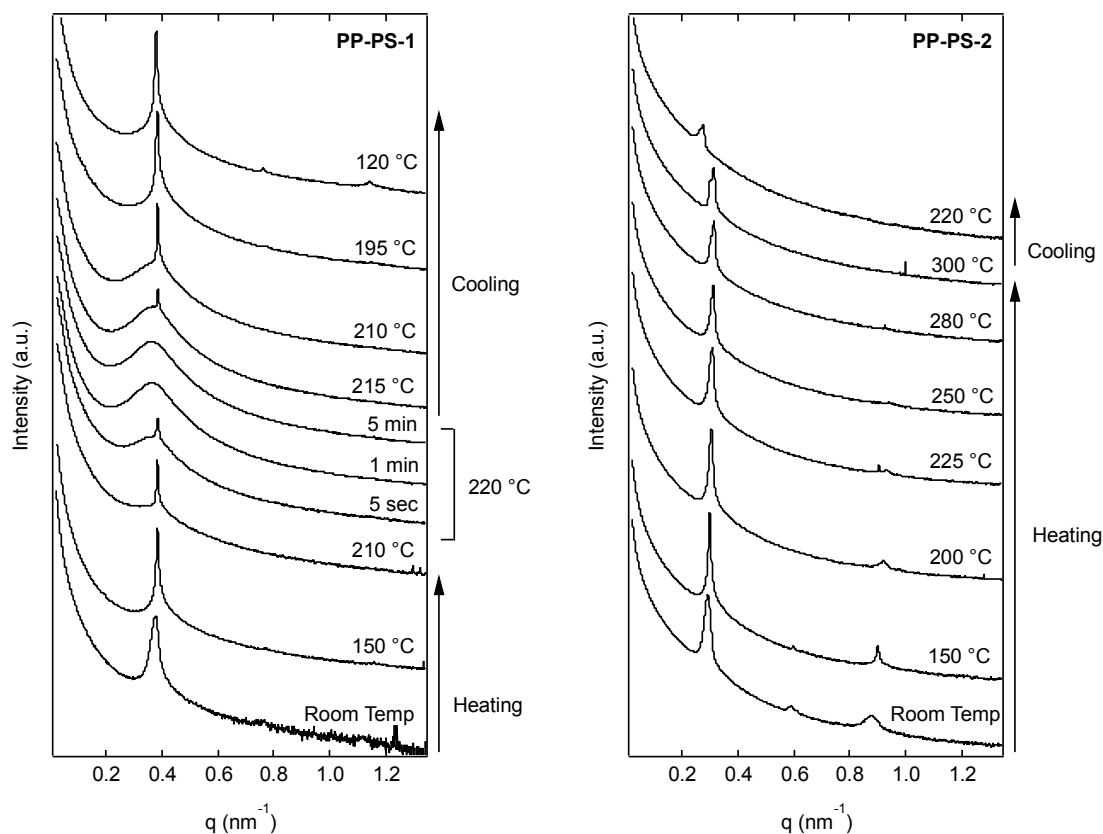
Figure 6.7. Temperature-dependent SAXS profiles for PP-PS-1 and PP-PS-2. A T_{ODT} occurs between 215 °C and 220 °C for PP-PS-1. No T_{ODT} occurs upon heating PP-PS-2 prior to thermal degradation at ~300 °C.
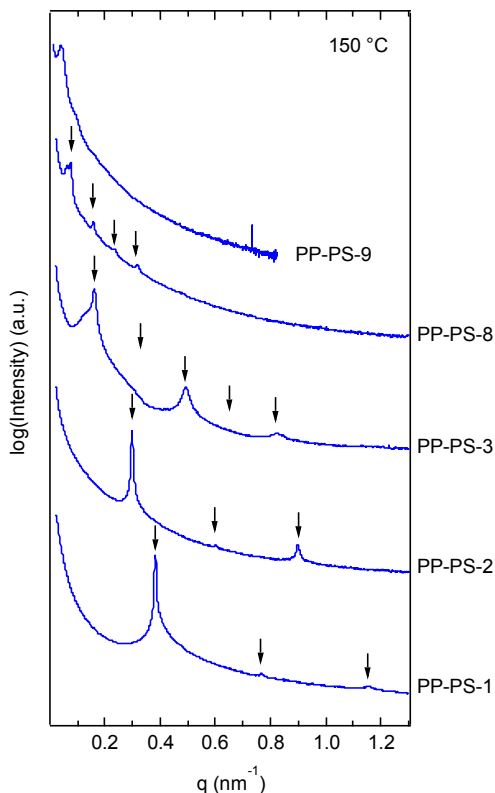
Figure 6.8. SAXS profiles for the most symmetric diblock samples listed in Table 6.2. Black arrows denote the expected lamellar reflections located at integer multiples of the primary peak (q*, 2q*, 3q*, *etc.*).

Four of the diblock samples listed in Table 6.2 were prepared with asymmetric volume fractions (80/20 v/v) to test if non-lamellar morphologies could be achieved in these bottlebrush polymers. Since the PS-NB(4.0k) macromonomer was about twice the molar mass of the aPP-NB macromonomer, yet had a smaller chain length in terms of carbon-carbon bonds, it was unclear whether any conformational asymmetry would affect the self-assembly. We therefore prepared samples of both aPP-rich and PS-rich bottlebrush polymers at two different molar masses each. Figure 6.9 presents the SAXS profiles obtained at 150 °C for all four samples. The anticipated reflections for hexagonally packed cylinders are designated with downward arrows.
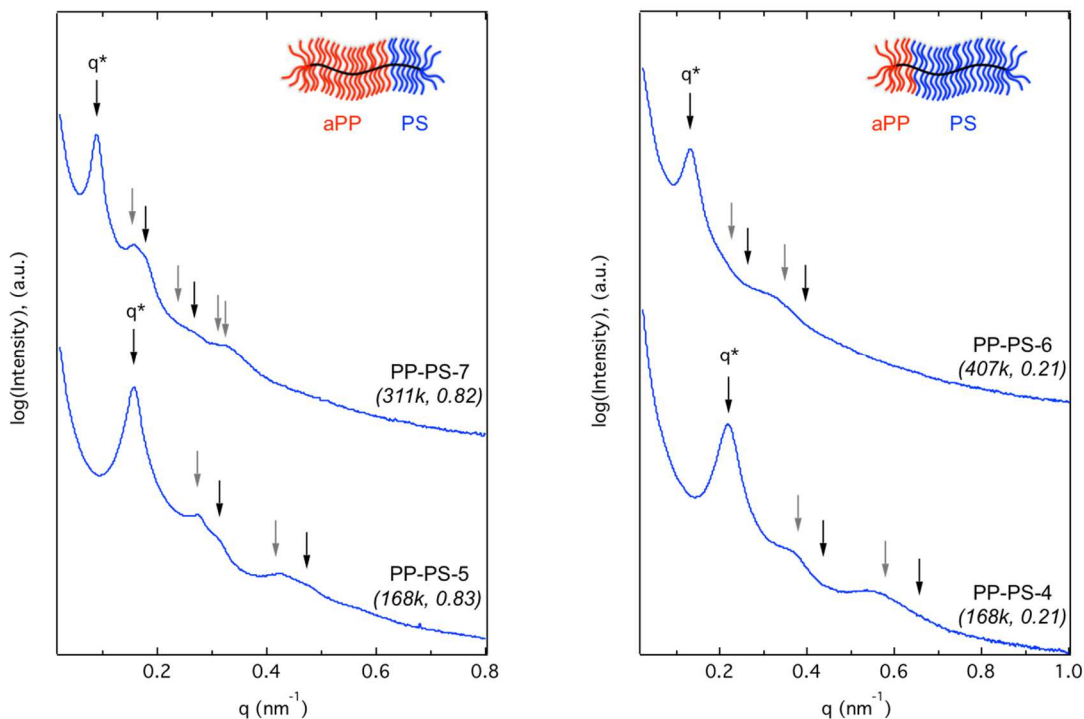
Figure 6.9. SAXS profiles of the aPP-rich (left) and PS-rich (right) asymmetric diblock samples at T = 150 °C. The reflections allowed by hexagonally packed cylinders are shown as arrows above each SAXS profile. The reflections that are also allowed by lamellar ordering are shown as black arrows (q/q* = 1, 2, 3).

The scattering profiles in Figure 6.9 reveal ordering into non-lamellar morphologies. Specifically, the aPP-rich samples PP-PS-5 and PP-PS-7 show scattering peaks indicative of hexagonal packing, presumably of cylindrical PS domains. The q/q* = √3 reflection is particularly evident in the patterns of both PP-PS-5 and PP-PS-7. This is an enticing result because the only examples of non-lamellar forming bottlebrush block polymers reported thus far in the literature involve significant side chain asymmetry between the two blocks,[24,73-75] whereas our PP-PS samples involve relatively symmetric side chain lengths. The scattering patterns for the PS-rich samples PP-PS-6 and PP-PS-8 are shown in the plot on the right in Figure 6.9. These profiles also do not exhibit lamellar ordering, but the morphology assignment is less definitive because the profiles are not as resolved as the aPP-rich polymers. We expect that the higher T_g of the PS matrix limits the

ordering kinetics of these samples compared to PP-PS-5 and PP-PS-7. Nonetheless, the SAXS profile for PP-PS-4 exhibits broad scattering peaks at $q/q^* = \sqrt{3}$ and $\sqrt{7}$, suggesting a degree of hexagonal packing. This supports the assertion that hexagonally packed structures are not induced by asymmetry in side chain length for these diblock polymers, since it occurs in both the majority aPP and majority PS diblocks. It is also feasible that the broad scattering features at high q in PP-PS-4 and PP-PS-6 are caused by form factor scattering of disordered cylindrical or spherical aPP domains. Further form factor fitting of these profiles would clarify this possibility.

Despite having an identical average molar mass, PP-PS-4 and PP-PS-5 do not display the same domain spacing, as estimated by $d_0 = 2\pi/q^*$. Instead, PP-PS-5 displays a considerably lower q*. This is attributed to the greater backbone length of PP-PS-5. Since the PS side chains are of higher molar mass than the aPP side chains, a longer backbone is required to achieve the same total molecular weight in the aPP-rich polymers. This leads to a self-assembled morphology with larger spacing between the domains. The same effect is seen in comparing PP-PS-6 and PP-PS-7. PP-PS-6 actually shows a higher q* (smaller d_0) than PP-PS-7 despite the significantly higher molar mass of the PP-PS-6 bottlebrushes. This is again consistent with the shorter backbone of PP-PS-6.

To further characterize the morphologies attained for these asymmetric diblocks, we attempted both transmission electron microscopy (TEM) and atomic force microscopy (AFM) of thin films. Unfortunately, the TEM efforts were largely unsuccessful due to difficulties in sample preparation. Since the bottlebrush polymer materials are non-entangled and are composed of PS (glassy and brittle) and aPP (soft and "gooey" when not entangled) domains, it is extremely difficult to microtome usable slices of the diblock materials for TEM imaging. AFM has therefore served as the primary imaging technique for the PP-PS samples. Figure 6.10 and Figure 6.11 display AFM images of the aPP-rich samples (PP-PS-5 and PP-PS-7), while Figure 6.12 and Figure 6.13 display images of the PS-rich samples (PP-PS-4 and PP-PS-6).
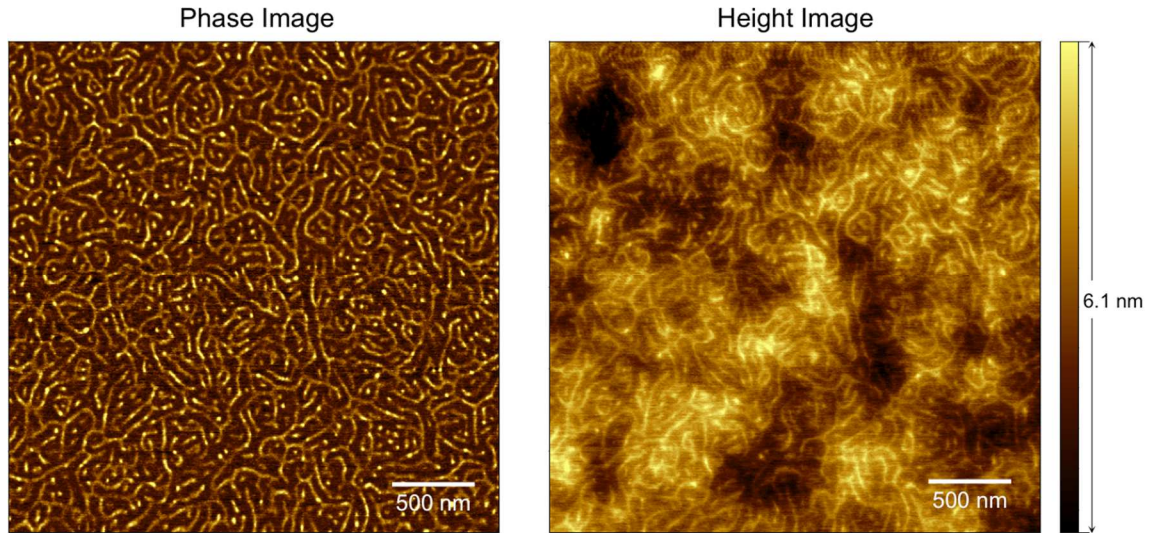
Figure 6.10. AFM images of PP-PS-5 acquired in tapping mode. The lighter phase corresponds to the PS domains in both images. Total image area is $3\mu m \times 3\mu m$.
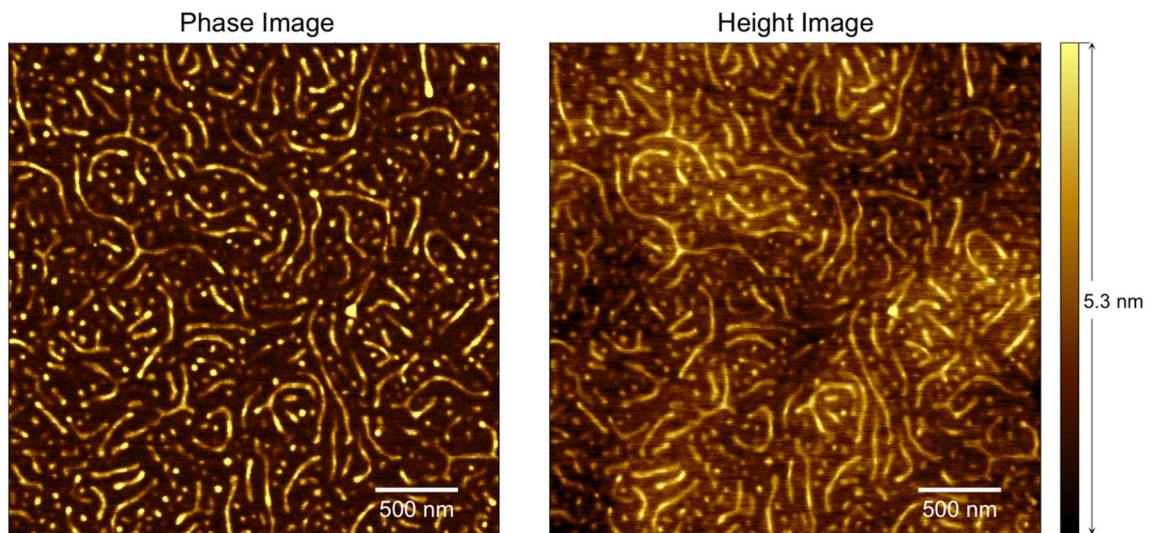
Figure 6.11. AFM images of PP-PS-7 acquired in tapping mode. The lighter phase corresponds to the PS domains in both images. Total image area is $3\mu m \times 3\mu m$.

AFM images of the aPP-rich asymmetric samples reveal wormlike cylindrical PS domains, some of which extend several microns in length. This confirms the ability of PP-PS-5 and PP-PS-7 to form cylindrical domains, however, neither image demonstrates a hexagonally packed structure. Instead the cylinders are shown to contain numerous junction points and even complete loops (Figure 6.10). The images for PP-PS-7 shown in Figure 6.11 display a very similar state as PP-PS-5, but with larger PS domains concomitant with the twofold higher molar mass of PP-PS-7. Figure 6.11 also shows a higher fraction of light "dots". These are possibly indicative of PS cylinders oriented normal to the surface, or may be small spherical domains.

The wormlike morphology observed in Figure 6.10 and Figure 6.11 is curiously reminiscent of cylindrical micelle structures commonly observed in systems of amphiphiles (such as diblock polymers) in selective solvent environments. Specific topological features such as cylinder end-caps, Y-junctions, and cylindrical loops are prevalent in the micellar systems and are known to represent entropically favorable defects.[191,192] Frequent junction points and cylinder end caps are evident in the AFM images and may derive from packing constraints of the bottlebrush polymers. Given the large cross-sectional area of individual bottlebrush molecules, the interfacial curvature associated with these defects may produce a more favorable packing scenario than oriented cylinders. It remains unclear what similarities may exist between these polymers and the micellar systems to provoke the similar morphological states, but the qualitative similarities are certainly worthy of comment.

Images for the PS-rich samples are displayed in Figure 6.12 and Figure 6.13. These images do not exhibit any of the same wormlike features and instead display circular aPP domains that may either indicate spherical domains or cylinders with exclusively perpendicular orientation. The PP-PS-4 sample shows very small aPP regions, corresponding to the smaller domain spacing associated with the SAXS profile in Figure 6.9 ($2\pi/q^* \approx 28$ nm). The aPP regions of PP-PS-6 ($2\pi/q^* \approx 48$ nm by SAXS) are more easily seen in Figure 6.13. While the thin film behavior does not necessarily coincide

with the bulk self-assembly, the images are useful in visualizing the morphologies for these molecules and the domain spacing of the microphase separated material.
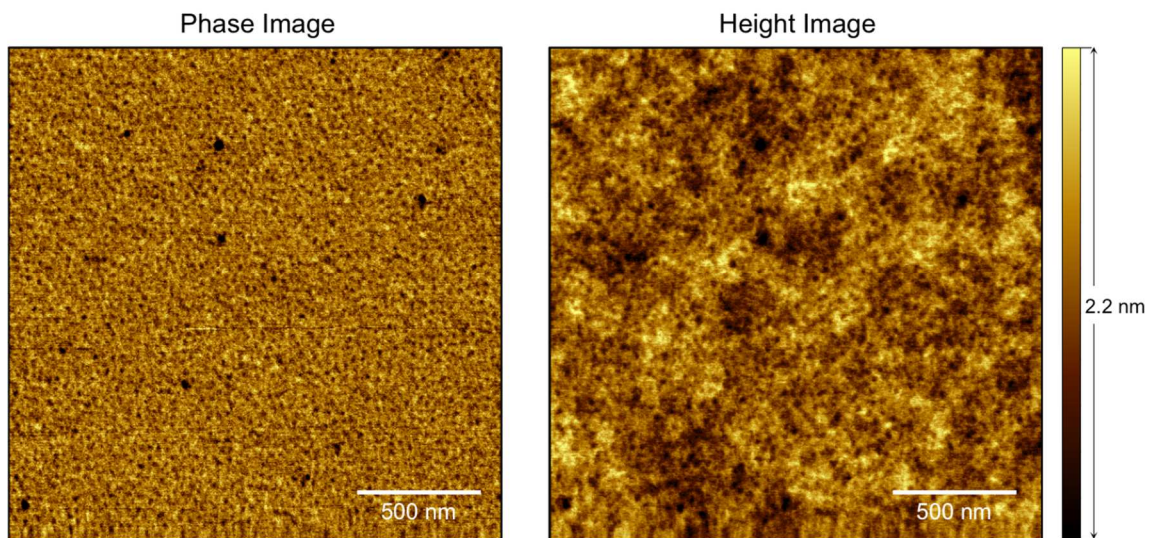
Figure 6.12. AFM images of PP-PS-4 acquired in tapping mode. The lighter phase corresponds to the PS domains in both images. Total image area is 2μm × 2μm.
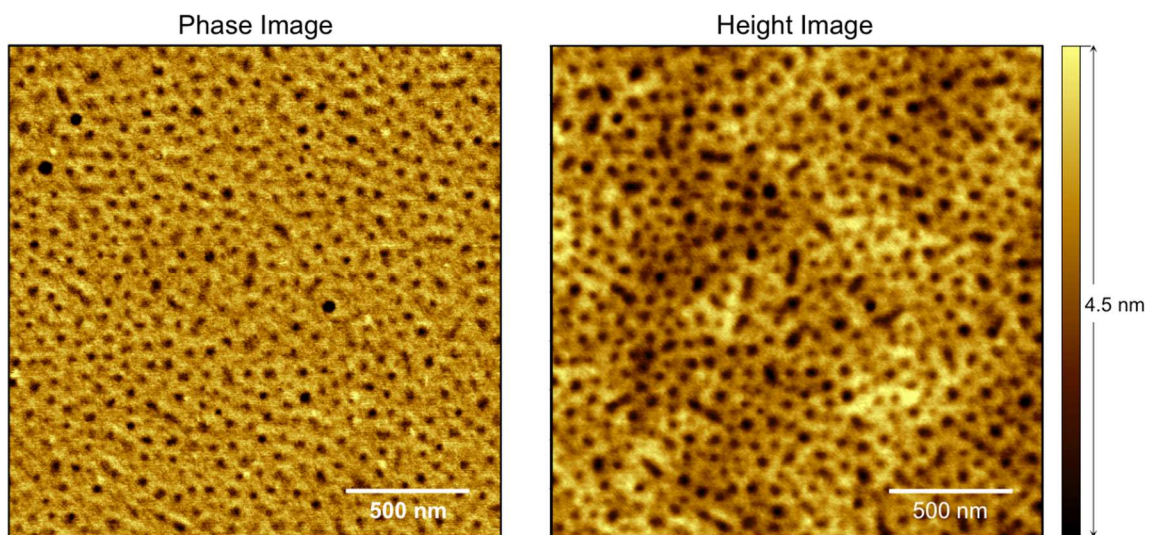
Figure 6.13. AFM images of PP-PS-6 acquired in tapping mode. The lighter phase corresponds to the PS domains in both images. Total image area is 2μm × 2μm.

6.3.2   Diblocks from aPP-NB and PS-NB(3.8k)

The diblocks made using PS-NB(4.0k) demonstrated successful ordering into lamellar (LAM) and hexagonally packed (HEX) cylindrical phases at symmetric and asymmetric volume fractions, respectively. To probe the transition between LAM and HEX morphologies with more precision, we next synthesized four sets of bottlebrush diblocks using PS-NB(3.8k) in which the volume fractions were adjusted systematically. Specifically, for each set of polymers the backbone length of one block was held constant while the other block size was steadily increased to adjust the overall composition. In the first set, the target aPP backbone length was $DP_{\text{aPP-NB}} = 20$ and the PS backbone length was adjusted to attain volume fractions of $\phi_{\text{aPP}} = 0.4$, 0.3, 0.2, and 0.1. Similarly, the PS backbone length was fixed in the other three sets, and the aPP backbone length was varied to achieve $\phi_{\text{aPP}} = 0.6$, 0.7, 0.8, and 0.9. Table 6.3 displays the molecular characterizations for all 16 diblock samples along with the targeted block lengths and compositions for each polymer.

6.3.2.1   Diblocks with consistent backbone length of the aPP block

The polymers listed in the first set of Table 6.3 (PP-PS-30 to 33) were synthesized by initiating a large batch of poly(aPP-NB) in the glove box and then splitting the reaction solution between four small reaction vials. Different amounts of PS-NB(3.8k) were then added to each vial to polymerize the second block and obtain diblocks with varied compositions. Consequently, each polymer in this set has the exact same poly(aPP-NB) block length, as shown in the SEC traces in section 6.6 (Figure 6.32), and attained volume fractions ranging from $\phi_{\text{aPP}} = 0.43$ to 0.13. Each of the polymers was prepared for SAXS by successive solvent casting and thermal annealing at 150 °C. The samples were then heated back to 150 °C on the SAXS beamline before taking measurements. The profiles for PP-PS-30, -31, -32, and -33 are presented in Figure 6.14a. The first arrow to the left represents q* for each profile. The remaining arrows represent HEX reflections, where the peaks that are also allowed by LAM ordering are shown in black. Numbers above the arrows indicate q/q* values for the most prominent reflections of each profile.

Table 6.3. Molecular characterizations for the bottlebrush diblock polymers using PS-NB(3.8k) as the macromonomer for the PS block.

Sample ID	Targeted Values $DP_{\text{PS-NB}}$ $(DP_{\text{aPP-NB}})$	ϕ_{aPP}	$M_{n,\text{ Diblock}}$ (kg/mol)[a]	$Đ$ [a]	ϕ_{aPP} [b]	$DP_{\text{aPP-NB}}$ [c]	$DP_{\text{PS-NB}}$ [c]
PP-PS-30	(20)	0.4	95.9	1.12	0.43	18	16
PP-PS-31	(20)	0.3	120	1.17	0.35	18	22
PP-PS-32	(20)	0.2	175	1.16	0.25	18	36
PP-PS-33	(20)	0.1	328	1.18	0.13	18	77
PP-PS-34	10	0.6	123	1.07	0.63	35	14
PP-PS-35	10	0.7	169	1.06	0.75	59	13
PP-PS-36	10	0.8	256	1.10	0.84	102	13
PP-PS-37	10	0.9	461	1.17	0.95	211	7.5
PP-PS-38	30	0.6	303	1.15	0.62	84	34
PP-PS-39	30	0.7	392	1.18	0.73	131	33
PP-PS-40	30	0.8	498	1.14	0.79	183	33
PP-PS-41	30	0.9	993	1.25	0.9	425	32
PP-PS-42	3	0.6	41.8	1.08	0.53	10	5.7
PP-PS-43	3	0.7	52.6	1.07	0.65	16	5.5
PP-PS-44	3	0.8	68.8	1.05	0.77	25	4.9
PP-PS-45	3	0.9	118	1.07	0.93	53	2.7

[a]Determined by SEC-MALLS in THF. [b]Volume fraction of aPP calculated based on the mass conversion of each macromonomer and the known densities of homopolymer melts (ρ_{aPP} = 0.85 g/mL and ρ_{PS} = 1.05 g/mL). [c]Number-average backbone degree of polymerization of each block using $M_{n,\text{aPP-NB}}$ = 2.05 kg/mol and $M_{n,\text{PS-NB}}$ = 3.8 kg/mol.
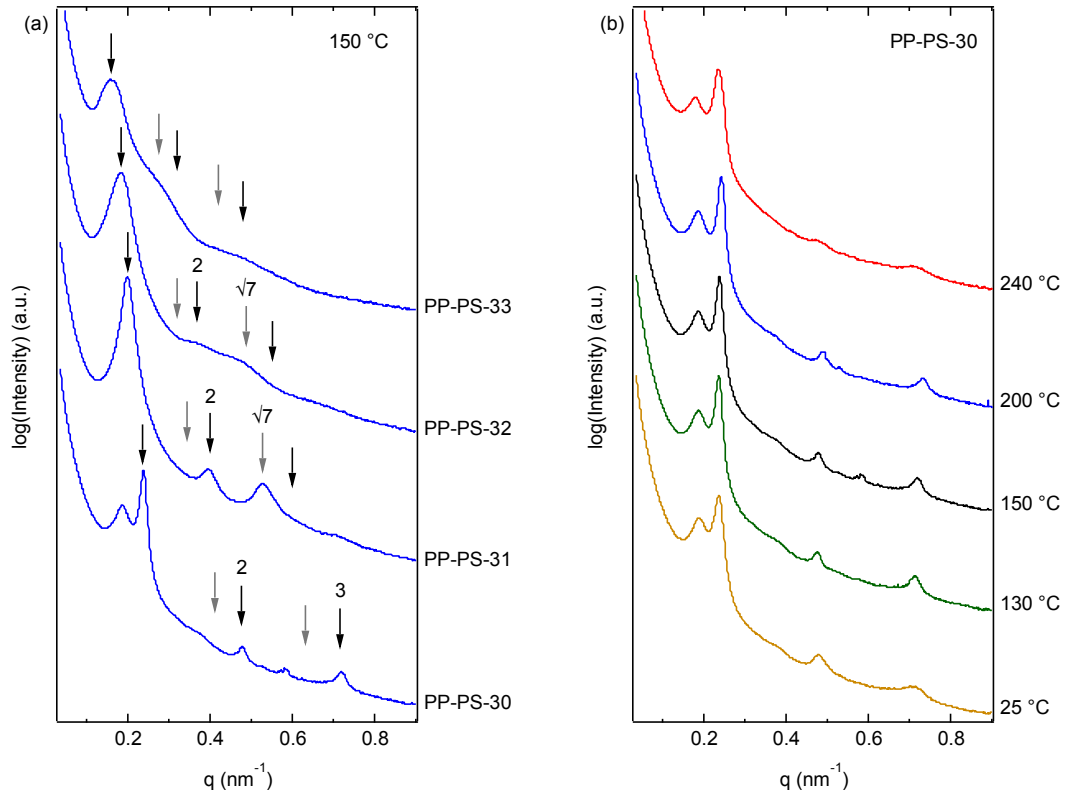
Figure 6.14. (a): SAXS profiles of PP-PS-30, PP-PS-31, PP-PS-32, and PP-PS-33 at 150 °C. The reflections allowed by HEX ordering are denoted with downward gray arrows. The integer multiples of q*, which are also allowed by LAM ordering, are designated with black arrows. Numerical q/q* values are provided for prominent peaks in each profile. (b): Temperature-dependent SAXS patterns for PP-PS-30, representing a steady temperature increase from 25 °C to 240 °C.

The continuous increase of the PS block size produces a steady shift of the primary scattering peak to lower q values from sample 30 to 33. The breadth of the primary peak also increases, demonstrating a decrease in domain spacing uniformity for the higher molar mass samples. The sharpness of the peak at q* for PP-PS-30, along with the distinct peaks at 2q* and 3q*, support the presence of LAM domains with a periodicity of $d_0 = 2\pi/q^* = 26$ nm. However, an extra peak is present in the PP-PS-30 profile at q < q*. This is a recurring feature in several of the SAXS profiles. For instance, some evidence of scattering intensity at q < q* appears for both PP-PS-3 and PP-PS-8 in Figure 6.8. We attribute this to the lack of complete sample annealing and the existence disordered

features at length scales greater than the lamellar period. For a block polymer melt to achieve its equilibrium phase, chains must rearrange to properly assemble into a state of minimal free energy. This reorganization requires polymer blocks to withdraw from one domain and migrate to another in order to balance the spacing across the bulk of the material. In a bottlebrush block polymer system, the process of chain pullout during sample annealing may incur a more substantial energetic barrier than linear polymer chains because the molecular structure requires extraction of a large number of polymer segments simultaneously. It is not clear why the low q features arise in some of the samples and not others. This may result from unintended experimental variations in the sample preparation, or from the presence of unreacted macromonomer species in the samples (though this seems unlikely based on the SEC trace of PP-PS-30). Additional annealing procedures (*e.g.,* shear alignment) may help to overcome this and to attain consistent order.

Variable temperature experiments were also carried out on PP-PS-30, and the SAXS results are shown in Figure 6.14b. The sample was steadily heated from room temperature to 240 °C and back down. The peak at $q < q^*$ shows a slight decrease in intensity relative to q^* at higher temperatures, which suggests an improvement in the ordering. There is also a low intensity peak at ~0.6 nm^{-1} in the PP-PS-30 profile at 150 °C in Figure 6.14a, but this appears to be an artifact of one particular measurement since it does not persist in the variable temperature SAXS data. Most notably, the data once again show a very consistent location of q^* over a temperature range of 200 °C. This is comparable to the variable temperature results for PP-PS-1 and PP-PS-2 (Figure 6.7).

Both PP-PS-31 and PP-PS-32 display higher order peaks at $q/q^* = 2$ and $\sqrt{7}$, where both peaks are particularly prominent in the PP-PP-31 profile. These secondary peaks then become less obvious with increased molar mass and increased asymmetry, and the PP-PS-33 profile shows a largely disordered profile. The transition observed here at ϕ_{aPP} ≈ 0.35 does not differ from the LAM/HEX transition in many linear diblock systems, which is somewhat unexpected and likely due to the conformational state of the relatively short minority block.

6.3.2.2   Diblocks with consistent backbone length of $DP_{PS-NB} = 10$

PP-PS-34 to 37 were prepared by targeting a constant $DP_{PS-NB} = 10$ and variable DP_{aPP-NB} to achieve compositions of $\phi_{aPP} = 0.6, 0.7, 0.8,$ and 0.9. Similar to the previous set, the fixed block size of ~ 40 kg/mol was the goal. The synthetic procedure was not exactly the same, because the variable aPP-NB block was first to be polymerized. Therefore, each ROMP reaction was set up independently instead of initiating one large batch. Nonetheless, a very consistent PS block length was achieved among the four samples as shown in Table 6.3. The only diblock that did not attain at least 10 PS chains was PP-PS-37, yielding an extremely asymmetric composition of $\phi_{aPP} = 0.95$. The SEC traces for each of the diblocks in this set are provided in section 6.6 (Figure 6.33). The traces for PP-PS-34, 35, and 36 show a consistent difference between the aPP block trace and diblock trace, demonstrating the equivalent size of the PS block in each case.

Figure 6.15 depicts an overlay of the SAXS profiles for samples 34 to 37 at 150 °C. As expected, the q* steadily decreases with increasing molar mass between the four samples. PP-PS-34 displays extraordinarily sharp peaks indicating a well-ordered LAM phase. PP-PS-35 also exhibits sharp peaks at q/q* = 1, 2, 4, and 5, with extinction of the q/q* = 3 peak caused by a composition near $\phi_{aPP} = 2/3$. However, this profile also displays evidence of a HEX phase with lower intensity peaks at q/q* = √3 and √7, which may demonstrate a coexistence of the two phases. To gain more information on the ordered state, these samples were subjected to variable temperature SAXS measurements. The data are presented in Figure 6.16 and Figure 6.17 along with specific peak assignments.

The SAXS data for PP-PS-34 was initially taken only at 150 °C. Given the unusual low intensity feature at ~ 0.5 nm^{-1}, the same sample was sent along on the next group trip to Argonne National Laboratories (two months later) for a second measurement at room temperature. This profile does not exhibit the same peak, and the LAM ordering was preserved as shown by the higher order reflections in Figure 6.16a. The PP-PS-35 SAXS patterns are shown in Figure 6.16b in chronological order from bottom to top. This sample was heated and cooled multiple times between 150 °C and 260 °C to assess any

changes in morphology. While the initial profile at 150 °C displays a primarily LAM phase, the HEX reflections at $q/q^* = \sqrt{3}$ and $\sqrt{7}$ became more evident as the LAM peak intensities dropped upon heating to 260 °C. The temperature was temporarily reduced to 200 °C before completing a second heating cycle. The intensities of the HEX peaks relative to LAM display a fairly reversible increase at high temperatures, as shown by the red traces of Figure 6.16b. The relative intensities of the LAM peaks then increase at cooler temperatures. Irreversible changes are also apparent in the first and final 150 °C measurements, indicating that the HEX ordering may have become more developed with the increased thermal annealing time.
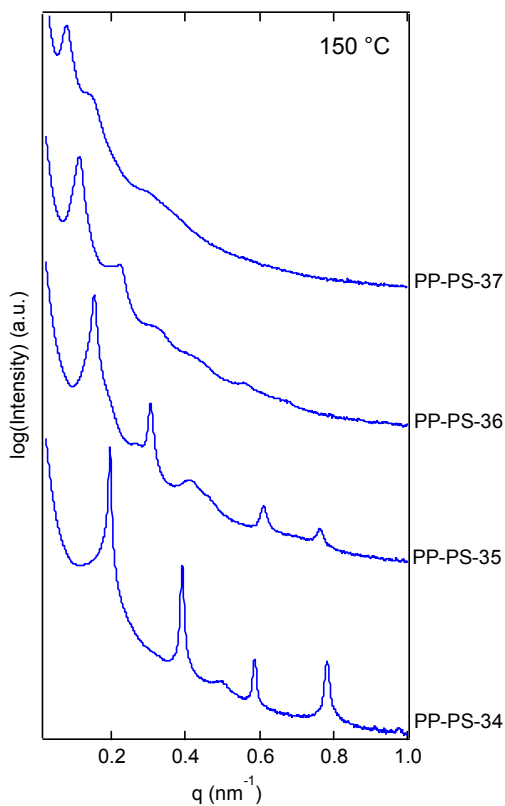
Figure 6.15. SAXS profiles of diblock samples PP-PS-34 to 37 at 150 °C. Peak assignments are given in the variable temperature SAXS data in Figure 6.16 and Figure 6.17
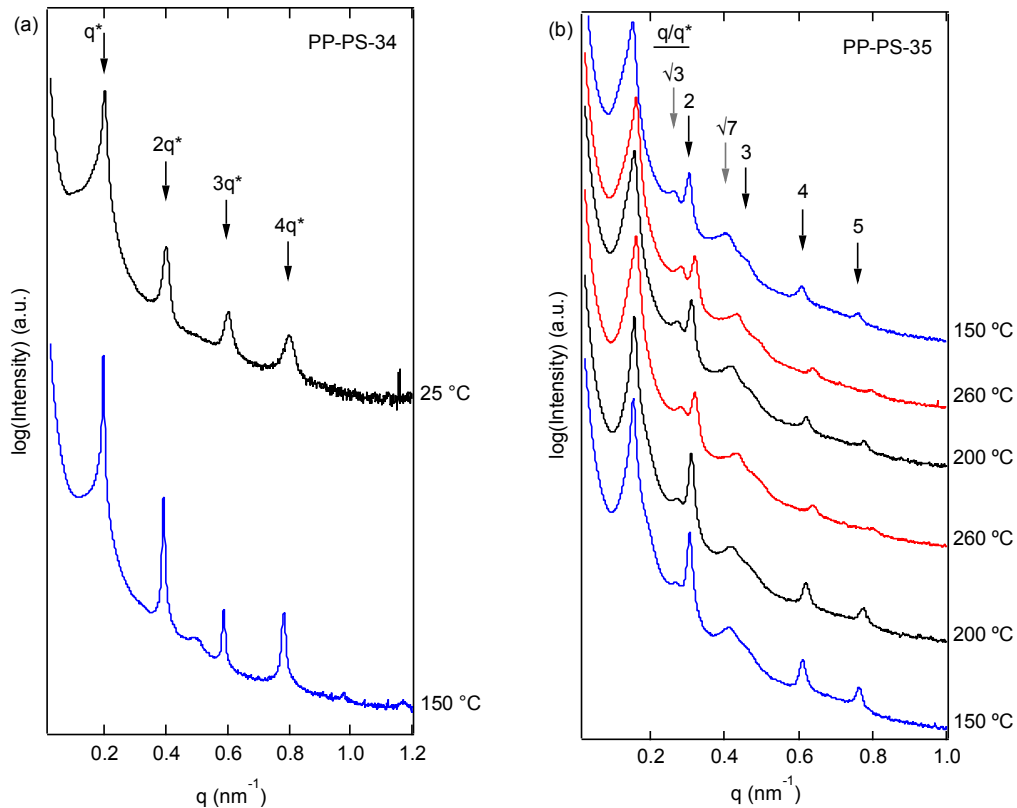
Figure 6.16. (a): SAXS profiles of PP-PS-34 at 150 °C and 25 °C. The reflections allowed by LAM ordering are denoted with downward black arrows. (b): Temperature-dependent SAXS patterns for PP-PS-35. The reflections allowed by HEX ordering are given with downward gray arrows, while those also allowed by LAM ordering are designated with black arrows. Profiles are placed with increasing time of the measurement from bottom to top, representing successive heating and cooling of the sample.

Figure 6.17 presents the SAXS patterns for PP-PS-36 and PP-PS-37. The ordering for PP-PS-36 (ϕ_{aPP} = 0.84) was initially unclear at 150 °C. However, a definitive HEX scattering pattern emerged after heating the sample slowly to 250 °C. The red trace in Figure 6.17a displays a prominent peak q/q* = $\sqrt{3}$ and higher order peaks at q/q* = 2, $\sqrt{7}$, 3, and $\sqrt{12}$. Upon cooling the sample back down to 150 °C, these peaks remained present but were not as sharp. The pattern was also changed from the initial data at 150 °C, suggesting that the initial measurements were not yet probing the equilibrium phase.

Alternatively, the data for PP-PS-37 in Figure 6.17b do not exhibit any significant temperature dependence. The SAXS profiles show similar behavior to other highly asymmetric samples (*e.g.,* PP-PS-33 or PP-PS-6), exhibiting broad secondary peaks corresponding to disordered PS domains within the aPP matrix.
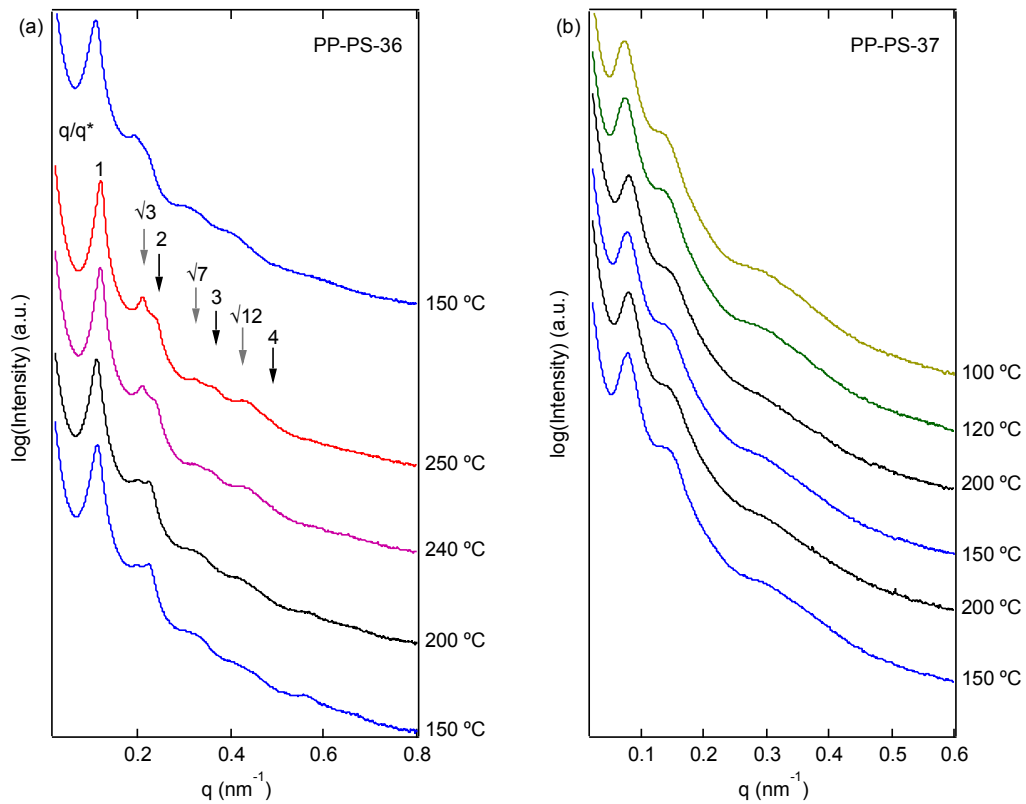
Figure 6.17. Temperature-dependent SAXS patterns, ordered with increasing time from bottom to top for each plot. (a): Profiles for PP-PS-36. The reflections allowed by HEX ordering are given with downward gray arrows, while those also allowed by LAM ordering are designated with black arrows. (b): Profiles for PP-PS-37.

The series of measurements taken for PP-PS-35 and PP-PS-36 demonstrate possible coexistence of LAM and HEX phases, where HEX may be more favored at higher temperatures (lower effective χ) and LAM may be favored at lower temperatures. Given the irreversibility of some of the features, there is uncertainty regarding the equilibrium state of the diblocks, and so it is difficult to strictly assign morphologies. However, given the strong LAM peaks out to $5q^*$ for PP-PS-35 (Figure 6.16b) at low temperature and the clear emergence of HEX peaks at high temperature, it is reasonable to infer coexisting phases in this sample.

6.3.2.3   Diblocks with consistent backbone lengths of $DP_{PS-NB} = 3$ and 30

The final two sets of diblock polymer samples aimed to replicate the previous set by maintaining a constant PS block size, but with a threefold larger ($DP_{PS-NB} = 30$) and smaller ($DP_{PS-NB} = 3$) PS block. Each of the samples were synthesized by sequential addition of aPP-NB and PS-NB(3.8k) to a **G3** catalyst solution, and the SEC results are shown in section 6.6.

Samples 38 – 41 represent some of the largest polymer molecules in this study. Since the target molar mass of the PS minority block was set to 114 kg/mol (*i.e.*, 30 × 3.8 kg/mol) the total diblock molar masses were very high, particularly for PP-PS-41 which aimed for a composition of $\phi_{aPP} = 0.9$. The SEC trace for PP-PS-41 displayed essentially no shift in the peak elution time before and after PS-NB addition. According to SEC-MALLS analysis, the molar mass of PP-PS-41 was increased by the desired amount following PS-NB addition, but the increased breadth of the final SEC trace and the unchanged peak location insinuate an ill-defined diblock sample compared to the other diblocks. In contrast, samples 42–45 were synthesized to very low molar mass. Only modest shifts appear in the SEC traces before and after PS-NB addition because only three PS branches were added to each backbone on average.

Figure 6.18 presents the SAXS profiles for both sets of diblock samples. Samples 38–40 are represented in Figure 6.18a. The profile for PP-PS-41 was omitted from this plot since it did not show any scattering features. This confirms the poorly defined molecular

structure of PP-PS-41 anticipated from the SEC results. The profiles for PP-PS-38 and 39 reveal well-ordered LAM phases with secondary peaks extending out to q = 6q* and 7q*, respectively. The results for PP-PS-39 demonstrate extinction of the 3q* and 6q* peaks indicating a composition near ϕ_{aPP} = 2/3. This polymer also shows some scattering at q < q*, as was observed in earlier samples. The high molar mass PP-PS-40 sample displays an obvious q* peak but does not include conclusive higher order reflections for morphology assignment.
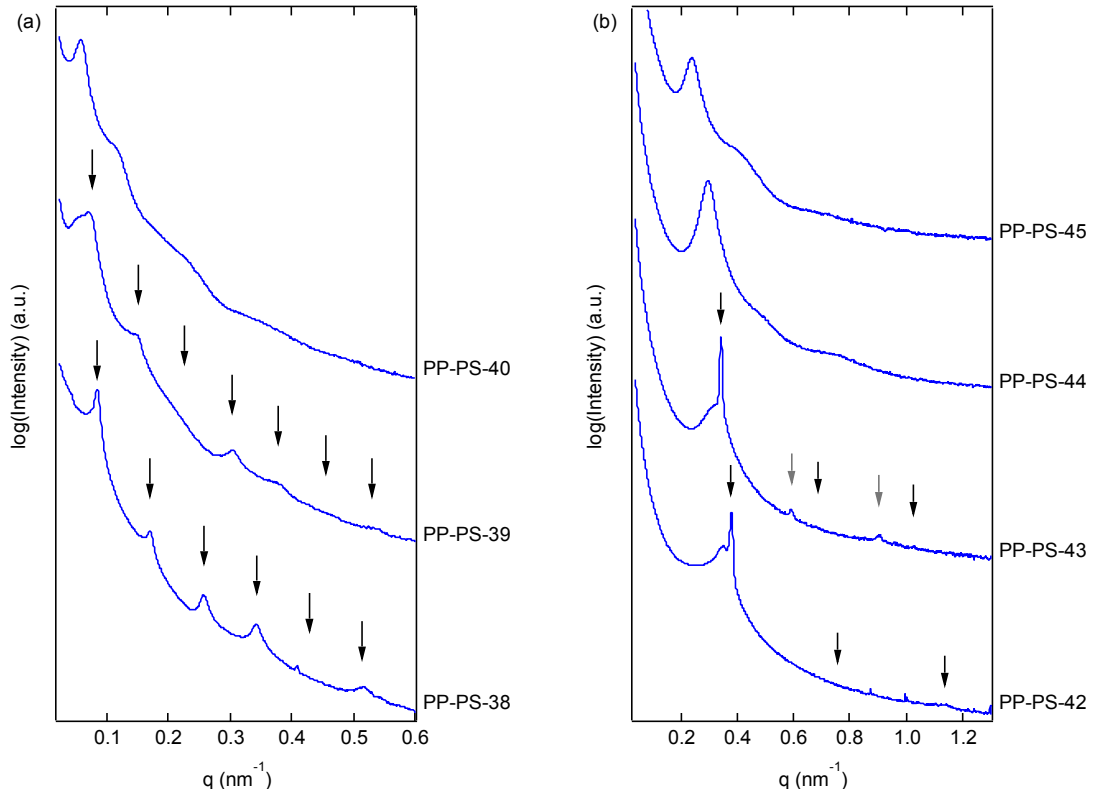
Figure 6.18. (a): SAXS profiles of high molar mass diblocks with target DP_{PS-NB} = 30. The reflections allowed by LAM ordering are denoted with downward black arrows. PP-PS-41 did not display any scattering pattern and was omitted from the plot. (b): SAXS profiles of low molar mass diblocks with target DP_{PS-NB} = 3. The reflections allowed by HEX ordering are given with downward gray arrows, while those also allowed by LAM ordering are designated with black arrows.

Samples 42 – 45 are among the smallest diblocks synthesized (note the higher q-vector scale in Figure 6.18b). Samples 42 and 43 display extraordinarily sharp primary peaks corresponding to $d_0 = 2\pi/q^* = 16.6$ and 18.4 nm, respectively. Despite the sharp primary peaks, only subtle secondary peaks arise. PP-PS-43 exhibits a HEX profile in which two higher peaks emerge at $q/q^* = \sqrt{3}$ and $\sqrt{7}$. Additionally, there is again a degree of scattering intensity at $q < q^*$ for both samples 42 and 43. As expected, PP-PS-44 and 45 exhibit primary peaks that shift left with increased molar mass. However, both samples reveal mostly disordered phases. An interesting result in comparing the two data sets in Figure 6.18 is that the LAM phase remains prevalent at more highly asymmetric compositions for the large diblock molecules. For example, PP-PS-39 ($\phi_{aPP} = 0.73$, $M_n = $ 392 kg/mol) displays LAM ordering, whereas PP-PS-43 ($\phi_{aPP} = 0.65$, $M_n = 52.6$ kg/mol) displays evidence of HEX packing. This suggests that polymers with the more cylindrical, high DP minority blocks are unable to pack favorably into cylindrical domains.

6.4   Phase Diagrams

6.4.1   Traditional Phase Diagram Using Experimental Results

SAXS analysis of the bottlebrush diblock polymers in this work revealed successful self-assembly into both LAM and HEX phases. Moreover, the HEX phase was identified in both aPP-rich and PS-rich samples, demonstrating that a large side chain length asymmetry is not critical for achieving non-LAM morphologies. (Although, unmatched side chain lengths likely provide a more stable packing scenario and a wider HEX phase envelope.) One of the goals of this study was to construct a phase diagram based on experimental results. To this end, we have created a preliminary phase map using the morphology assignments from SAXS results, χN values estimated from the literature, and ϕ values from molecular characterizations.

Figure 6.19 displays a phase map as χN versus ϕ_{aPP} and contains data points from the majority of diblock samples presented in section 6.3. The numbers placed next to each

data point represent the corresponding sample number. Markers in the plot signify four different phase states: LAM, HEX, LAM + HEX (referring to phase coexistence), and DIS (disordered). We estimated the segregation strength for this system using $\chi N = X(M_n/\rho RT)$ where $X = 1655/T(K) + 0.57$, which was determined for a linear PS-*b*-PEP system[193] with $v_{ref} = 118$ Å^3. Since this relationship only serves as a rough estimate for our diblocks, and because the temperature dependence is potentially substantially different for the bottlebrush diblock case, χN calculated at 150 °C was used for all samples.
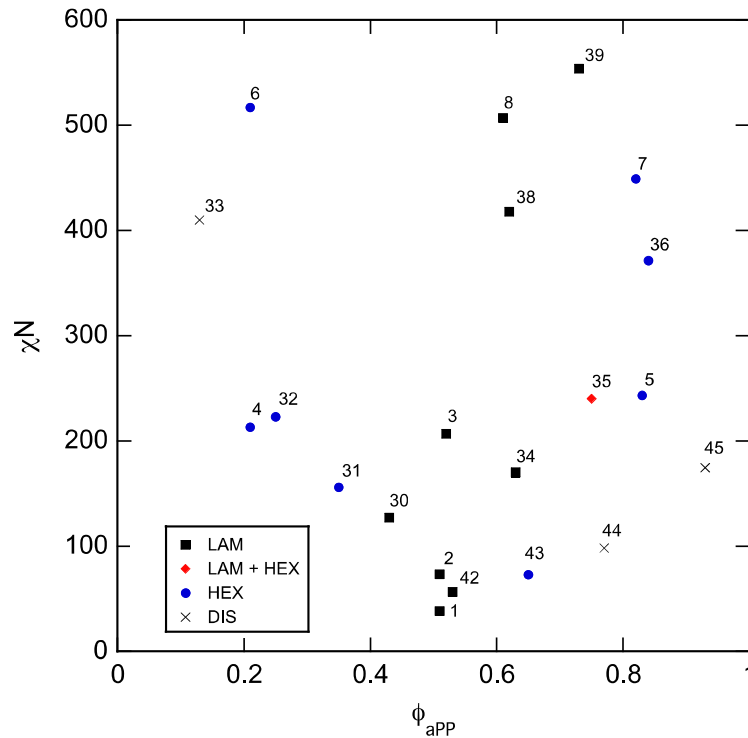
Figure 6.19. Phase map of PP-PS bottlebrush diblock polymers. Melt-state morphologies were characterized by SAXS analysis. Numbers adjacent to the data points represent sample numbers defined in Table 6.2 and Table 6.3. Values of χN were calculated using a literature relationship for linear PS-*b*-PEP system at 150 °C.

The overall form of the phase diagram in Figure 6.19 is not particularly different from that of a linear diblock polymer melt, given that LAM ordering is observed in the symmetric samples and a transition to HEX begins at $\phi_{aPP} \leq 0.35$ and $\phi_{aPP} \geq 0.65$ (for PP-PS-31 and PP-PS-43, respectively). One exceptional characteristic is the large magnitude of the χN values estimated for these samples. This derives from the ultrahigh molar mass of the bottlebrush polymers and is in accord with the immeasurably high T_{ODT} values of all samples, apart from PP-PS-1. The most asymmetric polymers presented in Figure 6.19 exhibit states of disorder, illustrating the difficulty of bottlebrush diblock molecules with highly asymmetric branch numbers to form any type of ordered spherical phases. A significant issue with this phase map, however, is that the geometrical packing constraints of bottlebrush molecules that hamper assembly into spherical phases cannot be explicitly represented. The structural aspects of bottlebrush polymers with different branch and backbone dimensions should be considered when interpreting the phase behavior of bottlebrush polymers, and ideas of how to depict these features are discussed in the following section.

6.4.2   Consideration of Molecular Parameters

Traditionally, the phase diagrams of linear diblock polymers are presented as χN versus ϕ, like the data plotted in Figure 6.19. These parameters represent two independent variables that provide a comprehensive description of linear diblock polymer molecules in terms of the equilibrium phase behavior. If we assume χ to be a constant between the two species (neglecting dependence on temperature, molar mass, or composition) these two parameters could be broken down into two purely structural independent parameters, N_A and N_B, representing the total size of each block normalized by common reference volume. Defining these two parameters is equivalent to defining the N and ϕ for the system as shown here,

$$N = N_A + N_A \tag{6.1}$$

$$\phi_A = \frac{N_A}{N_A + N_A} \tag{6.2}$$

Alternatively, the branched architecture of bottlebrush polymers introduces added structural parameters that contribute to the self-assembly. If we first consider a bottlebrush diblock polymer with equivalent side chain length on each block, it may seem satisfactory to represent the self-assembly phase space as χN versus ϕ since this molecule could be envisioned as a fat linear diblock. However, this representation would not be capable of distinguishing between molecules with different sized branches. For instance, the top two graphics in Figure 6.20 represent molecules with the same total molar mass and the same ϕ. Each diblock would therefore be represented by the same point on a phase diagram without any distinction. This brings up a third dimension in phase space introduced by the bottlebrush architecture: the aspect ratio of backbone length to side chain length. One could imagine that creating a 3-D phase diagram with this aspect ratio on a third axis would distinguish between these two molecules described above, but this would still not account for any asymmetry in side chain lengths between the two blocks. The third structure in Figure 6.20 also has the same total N and ϕ as the other two molecules, but again represents an entirely different diblock polymer. A fourth dimension in phase space would thus be required to account for this branch asymmetry. Note: a similar argument for this last effect could be made for linear diblocks with considerable disparity in the statistical segment length of each block. However, adjustment of this conformational asymmetry in linear diblocks requires a simultaneous adjustment of the system chemistry, which in turn changes the Flory-Huggins χ parameter. Adjustment of the architectural asymmetry of bottlebrush diblocks presents a much more tunable parameter without changes to the chemistry.

Based on this discussion, the phase maps of bottlebrush block polymers require at least two additional variables beyond χN and ϕ, which account for the backbone-to-branch length aspect ratio and the side chain asymmetry. Phase diagrams for bottlebrush

block polymers could potentially be mapped in the same fashion as is conventional for linear block polymers (*i.e.*, on 2-D axes) with two of the above parameters held constant. However, this is not an experimentally straightforward task. For example, the series of bottlebrush samples described in section 6.3.2 were created by adjusting only the backbone length of one block. This is a simple variation, but it produces changes to three of the four parameters. Therefore, we propose a slightly different representation.
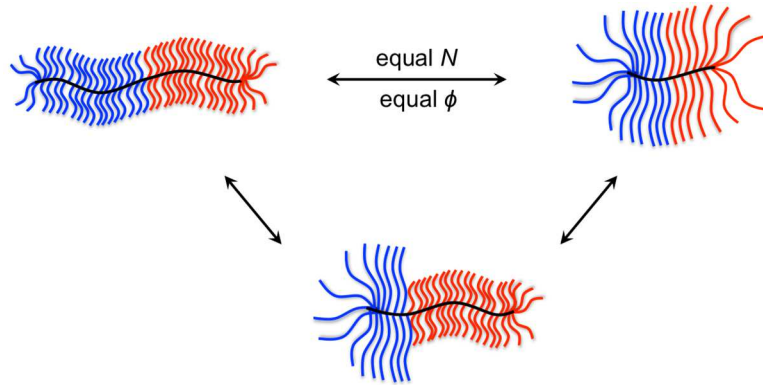
Figure 6.20. Graphic representation of bottlebrush diblock polymers with equivalent total N and ϕ, but differing side chain and backbone dimensions.

Just as with the linear diblocks, the four variables described above can be broken into four purely structural independent parameters: block A backbone length ($N_{A,bb}$), block A side chain length ($N_{A,sc}$), block B backbone length ($N_{B,bb}$), and block B side chain length ($N_{B,sc}$). These structural parameters entirely define the previous four variables:

$$N = N_{A,sc}\left(N_{A,bb}\right) + N_{B,sc}\left(N_{B,bb}\right) \tag{6.3}$$

$$\phi_A = \frac{N_{A,sc}\left(N_{A,bb}\right)}{N_{A,sc}\left(N_{A,bb}\right) + N_{B,sc}\left(N_{B,bb}\right)} \tag{6.4}$$

$$Aspect\ Ratio = \frac{N_{A,bb} + N_{B,bb}}{N_{A,sc}} \tag{6.5}$$

$$Side\ Chain\ Asymmetry = \frac{N_{B,sc}}{N_{A,sc}} \tag{6.6}$$

To employ these relationships, the A block could be defined as the block with the smaller side chains to avoid introducing two separate aspect ratio parameters for each block and to ensure that side chain asymmetry ≥ 1. Implementation of these four parameters enables a complete phase map to be represented as $N_{A,bb}$ versus $N_{B,bb}$ for any set of bottlebrush molecules created with the same two macromonomers (constant $N_{A,sc}$ and $N_{B,sc}$). This method likely provides the best way to map our data and provides a better way to visualize the effects of molecular conformation changes between blocks with short and long backbones.

One of the key results of our self-assembly data is that the high molar mass diblocks maintain a lamellar morphology over a wider range of ϕ_{aPP} than the smallest samples. A logical explanation for this is the difference in packing associated with the star-like conformation of bottlebrush blocks with short backbones compared to the cylindrical conformations of long bottlebrush blocks. Since the extended conformations of long bottlebrush molecules is believed to cause resistance to interfacial curvature, the short star-like blocks should be much more likely to adopt non-LAM phases. Correspondingly, it is possible that LAM would be exclusively favored when both blocks have relatively high backbone length, regardless of ϕ. Figure 6.21 displays a hypothesized phase diagram plotted as $N_{B,bb}$ versus $N_{A,bb}$ and assuming equivalent side chain sizes for block A and block B. This diagram suggests that non-LAM phases could only be thermodynamically favorable when the minority block is relatively short and conformationally star-like, and when there is sufficient compositional asymmetry. The limiting values of $\phi_A = 0.35$ and 0.65, as well as the conformational transition point of $N_{bb} = 30$, are arbitrary and used to illustrate the general form of the phase diagram. The locations of these points are expected to change with variations in $N_{A,sc}$ and $N_{B,sc}$ values.

An alternative representation of this plot could also utilize the total segments in each block by plotting $N_{A,bb}(N_{A,sc})$ vs. $N_{B,bb}(N_{B,sc})$. This would not change the phase maps of sample sets with fixed side chain dimensions. Instead, it would simply normalize each axis by the corresponding side chain length. However, it may provide a more universal representation to compare systems with different side chain lengths on a single plot.
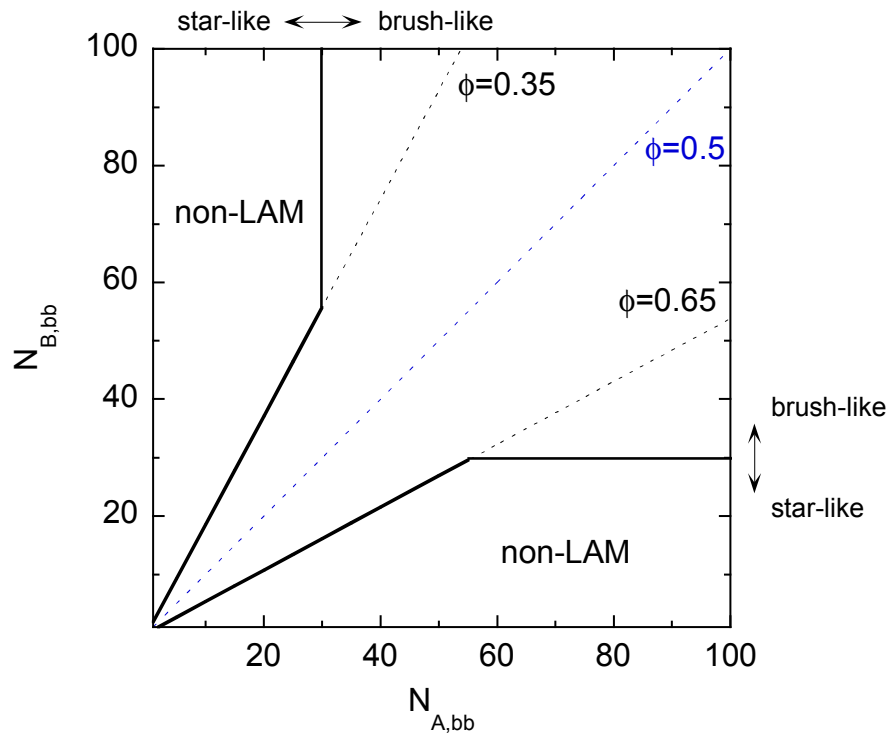
Figure 6.21. Proposed phase map for bottlebrush diblock polymers with equivalent side chain dimensions, $N_{A,sc} = N_{B,sc}$. Units for the backbone lengths, $N_{A,bb}$ and $N_{A,bb}$, and values for the constant ϕ limits (dotted lines) are arbitrary. Transitions from star-like to brush-like represent the qualitative conformation of the minority block.

To evaluate the proposed phase diagram in Figure 6.21, we re-plotted the experimental data as DP_{PS-NB} versus DP_{aPP-NB} and the results are shown in Figure 6.22. Indeed, the plot displays the anticipated trend in which the HEX phases are only accessed in samples with relatively short backbones of the minority block. Specifically, the data at

high DP_{aPP-NB} loosely indicate a plateau of LAM/HEX transition line. However, more data points near the phase transition are required to conclusively evaluate whether the hypothesized phase map is accurate. Further preparation of bottlebrush diblock samples with block sizes near the anticipated transition points would provide a more comprehensive experimental phase diagram.
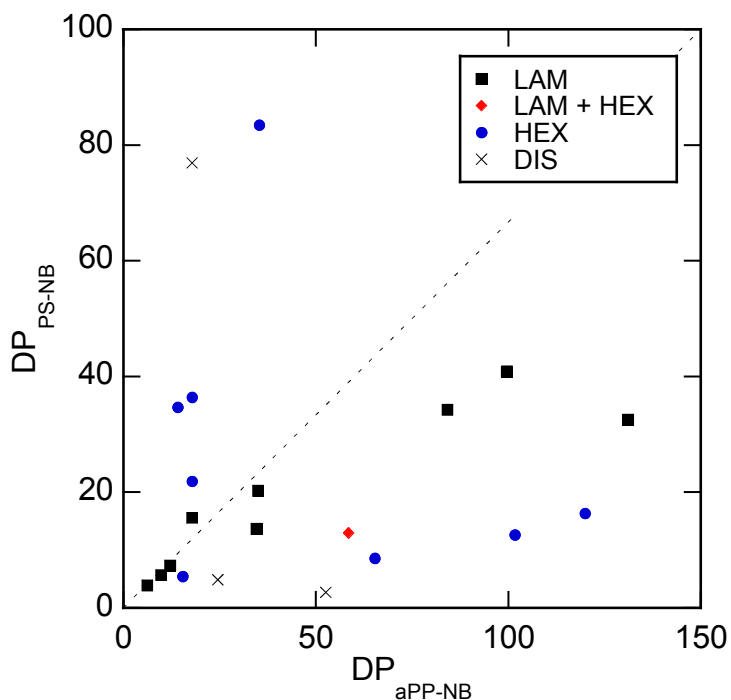
Figure 6.22. Experimental phase map of PP-PS bottlebrush diblock polymers plotted as DP_{PS-NB} vs. DP_{aPP-NB}. The same experimental samples used in Figure 6.19 are plotted here, using the representation proposed in Figure 6.21. The dotted line indicates $\phi_{aPP} = 0.5$, based on the following values: $M_{n,aPP-NB} = 2.05$ kg/mol, $M_{n,PS-NB} = 3.8$ kg/mol, $\rho_{aPP} = 0.85$ g/mL, $\rho_{PS} = 1.05$ g/mL.

Finally, it is worth mentioning that, in addition to the structural parameters already mentioned, the absolute backbone grafting density is a tunable molecular parameter that drastically affects the self-assembly behavior of bottlebrush block polymers. This should be represented as a fifth independent parameter, though it was not adjusted at all in this work. In fact, it is not a parameter that is systematically adjusted in many investigations

of bottlebrush self-assembly. All of the molecules made in this work have a grafting density of 0.2 branches per backbone bond, since all of the bottlebrush polymers were synthesized by ROMP of norbornene-functionalized macromonomers. However, many bottlebrush polymers made using grafting-from techniques, as well as samples made with grafting-through of vinyl monomers, achieve graft densities of 0.5 branches per backbone bond. This parameter needs to be considered when assessing the phase behavior, especially when comparing result from two different bottlebrush systems.

6.5   Conclusions

Several sets of bottlebrush block polymers were synthesized with aPP and PS branches of similar chain lengths to study the melt state self-assembly. The PS-NB macromonomers were prepared using two different synthetic methods, both of which proved successful in producing functional PS-NB species. The bottlebrush samples were synthesized by ROMP with catalyst **G3** *via* sequential addition of aPP-NB, followed by PS-NB. The order of addition turned out to be significant because of a preference of macromonomers to propagate from a poly(aPP-NB) backbone chain end rather than a poly(PS-NB) chain end.

Diblock samples were made to various molar masses and compositions to explore the accessible morphologies. While the most symmetric samples assembled into a LAM phase, several samples with asymmetric volume fractions successfully formed a HEX morphology. This is unlike examples in the literature, which describe persistent molecules that are unable to access non-LAM phases. This discrepancy may be due in part to the moderate grafting density of our polymers (0.2 branches per backbone bond) compared to the aforementioned studies (with 0.5 branches per backbone bond).[77] Additionally, the bottlebrush polymers with higher overall molar mass and longer backbone chains displayed a higher preference towards LAM ordering than the smaller diblocks. This demonstrates the effects of different molecular conformations (brush-like vs. star-like) on the self-assembly behavior.

Finally, we present a preliminary phase diagram of the experimental data and discuss its significant characteristics. We propose a framework for analyzing the bottlebrush block polymer phase behavior, emphasizing how specific aspects of the molecular structure that are not present in linear block polymers may strongly dictate the equilibrium state of the block polymers in the melt. While the many structural parameters present in bottlebrush block polymers can expand our ability to control the size and morphology of the self-assembled nanostructures, it also complicates the interpretation of empirical phase behavior data. Ultimately, a comprehensive understanding of these systems requires knowledge on a fundamental level. To this end, the lamellar forming bottlebrush block polymer samples are examined further in chapter 7 and compared with a new theoretical model developed in collaboration with Professor Mark Matsen.

6.6   Experimental Section

6.6.1   Molecular Characterization

Nuclear magnetic resonance (^{1}H NMR) measurements were taken on a Bruker Avance III 500 MHz spectrometer. Molecular characterization of bottlebrush polymers was primarily conducted using size exclusion chromatography with multi-angle laser light scattering detection (SEC-MALLS). Samples were analyzed at 25 °C in a THF mobile phase at 1.0 mL/min using an Agilent 1260 Infinity LC system equipped with three Waters Styragel columns in series, a Wyatt OPTILAB T-rEX refractive index (RI) detector, and a Wyatt DAWN Heleos II 18-angle laser light scattering detector. The aPP-block of each diblock was characterized by SEC-MALLS analysis of an aliquot removed from the polymerization and terminated immediately before adding the PS-NB macromonomer to the reaction flask. The absolute molar mass and volume fraction of the final diblock polymers were then determined using dn/dc values measured with the SEC instrument assuming 100% mass elution. This value was usually very close to the estimate calculated with a mass average of the pure component values (dn/dc_{aPP} = 0.079

mL/g and dn/dc_{PS} = 0.185) using $dn/dc = [w_{aPP} \times dn/dc_{aPP}] + [w_{PS} \times dn/dc_{PS}]$ where w_{aPP} and w_{aPP} are the feed weight fractions of each component.

6.6.2   SAXS Analysis and Sample Preparation

SAXS experiments were conducted at the Advanced Photon Source at Argonne National Laboratory on the DND-CAT beamline (Sector 5-ID-D). Two-dimensional SAXS patterns were acquired with a Rayonix area CCD detector using a sample-to-detector distance of 8.5 m. Patterns were azimuthally integrated to give one-dimensional plots of intensity versus q. X-rays of wavelength $\lambda = 0.729$ Å were used for all samples except for PP-PS-9, which used X-rays of $\lambda = 1.24$ Å to measure a lower q-range. Exposure times of either 1 or 2 s were used for all measurements. Samples were initially prepared by solvent casting. About 75 mg of each sample was dissolved in THF in 5 mL PTFE beakers, and the solvent was allowed to slowly evaporate over several days. To maintain a slow evaporation rate, the beakers were kept in a loosely covered Pyrex dish with ~1 cm of THF coating the bottom. The films were then dried under vacuum, loaded into aluminum DSC pans, hermetically sealed in a glove box under a nitrogen atmosphere, and thermally annealed at 150 °C for 4 h. High-temperature SAXS measurements were performed by heating samples back to 150 °C on the beamline using a Linkam hot stage equipped with liquid nitrogen cooling and equilibrating for 3-5 min before taking measurements. Variable-temperature SAXS measurements were carried out for several samples. Fast heating rates were used between temperatures (>100 °C/min), and the samples were held at each temperature for 2-5 min to equilibrate before taking measurements.

6.6.3   AFM Imaging

AFM experiments were carried out on a Bruker Nanoscope V Multimode 8 scanning probe microscopy instrument equipped with PeakForce QNM® (instrument SPM-2) in Shepherd Hall of the University of Minnesota Characterization Facility (CharFac). Images shown in Figure 6.10, Figure 6.11, Figure 6.12, and Figure 6.13 were acquired with tapping mode AFM. Thin films of the polymer samples were prepared by spin

coating onto silicon wafers from a 2 wt% toluene solution at 3000 rpm. The resulting films were either imaged as-cast or after a short time (15 min maximum) of solvent vapor annealing to achieve the best ordering. Longer annealing was generally required for higher molar mass samples. Sample thicknesses were measured using a VASE® spectroscopic ellipsometer, also located in Shepherd Hall of the CharFac, and were typically ~80 nm when spin cast from toluene.

6.6.4   Diblock Polymer Synthesis

Diblock bottlebrush polymers were synthesized by sequential addition of aPP-NB and PS-NB macromonomers to a living ROMP initiated with **G3** catalyst (Figure 6.6). The same aPP-NB macromonomer batch was used for all diblock polymers. Alternatively, three different PS-NB macromonomer batches were prepared using either anionic polymerization or RAFT polymerization. Synthetic procedures for both PS-NB batches are detailed below.

6.6.4.1   Synthesis of PS-NB(4.0k)

ω-hydroxyl polystyrene (PS-OH; M_n = 3.8 kg/mol by ^{1}H NMR) was initially synthesized by Morgan Schulze using anionic polymerization of styrene and purified by freeze-drying from a benzene solution. The PS-OH was then functionalized as follows. A flame-dried round-bottom flask was charged with *exo*-5-norbornenecarboxylic acid (460 mg, 3.3 mmol) and consecutive vacuum/argon cycles were carried out to remove air from the headspace. The solid *exo*-5-norbornenecarboxylic acid was dissolved with degassed toluene (5 mL), and oxalyl chloride was slowly injected with constant stirring. A bubbler attached to the argon line in the back of the hood was used to relieve excess pressure in the system. The reaction was stirred at room temperature for 30 min and then at 70 °C for 2 h. The mixture was then cooled to 0 °C using an ice bath. In a separate flask, a solution of PS-OH (2.46 g, 0.65 mmol), triethylamine (0.5 mL, 3.6 mmol), and toluene (20 mL) were degassed *via* freeze-pump-thaw cycles. This solution was cannulated into the reaction flask at 0 °C. After about 5 min, the reaction flask was allowed to heat to room

temperature and stirred for 18 h. Finally, the solution was opened to air, filtered twice to remove salts, and precipitated into methanol (400 mL).
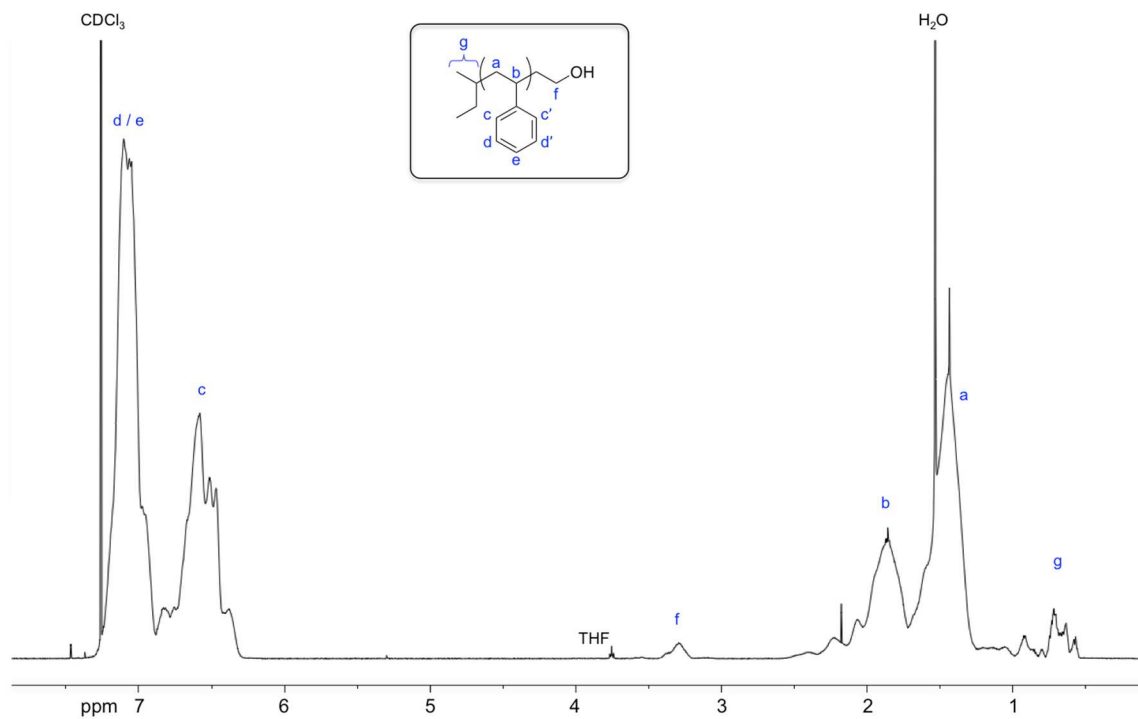
Figure 6.23. ^{1}H NMR of PS-OH (M_n = 3.8 kg/mol) synthesized by anionic polymerization of styrene and end-capped with one unit of ethylene oxide.
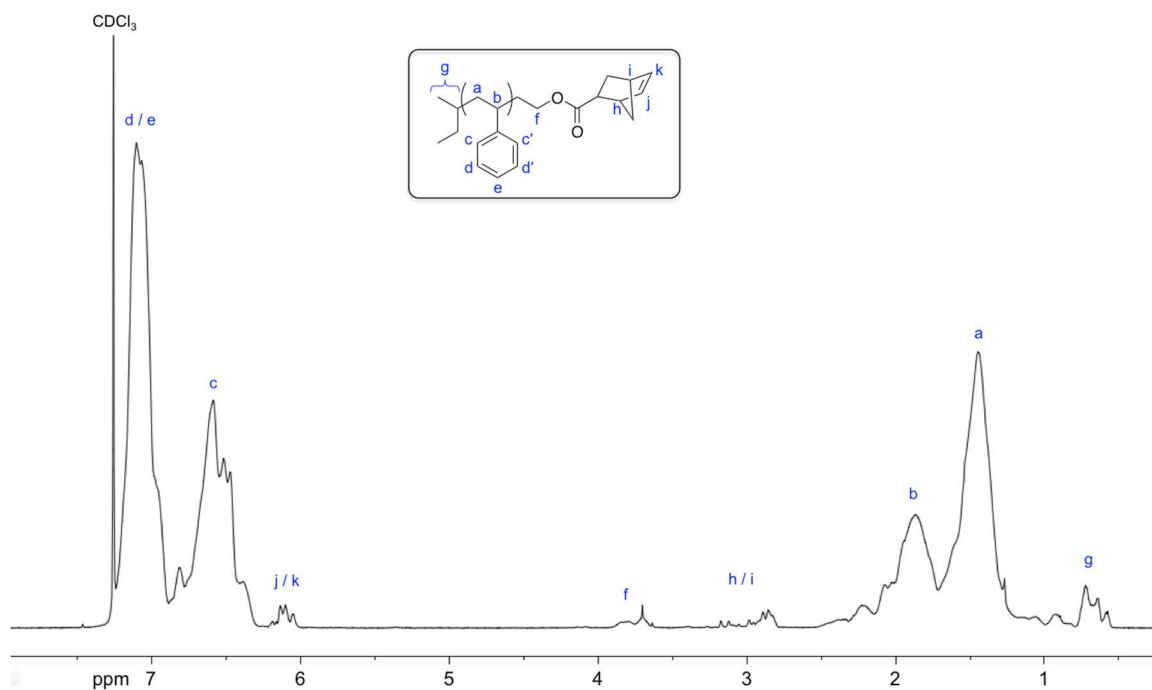
Figure 6.24. ^{1}H NMR of PS-NB(4.0k) (CDCl$_3$, 500 MHz).

6.6.4.2   Synthesis of norbornene-functionalized RAFT agent.[121,194,195]

S-Dodecyl-S′-(α,α′-dimethyl-α″-acetic acid)trithiocarbonate (**TTC-acid**; 1.30 g, 3.57 mmol) was loaded into a flame-dried 25 mL Schlenk flask and sealed with a rubber septum. Air was removed from the flask using consecutive vacuum-argon cycles and left under positive argon pressure. Oxalyl chloride (3.25 mL, 37.9 mmol) was injected with rapid stirring. The flask was connected to a bubbler and argon was allowed to flow through the flask headspace. After a few minutes, the **TTC-acid** became completely dissolved and the argon flow was ceased. Reaction progress was then monitored by evolution of gaseous byproducts (CO$_2$, CO, and HCl) from the bubbler. After stirring for 3 h, excess oxalyl choride was removed in vacuo. Once the resulting acyl chloride product was dried, the flask was recharged with positive argon pressure and exo-5-norbornene-2-methanol (0.43 mL, 3.57 mmol) was added *via* syringe while stirring. The solution quickly began bubbling with HCl(g) generation. After 1 h the bubbler was removed and the solution was allowed to stir under an argon atmosphere overnight. After

14 h, the flask was opened to air. Isopropanol (2 mL) was added and stirred for 2.5 h before removing under reduced pressure, yielding a dark yellow oil as the crude product. This product was purified by elution through a silica column (30 mm diameter column loaded with ~30 g silica gel) using a 50/50 hexanes/dichloromethane (v/v) mixture and collecting 5 mL fractions. The pure **TTC-NB** product was eluted in fractions 8-15 as confirmed by ^{1}H NMR (Figure 6.26) and collected by rotary evaporation. Yield: 1.23 g.
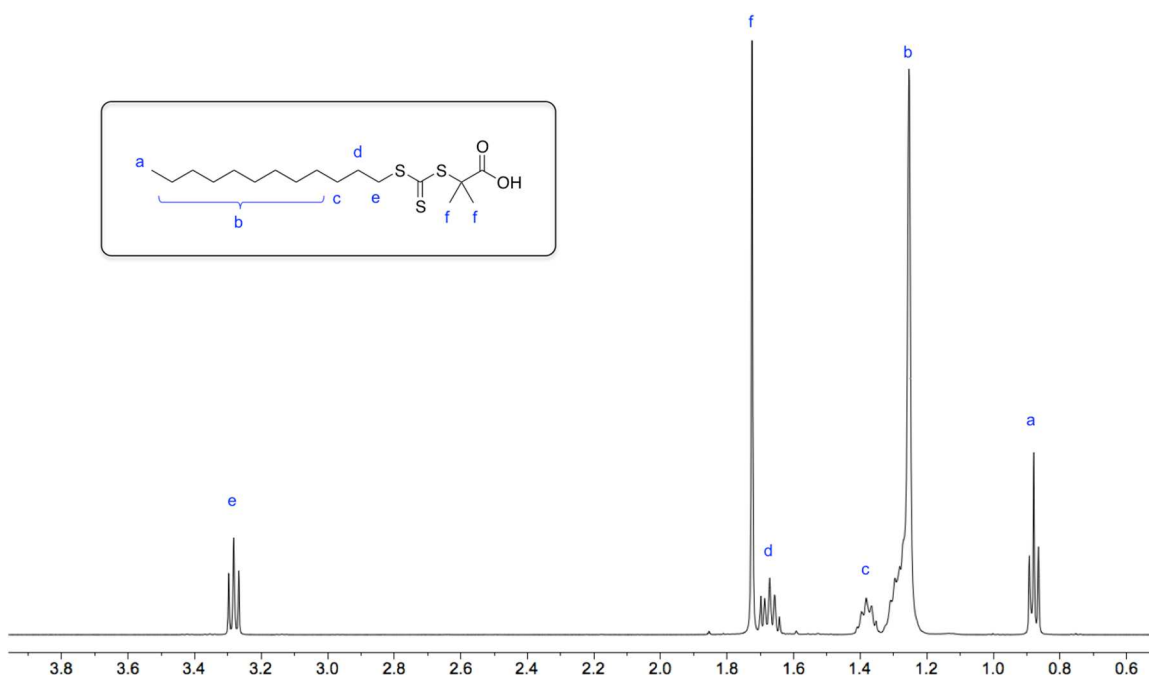
Figure 6.25. ^{1}H NMR of *S*-Dodecyl-*S′*-(α,α′-dimethyl-α″-acetic acid)trithiocarbonate (TTC-acid) (CDCl$_3$, 500 MHz).
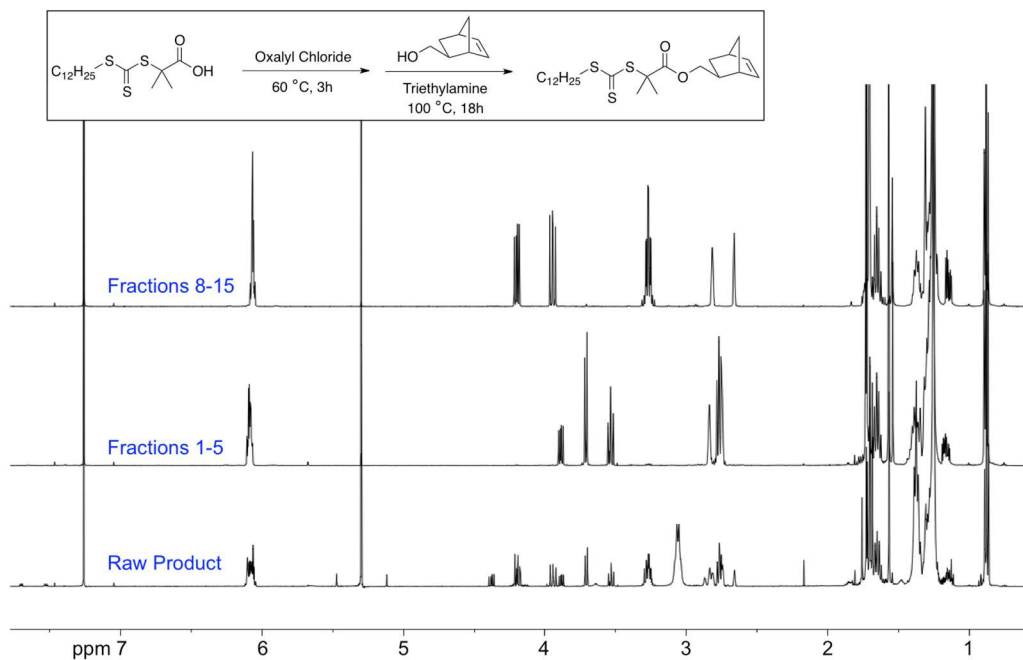
Figure 6.26. ¹H NMR of column chromatography fractions for purifying the norbornene-functionalized RAFT agent (TTC-NB) (CDCl₃, 500 MHz).
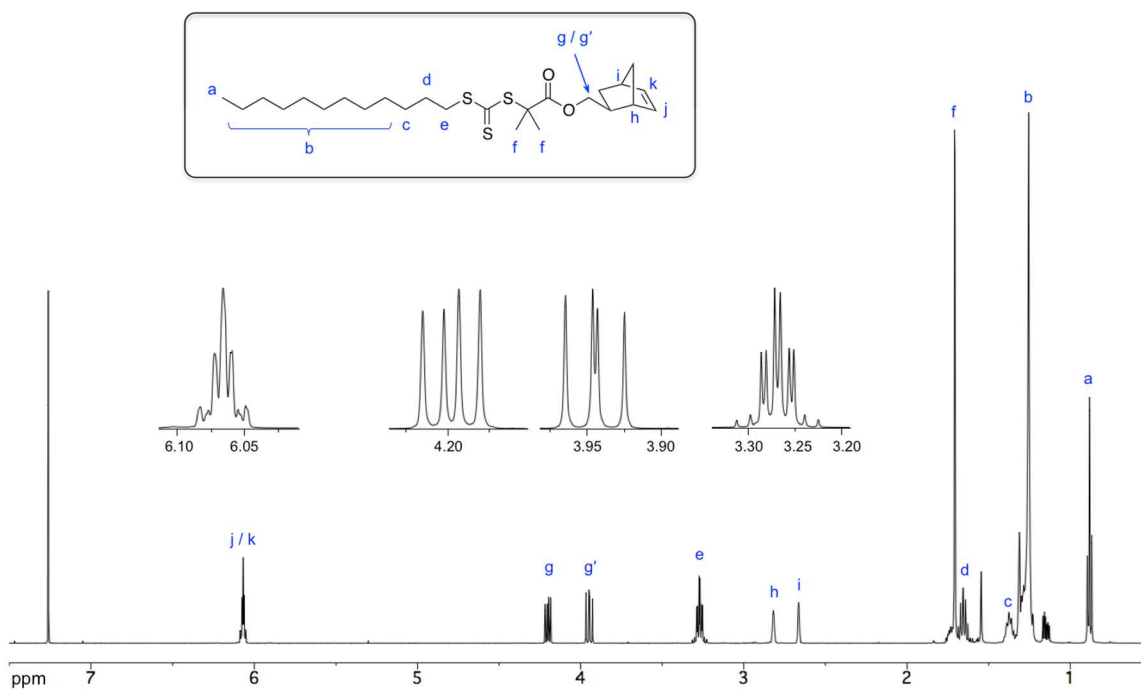
Figure 6.27. ¹H NMR of norbornene-functionalized RAFT agent (TTC-NB) (CDCl₃, 500 MHz).

6.6.4.3   Synthesis of PS-NB(3.8k) and PS-NB(20k).

For both polymerizations, styrene monomer was first purified by passage through a plug of basic alumina to remove inhibitor. **TTC-NB**, azobisisobutyronitrile (AIBN), and styrene were then mixed into a flame-dried Schlenk flask and the solution was degassed by three consecutive freeze-pump-thaw cycles. Following the final cycle, the reaction flask was backfilled with positive argon pressure. The solution was then heated to 70 °C and stirred under an argon atmosphere for several hours. Reaction progress was monitored by ^{1}H NMR analysis of removed aliquots, as shown for the PS-NB(20k) reaction in Figure 6.28. Conversion values were calculated by comparing the relative integrations of the entire aromatic region (which includes styrene and PS peaks) or of the low ppm region to the purely styrene peaks between 5 and 6 ppm. For the PS-NB(20k) sample, the reaction was terminated at 40% conversion by quenching in liquid N_2, opening the solution to air, and precipitating in methanol. (Reagent feed concentrations were loaded to target 50 kg/mol at 100% conversion). For the PS-NB(3.8k) sample, the polymerization was terminated at ~75% conversion. Reagent feed concentrations for this sample were loaded to target 5 kg/mol at 100% conversion in an attempt to achieve a 2 kg/mol product by quenching at 40% conversion as well. However, this reaction was left overnight and proceeded more rapidly than expected. This resulted in a higher molar mass product (3.8 kg/mol) and a larger yield of product mass. This likely caused the loss of some norbornene end groups due to termination events that are more prevalent at high monomer conversion,[190] as evidenced by the substantial amount of unreacted PS after ROMP of PS-NB(3.8k) in Figure 6.29.
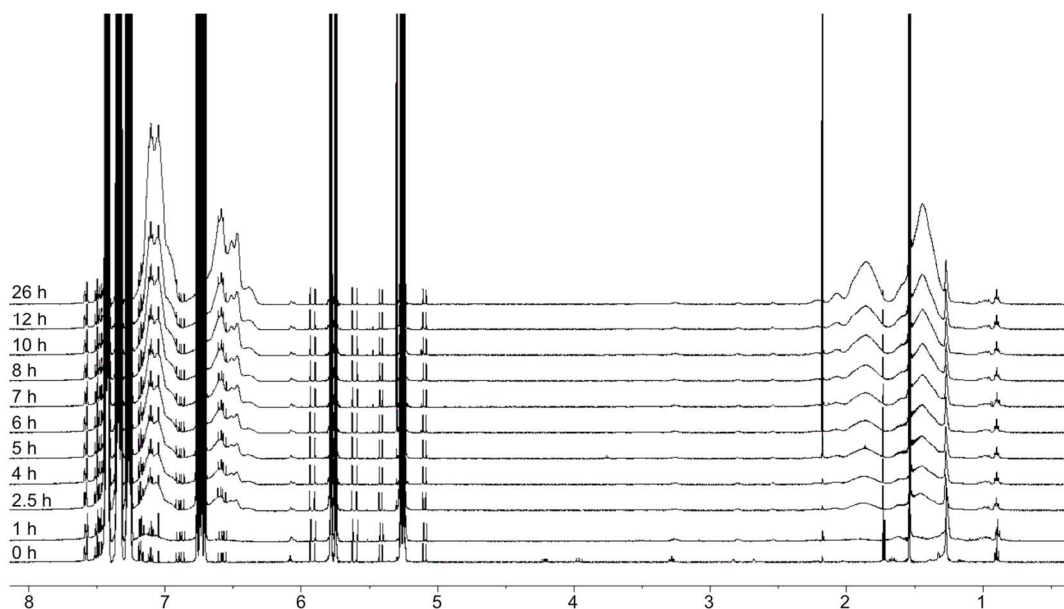
Figure 6.28. ^{1}H NMR of PS-NB(20k) at indicated reaction times (CDCl$_3$, 500 MHz). The styrene monomer peaks are very sharp and extend far above to top cutoff. The PS peaks are more broad and slowly grow with monomer conversion. The norbornene end group peaks are only faintly distinguishable because of the high molar mass of the sample (low end group concentration).
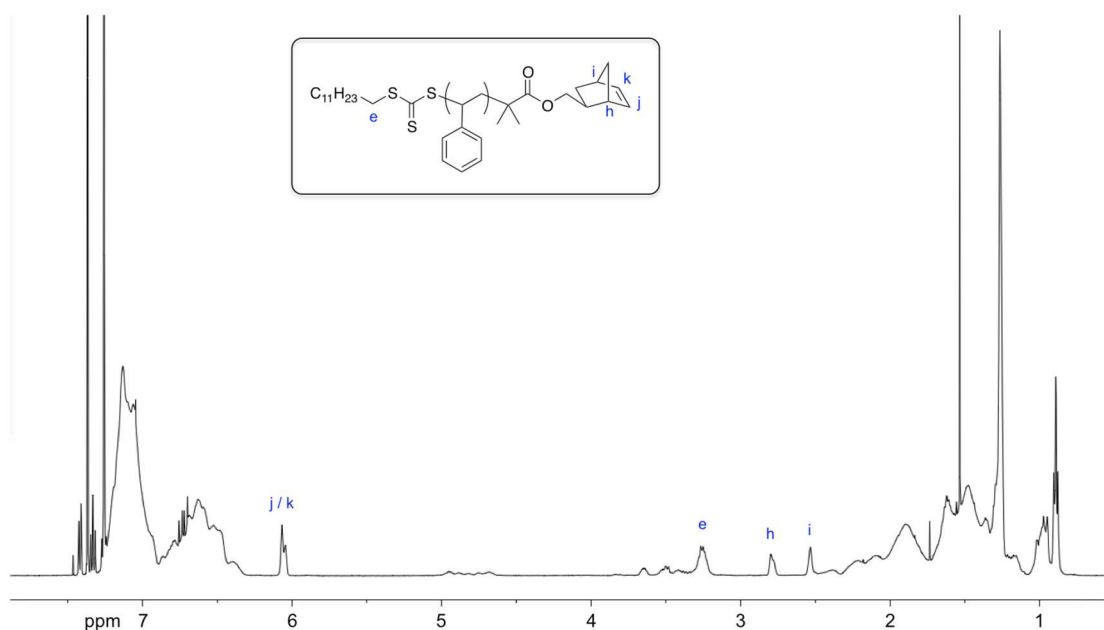
Figure 6.29. ^{1}H NMR of PS-NB(3.8k) (CDCl$_3$, 500 MHz). The end group peaks are much more prominent than in the PS-NB(20k) spectrum.

6.6.4.4   Synthesis of diblock bottlebrush polymers *via* sequential ROMP of macromonomers.

In a typical reaction, aPP-NB and PS-NB (~200 mg each depending on the target volume fraction) were loaded into separate oven-dried scintillation vials and brought into a glove box. Under a nitrogen atmosphere, both macromonomers were dissolved in degassed THF (50 mg/mL). In a separate scintillation vial, a desired amount of **G3** was dissolved in ~1 mL THF, and the aPP-NB solution was quickly added to the catalyst solution while stirring to initiate polymerization of block A. After 3 to 5 min (depending on target molecular weight) an aliquot was taken to characterize the first block, the PS-NB solution was added, and the reaction mixture was stirred for ~1 h. The reaction was terminated with excess ethyl vinyl ether, stirred for > 30 min, and precipitated into methanol. After drying under high vacuum, some of the samples revealed unreacted PS-NB macromonomers in the SEC traces. This indicates the presence of non-functionalized PS chains. To remove unreacted PS, the diblock products were stirred in ~10 mL acetone for several hours. The acetone was then decanted away from the non-dissolved polymer. The remaining product was again dried, and SEC analysis revealed that the fraction of low molar mass chains had either been reduced or completely removed.
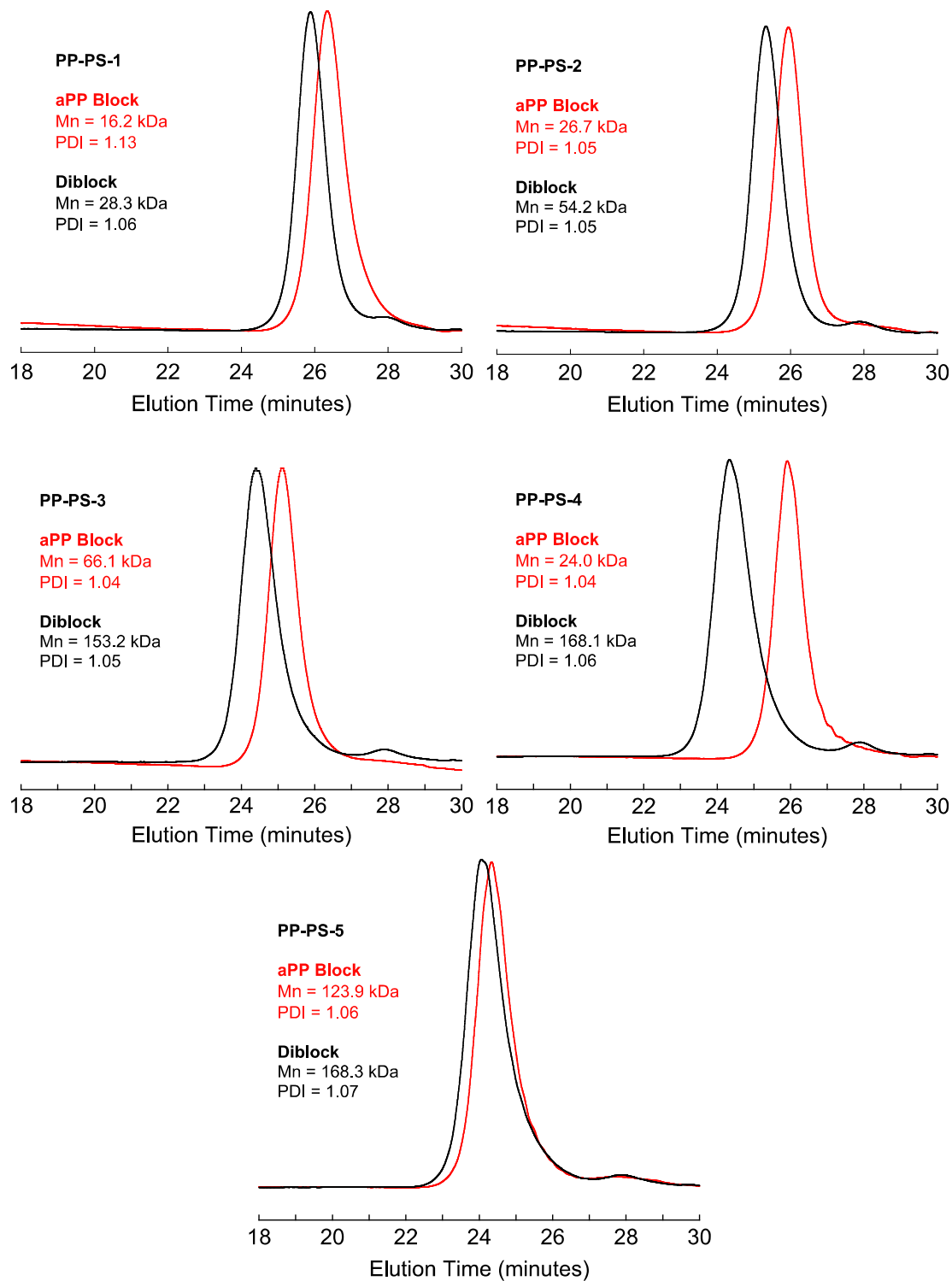
Figure 6.30. SEC traces of diblock samples from PP-PS-1 to PP-PS-5, along with the corresponding aPP block.

PP-PS-6

aPP Block
Mn = 61.1 kDa
PDI = 1.04

Diblock
Mn = 406.7 kDa
PDI = 1.24

PP-PS-7

PS Block
Mn = 72.5 kDa
PDI = 1.03

Diblock
Mn = 311.3 kDa
PDI = 1.23

PP-PS-8

PS Block
Mn = 166.5 kDa
PDI = 1.1

Diblock
Mn = 367.9 kDa
PDI = 1.2

PP-PS-9

aPP Block
Mn = 400.2 kDa
PDI = 1.12

Diblock
Mn = 696.4 kDa
PDI = 1.26
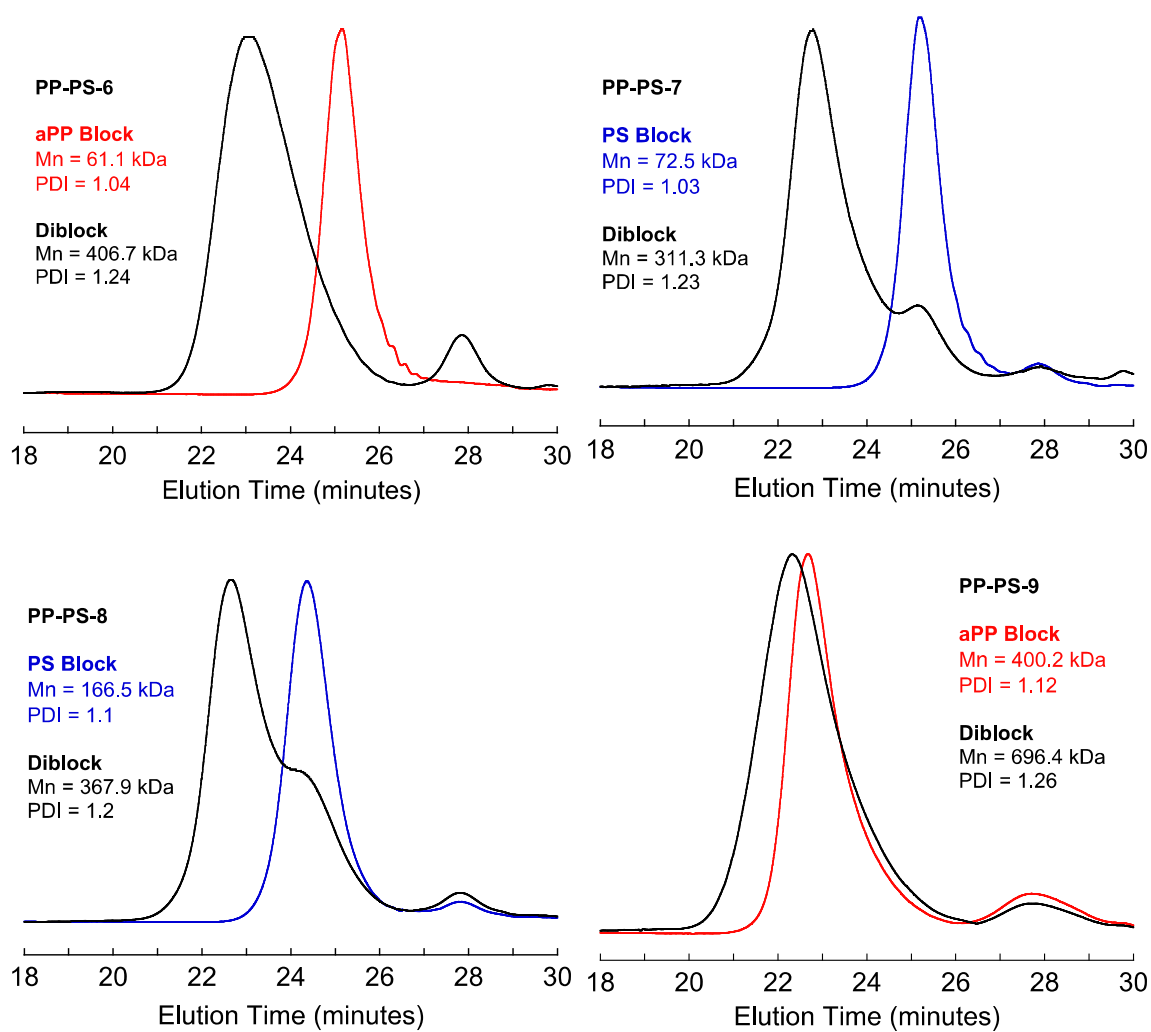
Figure 6.31. SEC traces of diblock samples from PP-PS-6 to PP-PS-9. Each plot displays the diblock trace as well as the trace of the first block only. M_n and $Đ$ (listed as PDI) values are provided for each trace.
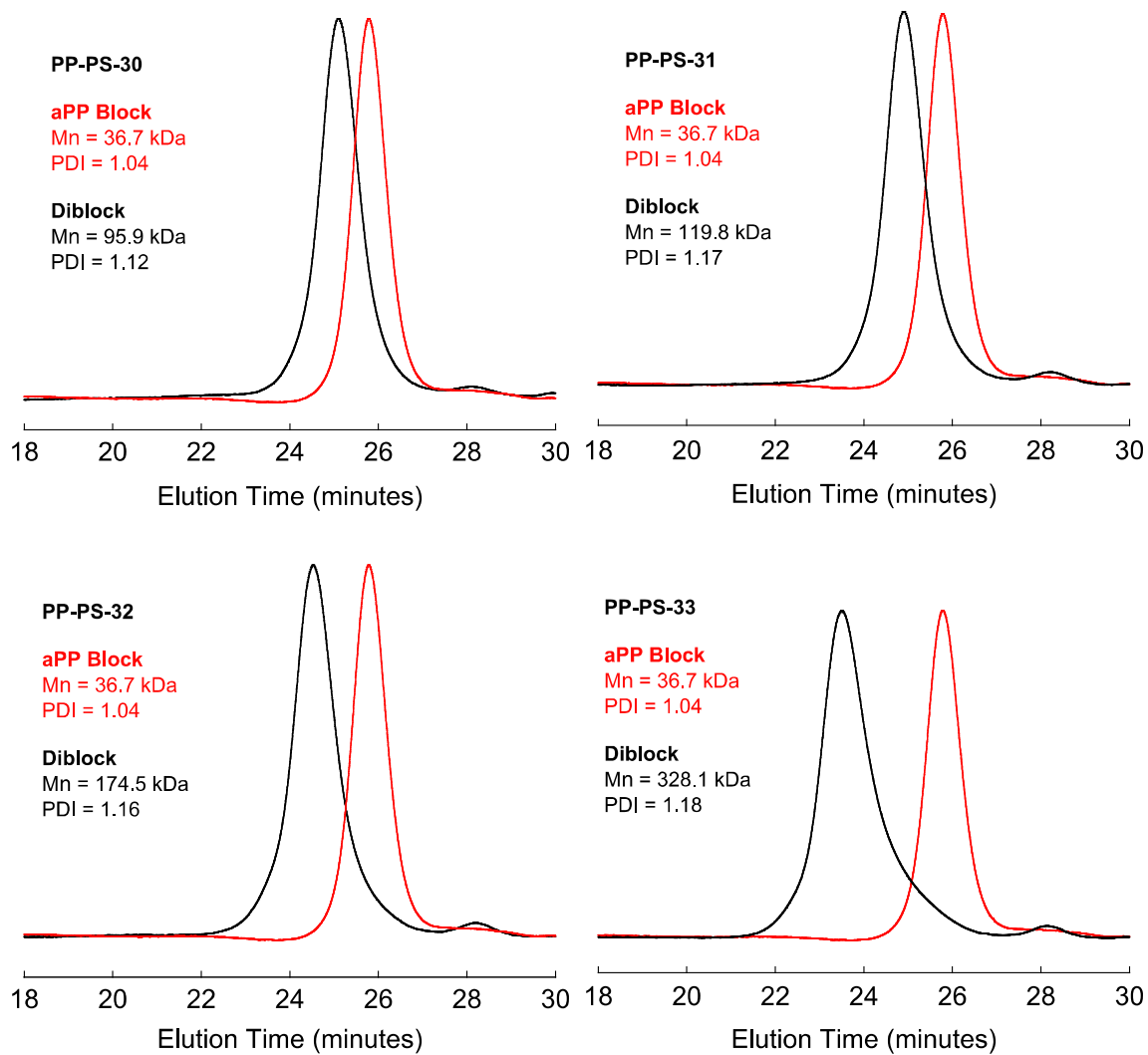
Figure 6.32. SEC traces of PP-PS-30, PP-PS-31, PP-PS-32, and PP-PS-33. Each plot displays the diblock (black trace) and the corresponding poly(aPP-NB) block prior to the second macromonomer addition (red trace). M_n and $Đ$ values are provided for each trace.
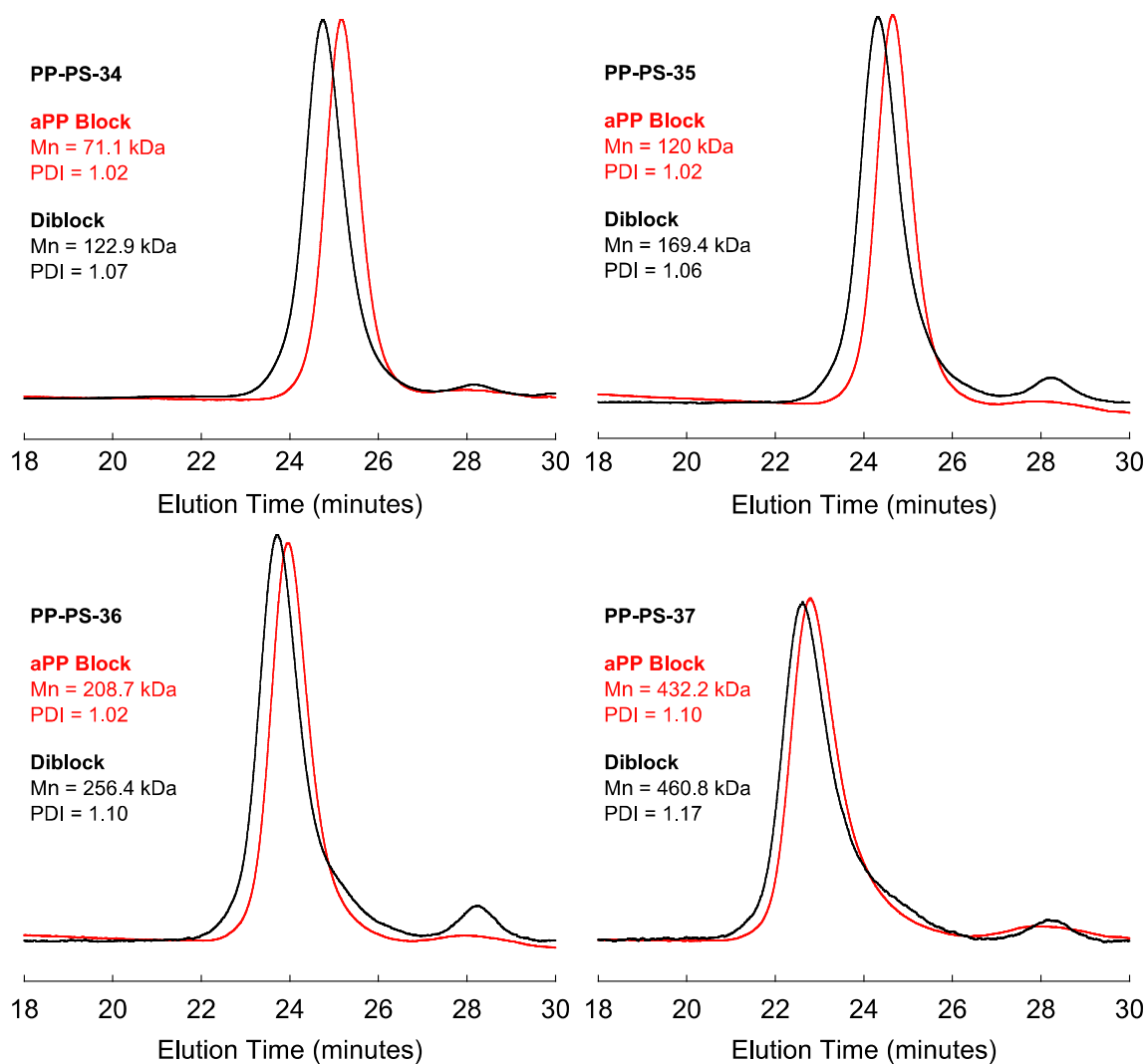
Figure 6.33. SEC traces of PP-PS-34, PP-PS-35, PP-PS-36, and PP-PS-37. Each plot displays the diblock (black trace) and the corresponding poly(aPP-NB) block prior to the second macromonomer addition (red trace). M_n and $Đ$ values are provided for each trace.
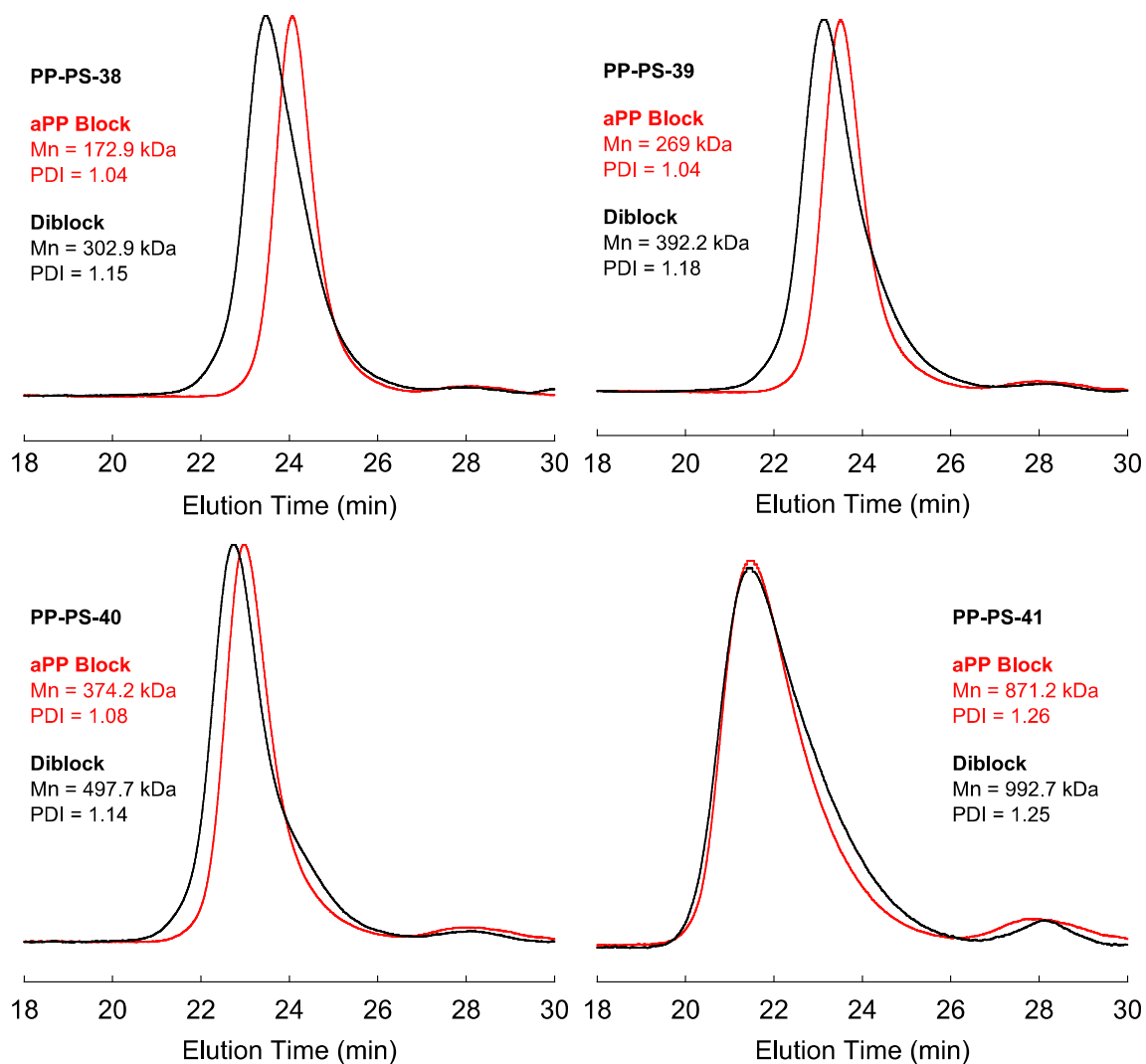
Figure 6.34. SEC traces of PP-PS-38, PP-PS-39, PP-PS-40, and PP-PS-41. Each plot displays the diblock (black trace) and the corresponding poly(aPP-NB) block prior to the second macromonomer addition (red trace). M_n and $Đ$ values are provided for each trace.
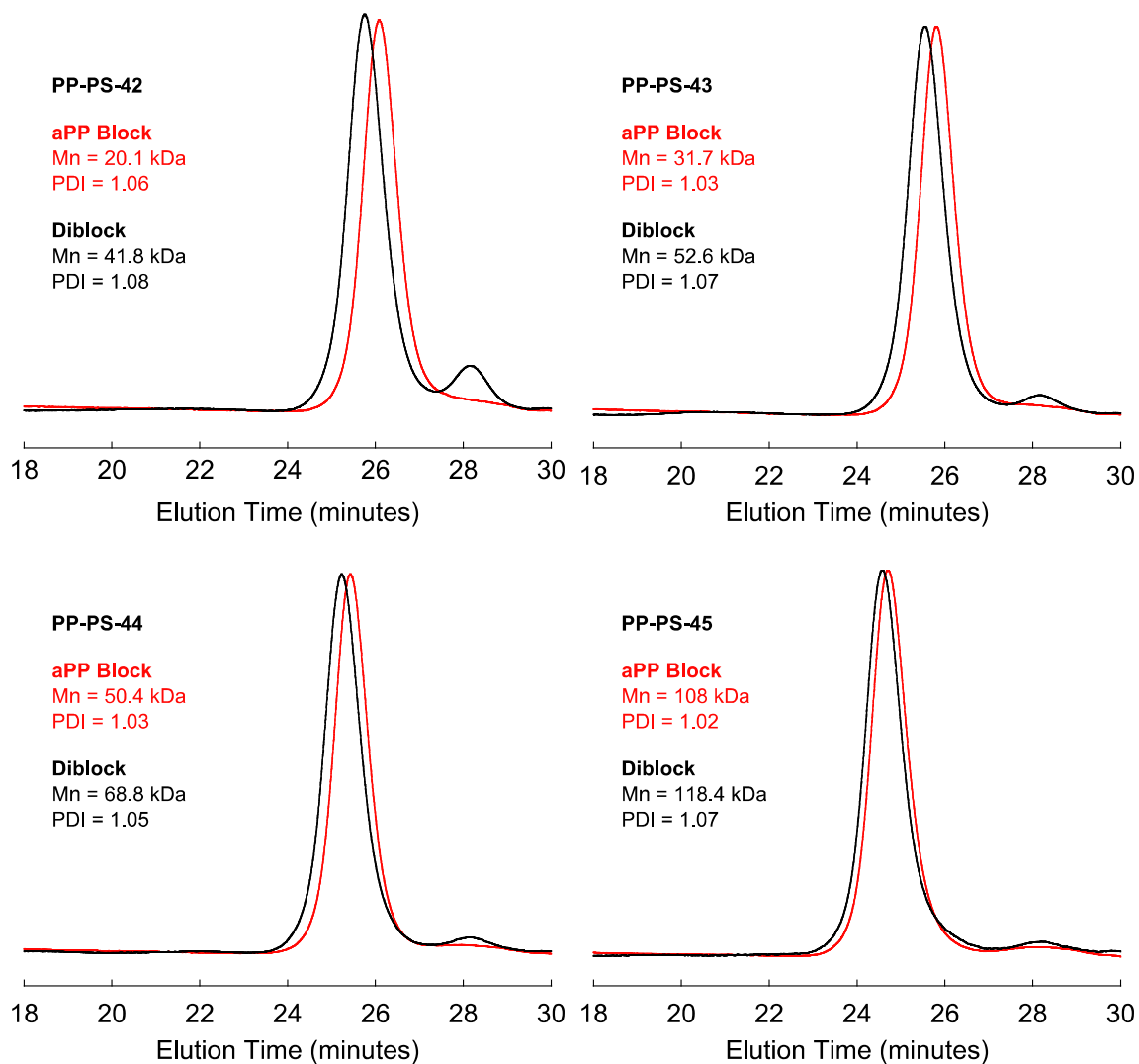
Figure 6.35. SEC traces of PP-PS-42, PP-PS-43, PP-PS-44, and PP-PS-45. Each plot displays the diblock (black trace) and the corresponding poly(aPP-NB) block prior to the second macromonomer addition (red trace). M_n and $Đ$ values are provided for each trace.

Chapter 7

Lamellar Phase of Bottlebrush Block Polymers

7.1 Introduction

A powerful approach to exploring block polymer self-assembly is through the development of predictive models to augment experimental results. However, the molecular complexity of bottlebrush molecules poses an immense challenge in understanding and predicting structural and dynamic behaviors. Bottlebrush diblocks involve far more molecular parameters than linear diblocks, the effects of which are difficult to resolve. One method for studying the effects of the different parameters is by simulation. This is not so practical for bottlebrushes, however, because of the computational demands of simulating such large molecules. As an example, Chremos and Theodorakis recently examined the assembly of bottlebrush block polymers by molecular dynamics simulations of a simple bead-spring model.[196] This method yielded morphology

diagrams of polymers with various degrees of architectural asymmetry, but was limited to a small number of beads per molecule. Consequently, either the branches were very short (often just one bead) or the number of branches was very small (as few as one A-type or one B-type branch). Gu *et al*. performed simulations similar to those of Chremos and Theodorakis, but with degrees of polymerization that were more representative of real bottlebrush polymers.[184,197] However, it does not appear that finite-size effects were addressed, potentially a significant limitation since some of the simulation boxes were barely larger than a single lamellar period. Consequently, their predictions for the scaling of lamellar domain sizes are questionable.

Adaptation of standard block polymer theories to these complex molecules is also a non-trivial task. The difficulty is that the usual mean-field approximation cannot explicitly handle the strong excluded-volume effects that exist in bottlebrushes due to the crowding of the densely packed side chains. Gu *et al*. presented a calculation based on the strong-segregation theory (SST) of Semenov[198] to supplement their experimental and simulation work. This implementation of SST assumed that the backbones form cylindrical domains with large diameters relative to the width of the polymer-polymer interface and small lengths relative to the contour length of the backbone. These assumptions do not conform to the molecules we are considering, since they require that the spacing between branches is large and that the lamellar period is small relative to the contour length of the backbone.

In this chapter, we couple state-of-the-art advances in theoretical modeling with our experimental results to address these outstanding problems. A new microscopic model for diblock bottlebrush polymers is first presented, which adapts self-consistent field theory (SCFT) to account for the strong steric interactions present in bottlebrush molecules. Next, experimental data of the ordered domain spacing for nine lamellae-forming diblock bottlebrush polymers, first introduced in chapter 6, are presented to determine how the periodicity varies with backbone chain length. Model parameters are matched to molecules from the experimental samples, and the corresponding lamellar periods are calculated using SCFT. Validated by quantitative agreement with our experimental

results, the SCFT is then used to elucidate details of how the molecules pack in the ordered state.

7.2   Theoretical Model

The research presented in this chapter was done in collaboration with Prof. Mark Matsen. We first worked together to develop a physically accurate model of the experimental bottlebrush molecules presented in chapter 6. This involved deciding on valid structural representations (*e.g.*, conformations of side chains and backbones, normalized chain lengths, branch spacing, *etc.*) and determining the appropriate simplifying assumptions. Prof. Matsen then ran all of the SCFT calculations. The results were analyzed jointly to evaluate the physical implications and to direct subsequent calculations. The remainder of this section describes the details of our theoretical model.

SCFT has an impeccable track record for modeling ordered block copolymer morphologies. One of its strengths is the ability to handle complex architectures like that of a bottlebrush diblock polymer containing a large number of independent side chains. However, the mean-field approach is unable to explicitly treat the crowding that occurs when the spacing between the side chains along the backbone is very small. It is understood that this crowding restricts the bending of the backbone, thus creating an effective backbone persistence length, ξ_b.[199] Fortunately, we are able to account for this simple effect by modeling the backbone as a worm-like chain[200] where the contour length, L, is fixed and ξ_b is an adjustable parameter. To the backbone, we attach m_A A-type side chains of polymerization degree N_A, and m_B B-type side chains of polymerization degree N_B sequenced to form a diblock molecular architecture. The $m = m_A + m_B$ side chains are spaced uniformly along the contour of the backbone and modeled using flexible Gaussian chains with distinct statistical lengths, a_A and a_B, for the A and B segments, respectively. For simplicity, we ignore the volume of the backbone and normalize the A and B segments to each occupy a common reference volume (v_{ref}), which implies that the melt is incompressible. Given the dense spacing of the side chains, the molecular interactions experienced by the backbone should remain relatively constant

(*i.e.*, B segments are unable to penetrate to the backbone of the A brush, and vice versa). This feature allows us to conveniently ignore all interactions involving the backbones, leaving only the A/B interactions, which we represent using the standard Flory-Huggins parameter χ.

Even with all these simplifications, our model still involves nine different parameters: L, ξ_b, χ, m_A, a_A, N_A, m_B, a_B and N_B. However, we are able to estimate all of these from experiment, apart from the effective persistence length of the backbone, ξ_b, which we treat as a fitting parameter. One further effect of the crowding that our mean-field approach misses is the stretching of the side chains. As a result, the thickness of the bottlebrush should be somewhat greater than the size of the unperturbed side chains, $a_A N_A^{1/2}$ or $a_B N_B^{1/2}$. This becomes significant for our smallest molecules, where the length of the bottlebrush is no longer large relative to its diameter. To compensate for this, we use values of a_A and a_B that are 50% larger than the experimental values.

7.3   Experimental Self-Assembly Results

Diblock bottlebrush polymers composed of aPP side chains and PS side chains (blocks A and B, respectively) were prepared by ROMP of macromonomers, and the self-assembled structures were analyzed by SAXS as discussed in the previous chapter. Here, nine of the lamellae-forming diblock samples were selected to compare the domain spacing, d_0, with SCFT predictions and to evaluate the scaling of d_0 with backbone length, L. The nomenclature has been modified with samples labeled [P(aPP)-*b*-P(PS)]$_{Mn}$ to compare symmetric diblock samples with the indicated total molar mass. Molecular characteristics and d_0 values for each diblock sample are summarized in Table 7.1. SAXS profiles recorded at 150 °C for all of the diblock polymers are also depicted in Figure 7.1.

Table 7.1. Molecular characterization and bulk domain spacing of diblock bottlebrush polymers.

Sample label	$M_{n,\text{Diblock}}$ (kg/mol)[a]	$DP_{\text{aPP-NB}}$[b]	$DP_{\text{PS-NB}}$[b]	d_0 (nm)[c]	Chapter 6 Sample ID
[P(aPP)-*b*-P(PS)]$_{28.3k}$	28.3	6.3	3.9	16.4	PP-PS-1
[P(aPP)-*b*-P(PS)]$_{41.8k}$	41.8	10	5.7	18.3	PP-PS-42
[P(aPP)-*b*-P(PS)]$_{54.2k}$	54.2	12	7.3	21.0	PP-PS-2
[P(aPP)-*b*-P(PS)]$_{95.9k}$	95.9	18	16	26.3	PP-PS-30
[P(aPP)-*b*-P(PS)]$_{123k}$	123	35	14	32.2	PP-PS-34
[P(aPP)-*b*-P(PS)]$_{153k}$	153	35	20	38.7	PP-PS-3
[P(aPP)-*b*-P(PS)]$_{303k}$	303	84	34	73.9	PP-PS-38
[P(aPP)-*b*-P(PS)]$_{368k}$	368	100	41	81.6	PP-PS-8
[P(aPP)-*b*-P(PS)]$_{696k}$	696	219	62	149.5	PP-PS-9

[a]Determined by SEC-MALLS with a THF mobile phase. [b]Number-average backbone degree of polymerization of each block. [c]Lamellar domain spacing calculated using the primary scattering peak ($d_0 = 2\pi/q^*$) from SAXS data at 150 °C.

The lamellar periodicity of each sample was calculated using $d_0 = 2\pi/q^*$, where q^* is the wavevector corresponding to the principal scattering peak. Imaging of the samples was employed using TEM and AFM for supplementary domain spacing characterization. Figure 7.2 and Figure 7.3 display examples obtained for [P(aPP)-*b*-P(PS)]$_{54.2k}$ and [P(aPP)-*b*-P(PS)]$_{123k}$, respectively. The TEM image in Figure 7.2 displays lamellar domains, faintly seen in a U-shape, with average domain spacing of $d_0 = 20 \pm 2$ nm as determined by analysis of the images at several different locations. (The uncertainty represents the standard deviation in d_0 estimates.) This value compares very closely with the value calculated from SAXS of $d_0 = 21$ nm. The domain spacing of [P(aPP)-*b*-P(PS)]$_{123k}$ was also estimated by analysis of cross sections in the AFM images shown in Figure 7.3 at 100 different locations, yielding an average value of $d_0 = 32 \pm 7$ nm. This is again consistent with the value determined from SAXS of $d_0 = 32.2$ nm.
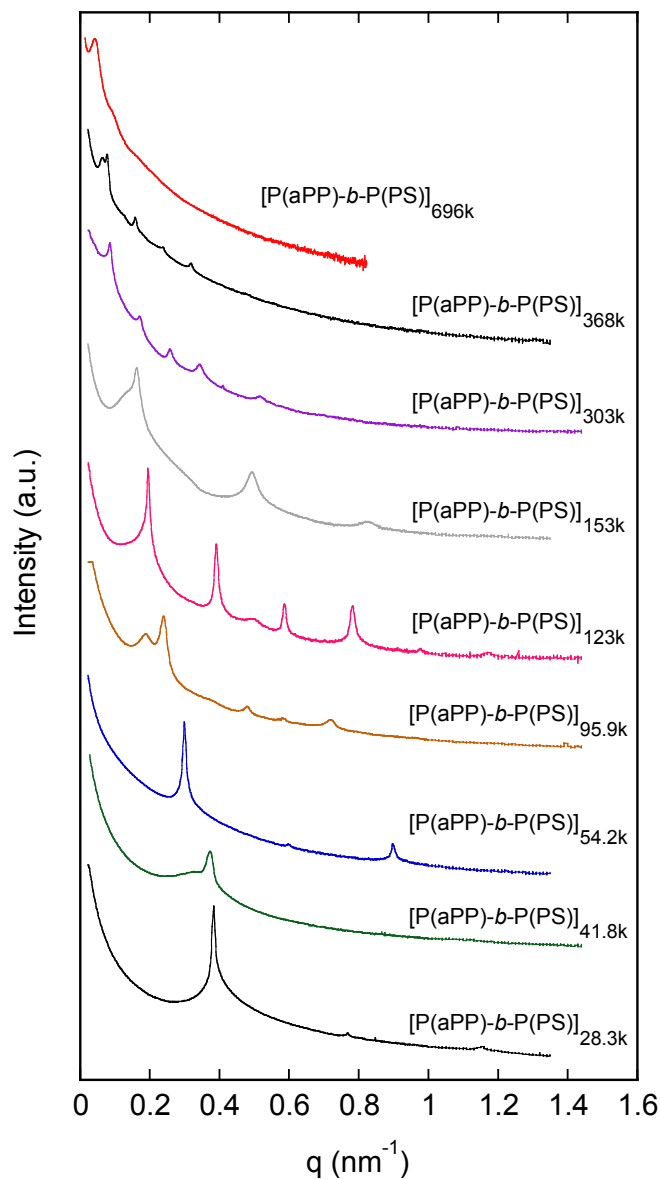
Figure 7.1. SAXS profiles of the diblock bottlebrush polymers at 150 °C. SAXS profiles are reproduced from several plots in chapter 6 to give a direct comparison of the symmetric samples of interest.
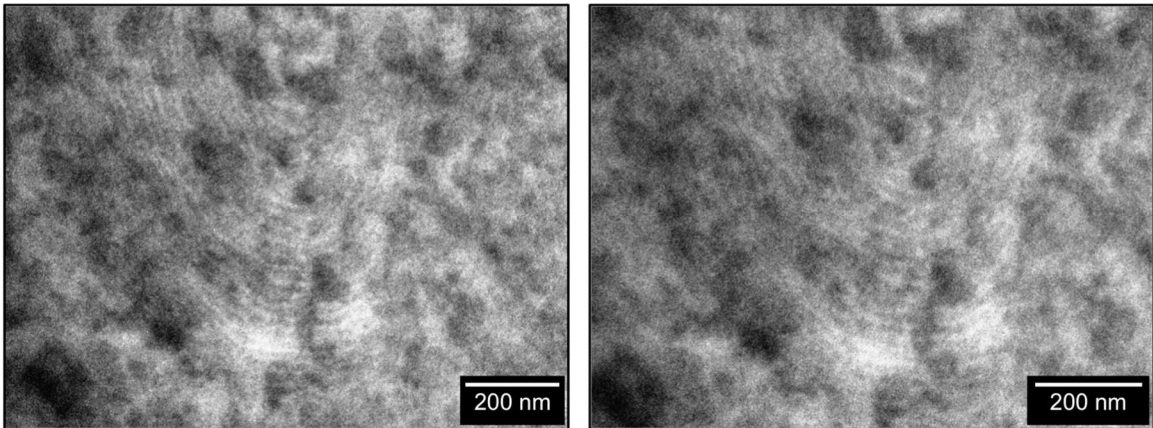
Figure 7.2. TEM images of [P(aPP)-*b*-P(PS)]$_{54.2k}$. Lamellae assemble as a faint fingerprint pattern in a U-shape. Image analysis yields a domain spacing of $d_0 = 20$ nm.
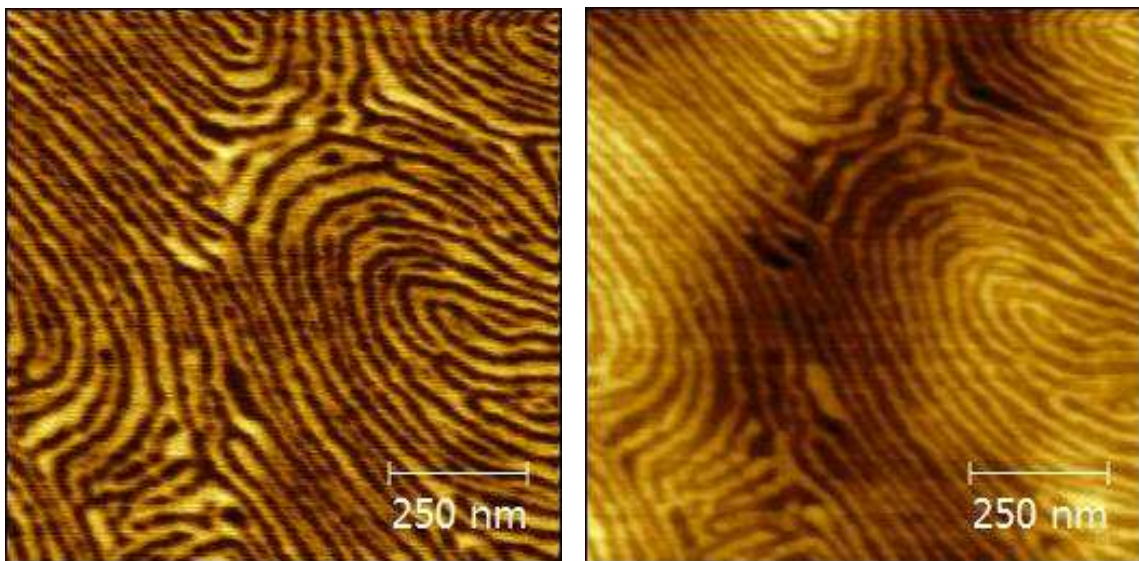
Figure 7.3. AFM phase (left) and height (right) images of [P(aPP)-*b*-P(PS)]$_{123k}$. Image analysis of the domain spacing taken at 100 locations yields $d_0 = 32 \pm 7$ nm, which matches the value from SAXS of $d_0 = 32.2$ nm.

Figure 7.4 depicts the lamellar periodicity of each diblock sample plotted as a function of the number-average backbone length L, where L is calculated using a constant contour length of 0.62 nm per poly(norbornene) backbone segment. The relationship $d_0 = 2L$ is also plotted as a blue dotted line, which represents the lamellar period for fully extended bottlebrush molecules packed in an end-to-end bilayer arrangement with negligible end effects. Over the wide range of L shown in Figure 7.4, it is clear that the average slope between data points on the log-log axes is not constant and continually increases, obviating a fit to the $d_0 \sim L^\gamma$ relationship with a constant scaling exponent γ. Instead, the scaling exponent transitions from $\gamma < 0.3$ to a value that approaches unity as L is increased. In particular, a power-law fit to our two largest molecules gives a scaling exponent of $\gamma = 0.88$, which is greater than the scaling of strongly segregated linear diblock polymers ($\gamma = 2/3$).[198] The large scaling exponent is consistent with prior experimental studies that accredited it to highly extended conformations of large, cylindrical bottlebrushes.[27,76,77,184] At small backbone lengths, the scaling exponent decreases considerably. A fit to the smallest two samples yields a scaling exponent of only $\gamma = 0.26$. In this size regime, the molecules no longer resemble cylindrical brushes since the contour lengths of the backbones are shorter than the side chains. In this limit the lamellar period is dominated by the side chain dimensions with only weak dependence on the backbone length, and it actually exceeds the $d_0 = 2L$ line as a consequence. As this line ignores end effects, it loses significance for the more star-like polymers at low L.
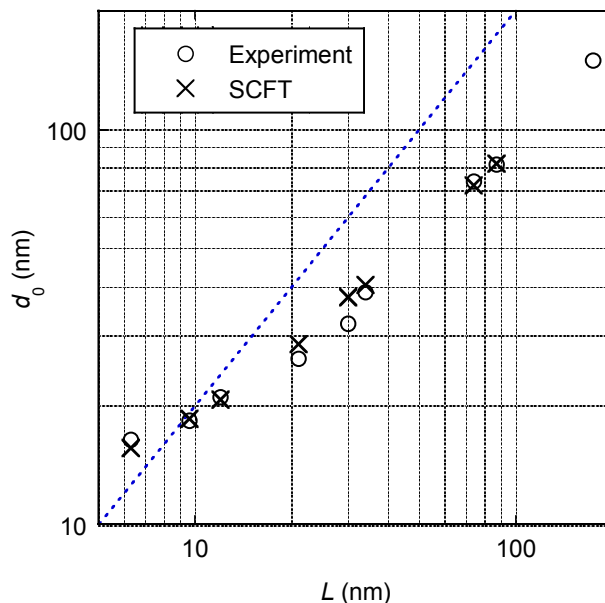
Figure 7.4. Lamellar periodicity, d_0, versus contour length of the backbone, L, obtained from the experimental SAXS measurements and the SCFT predictions. The blue dotted line denotes the $d_0 = 2L$ relationship, corresponding to a lamellar period consisting of two fully extended diblock monolayers.

7.4   Theory Results

Predictions of the lamellar period for each of the diblock bottlebrush polymers were made using the SCFT model described in section 7.2. The structural input parameters, given in Table 7.2, were calculated on the basis of the molecular characterizations. The number of branches per block (m_A and m_B) were taken as the number-average degree of polymerization of each block from Table 7.1, and the number of segments per branch (N_A and N_B) were normalized to a common reference volume of $v_{ref} = 118$ Å^3. The backbone persistence length (ξ_b) was the only parameter not estimated from experiment and was treated as a fitting parameter. Predictions of d_0 were obtained for eight of the nine samples, and the results are shown in Figure 7.4 along with the experimental data. (The SCFT calculations were not able to converge on a solution for the largest sample because of numerical difficulties resulting from the extreme level of segregation).

Table 7.2. Structural input parameters of diblock bottlebrush polymers for SCFT calculations.

Sample label	N_A[a]	N_B[a]	m_A[b]	m_B[b]	m[c]	L (nm)[d]	χN[e]
[P(aPP)-b-P(PS)]$_{28.3k}$	34	54	6	4	10	6.3	47
[P(aPP)-b-P(PS)]$_{41.8k}$	34	51	10	6	16	9.6	70
[P(aPP)-b-P(PS)]$_{54.2k}$	34	54	12	7	19	12	91
[P(aPP)-b-P(PS)]$_{95.9k}$	34	51	18	16	34	21	158
[P(aPP)-b-P(PS)]$_{123k}$	34	51	35	14	49	30	212
[P(aPP)-b-P(PS)]$_{153k}$	34	54	35	20	55	34	258
[P(aPP)-b-P(PS)]$_{303k}$	34	51	84	34	118	74	522
[P(aPP)-b-P(PS)]$_{368k}$	34	54	100	41	141	87	633
[P(aPP)-b-P(PS)]$_{696k}$	34	54	219	62	281	174	1220

[a]Number of segments per aPP branch (N_A) and per PS branch (N_B) based on a 118 Å³ reference volume. Values of N_B vary depending on the PS-NB macromonomer used. [b]Number of aPP branches per molecule (m_A) and PS branches per molecule (m_B) reported to the nearest integer. [c]Number of total branches per molecule. [d]Backbone contour length calculated by $L = (0.62 \text{ nm} \times m)$, based on a length of 0.62 nm per poly(norbornene) repeat unit. [e]Segregation strength. Initial estimates for these values were based on a PS-b-PEP system[193] using $\chi N = \text{X}(M_n/\rho RT)$ where $\text{X}_{PS\text{-}PEP} = 1655/T(\text{K}) + 0.57$ with $v_{ref} = 118$ Å³. The values given are 25% greater than the initial estimates and were used for all of the calculations in this chapter. [f]Statistical segment lengths used for aPP side chains and PS side chains were $a_A = 9.2$ Å and $a_B = 8.2$ Å, respectively. These lengths are 50 % greater than values reported in the literature[149] in order to account for chain stretching effects.

The agreement of the SCFT predictions with the experimental results is remarkable. Nearly all of the SCFT data points in Figure 7.4 are within 5% of the experimental values. Consequently, the observed trend of an increasing scaling exponent with increasing L is entirely captured by the theory. While ξ_b was the only variable without an initial estimate from experimental values, which we treated as a fitting parameter, we also adjusted the value of χ since our starting values were simply rough estimates based on literature values for a linear PS-b-PEP diblock system. The SCFT predictions for d_0 using four different values of ξ_b and two values of χ are provided in section 7.7.2 (Table 7.3). Select comparisons of these results are also plotted in Figure 7.5. We found that ξ_b has virtually no effect at low L, but becomes somewhat significant at high L. Alternatively,

increasing χ had the greatest, albeit modest, effect at low L. Specifically, a 25% increase in χ caused only a ~3% increase in d_0 for all samples except for the smallest diblock where d_0 increased by ~6%. In any case, the theoretical predictions of d_0 are not particularly sensitive to either ξ_b or χ. Therefore, the congruity with experiment demonstrates that the model intrinsically provides a good representation of the system. The SCFT data set using $\xi_b = 5$ backbone segments and the larger χ value is plotted in Figure 7.4. This optimum set of parameters is used for all the remaining calculations in this chapter. It is worth noting that recent simulations[201] found that the steric-induced Kuhn length of the backbone, $b_K = 2\xi_b$, is similar to the diameter of the bottlebrush, $2R_g \sim a_A N_A^{1/2} \sim a_B N_B^{1/2}$. As it turns out, these two quantities are also comparable in our system (both ~ 6 nm) given our chosen value of ξ_b.

The success of the SCFT in predicting the experimental domain spacing is encouraging and allows us to confidently use the theory to study the details of the molecular self-assembly. We first calculated composition profiles to examine the degree of segregation in the melt. Figure 7.6 compares the relative A-segment concentration, $\phi_A(z)$, over one lamellar period for four of the diblock samples. The domains of our shortest bottlebrush, [P(aPP)-b-P(PS)]$_{28.3k}$, contain a small but noticeable amount of the other component at their centers (*i.e.,* ~ 1%), and therefore we regard this sample as intermediately segregated. This is consistent with our ability to access the T_{ODT} of this polymer. The domains of the larger molecules become essentially pure, resulting in profiles that are more square-wave in nature. Therefore, these can be unambiguously classified as strongly segregated. However, the increased segregation does not imply that A/B interfaces are narrower. Figure 7.6b shows that the interfacial profiles in absolute units are virtually identical, with a common interfacial width of $w_{int} = 2.1$ nm, as determined by the dashed tangent line. Just as for conventional linear diblock copolymers, the interface is well approximated by that of a strongly segregated binary homopolymer blend. Indeed, our interfacial width is indistinguishable from the theoretical prediction $w_{int} = [(a_A^2 + a_B^2) / 3\chi]^{1/2}$ for the homopolymer blend.[202]
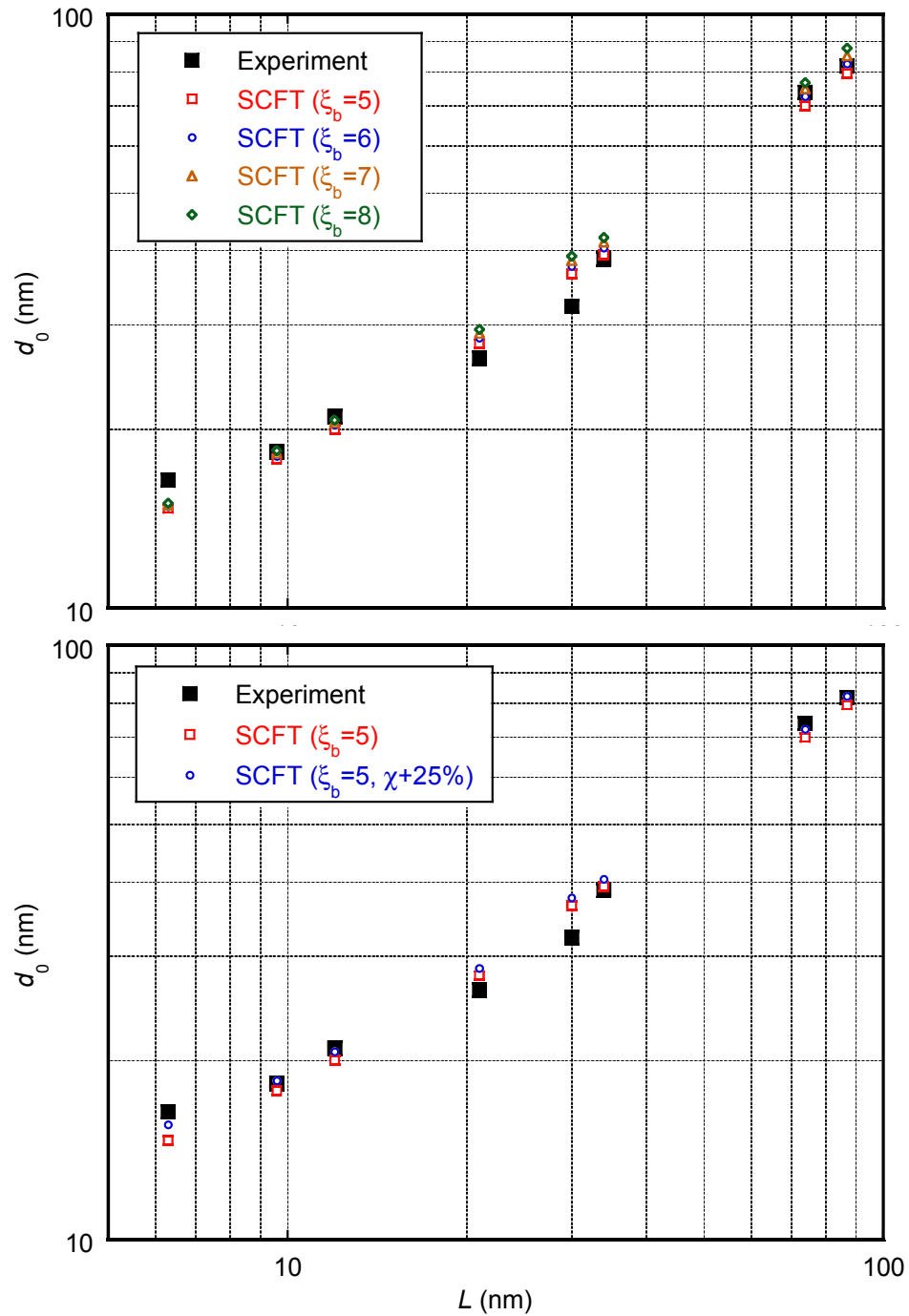
Figure 7.5. Lamellar periodicity (d_0) versus backbone length (L). *Top:* SCFT predictions using a constant χ value and variable persistence length (ξ_b) values in units of backbone segments. *Bottom:* SCFT predictions using two different values of χ.
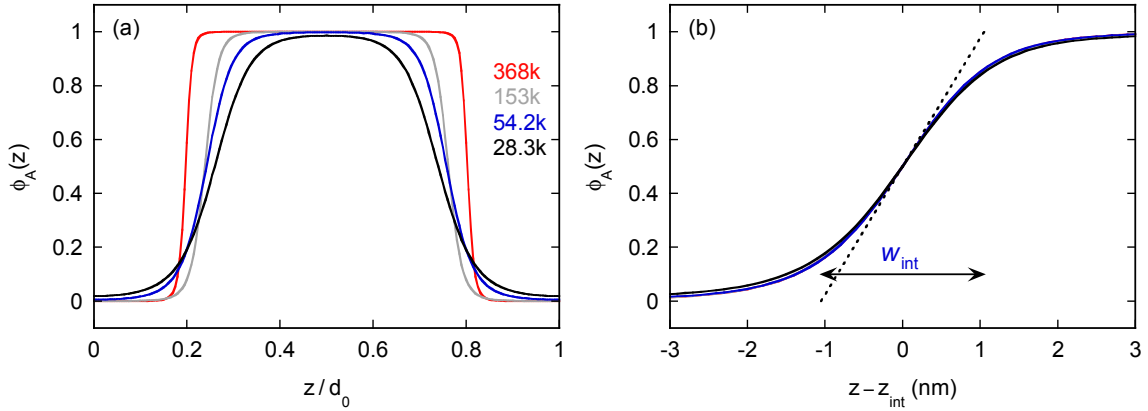
Figure 7.6. Composition profiles of four diblock samples plotted (a) in relative units over one complete lamellar period and (b) in absolute units centered about an A/B interface, z_{int}. The dashed line coincides with the predicted[202] interfacial width, $w_{int} = [(a_A^2 + a_B^2) / 3\chi]^{1/2}$.

To help understand how the bottlebrush molecules pack within the lamellar phase, we calculated the joint-distribution function, $p_{A,i}(z,u)$, for the position (z) and orientation (u) of the ith backbone unit along the A-block. The units are numbered sequentially from $i = 1$ at the A-B block junction to $i = m_A$ at the A-end of the backbone. Here we follow the standard convention of specifying the orientation of the backbone by $u = \cos(\theta)$, where θ is the angle of the backbone relative to the plane of the lamellar phase. Figure 7.7 shows $p_{A,i}(z,u)$ at various points along the A-block for the same four molecules considered in Figure 7.6. The dominant features are the two strong peaks for the $i = 1$ units. The peaks at $z/d_0 \approx 1/4$ and $u = \cos(0°) = 1$ indicate that the backbone junctions are highly localized at the interface and strongly oriented normal to the lamellae. Similarly, the peaks at $z/d_0 \approx 3/4$ and $u = \cos(180°) = -1$ indicate an equivalent localization at the neighboring interface but with the opposite orientation. As i increases, the distributions shift toward the center of the A-domains (i.e., $z/d_0 = 1/2$) and broaden in both the z and u directions, indicating a reduction in localization and orientation, respectively.
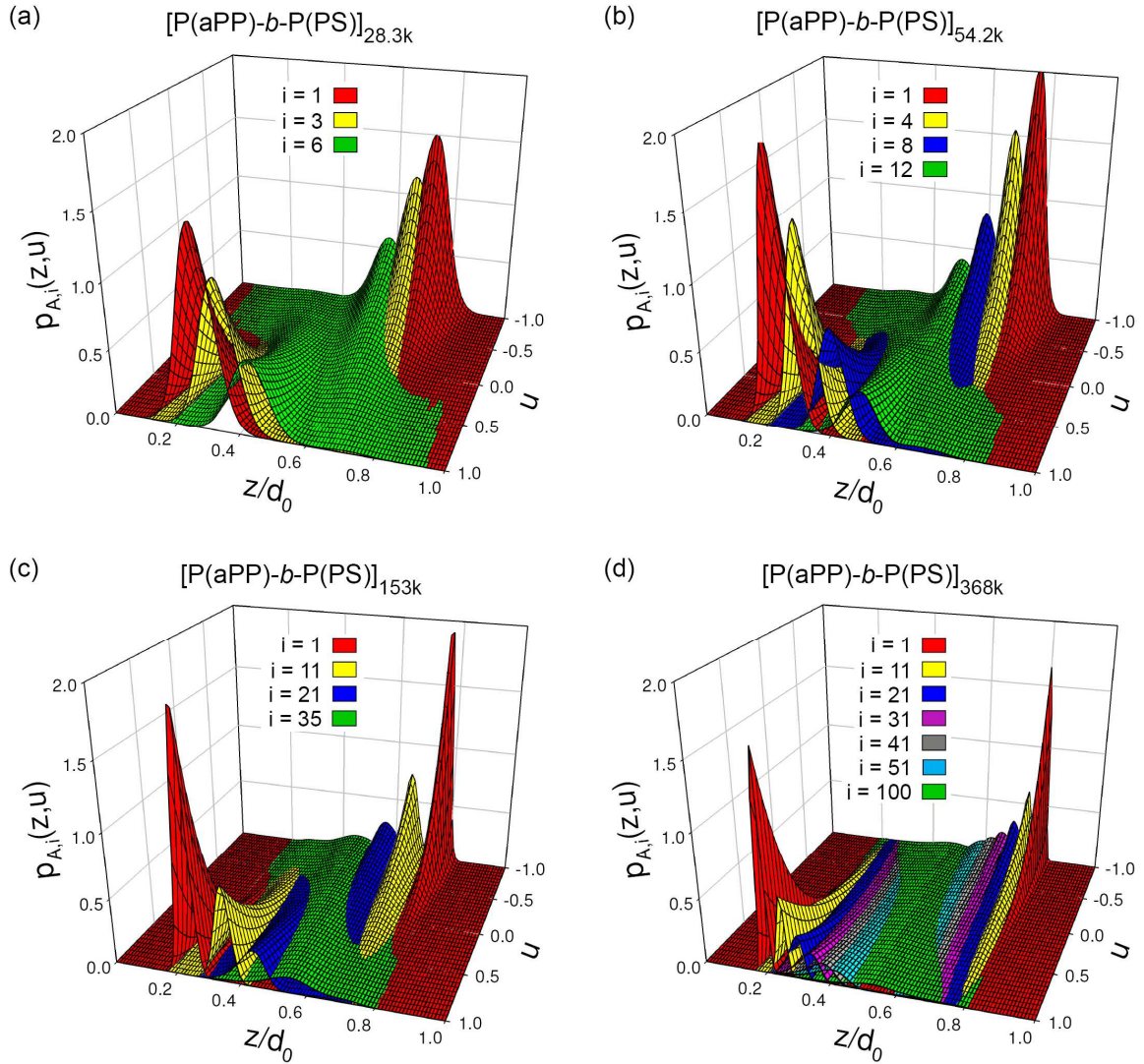
Figure 7.7. SCFT results for the four bottlebrushes considered in Figure 7.6 showing the joint-distribution function, $p_{A,i}(z,u)$, for the position, z, and orientation, $u = \cos(\theta)$, of various individual backbone segments, i, along the A-block.

   The 3D plots in Figure 7.7 provide a detailed picture of the molecular packing for bottlebrush block polymers of increasing backbone lengths. To highlight the assembly behavior of our more brush-like molecules, individual distributions of z and u for various values of i (see color legend) are plotted in Figure 7.8 for [P(aPP)-b-P(PS)]$_{368k}$, which is the largest bottlebrush that was modeled. Figure 7.8a shows the positional probability, $p_{A,i}(z)$, obtained by integrating $p_{A,i}(z,u)$ over all orientations, $u = -1$ to 1. This plot clearly shows the strong localization of the junctions ($i = 1$) at the two interfaces and the subsequent delocalization and progression towards the center of the A-domain with successive steps along the A-block in units of the Kuhn length (*i.e.*, $\Delta i = 10$, since $b_K = 2\xi_b$ and $\xi_b = 5i$). By five Kuhn lengths ($i = 51$), or halfway along the A-block, the distributions originating from the two neighboring interfaces are beginning to overlap in the middle of the A-domain. Figure 7.8b shows the orientation probability, $p_{A,i}(u)$, obtained by integrating $p_{A,i}(z,u)$ over one lamellar period, $z = 0$ to d_0. The junction point ($i = 1$) is highly oriented due to the strong gradient in the composition profile, but this orientational order quickly fades within a few units along the backbone as it exits the interfacial region. (Recall that the length of a backbone unit is 0.62 nm, which is comparable to the interfacial width in Figure 7.6b). The rapid decrease in orientational order is followed by a more gradual decrease to the point where the end of the A-block ($i = 100$) shows a relatively flat distribution, implying that all orientations are equally probable. Figure 7.8c displays the most probable location (*i.e.*, the peak in $p_{A,i}(z)$) of several backbone units along the A-block. The dashed line denotes the maximum possible progression of the backbone position corresponding to a fully extended chain. The data initially progress closely with this theoretical maximum, consistent with the high degree of orientation near $i = 1$. However, the progression slows as the backbone becomes less oriented. Ultimately, the end of the backbone ($i = 100$) gives a symmetric positional distribution centered in the middle of the A-domain.
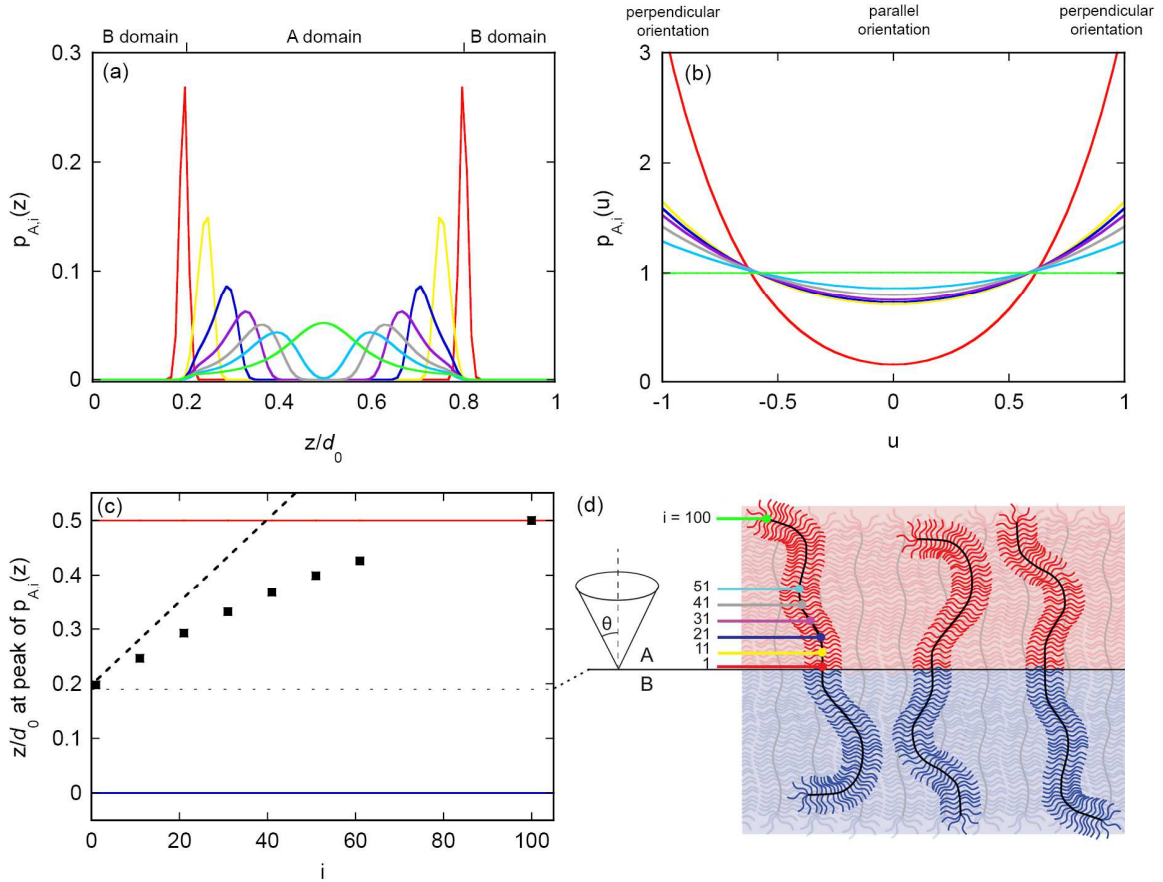
Figure 7.8. Probability distributions for A-block backbone segments, *i*, of [P(aPP)-*b*-P(PS)]$_{368k}$ calculated by SCFT. Backbone segments range from $i = 1$ to $i = 100$, indicating their distance from the A-B block junction. Different colored traces in plots a and b represent different backbone segments as defined in plot d. (a): Positional probability distribution, $p_{A,i}(z)$, of backbone segments within the A-domain.   (b): Orientational probability distribution, $p_{A,i}(u)$, of backbone segments relative to the A/B interface. (c): Most probable positions of backbone segments (black squares). The dashed black line indicates the maximum progression of backbone locations for a fully extended chain. The red and blue solid lines denote the center of the A-domain and B-domain, respectively, while the dotted line designates the A/B interface. (d): Graphic defining A-block backbone segments and the backbone orientation angle, θ.

We now examine how the length of the backbone affects the arrangement of the bottlebrushes within the lamellar phase by inspecting the other 3D plots in Figure 7.7, along with the corresponding plots of $p_{A,i}(z)$ and $p_{A,i}(u)$ in Figure 7.9, Figure 7.10, and

Figure 7.11. It is clear from these plots that the backbone orientation of the [P(aPP)-*b*-P(PS)]$_{153k}$ bottlebrushes vanishes towards their ends, much like that of [P(aPP)-*b*-P(PS)]$_{368k}$. However, the shorter [P(aPP)-*b*-P(PS)]$_{54.2k}$ molecules maintain a significant degree of orientation along their entire A-block. This is not too surprising since the A-block is only a single Kuhn length. Consequently, the ends of the A-blocks are much more localized at the center of the A-domain and have a reasonable preference for the $u = \pm 1$ orientations (see Figure 7.7b). Due to their more extended conformations, the lamellar period of [P(aPP)-*b*-P(PS)]$_{54.2k}$ approaches the blue dashed line ($d_0 = 2L$) in Figure 7.4. Furthermore, for our shortest [P(aPP)-*b*-P(PS)]$_{28.3k}$ molecules where the A-block is only half a Kuhn length, the lamellar period actually exceeds $d_0 = 2L$. This implies that the backbones are too short to reach the middle of the A-domain. Indeed, the separate peaks in $p_{A,i}(z)$ from molecules at the adjacent interfaces do not converge at the center of the A-domain even for $i = m_A = 6$ (see Figure 7.9). Instead, the side chains have to extend beyond the ends of the backbone to fill the middle of the domains. This is consistent with our characterization of molecules with short backbones as conformationally star-like.
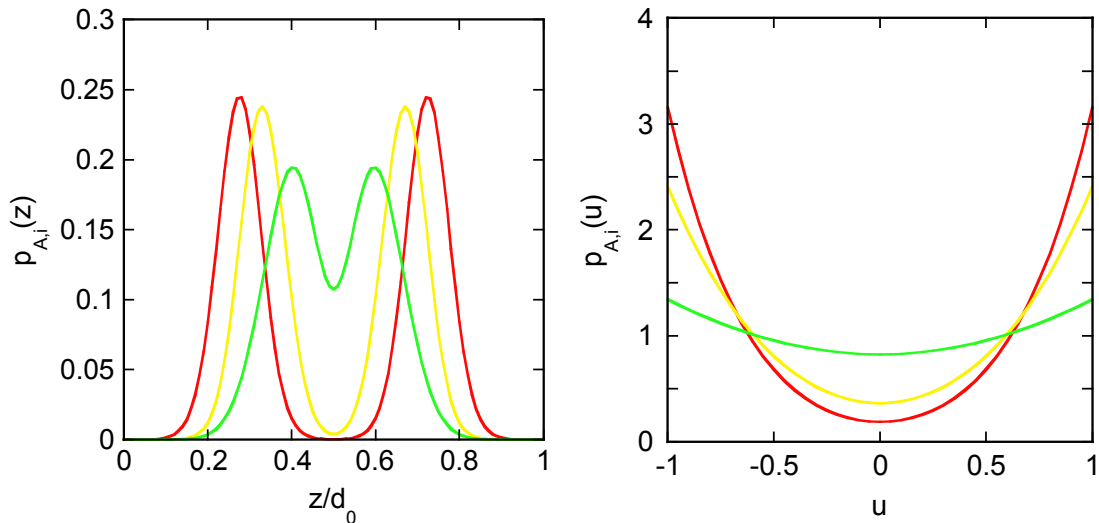
Figure 7.9. Probability distributions in position (left) and orientation (right) for A-block backbone segments (*i*) of [P(aPP)-*b*-P(PS)]$_{28.3k}$ calculated by SCFT. Traces correspond to $i = 1$ (red), $i = 3$ (yellow), and $i = 6$ (green).
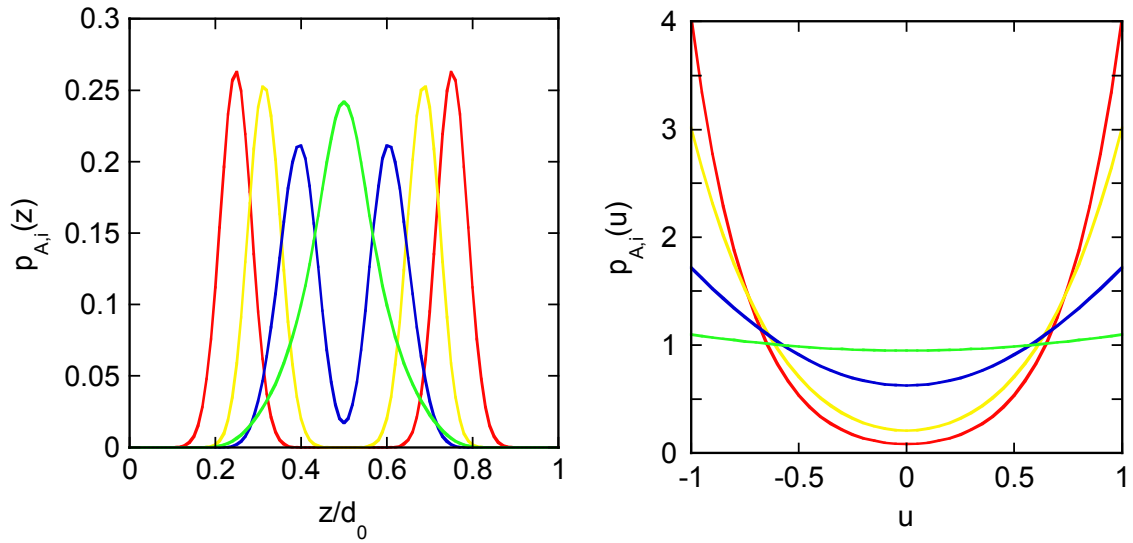
Figure 7.10. Probability distributions in position (left) and orientation (right) for A-block backbone segments (i) of [P(aPP)-b-P(PS)]$_{54.2k}$ calculated by SCFT. Traces correspond to $i = 1$ (red), $i = 4$ (yellow), $i = 8$ (blue), and $i = 12$ (green).
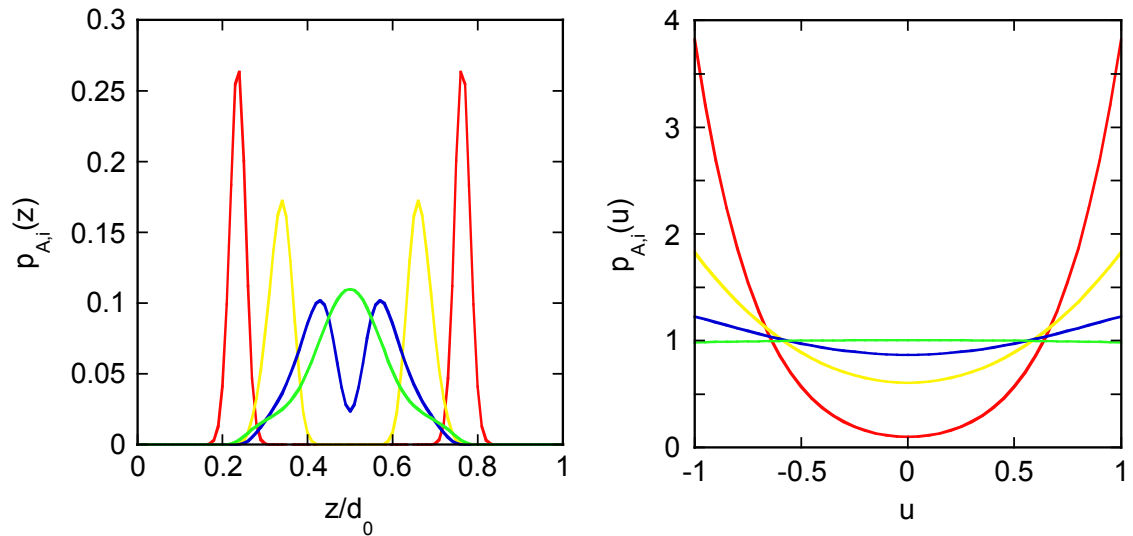
Figure 7.11. Probability distributions in position (left) and orientation (right) for A-block backbone segments (i) of [P(aPP)-b-P(PS)]$_{153k}$ calculated by SCFT. Traces correspond to $i = 1$ (red), $i = 11$ (yellow), $i = 21$ (blue), and $i = 35$ (green).

7.5   Discussion

The quantitative agreement between our experiment and SCFT allows us to challenge the prevailing belief that bottlebrush block polymers in an ordered lamellar state are highly extended in an orientation perpendicular to the lamellar plane. The only experimental evidence for this is the near-linear dependence of the domain spacing, d_0, with the molar mass (or DP) of the molecule. There are two space-filling ways for this to occur: either a bilayer arrangement with each block extending halfway across its respective domain or an interdigitated arrangement where each block extends completely across the domain. Apart from small deviations due to bending of the molecules and end effects, the domain spacing of these two possibilities would obey $d_0 = 2L$ and $d_0 = L$, respectively. In either case, d_0 scales linearly with L, which is proportional to DP. Surprisingly, the only previous study to report how the lamellar period compared with the length of a bottlebrush molecule was that of Xia et $al.$[76] The authors found that $d_0 \approx L$ and concluded that the molecular packing was interdigitated. However, no explanation was given as to why the molecules would pack this way. We posit that this type of packing is unlikely because interdigitation doubles the number of interfaces while offering no obvious free energy gain to compensate for the increase in interfacial energy. Gu et $al.$ have suggested the bilayer arrangement, but without confirming that their experimental data satisfied $d_0 \approx 2L$.[184] This conclusion was instead based on simulations, which predicted the ends of the backbone to be concentrated in the middle of the domains, consistent with our SCFT results.

Our study is the first to pay particular attention to how the lamellar period compares to the extended length of the backbone. Apart from our smallest molecules, d_0 is significantly less than $2L$ implying that the bottlebrushes are not highly extended. Of course, very short molecules will have extended backbones when the persistence length of the backbone is comparable to its length, which explains why d_0 is closer to $2L$ for short molecules. The fact that d_0 actually exceeds $2L$ for our smallest molecule is also easily explained. When the backbone becomes short relative to the side chains, the molecules start to resemble heteroarm star-block copolymers. Consequently, d_0 is then

dictated by the length of the side chains rather than the backbone, which in turn implies that the exponent γ must approach zero in the limit of small L. This is consistent with our results in Figure 7.4. The reduction in γ may also provide an explanation for previous experimental results by Gu *et al.* in which two distinct series of symmetric diblock bottlebrush polymers were synthesized with PS and polylactide (PLA) side chains.[184] The first series involved 2.4 kg/mol side chains on both blocks while the second series had blocks with ~4.5 kg/mol side chains. Both series where fit to a power law $d_0 \sim DP^\gamma$ assuming a constant exponent, *γ*, and the first series was found to exhibit a greater scaling exponent than the second series. The range of backbone DP in that study did not extend as low as our samples, but it may have been low enough to be effected by the finite length of the side chains relative to L. Naturally, the bottlebrushes with the longer side chains would have been affected by a greater degree, which could explain the slightly smaller exponent obtained for the second series of bottlebrushes.

For our larger molecules, where the length of the side chains is small relative to the backbone, we obtained results that are consistent with previous experimental studies. As was the case in the study by Xia *et al.*,[76] our lamellar periods are similar to the length of the backbone, $d_0 \approx L$. However, as clearly illustrated by our SCFT calculations, the reason is not the interdigitation of highly extended chains. Rather, it is because of the significant bending of the molecules. Furthermore, our exponent γ = 0.88 at large L is similar to the exponents γ = 0.91 and 0.84 reported by Gu *et al.* for their two different bottlebrush series.[184] Although these exponents are larger than those of linear diblocks, presumably because of the effective stiffness of the backbone due to crowding of the side chains, they are still less than unity, which is expected for highly extended conformations. Of course, the exponent is not universal and would likely adopt values closer to 1 for bottlebrushes with more crowded side chains. Note that Hong *et al.*[203] have reported exponents very close to 1, but this was for thin films where the bottlebrush assembly was constrained by a substrate that may have restricted their bending, thus resulting in more extended conformations and larger exponents.

Although the bottlebrushes produce significantly larger exponents than their linear counterparts, they should eventually behave the same in the limit of large L. Ultimately, the persistence length and diameter of the bottlebrush will become negligible relative to L, and the bottlebrush will begin to resemble a very large linear diblock with Gaussian statistics. Thus, the exponent should eventually decrease towards $\gamma = 2/3$, and the lamellar period should become small relative to L. It is unlikely that experiments would be able to access the equilibrium behavior in this extreme limit, but it may be possible to reach molar masses where the exponent starts to decrease.

7.6   Conclusions

We have developed the first quantitative theory for the melt state of bottlebrush block polymers and have validated its predictions with experimental results. Specifically, we synthesized lamellar-forming bottlebrush diblock polymers of different lengths, L, and determined their lamellar periods, d_0, using SAXS measurements. The scaling $d_0 \propto L^{\gamma}$ exhibited a variable exponent ranging from $\gamma < 0.3$ at small L and approaching $\gamma = 1$ at high L. We attribute this behavior to the transition from star-like to brush-like molecules as the backbone becomes long relative to the length of the side chains. The actual molecular parameters associated with the block polymer samples were then used to define the input parameters for the theoretical calculations, resulting in remarkable quantitative agreement between the theoretical predictions of the lamellar domain spacing and the experimental data. These theoretical results conclusively establish the molecular origins of the domain scaling behavior of lamellar forming diblock bottlebrush polymers.

The SCFT approach is based on a realistic microscopic model capable of explicitly incorporating the large number of branches (or side chains) characteristic of bottlebrush molecules. To account for the strong steric interactions resulting from the crowding of densely packed branches, which is responsible for reducing the flexibility of a bottlebrush, we model the backbone using a semiflexible worm-like chain with an adjustable persistence length, ξ_b. The dense packing of long branches allows us to ignore the volume of the backbone and its enthalpic interactions with the branches, yet the

model still involves nine different parameters. Nevertheless, all the parameters apart from ξ_b can be estimated from experiment.

The close agreement between theory and experiment was achieved using a persistence length of ξ_b = 5 backbone units (*i.e.,* 3.1 nm). This result implies that bottlebrushes are more flexible in the melt state than generally assumed, consistent with recent simulations by Cao *et al.*[201] who find that the effective Kuhn length of the backbone ($b_K = 2\xi_b$) in the melt is comparable to the diameter of the bottlebrush. Such macromolecular flexibility directly influences packing of the bottlebrushes within the lamellar morphology. Contrary to the generally accepted hypothesis that the chains are highly extended in either an interdigitated (*i.e.,* $d_0 \approx L$) or end-to-end bilayer (*i.e.,* $d_0 \approx 2L$) arrangement, our calculations predict considerable bending of the backbones. Although the backbones are highly oriented at the A-B block junction, the orientational order drops off precipitously as the molecules emerge from the interfacial region. A more gradual decline in orientation follows within the essentially pure A and B domains of the high molar mass diblocks, and the ends of the backbones show broad positional distributions with no orientational preference. This behavior is indicative of a random walk, albeit with a sizable step size (or Kuhn length).

This investigation highlights the importance of combining the development of state-of-the-art theory with advances in experimental polymer science. The iterative interplay between the theoretical model presented here, and the synthesis and characterization of a judiciously chosen set of model materials, has produced definitive explanations for the self-assembly behavior of bottlebrush block polymers.

7.7   Methods and Experimental Details

7.7.1   Characterization Methods

SAXS and AFM instrumentation and sample preparation are described in chapter 6. AFM images in Figure 7.3 were taken using PeakForce mode AFM and analyzed by Tom Rions-Maehren. TEM samples were prepared by first solvent casting from a dilute THF

solution in 5-mL PTFE beakers. The THF was allowed to evaporate over several days before drying under vacuum and thermally annealing at 150 °C for 4 h. Ultrathin films of ~50 nm thickness were then cut from the samples using an ultra-microtome and stained with OsO_4. TEM samples were prepared and imaged by Yusuke Asai.

7.7.2   Theoretical Calculations

Prof. Mark Matsen carried out all SCFT calculations to obtain the theory data for this chapter. Details of the calculation methods were composed by Prof. Matsen and are provided below for completeness.

The solution of the SCFT for our theoretical model follows well-established procedures.[204-206] Because we can ignore the interactions involving the backbone, there are only fields acting on the A and B segments, $w_A(\mathbf{r})$ and $w_B(\mathbf{r})$, respectively. The first step in the calculation is to solve the statistical mechanics for the A and B concentrations, $\phi_A(\mathbf{r})$ and $\phi_B(\mathbf{r})$, of a single bottlebrush subject to the fields. In doing so, we ignore the small volume occupied by the backbones. The mathematics for the worm-like backbone are performed using the spectral method in ref 204 and the Gaussian side chains are handled with the simpler spectral method introduced in ref 205. The next step in the calculation is to adjust the fields so as to satisfy $w_A(\mathbf{r}) - w_B(\mathbf{r}) = \chi N[\phi_B(\mathbf{r}) - \phi_A(\mathbf{r})]$ and $\phi_A(\mathbf{r}) + \phi_B(\mathbf{r}) = 1$, where $N = m_A N_A + m_B N_B$ is the total polymerization of the bottlebrush. This is done using the Anderson-mixing scheme described in ref 206. The final step in the calculation is to minimize the free energy with respect to the lamellar period, d_0, for which we again follow ref 206.

Table 7.3 provides the SCFT predictions of d_0 using different input values of the ξ_b and χ parameters, many of which were plotted in Figure 7.5.

Table 7.3. SCFT predictions of d_0 (nm) calculated with different values of ξ_b and χ.

Sample Label	Experiment		SCFT[a]				SCFT (χ + 25%)[b]			
	L	d_0	$\xi_b = 5$	$\xi_b = 6$	$\xi_b = 7$	$\xi_b = 8$	$\xi_b = 4$	$\xi_b = 5$	$\xi_b = 6$	$\xi_b = 7$
[P(aPP)-b-P(PS)]$_{28.3k}$	6.3	16.4	14.7	14.8	14.9	15.0	15.5	15.6	15.7	15.8
[P(aPP)-b-P(PS)]$_{41.8k}$	9.6	18.3	17.8	18.0	18.2	18.4	18.2	18.5	18.8	18.9
[P(aPP)-b-P(PS)]$_{54.2k}$	12.1	21.0	20.0	20.3	20.5	20.7	20.3	20.7	21.0	21.2
[P(aPP)-b-P(PS)]$_{95.9k}$	20.8	26.3	27.8	28.5	29.0	29.4	27.8	28.6	29.3	29.8
[P(aPP)-b-P(PS)]$_{123k}$	30.0	32.2	36.5	37.6	38.4	39.1	36.3	37.6	38.6	39.5
[P(aPP)-b-P(PS)]$_{153k}$	34.3	38.7	39.3	40.4	41.3	42.0	39.0	40.4	41.5	42.3
[P(aPP)-b-P(PS)]$_{303k}$	73.6	73.9	69.9	72.6	74.8	76.6	68.9	72.2	74.8	77.0
[P(aPP)-b-P(PS)]$_{368k}$	87.2	81.6	79.3	82.4	85.0	87.6	78.2	82.0	85.0	87.6

[a]SCFT predictions using an estimated χ based on the relationship $\chi N = X*(M_n/\rho RT)$ where $X_{PS-PEP} = 1655/T(K) + 0.57$ using a $v_{ref} = 118$ Å^3.[193] [b]SCFT predictions with χ increased by 25% relative to the initial estimates. Persistence length ξ_b is quoted in terms of backbone units (0.62 nm), and all other lengths are in units of nm.

Chapter 8

Outlook for Ongoing Research and Preliminary Results

8.1 Introduction

The research presented in this dissertation encompasses several facets of newly developed bottlebrush polymer systems, including methods of molecular synthesis, rheological properties, and the self-assembly of bottlebrush block polymer materials. While the results achieved in these areas provide advancements to our understanding of bottlebrush polymers, they also incite new questions and stimulate ongoing research opportunities. In this chapter, we describe potential directions for future research on linear/bottlebrush polymer blends (section 8.2) and for additional diblock polymer systems (section 8.3). Preliminary results are also presented, which describe the rheological properties of several linear/bottlebrush aPP blends.

8.2   Bottlebrush/Linear Polymer Blends

8.2.1   Phase Behavior of Blends by SANS

Investigation of polymer blends containing both linear and bottlebrush components is of fundamental and practical interest. First, specific architectural contributions to the free energy of mixing imposed by bottlebrush molecules have not been quantitatively determined in the literature, and are expected to introduce significant excess entropy effects. A recent study by Mitra *et al.*[207] examined the miscibility of linear/bottlebrush PS blends in a thin film geometry using secondary ion mass spectroscopy (SIMS). The results displayed phase miscibility in blends with a short linear PS component, but phase separation when the linear PS was sufficiently large (> 8 times the bottlebrush side chain length). Furthermore, the phase separated blends revealed a preferential migration of the bottlebrush species to the thin film interfaces (both surface and substrate). Investigations of linear/bottlebrush polymer blends in the bulk remain unexplored and may facilitate determination of entropically driven architectural contributions to the free energy of mixing. Specifically, small-angle neutron scattering (SANS) analysis of carefully prepared athermal blends may enable quantitative evaluation of the effective χ interaction parameter. To this end, polyolefin blends provide model systems. The simple chemical makeup introduces minimal van der Waals enthalpic interactions and negligible combinatorial entropy effects, resulting in a lack of any dominant factor controlling the mixing thermodynamics.[208] Consequently, the stability of polyolefins blends is particularly sensitive to structural differences between components. Future research directed towards SANS investigation of either aPP- or PEP-based linear/bottlebrush blends would provide essential new information in this area.

To achieve adequate scattering contrast for SANS measurements, one of the blend components must be sufficiently deuterium labeled. If blends are prepared using linear and bottlebrush PEP (as opposed to aPP) then the labeling will be relatively straightforward. Typical synthesis of PEP involves anionic polymerization of 1,4-poly(isoprene) followed by catalytic hydrogenation of the double bonds. This route

affords the ability to prepare different batches of hydrogenated PEP (h-PEP) and deuterated PEP (d-PEP) by saturating the poly(isoprene) precursor with H_2 and D_2 gas, respectively. Therefore h-PEP or d-PEP could be used directly as the linear blend component, and a hydroxyl-terminated h-PEP or d-PEP could be used for macromonomer synthesis (and ultimately bottlebrush synthesis) following the procedures outlined in chapter 5. This allows either the linear or bottlebrush component to be deuterium labeled. Blend samples based on PEP components may also benefit from the low T_g. This promotes relatively fast dynamics at room temperature and minimizes annealing efforts or any kinetic difficulties in achieving the equilibrium state.

If SANS studies are to be carried out using aPP components, the polymers would not be as easy to deuterate since no initial unsaturations are present. Although, researchers in our group have recently discovered that saturated polyolefins can be deuterium labeled by hydrogen-deuterium (H-D) exchange using the heterogeneous Pt–Re/SiO$_2$ catalyst.[209] This enables fractional deuteration of linear aPP, up to ~25% exchange, which may be adequate for providing SANS contrast. However, labeling of the bottlebrush component has been attempted over the course of this thesis work and has not yet been successful. Given the full synthetic scheme for creating aPP bottlebrushes there are four different points in which H-D exchange of the aPP chains could be carried out, *viz.*, vinyl-terminated aPP (aPP-VT), hydroxyl-terminated aPP (aPP-OH), norbornene-terminated aPP (aPP-NB), and the final poly(aPP-NB) bottlebrushes. Attempting the H-D exchange reaction, which utilizes the same conditions as typical heterogeneous hydrogenation (*i.e.,* high temperature and high pressure gas), on either aPP-VT or aPP-NB would irreversibly saturate the functional end-group needed for bottlebrush synthesis. Furthermore, H-D exchange directly on the poly(aPP-NB) bottlebrush molecules was impractical, because (1) the aPP branches are connected to the backbone with an ester bond that does not remain protected under the H-D exchange conditions, and (2) the mechanism for H-D exchange requires specific binding of the polymer chain on the catalyst active sites that are almost certainly inhibited by the densely branched bottlebrush structure. Therefore, the most logical intermediate to attempt H-D exchange was the aPP-OH molecules. Four

H-D exchange attempts were carried out at 100 °C (typical for hydroxyl-terminated polymers), 120 °C, 145 °C, and 170 °C (typical for H-D exchange reactions). Analysis of each product by ^{1}H NMR and ^{2}H NMR revealed a temperature gap in which the hydroxyl end groups were deleteriously affected prior to any effective H-D exchange. Specifically, no successful deuteration was measured below 170 °C, while all of the hydroxyl chain ends were lost by 145 °C. These results point to the advantage in using PEP, or other species with unsaturated precursors, for the proposed SANS studies of the bottlebrush/linear blends.

8.2.2   Rheology of Blends

The investigation of polyolefin-based blends is also motivated by their potential utility in practical applications. Blending is a common industrial practice used to tailor material properties such as toughness, impact strength, recyclability, and processability. Modifications can be straightforward in the case of miscible blends, in which the hybrid material exhibits intermediate properties relative to the pure components. However, most polymer blends are immiscible, leading to characteristics that are highly dependent on the processing conditions and the resultant two-phase blend morphology. Thus, knowledge of the component miscibility is imperative for effective design of new polymer blends. Beyond binary blends with a significant fraction of both components, the rheological properties of polymers can also be altered substantially with only minor fractions of an additive agent. The use of additives is frequently used in polymeric materials to tune flow properties such as viscosity, yield stress, adhesion or thixotropy.[210] Since bottlebrush polymers are "specialty" molecules with no current large-scale production, any significant improvements to low-cost commodity polymers (such as polypropylene) produced by blending with small quantities of a bottlebrush component may prove to be a valuable advancement. Further research focused on the rheology of linear/bottlebrush aPP blends would yield information as to how the presence of bottlebrushes influences the viscosity and elasticity of the polymer melts. Furthermore, aPP is known to be melt miscible with isotactic polypropylene (iPP).[211-213] Therefore, it may also be prudent to

explore the rheology of linear/bottlebrush blends with a commercially viable iPP linear component.

8.2.3   Preliminary Data: Linear/Bottlebrush Blend Rheology

This section presents the preliminary rheological data acquired for linear/bottlebrush aPP blends. Three of the poly(aPP-NB) bottlebrushes presented in chapter 4 with backbone *DP*s of 26, 74, and 215 were chosen to create blends with a linear aPP material, which was provided by ExxonMobil and is also characterized in chapter 4. Blends were prepared by co-dissolving both components in benzene and freeze-drying under high vacuum, yielding optically transparent blend samples. Eight different blends were produced at compositions of 50 wt%, 25 wt%, and 10 wt% of the bottlebrush species as summarized in Table 8.1. The linear rheological behavior of each blend was analyzed *via* small-amplitude oscillatory shear measurements employing the same procedures utilized for the neat bottlebrush samples in chapters 4 and 5.

Table 8.1. Summary of linear/bottlebrush aPP blends.

Blend Sample	poly(aPP-NB) bottlebrush specifications [a]			
	M_w (kg/mol)[b]	Đ [b]	*DP* [c]	wt% in blend
linear/brush_26 (50/50)	53.1	1.03	26	50
linear/brush_26 (75/25)	53.1	1.03	26	25
linear/brush_26 (90/10)	53.1	1.03	26	10
linear/brush_74 (50/50)	152	1.03	74	50
linear/brush_74 (75/25)	152	1.03	74	25
linear/brush_74 (90/10)	152	1.03	74	10
linear/brush_215 (50/50)	440	1.12	215	50
linear/brush_215 (75/25)	440	1.12	215	25

[a]Bottlebrush sample characterizations reproduced from Table 4.1. [b]Determined by SEC-MALLS in THF. [c]Weight-average degree of polymerization of poly(norbornene) backbone using M_{branch} = 2.05 kg/mol. The same linear component was used for each blend. This aPP_Linear sample was characterized in Table 4.1 with M_w = 203 kg/mol and Đ = 1.57.

8.2.3.1   Master Curves of Linear/Bottlebrush Blends

Figures 8.1, 8.2, and 8.3 display the pure component master curves of aPP_Linear and poly(aPP-NB) in black and gray, respectively, along with that of the corresponding blend sample. Each blend master curve was assembled by TTS of frequency sweep data obtained at various temperatures, and normalized to a common reference temperature of $T_{ref} = T_g + 34$ °C. The master curves for linear/brush_26 blends are shown in Figure 8.1. The 50/50 blend displays intermediate relaxation scaling between the two pure components with no indication of a rubbery plateau. A dramatic shift is then observed moving to the 75/25 blend, which displays relaxation much closer aPP_Linear. This blend retains a rubbery plateau region indicative of a well-entangled network, albeit with a lower plateau modulus and a reduced longest relaxation time relative to aPP_Linear. The 90/10 sample shows almost identical behavior to aPP_Linear, indicating the minimal affect of only 10 wt% added poly(aPP-NB)_26.

Figure 8.2 shows the master curves for the linear/brush_74 blends. The 50/50 blend displays similar behavior to linear/brush_26(50/50) with slightly more extended intermediate regime concomitant with the longer relaxation time of neat poly(app-NB)_74 compared to poly(aPP-NB)_26. The master curve of the 75/25 blend does not change as substantially as was seen in the linear/brush_26 blends. In this case, the rubbery plateau re-appears but is not as expansive as linear/brush_26(75/25). In fact, the plateau does not achieve a similar shape to linear/brush_26(75/25) until the 90/10 blend, shown as the bottom plot in Figure 8.2. This suggests that 10% of the poly(aPP-NB)_74 has a larger impact on entanglement network than 10% of poly(aPP-NB)_26.
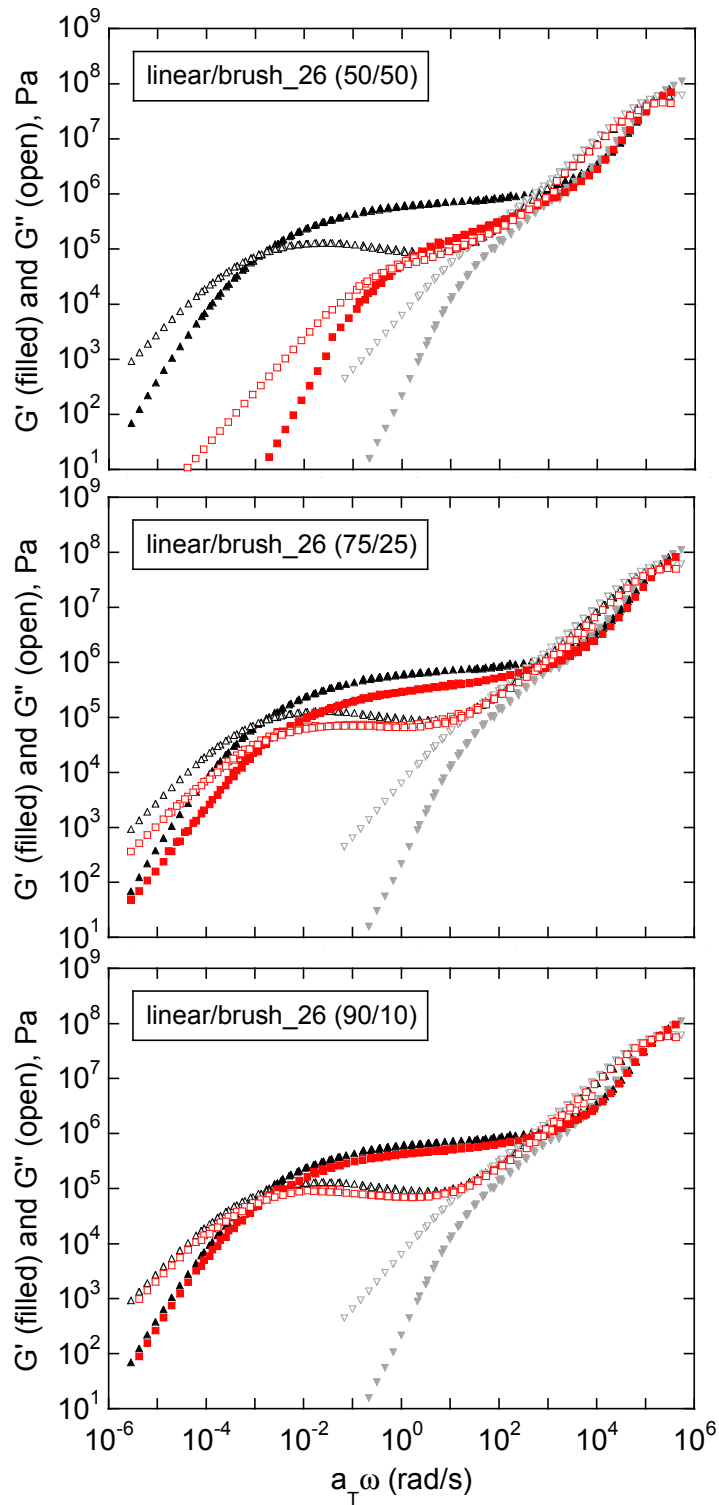
Figure 8.1. Master curves of linear/brush_26 blend samples (red squares). Master curves of neat aPP_Linear (black triangles) and poly(aPP-NB)_26 (gray inverse triangles) are provided in each plot for reference.
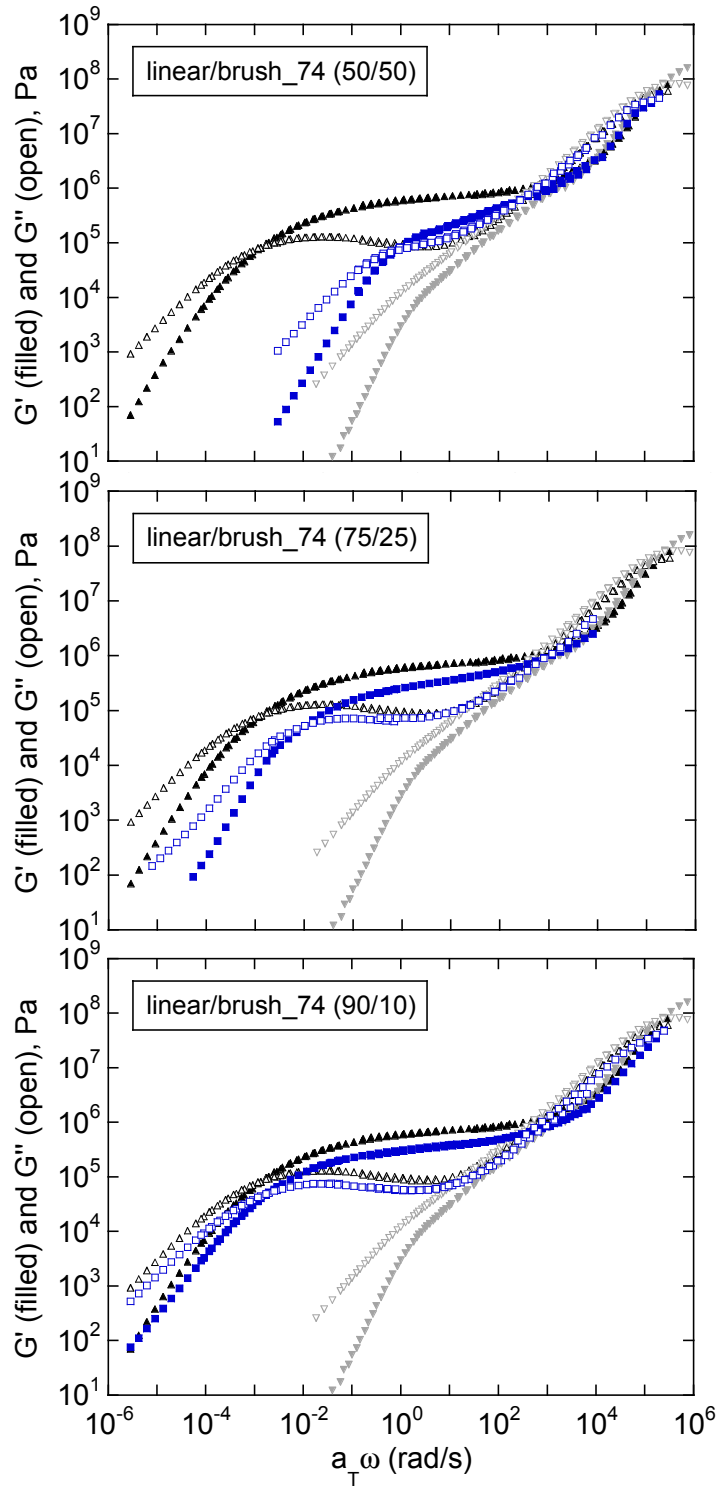
Figure 8.2. Master curves of linear/brush_74 blend samples (blue squares). Master curves of neat aPP_Linear (black triangles) and poly(aPP-NB)_74 (gray inverse triangles) are provided in each plot for reference.
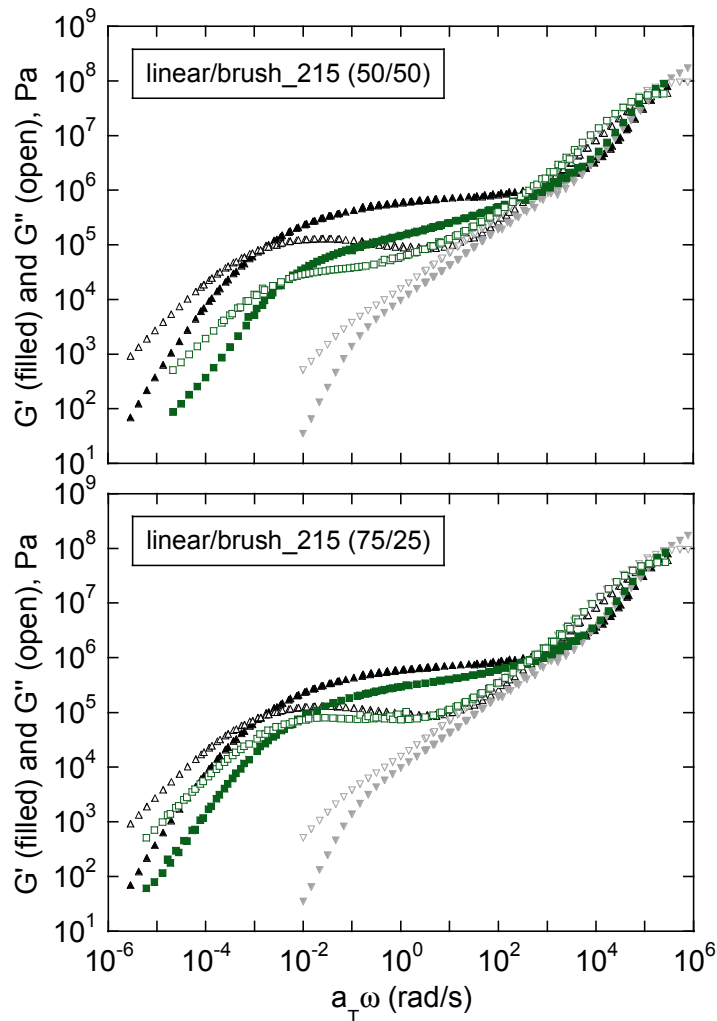
Figure 8.3. Master curves of linear/brush_215 blend samples (green squares). Master curves of neat aPP_Linear (black triangles) and poly(aPP-NB)_215 (gray inverse triangles) are provided in each plot for reference.

The final blend series using poly(aPP-NB)_215 includes only the 50/50 and 75/25 blends due to limited materials (Figure 8.3). The intermediate region of the 50/50 blend extends to a much longer relaxation time than the previous two 50/50 blends, demonstrating a lower degree of entanglement dilution. There are two potential explanations for this behavior. First, the poly(aPP-NB)_215 molecules have 10 times the molar mass of poly(aPP-NB)_26. Blends with the same weight fraction of bottlebrush molecules will therefore contain a tenfold higher concentration of poly(aPP-NB)_26

molecules compared to poly(aPP-NB)_215. Consequently, the smaller bottlebrush molecules in linear/brush_26 blends are able to effectively disrupt entanglements, whereas blends with larger poly(aPP-NB)_215 molecules may contain a higher percentage of regions that are locally devoid of the bottlebrush species. A second possibility is that the higher molar mass of the poly(aPP-NB)_215 bottlebrush component more strongly promotes phase separation, leading to an inhomogeneous blend with large domains of pure aPP_Linear. Despite the fact that our samples were optically transparent following blend preparation, we cannot say with certainty that all of the blends remained in a single-phase state because the refractive indices of the two components are expected to be equivalent. With no contrast in refractive index, even a phase-separated mixture may appear optically transparent. Furthermore, DSC measurements were unable to give any information regarding miscibility, since both components in all the blends have T_g's within 3 °C. This is not within the sensitivity of a typical T_g measurement, so only one transition arises regardless of the component miscibility.

8.2.3.2   Van Gurp-Palmen Plots

Figure 8.4 displays the dynamic response data for each blend sample plotted as phase angle (δ) versus complex modulus (G*). Each plot overlays the aPP_Linear data as a reference for the linear/bottlebrush blends. The plots exhibit a single, well-defined minimum, corresponding to the rubbery plateau region in the dynamic master curves. While the independent side chain and backbone relaxation processes were distinguishable in similar plots of the pure poly(aPP-NB) samples, only one predominant relaxation minimum is observed for the curves in Figure 8.4. This is because the elasticity of the blend responses is dominated by the entanglement of aPP_Linear component, which overpowers the subtle changes in phase angle corresponding to the bottlebrush relaxation modes.
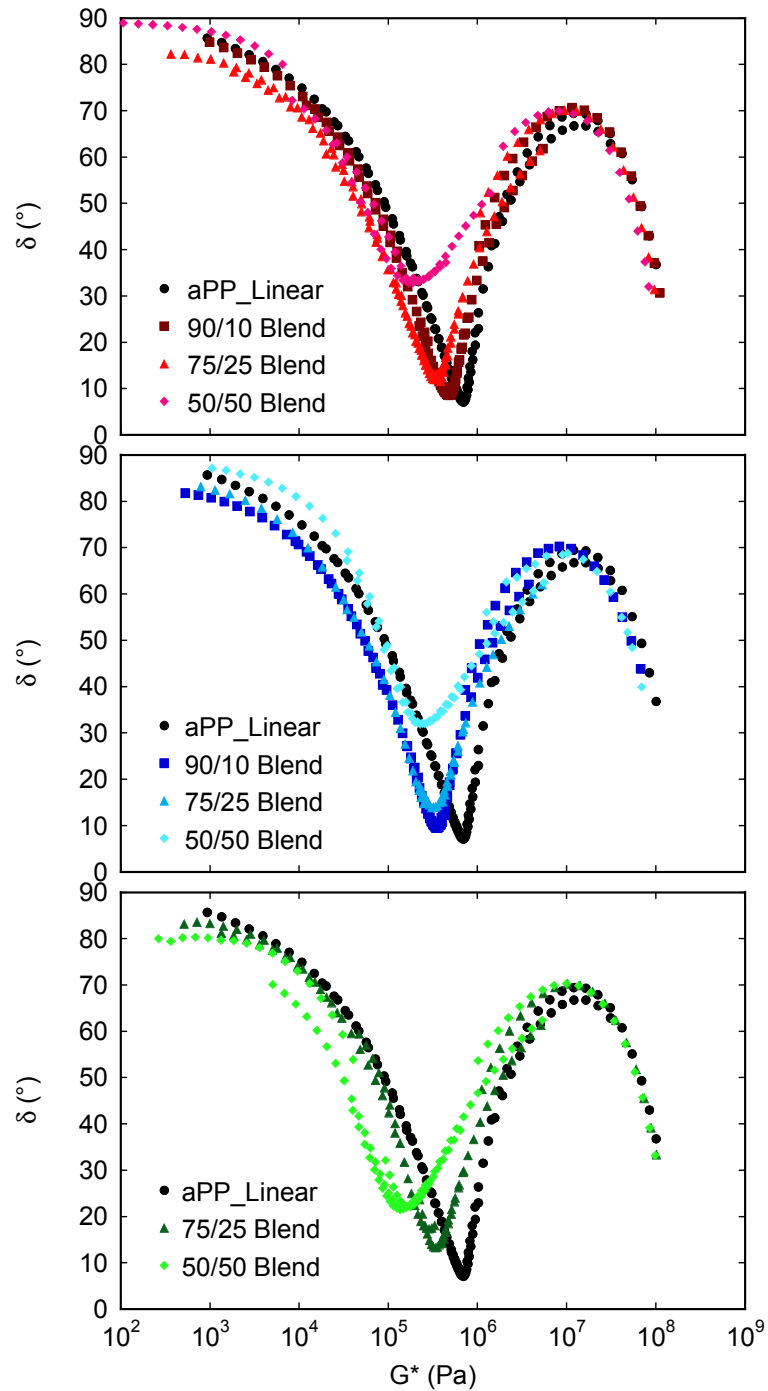
Figure 8.4. Van Gurp-Palmen plots of linear/brush_26 blends (top), linear/brush_74 blends (middle), and linear/brush_215 blends (bottom). The data for neat aPP_Linear is provided in each plot for reference. The linear/brush volume ratios are given in the plot legends.

The plots in Figure 8.4 exhibit curves with minima that shift to a lower G* and a higher phase angle with increasing bottlebrush content. This behavior corresponds to the increasing entanglement dilution effects imposed by poly(aPP-NB) addition.[156] No significant decrease in elasticity is observed in the blends until the 50/50 sample in each plot, and the resulting minimum phase angle is comparable in each case.

These plots also display some effects of thermorheological complexity that may indicate phase separation. Each of the curves exhibits discontinuities in the high modulus regions. This is consistent with the results in section 4.3.5 and arises because of the intrinsic segmental relaxation dynamics of aPP melts.[214] However, the low modulus (high temperature) data, specifically of the linear/brush_215 blends, display additional discontinuities. This could be caused by differences in temperature dependences of two distinct domains within a two-phase mixture. These discontinuities are not shown in the other two blend series with poly(aPP-NB) DPs of 26 and 74, which reinforces the notion that the higher molar mass components may have caused phase separation.

8.2.3.3   Zero-Shear Viscosity

The reduced zero shear viscosity (η_0) of each sample is plotted as a function of weight average molar mass on a log-log scale in Figure 8.5. These data points were calculated using the complex viscosity information from the SAOS measurements as defined by equation 4.1. The values at the extremes of the plot reflect the pure component η_0 values. These viscosities converge on the left since the same aPP_Linear sample was used for all the blends, whereas the poly(aPP-NB)_26, 74, and 215 samples exhibit distinct values on the right-hand side. Unfortunately, there does not seem to be any clear trend that emerges in comparing the data with different bottlebrush components. The most striking feature of this plot is the differences in η_0 for the 50 wt% blends. The linear/brush_215 (50/50) blend exhibits a η_0 value that is 100 times greater than the other two samples at the same composition. This is another indication that phase separation may have occurred.
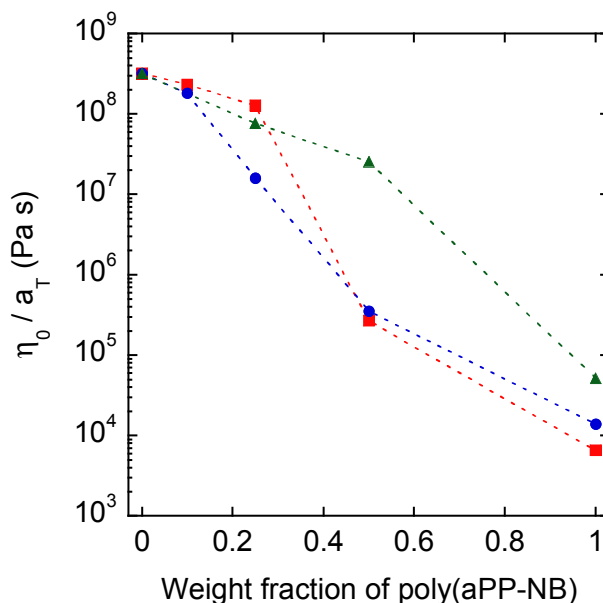
Figure 8.5. Reduced zero-shear viscosity versus weight fraction of the poly(aPP-NB) bottlebrush component for each blend sample. Markers denote the linear/brush_26 blends (squares), linear/brush_74 blends (circles), and linear/brush_215 blends (triangles).

8.2.3.4   Discussion

Analysis of the rheological behavior is essential to understanding the properties of linear/brush blends. However, without a definitive knowledge of the miscibility and phase behavior of these systems, it is difficult to draw sound conclusions. Although complete miscibility was assumed at the beginning of the section, the data presented shows potential indications of phase separation, such as the lack of clean superposition in the van Gurp-Palmen plots. SANS investigation of model linear/bottlebrush blend samples would provide key insight into the phase behavior. In addition, rheological investigation of more blend samples, potentially with bottlebrush components of more extreme cylindrical or star-like conformations could supplement the existing data, and elucidate trends that were not conclusively determined thus far. With a better understanding of how the backbone and side chain lengths alter the bulk properties of the blends, highly tuned materials can by produced toward specific applications. From a practical standpoint, it may be particularly interesting to blend bottlebrushes with

crystalline iPP, or even incorporate them into epoxy materials, to examine if there are any attractive toughening effects.

8.2.3.5   Experimental Section

Blends were prepared by co-dissolving the desired amount of each component in benzene to give a 10 wt% polymer solution. Generally, aPP_Linear required several hours to fully dissolve because of its high entanglement density. The poly(aPP-NB) bottlebrushes typically dissolved in less than 10 min. Once both components were fully dissolved the solution was vitrified by submerging the flask in liquid nitrogen, the headspace was evacuated under high vacuum, and the liquid nitrogen was then removed to allow the flask to warm to room temperature. The flask was left under dynamic vacuum overnight to permit slow sublimation of the benzene away from the polymer. The resulting blends were optically transparent and were usually very "stretchy" materials. Qualitatively, the samples could be stretched to extensional strains far greater than either of the pure components. This is likely because the blends were softer than the aPP_Linear, which behaved like a hard rubber, but more solid-like than the neat bottlebrush samples, which generally behaved as extremely viscous, sticky liquids. The blend samples could be stretched several meters without fracturing for a samples with initial cross sections of ~1 cm^2. Tensile testing of the blends may yield more quantitative data on extensional properties. However, no tensile tests were performed because of the substantial time-dependence of the viscoelastic properties. Unlike elastomers, the aPP_Linear and blend samples display elasticity because of the transient entanglement network and do not contain any permanent chemical crosslinks. Therefore, a significant amount of stress relaxation is expected to occur over the tensile experiment time, resulting in unreliable stress (or modulus) data.

The dynamic responses for all of the linear/brush blends were measured by SAOS with 8-mm parallel plates at various temperatures over a frequency range of 0.01–100 rad/s. Considerable care was taken in shifting the blend rheology data by TTS in order to properly reference to $T_{ref} = T_g + 34$ °C and appropriately compare the blend master curves with the aPP_Linear and poly(aPP-NB) samples. This was not always a straightforward

task because the T_g of each blend differed by ±2 °C, while the measurements for each blend were taken at the same temperatures (*i.e.* −4, 0, 10, 25, and 40 °C). Thus, the 25 °C data set did not always match precisely with T_g + 34 °C. To appropriately shift the data, the 25 °C set was chosen to complete the TTS shifting, and then the whole master curve was shifted slightly to reflect the same T_{ref} as the linear and pure poly(aPP-NB) samples. The results of these shifting procedures are presented as the master curves in Figures 8.1, 8.2, and 8.3.

8.3 Bottlebrush Block Polymers

The most recent research for this project has focused on the self-assembly of diblock bottlebrush polymers. This is a relatively new area of study with many unexplored questions that present opportunities for further research. For instance, what is the threshold segregation strength $(\chi N)_{ODT}$ required for an order-disorder transition to occur? Is it even valid to combine χ and N as a parameter of interest in bottlebrush systems? How is N defined in this case? How are the individual enthalpic and entropic driving forces for self-assembly different from linear diblocks? How do the adjustable molecular geometries affect the free energy of different ordered phases? These are all important questions that merit further experimental and theoretical investigation.

8.3.1 Order-Disorder Phase Transition

One of the enticing open research questions relating to bottlebrush block polymers is how the molecular architecture influences the ordering transitions from a thermodynamic perspective. For linear A-B diblock polymers, the transition to an ordered phase from the homogenous disordered state is driven by minimization of unfavorable A/B segment contacts. A balance between minimizing the interfacial area of A/B domains and maximizing the conformational entropy of polymer chains then dictates the particular ordered phase that develops. It is expected that these effects would be considerably altered in diblock bottlebrush polymers. For instance, densely branched bottlebrush molecules contain shielded polymer segments near the backbone chains that do not

encounter frequent intermolecular interactions. This changes the amount of A/B contacts per mass and changes the effective χ interaction parameter for a diblock bottlebrush melt. Accordingly, the change in system enthalpy (ΔH) upon ordering may not be as large as in the corresponding linear diblock system. The change in entropy upon ordering (ΔS) may also be quite different. Bottlebrush polymers are composed of tethered side chains that are much more constrained, even in the disordered phase, than linear Gaussian coils. Therefore, the degree of chain stretching may not change substantially upon ordering, causing a reduced ΔS of transition compared to linear diblocks. Based on these considerations, there is reason to believe that both entropic and enthalpic contributions to χ may be reduced compared to linear diblock polymers, which could lead to a more sensitive balance between the competing effects. (Note: this argument does not discuss the configurational entropy, which always favors the well-mixed disordered phase).

Evaluating the segregation strength introduces a further complexity of bottlebrush polymer phase behavior. For linear block polymers, χN is utilized as a combined parameter for segregation strength that quantifies the incompatibility between the constituent blocks. Mean field theory predicts a constant value of $\chi N = 10.5$ at the order-disorder transition for symmetric ($\phi = 0.5$) A-B diblock polymers.[215] However, simplifying assumptions of linear diblock polymers that lead to this prediction are invalid for bottlebrush molecules, and this prediction is expected to fail. Moreover, it is unlikely that using χN as a single compound parameter is strictly acceptable for these polymers since the individual terms of interfacial energy and chain stretching energy that govern phase behavior likely scale differently with χ and N. Consider, for example, the interfacial area per molecule in the lamellar phase. For a linear diblock polymer, the interfacial area per chain is assumed to exhibit a constant scaling with N. However, this may not be the case for bottlebrush molecules based on our results for lamellar domain spacing (d_0) with increased backbone length (L) presented in chapter 7, in which a scaling of $d_0 \sim L$ was approached at high molar mass. This result implies that the scaling of interfacial area per chain would decrease with increasing N and the absolute interfacial area per molecule may plateau in the high N limit. Therefore, the interfacial energy term

could not be modeled with constant dependence on N. Moreover, increasing N would certainly not be equivalent to decreasing χ in terms of the total segregation strength, signifying a non-constant $(\chi N)_{ODT}$ in this scenario. To appropriately evaluate the conjectures posed here, further experimental results of model diblock polymer melts are needed. Advancements to the theoretical model described in chapter 7 will also be imperative to gain a better understanding of these systems.

8.3.1.1   Suggestions for Future Experiments

Thus far we have only been able to access a T_{ODT} for one of our bottlebrush diblock polymers (PP-PS-1; M_n = 28.3 kg/mol and ϕ_{aPP} = 0.51), presumably due to the high overall molar mass of the majority of our samples. To examine the true architectural impact on the order-disorder transition, it would be instructive to create new bottlebrush diblocks with shorter side chain lengths (*e.g.*, 1 kg/mol per branch). These molecules would enable measurement of T_{ODT} for many samples with variable backbone lengths to gain quantitative information on the N dependence of the transition. Furthermore, a specific diblock sample made to M_n = 28.3 kg/mol and ϕ_{aPP} = 0.51, but with short side chains could be compared with PP-PS-1. Any significant difference in the measured T_{ODT} would provide a direct example of how the molecular architecture affects the order-disorder transition since both polymers would have the same total N and ϕ. Lastly, diblocks with shorter side chains would represent more brush-like, cylindrical molecules at lower molar mass. Thus, exploring these systems would reduce the complexities associated with star-like conformational effects.

From a synthetic standpoint, preparation of bottlebrushes with smaller side chain lengths would introduce larger effects of the side chain end groups. Thus, it may advantageous to prepare macromonomers by anionic polymerization rather than RAFT polymerization to reduce the size of the resultant macromonomer end groups. This method was also advised in a recent study by Teo and Xia[216] to ensure ultimate bottlebrush products with narrow dispersities. This report demonstrated a higher purity of the desired monotelechelic macromonomer species by using a "growth-then-coupling"

technique (which is what the anionic route would entail) rather than a "direct-growth" technique (such as the RAFT polymerization route).

Many of the SAXS results for the initial diblock samples presented in chapter 6 displayed irreversible changes in the profiles upon heating to ~250 °C, in which the scattering patterns often became more resolved. This suggests that the samples that were annealed at 150 °C may have benefited from higher annealing temperature (or time) to evolve towards the equilibrium state. Adjusting these annealing procedures may augment future SAXS experiments.

8.3.2   Highly Asymmetric Branches

We discussed the importance of the specific molecular conformations and how they govern the equilibrium phase of self-assembled bottlebrush diblocks. We mentioned the influence of side chain length asymmetry, but have not explored many systems where this was adjusted. Therefore, a potential area of further research would involve the systematic adjustment of side chain lengths to determine how the phase diagram is changed and to explore whether new spherical or network phases could be attained by tuning this parameter.

The architectural asymmetry introduced by side chain length mismatch is expected to skew the equilibrium phase space and may be exploited to stabilize non-lamellar morphologies. This is comparable to the conformational asymmetry effect of linear diblock polymers with disparate statistical segment length, b, between the two blocks. However, the details of these effects are not necessarily intuitive. In linear diblocks, the block with higher b pervades more space per segment volume ($R_g \sim bN^{1/2}$). It may seem natural to envision the block with a higher b value as analogous to the block with larger side chains in a bottlebrush diblock polymer. However, it is the opposite in terms of conformational asymmetry. The block with smaller b in linear diblocks drives towards a larger interfacial area, because the smaller R_g causes more of the chain segments to reside near the domain interface. The segments of that domain have less freedom to allow a concave interface, and the phase map instead skews to prefer non-lamellar phases in

which the block with a smaller b forms the matrix. This is related to the bottlebrush diblock case in that the block with longer side chains has more segments per molecule that are forced to remain near the interface, which allows that block to preferentially form the matrix phase. Therefore, the effective conformational asymmetry at the interface can be strongly influenced by the choice of side chain length in bottlebrush diblocks with sufficiently long backbones (neglecting brush end effects).

Another competing effect directing the phase behavior is the packing of molecules away from the interfaces. We discussed how differences in preferred interfacial area drive different morphologies, but the morphologies must also be stabilized by favorable packing conditions. In linear polymers, the chains simply seek to avoid stretching and retain Gaussian statistics. For the extreme case of rigid bottlebrushes, packing frustration would be encountered for any non-lamellar phase because the backbones would prefer orientation normal to the domain interfaces. This effect is at odds with any introduced architectural asymmetry, as demonstrated by a study by Rzayev[77] in which a slight decrease in side chain length on one side of a bottlebrush diblock led to an extension in the backbone conformation of the other block to equilize the interfacial area and maintain a lamellar morphology. The polymers used in that study contained significantly higher grafting density (up to 1 branch per backbone bond), so the rigid brush approximation was more suited for that system. Our molecules do not adhere to the assumption of rigid brushes, as demonstrated by the theory results in chapter 7. Therefore, the equilibrium morphologies may be more easily directed by the side chain asymmetry to control the interfacial curvature without incurring restrictions of unfavorable space filling far from the interface. Additional proof of this concept in our molecules would be particularly useful to researchers in the field, since a high percentage of experimental bottlebrush polymer studies utilize ROMP of norbornene-functional macromonomers and attain the same branch density as our polymers.

An alternative to conducting exploratory research to discover how side chain asymmetries influence the thermodynamic phase diagram, specific morphologies could be targeted with designed molecular geometries. From a space-filling standpoint,

stabilizing cylindrical or spherical phases using compact molecular building blocks would require wedge-like or conical block dimensions (to form cylinders or spheres, respectively). An ideal scenario for diblock bottlebrush molecules may be a smooth gradient in side chain length, in which the end of the majority block backbone possesses the longest side chains and the end of the minority block contains the smallest side chains. This would undoubtedly entail demanding synthetic procedures to accomplish, but it may serve well as a proof of concept to stabilize desired phases.

The final consideration here refers to the very practical limit in which backbone chains are not significantly longer than the side chains. This is the region where we claim the molecules are becoming increasingly compact due to the addition of more branches to the same local space (chapter 4). This is also the region in which the lamellar domain size scaling revealed a very weak dependence near $d_0 \sim L^{0.3}$ (chapter 7). To maintain constant density, this implies that the interfacial area per molecule is a very strong function of L and therefore of the number of branches per bottlebrush in this regime (# of branches $\sim$ $DP \sim L$). Consequently, the side chain asymmetry must become of less relative importance, because the effective interfacial area per chain is more dictated by pure number of branches per molecule. This would surely complicate the interpretation of experimental data if both blocks are not in the high L limit, because the effective asymmetry in terms of preferred interfacial area would be a combined function of branch length and branch number. We can use these considerations to predict that the side chain asymmetry in bottlebrush diblocks has a sizeable influence on the equilibrium morphologies provided that (1) the branch densities are not so large as to induce extreme backbone rigidity and prohibit non-lamellar phases and that (2) the backbone chains are sufficiently long in each block.

References

1. Ober, C. K.; Cheng, S. Z. D.; Hammond, P. T.; Muthukumar, M.; Reichmanis, E.; Wooley, K. L.; Lodge, T. P. *Macromolecules* **2009**, *42*, 465–471.

2. Sheiko, S. S.; Sumerlin, B. S.; Matyjaszewski, K. *Prog. Polym. Sci.* **2008**, *33*, 759–785.

3. Peng, S.; Bhushan, B. *RSC Advances* **2012**, *2*, 8557–8578.

4. Zhang, M.; Müller, A. H. E. *J. Polym. Sci. A Polym. Chem.* **2005**, *43*, 3461–3481.

5. Wintermantel, M.; Schmidt, M.; Tsukahara, Y.; Kajiwara, K.; Kohjiya, S. *Macromol. Rapid Commun.* **1994**, *15*, 279–284.

6. Wintermantel, M.; Gerle, M.; Fischer, K.; Schmidt, M.; Wataoka, I.; Urakawa, H.; Kajiwara, K.; Tsukahara, Y. *Macromolecules* **1996**, *29*, 978–983.

7. Iwawaki, H.; Urakawa, O.; Inoue, T.; Nakamura, Y. *Macromolecules* **2012**, *45*, 4801–4808.

8. Johnson, J. A.; Lu, Y. Y.; Burts, A. O.; Xia, Y.; Durrell, A. C.; Tirrell, D. A.; Grubbs, R. H. *Macromolecules* **2010**, *43*, 10326–10335.

9. Yang, Y. Q.; Guo, X. D.; Lin, W. J.; Zhang, L. J.; Zhang, C. Y.; Qian, Y. *Soft Matter* **2012**, *8*, 454–464.

10. Xu, H.; Sun, F. C.; Shirvanyants, D. G.; Rubinstein, M.; Shabratov, D.; Beers, K. L.; Matyjaszewski, K.; Sheiko, S. S. *Adv. Mater.* **2007**, *19*, 2930–2934.

11. Nese, A.; Lebedeva, N. V.; Sherwood, G.; Averick, S.; Li, Y.; Gao, H.; Peteanu, L.; Sheiko, S. S.; Matyjaszewski, K. *Macromolecules* **2011**, *44*, 5905–5910.

12. Rzayev, J. *ACS Macro Lett.* **2012**, *1*, 1146–1149.

13. Namba, S.; Tsukahara, Y.; Kaeriyama, K.; Okamoto, K.; Takahashi, M. *Polymer* **2000**, *41*, 5165–5171.

14. Vlassopoulos, D.; Fytas, G.; Loppinet, B.; Isel, F.; Lutz, P.; Benoit, H. *Macromolecules* **2000**, *33*, 5960–5969.

15. Tsukahara, Y.; Namba, S.-I.; Iwasa, J.; Nakano, Y.; Kaeriyama, K.; Takahashi, M. *Macromolecules* **2001**, *34*, 2624–2629.

16. Pakula, T.; Zhang, Y.; Matyjaszewski, K.; Lee, H.-I.; Boerner, H.; Qin, S.; Berry, G. C. *Polymer* **2006**, *47*, 7198–7206.

17. Hu, M.; Xia, Y.; McKenna, G. B.; Kornfield, J. A.; Grubbs, R. H. *Macromolecules* **2011**, *44*, 6935–6943.

18. Inoue, T.; Matsuno, K.; Watanabe, H.; Nakamura, Y. *Macromolecules* **2006**, *39*, 7601–7606.

19. Iwawaki, H.; Inoue, T.; Nakamura, Y. *Macromolecules* **2011**, *44*, 5414–5419.

20. Dalsin, S. J.; Hillmyer, M. A.; Bates, F. S. *ACS Macro Lett.* **2014**, *3*, 423–427.

21. Dalsin, S. J.; Hillmyer, M. A.; Bates, F. S. *Macromolecules* **2015**, *48*, 4680–4691.

22. Lee, S.; Spencer, N. D. *Science* **2008**, *319*, 575–576.

23. Li, X.; Prukop, S. L.; Biswal, S. L.; Verduzco, R. *Macromolecules* **2012**, *45*, 7118–7127.

24. Bolton, J.; Bailey, T. S.; Rzayev, J. *Nano Lett.* **2011**, *11*, 998–1001.

25. Miyake, G. M.; Piunova, V. A.; Weitekamp, R. A.; Grubbs, R. H. *Angew. Chem. Int. Ed.* **2012**, *51*, 11246–11248.

26. Miyake, G. M.; Weitekamp, R. A.; Piunova, V. A.; Grubbs, R. H. *J. Am. Chem. Soc.* **2012**, *134*, 14249–14254.

27. Sveinbjörnsson, B. R.; Weitekamp, R. A.; Miyake, G. M.; Xia, Y.; Atwater, H. A.; Grubbs, R. H. *P. Natl. Acad. Sci. USA* **2012**, *109*, 14332–14336.

28. Verduzco, R.; Li, X.; Pesek, S. L.; Stein, G. E. *Chem. Soc. Rev.* **2015**, *44*, 2405–2420.

29. Lee, H.-I.; Pietrasik, J.; Sheiko, S. S.; Matyjaszewski, K. *Prog. Polym. Sci.* **2010**, *35*, 24–44.

30. Gao, H.; Matyjaszewski, K. *J. Am. Chem. Soc.* **2007**, *129*, 6633–6639.

31.   Lanson, D.; Schappacher, M.; Borsali, R.; Deffieux, A. *Macromolecules* **2007**, *40*, 5559–5565.

32.   Helms, B.; Mynar, J. L.; Hawker, C. J.; Fréchet, J. M. J. *J. Am. Chem. Soc.* **2004**, *126*, 15020–15021.

33.   Neugebauer, D.; Zhang, Y.; Pakula, T.; Matyjaszewski, K. *Polymer* **2003**, *44*, 6863–6871.

34.   Zhang, M.; Breiner, T.; Mori, H.; Müller, A. *Polymer* **2003**, *44*, 1449–1458.

35.   Sumerlin, B. S.; Neugebauer, D.; Matyjaszewski, K. *Macromolecules* **2005**, *38*, 702–708.

36.   Börner, H. G.; Beers, K.; Matyjaszewski, K.; Sheiko, S. S.; Möller, M. *Macromolecules* **2001**, *34*, 4375–4383.

37.   Cheng, C.; Qi, K.; Khoshdel, E.; Wooley, K. L. *J. Am. Chem. Soc.* **2006**, *128*, 6808–6809.

38.   Matyjaszewski, K.; Qin, S.; Boyce, J. R.; Shirvanyants, D.; Sheiko, S. S. *Macromolecules* **2003**, *36*, 1843–1849.

39.   Bolton, J. M.; University at Buffalo: Doctoral Thesis, **2012**.

40.   Yamada, K.; Miyazaki, M.; Ohno, K.; Fukuda, T.; Minoda, M. *Macromolecules* **1999**, *32*, 290–293.

41.   Larson, R. G. *The Structure and Rheology of Complex Fluids*; Oxford University Press, **1999**.

42.   Macosko, C. W. *Rheology: Principles, Measurements, and Applications*; Wiley-VHC, **1994**.

43.   Berry, G. C.; Fox, T. G. *Adv. Polym. Sci.* **1968**, *5*, 261–357.

44.   Gahleitner, M. *Prog. Polym. Sci.* **2001**, *26*, 895–944.

45.   Lohse, D. J.; Milner, S. T.; Fetters, L. J.; Xenidou, M.; Hadjichristidis, N.; Mendelson, R. A.; García-Franco, C. A.; Lyon, M. K. *Macromolecules* **2002**, *35*, 3066–3075.

46.   Ajji, A.; Sammut, P.; Huneault, M. A. *J. Appl. Polym. Sci.* **2003**, *88*, 3070–3077.

47.   Stange, J.; Uhl, C.; Münstedt, H. *J. Rheol.* **2005**, *49*, 1059–1079.

48.   Tabatabaei, S. H.; Carreau, P. J.; Ajji, A. *Chem. Eng. Sci.* **2009**, *64*, 4719–4731.

49.   Flory, P. J. *J. Chem. Phys.* **1942**, *10*, 51–61.

50.   Huggins, M. L. *J. Am. Chem. Soc.* **1942**, *64*, 1712–1719.

51.   Hiemenz, P.C.; Lodge, T. P. *Polymer Chemistry, Second Edition*; Taylor & Francis, **2007**.

52.   Dudowicz, J.; Freed, K. F. *Macromolecules* **1991**, *24*, 5076–5095.

53.   Dudowicz, J.; Freed, K. F. *Macromolecules* **1996**, *29*, 8960–8972.

54.   Schweizer, K. S. *Macromolecules* **1993**, *26*, 6050–6067.

55.   Schweizer, K.; Curro, J. *Adv. Polym. Sci.* **1994**, *116*, 319–377.

56.   Graessley, W. W.; Krishnamoorti, R.; Reichart, G. C.; Balsara, N. P.; Fetters, L. J.; Lohse, D. J. *Macromolecules* **1995**, *28*, 1260–1270.

57.   Graessley, W.; Krishnamoorti, R.; Balsara, N.; Butera, R.; Fetters, L.; Lohse, D.; Schulz, D.; Sissano, J. *Macromolecules* **1994**, *27*, 3896–3901.

58.   Fredrickson, G.; Liu, A.; Bates, F. *Macromolecules* **1994**, *27*, 2503–2511.

59.   Bates, F. *Macromolecules* **1994**, *27*, 1065–1067.

60.   Bates, F. S.; Schulz, M. F.; Rosedale, J. H.; Almdal, K. *Macromolecules* **1992**, *25*, 5547–5550.

61.   Tsukahara, Y.; Inoue, J.; Ohta, Y.; Kohjiya, S. *Polymer* **1994**, *35*, 5785–5789.

62.   Chen, Y. Y.; Lodge, T. P.; Bates, F. S. *J. Polym. Sci. B Polym. Phys.* **2002**, *40*, 466–477.

63.   Chen, Y. Y.; Lodge, T. P.; Bates, F. S. *J. Polym. Sci. B Polym. Phys.* **2000**, *38*, 2965–2975.

64. Bates, F. S.; Hillmyer, M. A.; Lodge, T. P.; Bates, C. M.; Delaney, K. T.; Fredrickson, G. H. *Science* **2012**, *336*, 434–440.

65. Bates, F. S.; Fredrickson, G. H. *Phys. Today* **1999**, *52*, 32–38.

66. Lodge, T. P. *Macromol. Chem. Phys.* **2003**, *204*, 265–273.

67. Bates, F. S.; Fredrickson, G. H. *Annu. Rev. Phys. Chem.* **1990**, *41*, 525–557.

68. Matsen, M. W. *J. Phys.: Condens. Matter* **2002**, *14*, R21.

69. Lynd, N. A.; Meuler, A. J.; Hillmyer, M. A. *Prog. Polym. Sci.* **2008**, *33*, 875–893.

70. Meuler, A. J.; University of Minnesota: Doctoral Thesis, **2009**.

71. Matsen, M. W.; Bates, F. S. *J. Polym. Sci. B Polym. Phys.* **1997**, *35*, 945–952.

72. Macfarlane, R. J.; Kim, B.; Lee, B.; Weitekamp, R. A.; Bates, C. M.; Lee, S. F.; Chang, A. B.; Delaney, K. T.; Fredrickson, G. H.; Atwater, H. A.; Grubbs, R. H. *J. Am. Chem. Soc.* **2014**, *136*, 17374–17377.

73. Bolton, J.; Rzayev, J. *ACS Macro Lett.* **2012**, *1*, 15–18.

74. Runge, M. B.; Lipscomb, C. E.; Ditzler, L. R.; Mahanthappa, M. K.; Tivanski, A. V.; Bowden, N. B. *Macromolecules* **2008**, *41*, 7687–7694.

75. Runge, M. B.; Bowden, N. B. *J. Am. Chem. Soc.* **2007**, *129*, 10551–10560.

76. Xia, Y.; Olsen, B. D.; Kornfield, J. A.; Grubbs, R. H. *J. Am. Chem. Soc.* **2009**, *131*, 18525–18532.

77. Rzayev, J. *Macromolecules* **2009**, *42*, 2135–2141.

78. Moad, G.; Rizzardo, E.; Thang, S. H. *Aust. J. Chem.* **2005**, *58*, 379–410.

79. Moad, G.; Rizzardo, E.; Thang, S. H. *Polymer* **2008**, *49*, 1079–1131.

80. Chiefari, J.; Chong, Y. K. B.; Ercole, F.; Krstina, J.; Jeffery, J.; Le, T. P. T.; Mayadunne, R. T. A.; Meijs, G. F.; Moad, C. L.; Moad, G.; Rizzardo, E.; Thang, S. H. *Macromolecules* **1998**, *31*, 5559–5562.

81. Barner-Kowollik, C.; Buback, M.; Charleux, B.; Coote, M. L.; Drache, M.; Fukuda, T.; Goto, A.; Klumperman, B.; Lowe, A. B.; Mcleary, J. B.; Moad, G.; Monteiro, M. J.; Sanderson, R. D.; Tonge, M. P.; Vana, P. *J. Polym. Sci. A Polym. Chem.* **2006**, *44*, 5809–5831.

82. Moad, G.; Chong, Y. K.; Postma, A.; Rizzardo, E.; Thang, S. H. *Polymer* **2005**, *46*, 8458–8468.

83. Grubbs, R. H. *Handbook of Metathesis*; Wiley-VHC, **2003**.

84. Kress, J.; Osborn, J. A.; Greene, R. M. E.; Ivin, K. J.; Rooney, J. J. *J. Am. Chem. Soc.* **1987**, *109*, 899–901.

85. Sutthasupa, S.; Shiotsuki, M.; Sanda, F. *Polym J.* **2010**, *42*, 905–915.

86. Xia, Y.; California Institute of Technology: Doctoral Thesis, **2010**.

87. Schrock, R. R. *Acc. Chem. Res.* **1990**, *23*, 158–165.

88. Schrock, R. R.; Murdzek, J. S.; Bazan, G. C.; Robbins, J.; DiMare, M.; O'Regan, M. *J. Am. Chem. Soc.* **1990**, *112*, 3875–3886.

89. Love, J. A.; Sanford, M. S.; Day, M. W.; Grubbs, R. H. *J. Am. Chem. Soc.* **2003**, *125*, 10103–10109.

90. Webster, O. W. *Science* **1991**, *251*, 887–893.

91. Hadjichristidis, N.; Iatrou, H.; Pispas, S.; Pitsikalis, M. *J. Polym. Sci. A Polym. Chem.* **2000**, *38*, 3211–3234.

92. Baskaran, D.; Müller, A. H. E. Anionic Vinyl Polymerization. In *Controlled and Living Polymerizations: From Mechanisms to Applications*, Wiley-VHC, **2009**, 1–56.

93. Hyun, K.; Wilhelm, M.; Klein, C. O.; Cho, K. S.; Nam, J. G.; Ahn, K. H.; Lee, S. J.; Ewoldt, R. H.; McKinley, G. H. *Prog. Polym. Sci.* **2011**, *36*, 1697–1753.

94. Bailey, T. S.; University of Minnesota: Doctoral Thesis, **2001**.

95. Hahn, T. *International Tables for Crystallography, Space-Group Symmetry*; Wiley-VHC, **2005**.

96.   Lodge, T. *Mikrochim. Acta* **1994**, *116*, 1–31.

97.   Schappacher, M.; Deffieux, A. *Macromolecules* **2005**, *38*, 7209–7213.

98.   Feuz, L.; Strunz, P.; Geue, T.; Textor, M.; Borisov, O. *Eur. Phys. J. E.* **2007**, *23*, 237–245.

99.   Rose, J. M.; Mourey, T. H.; Slater, L. A.; Keresztes, I.; Fetters, L. J.; Coates, G. W. *Macromolecules* **2008**, *41*, 559–567.

100. Kaneko, H.; Kojoh, S.; Kawahara, N.; Matsuo, S.; Matsugi, T.; Kashiwa, N. **2004**, *213*, 335–345.

101. Tsukahara, Y.; Mizuno, K.; Segawa, A.; Yamashita, Y. *Macromolecules* **1989**, *22*, 1546–1552.

102. Tsukahara, Y.; Tsutsumi, K.; Yamashita, Y.; Shimada, S. *Macromolecules* **1990**, *23*, 5201–5208.

103. Tsukahara, Y.; Tsutsumi, K.; Okamoto, Y. *Makromol. Chem-Rapid* **1992**, *13*, 409–413.

104. Brant, P.; Narvaez, A. G.; Crowther, D. J. *Polymacromonomer and Process for Production Thereof*. U.S. Patent 8283428 B2, **2012**.

105. Brant, P.; Crowther, D. J.; Narvaez, A. G. *High Vinyl Terminated Propylene Based Oligomers*. U.S. Patent 8372930 B2, **2013**.

106. Kaneko, H.; Kojoh, S.-I.; Kawahara, N.; Matsuo, S.; Matsugi, T.; Kashiwa, N. *J. Polym. Sci. A Polym. Chem.* **2005**, *43*, 5103–5118.

107. Hong, S. C.; Jia, S.; Teodorescu, M.; Kowalewski, T.; Matyjaszewski, K.; Gottfried, A. C.; Brookhart, M. *J. Polym. Sci. A Polym. Chem.* **2002**, *40*, 2736–2749.

108. Mao, G.; Wang, J.; Clingman, S. R.; Ober, C. K.; Chen, J. T.; Thomas, E. L. *Macromolecules* **1997**, *30*, 2556–2567.

109. Lee, K. M.; Han, C. D. *Macromolecules* **2002**, *35*, 760–769.

110. Chung, T.; Raate, M.; Berluche, E.; Schulz, D. *Macromolecules* **1988**, *21*, 1903–1907.

111. Bracher, F.; Litz, T. *J. Prak. Chem.-Chem. Ztg.* **1996**, *338*, 386–389.

112. Kojoh, S. I.; Tsutsui, T.; Kioka, M.; Kashiwa, N. *Polym J.* **1999**, *31*, 332–335.

113. Moad, G.; Rizzardo, E.; Thang, S. H. *Material Matters* **2010**, *5*, 1–8.

114. Vougioukalakis, G. C.; Grubbs, R. H. *Chem. Rev.* **2010**, *110*, 1746–1787.

115. Trnka, T. M.; Grubbs, R. H. *Acc. Chem. Res.* **2001**, *34*, 18–29.

116. Grubbs, R. H. *Tetrahedron* **2004**, *60*, 7117–7140.

117. Wiberg, K. B. *Agnew. Chem. Int. Ed. Engl.* **1986**, *25*, 312–322.

118. Jha, S.; Dutta, S.; Bowden, N. B. *Macromolecules* **2004**, *37*, 4365–4374.

119. Anderson-Wile, A. M.; Coates, G. W.; Auriemma, F.; De Rosa, C.; Silvestre, A. *Macromolecules* **2012**, *45*, 7863–7877.

120. Xia, Y.; Kornfield, J. A.; Grubbs, R. H. *Macromolecules* **2009**, *42*, 3761–3766.

121. Li, Z.; Zhang, K.; Ma, J.; Cheng, C.; Wooley, K. L. *J. Polym. Sci. A Polym. Chem.* **2009**, *47*, 5557–5563.

122. Bielawski, C. W.; Grubbs, R. H. *Prog. Polym. Sci.* **2007**, *32*, 1–29.

123. Love, J. A.; Morgan, J. P.; Trnka, T. M.; Grubbs, R. H. *Angew. Chem. Int. Ed.* **2002**, *41*, 4035–4037.

124. Choi, T.-L.; Grubbs, R. H. *Angew. Chem. Int. Ed.* **2003**, *42*, 1743–1746.

125. Xu, Z.; Mays, J.; Chen, X.; Hadjichristidis, N.; Schilling, F.; Bair, H.; Pearson, D. S.; Fetters, L. J. *Macromolecules* **1985**, *18*, 2560–2566.

126. Montaudo, G.; Lattimer, R. P. In *Mass spectrometry of polymers*; CRC Press, **2002**, 498–499.

127. Fetters, L. J.; Kiss, A. D.; Pearson, D. S.; Quack, G. F.; Vitus, F. J. *Macromolecules* **1993**, *26*, 647–654.

128. Milner, S. T.; McLeish, T. *Macromolecules* **1997**, *30*, 2159–2166.

129. Milner, S. T.; McLeish, T. C. B. *Macromolecules* **1998**, *31*, 7479–7482.

130. Pakula, T.; Vlassopoulos, D.; Fytas, G.; Roovers, J. *Macromolecules* **1998**, *31*, 8931–8940.

131. Kharchenko, S. B.; Kannan, R. M. *Macromolecules* **2003**, *36*, 407–415.

132. Ruymbeke, E. V.; Muliawan, E. B.; Vlassopoulos, D.; Gao, H.; Matyjaszewski, K. *Eur. Polym. J.* **2011**, *47*, 746–751.

133. Snijkers, F.; Cho, H. Y.; Nese, A.; Matyjaszewski, K.; Pyckhout-Hintzen, W.; Vlassopoulos, D. *Macromolecules* **2014**, *47*, 5347–5356.

134. Lin, Y.; Zheng, J.; Yao, K.; Tan, H.; Zhang, G.; Gong, J.; Tang, T.; Xu, D. *Polymer* **2015**, *59*, 252–259.

135. Kempf, M.; Ahirwal, D.; Cziep, M.; Wilhelm, M. *Macromolecules* **2013**, *46*, 4978–4994.

136. Kirkwood, K. M.; Leal, L. G.; Vlassopoulos, D.; Driva, P.; Hadjichristidis, N. *Macromolecules* **2009**, *42*, 9592–9608.

137. Bailly, C.; Stephenne, V.; Muchtar, Z.; Schappacher, M.; Deffieux, A. *J. Rheol.* **2003**, *47*, 821.

138. Roovers, J.; Graessley, W. W. *Macromolecules* **1981**, *14*, 766–773.

139. Kapnistos, M.; Vlassopoulos, D.; Roovers, J.; Leal, L. G. *Macromolecules* **2005**, *38*, 7852–7862.

140. Daniels, D. R.; McLeish, T. C. B.; Crosby, B. J.; Young, R. N.; Fernyhough, C. M. *Macromolecules* **2001**, *34*, 7025–7033.

141. McLeish, T. C. B.; Allgaier, J.; Bick, D. K.; Bishko, G.; Biswas, P.; Blackwell, R.; Blottière, B.; Clarke, N.; Gibbs, B.; Groves, D. J.; Hakiki, A.; Heenan, R. K.; Johnson, J. M.; Kant, R.; Read, D. J.; Young, R. N. *Macromolecules* **1999**, *32*, 6734–6758.

142. van Ruymbeke, E.; Kapnistos, M.; Vlassopoulos, D.; Huang, T.; Knauss, D. M. *Macromolecules* **2007**, *40*, 1713–1719.

143. Park, S. J.; Shanbhag, S.; Larson, R. G. *Rheol. Acta* **2004**, *44*, 319–330.

144. Chen, X.; Rahman, M. S.; Lee, H.; Mays, J.; Chang, T.; Larson, R. *Macromolecules* **2011**, *44*, 7799–7809.

145. Lee, J. H.; Fetters, L. J.; Archer, L. A. *Macromolecules* **2005**, *38*, 10763–10771.

146. López-Barrón, C. R.; Brant, P.; Eberle, A. P. R.; Crowther, D. J. *J. Rheol.* **2015**, *59*, 865–883.

147. Burfield, D. R.; Doi, Y. *Macromolecules* **1983**, *16*, 702–704.

148. Williams, M. L.; Landel, R. F.; Ferry, J. D. *J. Am. Chem. Soc.* **1955**, *77*, 3701–3707.

149. Fetters, L. J.; Lohse, D. J.; Richter, D.; Witten, T. A.; Zirkel, A. *Macromolecules* **1994**, *27*, 4639–4647.

150. Fetters, L. J.; Lohse, D. J.; Colby, R. H. Chain Dimensions and Entanglement Spacings. In *Physical Properties of Polymers Handbook*; Springer New York, **2007**, 447–454.

151. Plazek, D. L.; Plazek, D. J. *Macromolecules* **1983**, *16*, 1469–1475.

152. Fetters, L. J.; Lohse, D. J.; García-Franco, C. A.; Brant, P.; Richter, D. *Macromolecules* **2002**, *35*, 10096–10101.

153. Plazek, D. J. *J. Rheol.* **1996**, *40*, 987–1014.

154. van Gurp, M.; Palmen, J. *Rheol. Bull.* **1998**, *67*, 5–8.

155. Trinkle, S.; Friedrich, C. *Rheol. Acta* **2001**, *40*, 322–328.

156. Trinkle, S.; Walter, P.; Friedrich, C. *Rheol. Acta* **2002**, *41*, 103–113.

157. McLeish, T. C.; Milner, S. T. *Adv. Polym. Sci.* **1999**, *143*, 195–256.

158. Lee, J. H.; Orfanou, K.; Driva, P.; Iatrou, H.; Hadjichristidis, N.; Lohse, D. J. *Macromolecules* **2008**, *41*, 9165–9178.

159. Hutcheson, S. A.; McKenna, G. B. *J. Chem. Phys.* **2008**, *129*, 074502.

160. Schröter, K.; Hutcheson, S. A.; Shi, X.; Mandanici, A.; McKenna, G. B. *J. Chem. Phys.* **2006**, *125*, 214507.

161. Plazek, D. J. *J. Polym. Sci. A2.* **1968**, *6*, 621–638.

162. Ngai, K. L.; Roland, C. M. *J. Chem. Phys.* **2013**, *139*, 036101.

163. de Gennes, P. G. *J. Phys.-Paris* **1975**, *36*, 1199–1203.

164. Klein, J.; Fletcher, D.; Fetters, L. J. *Nature* **1983**, *304*, 526–527.

165. Needs, R. J.; Edwards, S. F. *Macromolecules* **1983**, *16*, 1492–1495.

166. Frischknecht, A. L.; Milner, S. T. *Macromolecules* **2000**, *33*, 9764–9768.

167. Hsu, H.-P.; Paul, W.; Rathgeber, S.; Binder, K. *Macromolecules* **2010**, *43*, 1592–1601.

168. Pesek, S. L.; Li, X.; Hammouda, B.; Hong, K.; Verduzco, R. *Macromolecules* **2013**, *46*, 6998–7005.

169. Declet-Pérez, C.; University of Minnesota: Doctoral Thesis, **2014**.

170. Berry, G. C.; Kahle, S.; Ohno, S.; Matyjaszewski, K.; Pakula, T. *Polymer* **2008**, *49*, 3533–3540.

171. Neugebauer, D.; Zhang, Y.; Pakula, T.; Sheiko, S. S.; Matyjaszewski, K. *Macromolecules* **2003**, *36*, 6746–6755.

172. de Gennes, P. G. *J. Chem. Phys.* **1971**, *55*, 572–579.

173. Ball, R. C.; McLeish, T. *Macromolecules* **1989**, *22*, 1911–1913.

174. Rouse, P. E. *J. Chem. Phys.* **1953**, *21*, 1272–1280.

175. Zimm, B. H. *J. Chem. Phys.* **1956**, *24*, 269–278.

176. Hillmyer, M. A.; Bates, F. S. *Macromolecules* **1996**, *29*, 6994–7002.

177. Schmidt, S. C.; Hillmyer, M. A. *Macromolecules* **1999**, *32*, 4794–4801.

178. Hucul, D. A.; Hahn, S. F. *Adv. Mater.* **2000**, *12*, 1855–1858.

179. Bates, F. S. *Science* **1991**, *251*, 898–905.

180. Mai, Y.; Eisenberg, A. *Chem. Soc. Rev.* **2012**, *41*, 5969.

181. Gerle, M.; Fischer, K.; Roos, S.; Müller, A. H. E.; Schmidt, M.; Sheiko, S. S.; Prokhorova, S.; Möller, M. *Macromolecules* **1999**, *32*, 2629–2637.

182. Lecommandoux, S.; Chécot, F.; Borsali, R.; Schappacher, M.; Deffieux, A.; Brûlet, A.; Cotton, J. P. *Macromolecules* **2002**, *35*, 8878–8881.

183. Sun, G.; Cho, S.; Clark, C.; Verkhoturov, S. V.; Eller, M. J.; Li, A.; Pavía-Jiménez, A.; Schweikert, E. A.; Thackeray, J. W.; Trefonas, P.; Wooley, K. L. *J. Am. Chem. Soc.* **2013**, *135*, 4203–4206.

184. Gu, W.; Huh, J.; Hong, S. W.; Sveinbjornsson, B. R.; Park, C.; Grubbs, R. H.; Russell, T. P. *ACS Nano* **2013**, *7*, 2551–2558.

185. Zhang, H.; Zhang, Z.; Gnanou, Y.; Hadjichristidis, N. *Macromolecules* **2015**, *48*, 3556–3562.

186. Onbulak, S.; Rzayev, J. *Polym. Chem.* **2014**, *6*, 764–771.

187. Kim, J. G.; Coates, G. W. *Macromolecules* **2012**, *45*, 7878–7883.

188. Tang, H.; Li, Y.; Lahasky, S. H.; Sheiko, S. S.; Zhang, D. *Macromolecules* **2011**, *44*, 1491–1499.

189. Huang, K.; Rzayev, J. *J. Am. Chem. Soc.* **2009**, *131*, 6880–6885.

190. Albertin, L.; Stenzel, M.; Barner-Kowollik, C.; Foster, L. J. R.; Davis, T. P. *Macromolecules* **2004**, *37*, 7530–7537.

191. Dan, N.; Safran, S. A. *Adv. Colloid Interfac.* **2006**, *123*, 323–331.

192. Jain, S.; Bates, F. S. *Science* **2003**, *300*, 460–464.

193. Lai, C.; Russel, W. B.; Register, R. A.; Marchand, G. R.; Adamson, D. H. *Macromolecules* **2000**, *33*, 3461–3466.

194. Li, Z.; Ma, J.; Cheng, C.; Zhang, K.; Wooley, K. L. *Macromolecules* **2010**, *43*, 1182–1184.

195. Mahanthappa, M. K.; Bates, F. S.; Hillmyer, M. A. *Macromolecules* **2005**, *38*, 7890–7894.

196. Chremos, A.; Theodorakis, P. E. *ACS Macro Lett.* **2014**, *3*, 1096–1100.

197. Gu, W.; Huh, J.; Hong, S. W.; Sveinbjornsson, B. R.; Park, C.; Grubbs, R. H.; Russell, T. P. *ACS Nano* **2015**, *9*, 7729–7729.

198. Semenov, A. N. *Sov. Phys. JETP* **1985**, *61*, 733–742.

199. Mikhaylov, I. V.; Darinskii, A. A. *Polym. Sci. Ser. A* **2015**, *57*, 239–250.

200. Saitô, N.; Takahashi, K.; Yunoki, Y. *J. Phys. Soc. Jpn.* **1967**, *22*, 219–226.

201. Cao, Z.; Carrillo, J.-M. Y.; Sheiko, S. S.; Dobrynin, A. V. *Macromolecules* **2015**, *48*, 5006–5015.

202. Helfand, E.; Sapse, A. M. *J. Chem. Phys.* **1975**, *62*, 1327–1331.

203. Hong, S. W.; Gu, W.; Huh, J.; Sveinbjornsson, B. R.; Jeong, G.; Grubbs, R. H.; Russell, T. P. *ACS Nano* **2013**, *7*, 9684–9692.

204. Matsen, M. W. *J. Chem. Phys.* **1996**, *104*, 7758–7764.

205. Matsen, M.; Schick, M. *Phys. Rev. Lett.* **1994**, *72*, 2660–2663.

206. Matsen, M. W. *Eur. Phys. J. E* **2009**, *30*, 361–369.

207. Mitra, I.; Li, X.; Pesek, S. L.; Makarenko, B.; Lokitz, B. S.; Uhrig, D.; Ankner, J. F.; Verduzco, R.; Stein, G. E. *Macromolecules* **2014**, *47*, 5269–5276.

208. Chen, Y. Y.; University of Minnesota: Doctoral Thesis, **2013**.

209. Habersberger, B. M.; Lodge, T. P.; Bates, F. S. *Macromolecules* **2012**, *45*, 7778–7782.

210. Sadiku-Agboola, O.; Sadiku, E. R.; Adegbola, A. T.; Biotidara, O. F. *Materials Sciences and Applications* **2011**, *2*, 30–41.

211. Lohse, D. J. *Polym. Eng. Sci.* **1986**, *26*, 1500–1509.

212. Lohse, D. J.; Wissler, G. *J. Mater. Sci.* **1991**, *26*, 743–748.

213. Weimann, P. A.; Jones, T. D.; Hillmyer, M. A.; Bates, F. S.; Londono, J.; Melnichenko, Y.; Wignall, G. D.; Almdal, K. *Macromolecules* **1997**, *30*, 3650–3657.

214. Roland, C. M.; Ngai, K. L.; Santangelo, P. G.; Qiu, X. H.; Ediger, M. D.; Plazek, D. J. *Macromolecules* **2001**, *34*, 6159–6160.

215. Leibler, L. *Macromolecules* **1980**, *13*, 1602–1617.

216. Teo, Y. C.; Xia, Y. *Macromolecules* **2015**, *48*, 5656–5662.